



# Binary tomography reconstruction of bone microstructures from a limited number of projections

Lin Wang

## ► To cite this version:

Lin Wang. Binary tomography reconstruction of bone microstructures from a limited number of projections. Medical Imaging. Université de Lyon, 2016. English. NNT: 2016LYSEI054 . tel-01496931

HAL Id: tel-01496931

<https://theses.hal.science/tel-01496931>

Submitted on 28 Mar 2017

**HAL** is a multi-disciplinary open access archive for the deposit and dissemination of scientific research documents, whether they are published or not. The documents may come from teaching and research institutions in France or abroad, or from public or private research centers.

L'archive ouverte pluridisciplinaire **HAL**, est destinée au dépôt et à la diffusion de documents scientifiques de niveau recherche, publiés ou non, émanant des établissements d'enseignement et de recherche français ou étrangers, des laboratoires publics ou privés.

Numéro d'ordre : 2016LYSEI054

Année 2016

THÈSE

présentée devant

**L’Institut National des Sciences Appliquées de Lyon**  
Spécialité : pour obtenir

**LE GRADE DE DOCTEUR**

ÉCOLE DOCTORALE: ÉLECTRONIQUE, ÉLECTROTECHNIQUE, AUTOMATIQUE

par

**Lin WANG**

**Binary tomography reconstruction of  
bone microstructures from a limited  
number of projections**

Soutenue publiquement le 8 Juin 2016

Jury

**Thomas Rodet**

Professeur à l’ENS Cachan rattaché au SATIE

Rapporteur

**Jan Sijbers**

Professeur de University of Antwerp

Rapporteur

**Ali Mohammad-Djafari**

Directeur de recherche au LSS-CNRS

Examinateur

**Bruno Sixou**

Maitre de conférences HDR , INSA de Lyon

Directeur de thèse

**Françoise Peyrin**

Directeur de recherche CREATIS

Co-directeur de thèse

## Département FEDORA – INSA Lyon - Ecoles Doctorales – Quinquennal 2016-2020

SIGLE	ECOLE DOCTORALE	NOM ET COORDONNEES DU RESPONSABLE
CHIMIE	<b>CHIMIE DE LYON</b> <a href="http://www.edchimie-lyon.fr">http://www.edchimie-lyon.fr</a>  Sec : Renée EL MELHEM Bat Blaise Pascal 3 <sup>e</sup> etage <a href="mailto:secretariat@edchimie-lyon.fr">secretariat@edchimie-lyon.fr</a> Insa : R. GOURDON	M. Stéphane DANIELE Institut de Recherches sur la Catalyse et l'Environnement de Lyon IRCELYON-UMR 5256 Équipe CDFA 2 avenue Albert Einstein 69626 Villeurbanne cedex <a href="mailto:directeur@edchimie-lyon.fr">directeur@edchimie-lyon.fr</a>
E.E.A.	<b>ELECTRONIQUE, ELECTROTECHNIQUE, AUTOMATIQUE</b> <a href="http://edea.ec-lyon.fr">http://edea.ec-lyon.fr</a>  Sec : M.C. HAVGOUDOUKIAN <a href="mailto:Ecole-Doctorale.eea@ec-lyon.fr">Ecole-Doctorale.eea@ec-lyon.fr</a>	M. Gérard SCORLETTI Ecole Centrale de Lyon 36 avenue Guy de Collongue 69134 ECULLY Tél : 04.72.18 60.97 Fax : 04 78 43 37 17 <a href="mailto:Gerard.scorletti@ec-lyon.fr">Gerard.scorletti@ec-lyon.fr</a>
E2M2	<b>EVOLUTION, ECOSYSTEME, MICROBIOLOGIE, MODELISATION</b> <a href="http://e2m2.universite-lyon.fr">http://e2m2.universite-lyon.fr</a>  Sec : Safia AIT CHALAL Bat Darwin - UCB Lyon 1 04.72.43.28.91 Insa : H. CHARLES <a href="mailto:Safia.ait-chalal@univ-lyon1.fr">Safia.ait-chalal@univ-lyon1.fr</a>	Mme Gudrun BORNETTE CNRS UMR 5023 LEHNA Université Claude Bernard Lyon 1 Bât Forel 43 bd du 11 novembre 1918 69622 VILLEURBANNE Cédex Tél : 06.07.53.89.13 <a href="mailto:e2m2@univ-lyon1.fr">e2m2@univ-lyon1.fr</a>
EDISS	<b>INTERDISCIPLINAIRE SCIENCES-SANTE</b> <a href="http://www.ediss-lyon.fr">http://www.ediss-lyon.fr</a> Sec : Safia AIT CHALAL Hôpital Louis Pradel - Bron 04 72 68 49 09 Insa : M. LAGARDE <a href="mailto:Safia.ait-chalal@univ-lyon1.fr">Safia.ait-chalal@univ-lyon1.fr</a>	Mme Emmanuelle CANET-SOULAS INSERM U1060, CarMeN lab, Univ. Lyon 1 Bâtiment IMBL 11 avenue Jean Capelle INSA de Lyon 696621 Villeurbanne Tél : 04.72.68.49.09 Fax : 04 72 68 49 16 <a href="mailto:Emmanuelle.canet@univ-lyon1.fr">Emmanuelle.canet@univ-lyon1.fr</a>
INFOMATHS	<b>INFORMATIQUE ET MATHEMATIQUES</b> <a href="http://infomaths.univ-lyon1.fr">http://infomaths.univ-lyon1.fr</a>  Sec : Renée EL MELHEM Bat Blaise Pascal 3 <sup>e</sup> etage <a href="mailto:infomaths@univ-lyon1.fr">infomaths@univ-lyon1.fr</a>	Mme Sylvie CALABRETO LIRIS – INSA de Lyon Bat Blaise Pascal 7 avenue Jean Capelle 69622 VILLEURBANNE Cedex Tél : 04.72. 43. 80. 46 Fax 04 72 43 16 87 <a href="mailto:Sylvie.calabreto@insa-lyon.fr">Sylvie.calabreto@insa-lyon.fr</a>
Matériaux	<b>MATERIAUX DE LYON</b> <a href="http://ed34.universite-lyon.fr">http://ed34.universite-lyon.fr</a>  Sec : M. LABOUNE PM : 71.70 –Fax : 87.12 Bat. Saint Exupéry <a href="mailto:Ed.materiaux@insa-lyon.fr">Ed.materiaux@insa-lyon.fr</a>	M. Jean-Yves BUFFIERE INSA de Lyon MATEIS Bâtiment Saint Exupéry 7 avenue Jean Capelle 69621 VILLEURBANNE Cedex Tél : 04.72.43 71.70 Fax 04 72 43 85 28 <a href="mailto:Ed.materiaux@insa-lyon.fr">Ed.materiaux@insa-lyon.fr</a>
MEGA	<b>MECANIQUE, ENERGETIQUE, GENIE CIVIL, ACOUSTIQUE</b> <a href="http://mega.universite-lyon.fr">http://mega.universite-lyon.fr</a>  Sec : M. LABOUNE PM : 71.70 –Fax : 87.12 Bat. Saint Exupéry <a href="mailto:mega@insa-lyon.fr">mega@insa-lyon.fr</a>	M. Philippe BOISSE INSA de Lyon Laboratoire LAMCOS Bâtiment Jacquard 25 bis avenue Jean Capelle 69621 VILLEURBANNE Cedex Tél : 04.72 .43.71.70 Fax : 04 72 43 72 37 <a href="mailto:Philippe.boisse@insa-lyon.fr">Philippe.boisse@insa-lyon.fr</a>
ScSo	<b>ScSo*</b> <a href="http://recherche.univ-lyon2.fr/scso/">http://recherche.univ-lyon2.fr/scso/</a>  Sec : Viviane POLSINELLI Brigitte DUBOIS Insa : J.Y. TOUSSAINT <a href="mailto:viviane.polsinelli@univ-lyon2.fr">viviane.polsinelli@univ-lyon2.fr</a>	Mme Isabelle VON BUELTINGLOEWEN Université Lyon 2 86 rue Pasteur 69365 LYON Cedex 07 Tél : 04.78.77.23.86 Fax : 04.37.28.04.48

\*ScSo : Histoire, Géographie, Aménagement, Urbanisme, Archéologie, Science politique, Sociologie, Anthropologie

# Acknowledgements

I would like to thank everyone who gave their help and support during my PhD life in CREATIS.

First and sincere appreciation goes to Dr. Bruno Sixou and Dr. Françoise Peyrin for giving me this excellent opportunity to work in CREATIS and for their patient guidance and constant support throughout my PhD study. Apart from knowledge, I have learned serious attitude, scientific working mode and independent ability of thinking from them. This will help me a lot in my future work and life. Their encouragement and kindness really inspired me a lot when I was trapped in difficulties.

I would like to thank the jury members of my thesis, Dr.Thomas Rodet, Dr. Ali Mohammad-Djafari, Dr. Jan Sijbers, Dr. Bruno Sixou and Dr. Françoise Peyrin, for reading my thesis carefully, providing valuable comments and attending my defense.

I express my acknowledge to everyone in tomographic team for their greatly help, wonderful discussion and collaboration. Especially, I would like to show my sincerely thanks to Dr.Simon Rit and Dr. Cyril Mory for their altruistic training on RTK (Reconstruction Toolkit).

I am greatly grateful to my colleges in CREATIS. I would like to thank Pierre Ferrier and Fabrice Bellet for providing software support, linux training and operating system maintenance. I would like to thank Pierrick Serrand and Yasmina Salhi for making order missions, buying tickets and providing useful suggestions during my official business tips. I would like to thank Nadzeu Lao, Roxane Galmiche, and Isabelle Magnin for their help and support with the laboratory business during the last three years. I would like to thank all my former and present office colleges and all my friends for keeping my companies in France.

Many thanks go to China Scholarship council for the financial support that make the memorable PhD life possible for me.

Last but not least, I would like to give my sincere thanks to my dear parents and my little brother, who have supported me during my student life, encouraged me when I was in difficult time, especially during the most arduous task of thesis writing.



# Contents

<b>Contents</b>	<b>vii</b>
<b>Abstract</b>	<b>viii</b>
<b>Resume Etendu</b>	<b>xii</b>
<b>Abbreviations and Symbols</b>	<b>xxxix</b>
<b>I Background</b>	<b>1</b>
<b>1 Introduction</b>	<b>3</b>
1.1 Overview . . . . .	3
1.2 Thesis Objective . . . . .	4
1.3 Structure of the Thesis . . . . .	4
<b>2 Bone Medical Contexts and X-Ray Imaging</b>	<b>7</b>
2.1 Human Bones and Osteoporosis . . . . .	7
2.2 Bone Tissue and Bone Dynamics . . . . .	9
2.2.1 Hierarchical structure of bone . . . . .	9
2.2.2 Microstructure of bone tissue . . . . .	9
2.2.3 Bone dynamics . . . . .	11
2.3 X-Ray Imaging of Bone . . . . .	13
2.3.1 Radiography images of osteoporotic bone . . . . .	13
2.3.2 X-Ray Computed Tomography (CT) . . . . .	14
2.3.3 Dual X-ray Absorptiometry (DXA) . . . . .	14
2.3.4 Micro-CT and Synchrotron Radiation (SR) micro-CT . . . . .	15
2.4 Conclusion . . . . .	17
<b>3 Tomography Reconstruction Methods</b>	<b>19</b>
3.1 Physical Principle of X-Ray CT Reconstruction . . . . .	19
3.1.1 X-Ray attenuation . . . . .	19
3.1.2 CT projections . . . . .	20
3.1.3 Radon transform and tomography reconstruction . . . . .	21

3.2	Reconstruction Methods for Continuous Tomography . . . . .	22
3.2.1	Analytical image reconstruction methods . . . . .	22
3.2.2	Iterative image reconstruction methods . . . . .	23
3.2.3	Regularized reconstruction methods . . . . .	24
3.3	Reconstruction Methods for Discrete Tomography . . . . .	25
3.3.1	Discrete Algebraic Reconstruction Technique(DART) . . . . .	26
3.3.2	Statistical reconstruction methods . . . . .	27
3.3.3	Convex analysis methods . . . . .	31
3.4	Conclusion . . . . .	34
<b>II</b>	<b>Contribution</b>	<b>35</b>
<b>4</b>	<b>Binary Tomography Reconstruction of Bone Microstructure from a Limited Number of Projections</b>	<b>37</b>
4.1	Introduction . . . . .	37
4.2	Total Variation (TV) regularization and ADMM approach . . . . .	38
4.3	Level-set Regularization Algorithm of the Binary Tomography . . . . .	41
4.3.1	Level-set formulation of the binary tomography problem . . . . .	41
4.3.2	Piecewise Constant Level-set (PCLS) with an augmented Lagrangian approach . . . . .	42
4.4	Quantification and Error Criteria of the Binary Reconstructed Images . . . . .	43
4.5	Simulations and Discussions . . . . .	44
4.5.1	Simulation details . . . . .	45
4.5.2	Numerical results . . . . .	47
4.6	Conclusion . . . . .	64
<b>5</b>	<b>Stochastic Optimization Methods for Binary Tomography Reconstruction</b>	<b>67</b>
5.1	Introduction . . . . .	67
5.2	Stochastic Optimization Methods Based on Level-set and TV regularizations . . . . .	68
5.2.1	Global optimization strategy . . . . .	68
5.2.2	Stochastic optimization based on Level-set regularization method . . . . .	70
5.2.3	Stochastic optimization based on Total Variation regularization method . . . . .	72
5.3	Simulations and Discussions . . . . .	76
5.3.1	Simulation details . . . . .	76
5.3.2	Numerical results . . . . .	80
5.4	Conclusion . . . . .	95
<b>6</b>	<b>Binary Reconstruction with Total Variation with a box constraint method on 3D images</b>	<b>97</b>
6.1	Introduction . . . . .	97

6.2	3D Reconstruction with TV Regularization with a Box Constraint Method on RTK . . . . .	99
6.2.1	The implementation of TV regularization with a box constraint for 3D volumes . . . . .	100
6.2.2	TVbox-ADMM filter . . . . .	101
6.2.3	Basic global threshold method . . . . .	102
6.3	Numerical Simulations . . . . .	103
6.3.1	Simulation details . . . . .	103
6.4	Conclusion . . . . .	111
<b>7</b>	<b>Multi-level Reconstruction from a Limited Number of Projections</b>	<b>117</b>
7.1	Introduction . . . . .	117
7.2	Level-set Regularization for Multi-level Tomography . . . . .	118
7.2.1	New level-set regularization formulation . . . . .	118
7.2.2	Implementation of the level-set regularization approach . . . . .	119
7.3	Simulations and Discussions . . . . .	120
7.3.1	Simulation details . . . . .	120
7.3.2	Numerical results . . . . .	121
7.4	Conclusion . . . . .	124
<b>8</b>	<b>Conclusions and perspectives</b>	<b>127</b>
8.1	Conclusions . . . . .	127
8.2	Perspectives . . . . .	129
<b>Appendix</b>		<b>133</b>
<b>A</b>	<b>Mathematic Definitions of <math>L^2</math>-norm, <math>H_1</math>-norm and the least square prob- lem</b>	<b>133</b>
<b>B</b>	<b>Basic Notions of TV regularization</b>	<b>135</b>
<b>C</b>	<b>Appendix about Level-set Method</b>	<b>137</b>
<b>D</b>	<b>Cone Beam CT and image Physical Informations on RTK</b>	<b>139</b>
<b>Publications</b>		<b>143</b>
<b>Bibliography</b>		<b>155</b>

# Abstract

Imaging bone microarchitecture is important in the context of the diagnosis of osteoporosis, which is a frequent bone fragility disease. X-ray Computerized Tomography (CT) is well suited to image bone mineral tissue, however it is associated to X-ray dose deposition. Since a high spatial resolution is required to image a small bone trabeculae (about  $100 \mu\text{m}$ ), X-ray CT imaging of bone microarchitecture may be associated to a high radiation dose and a long scanning times. One way to reduce patient dose exposition is to limit the number of projections. However, this method makes the reconstruction problem highly ill-posed. A common approach to get a simpler problem is to reconstruct only a finite number of intensity levels, called discrete tomography. In this work, we investigate the discrete tomography methods, especially in the case of binary tomography, with applications to the reconstruction of bone microarchitecture.

Many approaches have been investigated to address the binary tomography problem. In our work, we consider variational regularization methods. Two types of Total Variation (TV) regularization approaches minimized with the Alternate Direction of Minimization Method (ADMM) and two schemes based on Level-set (LS) regularization methods are applied to two experimental bone cross-section images (pixel size:  $15 \mu\text{m}$ ) acquired with synchrotron micro-CT. Images of various sizes and with several additive Gaussian noise levels added to the raw projection data are used to study the efficiency of the regularization methods. The numerical experiments have shown that good reconstruction results were obtained with TV regularization methods and that level-set regularization outperforms the TV regularization for large bone image with complex structures. Yet, for both TV and LS methods, some reconstruction errors are still located on the boundaries and some regions are lost when the projection number is low. Local minima have been obtained with these deterministic methods.

A global optimization approach is necessary to improve the results. Stochastic perturbations can be a very useful way to escape the local minima. As a first approach, a stochastic differential equation based on level-set regularization was studied. This method improves the reconstruction results but only modifies the boundaries between the 0 and 1 regions. It is neither able to reveal the lost regions and it is not adapted to high noise levels. Then partial stochastic differential equation obtained with the TV regularization semi-norm were studied to improve the stochastic level-set method. The random change of the boundary are performed in a new way with the gradient or wavelet decomposition of the reconstructed image. Random topological changes are included to find the lost regions in the reconstructed images. In our work, the stochastic level-set and TV regularization methods were used to decrease the reconstruction errors obtained with the corresponding deterministic schemes and a large improvement was obtained. Moreover, for stochastic TV method, the microlocal analysis was also used to refine the reconstruction results.

At the end of our work, we extended the TV regularization method to 3D images with real data. This algorithm was implemented on RTK (Reconstruction Toolkit), an open

source reconstruction software developed in our team.

Finally, we also extended the level-set approach used for the binary tomography problem to the multi-level case. We compare the reconstruction results obtained with multi-level regularization or with the TV regularization method. The comparison is implemented on a simple Shepp-Logan phantom with several noise levels and different number of projections.

# Résumé

La reconstruction en tomographie discrète de la microstructure de l'os joue un rôle très important pour le diagnostic de l'ostéoporose, une maladie des os très fréquente. Le diagnostic clinique est basé sur l'absorbiométrie duale de rayons X. Avec la tomographie de rayons X, une résolution spatiale élevée avec des images reconstruites *in vivo* requiert une dose d'irradiation élevée et un temps de balayage long, ce qui est dangereux pour le patient. Une des méthodes pour résoudre ce problème est de limiter le nombre de projections. Cependant, avec cette méthode le problème de reconstruction devient mal posé. Une approche commune pour obtenir un problème plus simple est de reconstruire seulement un nombre fini de niveaux d'intensité. Dans ce travail, nous étudions ce problème de tomographie discrète et en particulier le problème de reconstruction tomographique binaire quand seulement deux niveaux sont considérés.

De nombreuses approches ont été étudiées pour le problème de tomographie binaire. Dans notre travail, nous considérons des méthodes de régularisation variationnelles. Deux types de régularisation par Variation Totale minimisées avec la méthode Alternate Direction of Minimization Method (ADMM) et deux schémas basés sur les méthodes de régularisation Level-set sont appliquées à deux images d'os expérimentales acquises avec un synchrotron (pixel size:  $15 \mu\text{m}$ ). Des images de tailles variées et avec différents niveaux de bruit Gaussien additifs ajoutés aux projections sont utilisées pour étudier l'efficacité des méthodes de régularisation. Les expériences numériques ont montré que de bons résultats de reconstruction sont obtenus avec la régularisation TV et que la méthode level-set dépasse la régularisation TV pour de grandes images d'os avec des structures complexes. Cependant, pour les méthodes TV et LS des erreurs de reconstruction sont encore situées sur les frontières et des régions sont perdues quand le nombre de projection est bas. Des minima locaux sont obtenus avec ces méthodes déterministes.

Une approche globale d'optimisation est nécessaire pour améliorer les résultats. Des perturbations stochastiques peuvent être un moyen très utile pour échapper aux minima locaux. Dans une première approche, une équation différentielle stochastique basée sur la régularisation level-set est étudiée. Cette méthode améliore les résultats de reconstruction mais ne modifie que les frontières entre les régions 0 et 1. Elle n'est pas capable de révéler les régions manquantes et elle n'est pas adaptée aux niveaux de bruit élevés. Ensuite une équation aux dérivées partielles stochastique est obtenue avec la régularisation TV pour améliorer la méthode stochastique level-set. Le changements aléatoires de la surface sont accomplis d'une nouvelle façon avec le gradient ou avec des décompositions en ondelettes de l'image reconstruite. Des changements topologique aléatoires sont inclus pour trouver les régions manquantes dans les images reconstituées. Dans notre travail, les méthodes de régularisation level-set et TV sont utilisées pour diminuer les erreurs de reconstruction obtenues avec les schémas déterministes et de grandes améliorations sont obtenues. De plus, pour la méthode TV stochastique l'analyse microlocale est aussi utilisée pour raffiner les résultats.

A la fin de notre travail, nous avons étendu la méthode de régularisation à des images 3D avec des données réelles. Cette algorithme a été implémenté avec RTK. Nous avons aussi étendu l'approche level-set utilisée pour la tomographie binaire au cas multi-level. Nous comparons les résultats de reconstruction obtenus avec la régularisation multi-level et avec la méthode TV. La comparaison est mise en oeuvre sur un simple Shepp-Logan avec différents niveaux de bruit et différents nombres de projections.

# Résumé étendu

## Partie I: Etat de l'art

### Chapitre 1: Introduction

**Résumé** L'ostéoporose est une forme de maladie des os qui conduit à des fractures. Selon des études de la fondation Internationale pour l'Osteoporose, il est établi que l'ostéoporose cause plus de 8.9 millions de fractures chaque année, ce qui correspond à une fracture toutes les 3 secondes. Au niveau microscopique, les principales caractéristiques de l'ostéoporose sont la taille réduite des travées dans l'os. Par conséquent l'étude de la microstructure de l'os est importante pour le diagnostic de l'ostéoporose.

La structure des travées dans l'os peut être imaginée par tomographie des rayons X, et de nombreuses recherches visent à réduire la dose et/ou le temps de pose. Une bonne méthode pour réduire la dose est de réduire le nombre d'angles de projections, ce qui fait du problème de reconstruction avec un nombre fini de niveaux d'intensité un problème inverse très mal posé.

Dans ce travail, nous utilisons des méthodes de régularisation par Level-set et par Variation Totale pour résoudre ce problème. Certaines erreurs de reconstruction sont localisées sur les bords des images et certaines régions ne sont pas du tout reconstruites. Des minima locaux sont obtenus. Par conséquent, il est très intéressant d'échapper au minima locaux pour trouver des optima globaux. Une méthode d'optimization globale est utilisée pour le problème de reconstruction. Dans ce travail, il est montré qu'une perturbation stochastique peut être utile pour échapper à ce minimum local pour trouver un optimum global.

**Objectif de la thèse** Le principal but de cette thèse est d'étudier les trois aspects suivants: 1) Développer des méthodes de reconstruction à partir d'un nombre limité de projections pour des images d'os à partir de régularisations Level-set (LS) et Total Variation (TV). 2) Utiliser des méthodes stochastiques pour une optimisation globale afin d'améliorer les résultats de reconstruction par les méthodes LS et TV en particulier quand existe un bruit élevé pour les données de projections. 3) Etendre la régularisation TV des images à des volumes 3D.

**Structure de la thèse** Le manuscrit est organisé de la façon suivante:

- Contexte: Cette partie comprend trois chapitres: présentation du contexte, généralités sur l'os humain, tomographie des rayons X et présentation des méthodes de reconstruction des images CT.
  - Chapitre 1: brève introduction du contexte général, but principal de la thèse et structure du manuscrit.

- Chapitre 2: ce chapitre décrit la structure hiérarchique, les fonctionnalités et les processus de remodelage et de réparation de l'os. En même temps, les relations entre le tissu osseux humain et les maladies de l'os comme l'ostéoporose sont introduites. Les avantages du rayonnement synchrotron pour la micro-CT par rapport au rayonnement usuel sont présenté à la fin de cette chapitre.
- Chapitre 3: ce chapitre explique les principaux principes de la tomographie par rayons X. A la fin de ce chapitre, nous présentons les méthodes de reconstruction pour les images CT.
- Contribution: Cette partie présente nos principales contributions au problème de reconstruction par tomographie binaire de la microstructure de l'os à partir d'un nombre limité de projections.
  - Chapitre 4: ce chapitre présente deux méthodes de régularisation, méthodes level-set et régularisation par Variation Totale. Les deux méthodes de régularisation sont comparées pour différents niveaux de bruit sur de petites et de grandes images avec des nombres de projections différents.
  - Chapitre 5: ce chapitre tente d'améliorer les résultats de reconstruction obtenus au chapitre 4 en utilisant une méthode d'optimisation stochastique. Nous montrons que les méthodes stochastiques sont très utiles pour une reconstruction obtenue avec un petit nombre de projections et un niveau de bruit élevé avec les méthodes déterministes LS et TV.
  - Chapitre 6: ce chapitre étend les méthodes de reconstruction TV des images 2D aux volumes 3D. Cette méthode a été implémentée avec le Reconstruction toolkit (RTK) développé par le laboratoire CREATIS.
  - Chapitre 7: ce chapitre vise à étendre l'algorithme level-set du cas binaire à la reconstruction de plus de deux niveaux de gris ("multi-level").
- Conclusion et perspectives:
  - Le chapitre 8 conclut ce manuscrit et donne une perspectives pour des travaux futurs.
- Annexes et Bibliographie.

## Chapitre 2: Tissu osseux et ostéoporose

L'ostéoporose est une maladie des os qui diminue la résistance des os et augmente le risque de fracture osseuse [Kanis *et al.* (1994), Golob and Laya (2015)]. La principale raison qui explique l'ostéoporose est la perte osseuse plus élevée que la moyenne, qui conduit à une déterioration de la micro-architecture du tissu osseux [Bonjour *et al.* (1994), Heaney *et al.* (2000)].

La méthode principalement utilisée pour le diagnostic de l'ostéoporose est reposé sur la mesure de la densité minérale osseuse (bone mineral density, BMD) [Guglielmi and Scalzo (2010)]. La méthode usuelle pour la mesurer est l'absorptiométrie de rayons X bi-énergie. Bien que la radiographie soit relativement insensible à la détection des premiers stades de la maladie et qu'elle requiert une perte importante de masse osseuse (environ 30%) pour apparaître sur les images de rayons X, la radiographie X usuelle est cependant utile, seule ou en conjonction avec la tomographie ou la RMN pour détecter la masse osseuse.

Le tissu osseux est un type de tissu conjonctif dense. Le tissu osseux est une structure dynamique composée de tissus vivants comme les cellules osseuses, de cellules graisseuses, de vaisseaux sanguins et de matériaux non vivants comme l'eau ou des minéraux [Dorozhkin (2010), Barkaoui and Hamblin (2011)]. Afin de comprendre les fonctions biologiques ou mécaniques des os, une approche multi-échelle est nécessaire [Barkaoui *et al.* (2014)]. Cinq niveaux [Sato and Webster (2004), Jung and Kleinheinz (2013)] de structure peuvent être distingués. En raison de la structure complexe de l'os, les propriétés mécaniques de l'os, en particulier au niveau de la micro et nanostructure restent mal comprises. Par conséquent, de nombreuses recherches ont été faites pour étudier les caractéristiques de l'os humain à ces deux niveaux. Les études de cette thèse insistent sur la structure des travées qui est reliée au diagnostic de l'ostéoporose, au niveau de la microstructure locale avec une échelle d'observation de 10 µm à 500 µm.

Au niveau macroscopique les os qui se fracturent usuellement suite à des problèmes d'ostéoporose incluent des os longs comme les os des avant bras, des os plats comme ceux de la hanche ou des os irréguliers comme ceux des vertèbres. Au niveau microscopique des structures osseuses, l'os humain est fait deux parties distinctes: les os corticaux et les os trabéculaires [Schaffler and Burr (1988)]. L'os cortical est appelé os compact, formant l'enveloppe de l'os humain et assurant la fonction mécanique de support et de protection. L'os compact est la partie la plus dense de l'os humain et contribue à 80% de la masse totale du squelette. L'os trabéculaire forme la partie intérieure de l'os que l'on trouve à l'extrémité des os longs comme le fémur ou dans des os irréguliers comme la hanche ou les vertèbres [Shi *et al.* (2010)]. L'os trabéculaire est un réseau complexe en forme d'éponge formé de travées, structures en forme de tige ou de plaque avec une épaisseur de l'ordre de 100-300 µm [Launey *et al.* (2010)].

Au niveau microscopique, l'os fibreux et l'os lamellaire sont les deux principales architectures de l'os cortical et de l'os trabéculaire. L'os fibreux est appelé os primaire. Il est immature avec un petit nombre de fibres orientées de collagène présentes initialement

quand l'os se forme. L'os fibreux est remplacé par l'os lamellaire rapidement qui est caractérisé par un alignement du collagène en lamelles. L'os lamellaire est appelé os secondaire. Il est très organisé en feuilles concentriques avec une proportion beaucoup plus faible en ostéocytes. L'os lamellaire est le type normal d'os adulte. Comparé à l'os fibreux, l'os lamellaire est beaucoup plus fort et moins flexible.

L'os est un matériaux dynamique. L'os change sa masse et sa structure constamment au cours de la vie avec trois mécanismes biologiques: croissance, modelage et remodelage. Le processus au cours duquel l'os fibreux est remplacé par l'os lamellaire joue un rôle très important dans les trois mécanismes biologiques et dans la réparation de l'os qui advient après les fractures. En particulier, le remodelage osseux est un processus qui dure tout au long de la vie quand l'ancien tissu osseux est remplacé par un os nouveau avec une production de calcium et de phosphate pour maintenir la masse osseuse [Clarke (2008), Hadjidakis and Androulakis (2006)]. Au cours de la première année de la vie, environ 100% du squelette est remplacé. Chez les adultes le remodelage osseux concerne environ 10% des os chaque année [Bon (2016)]. Dans les squelettes adultes, le remodelage osseux est équilibré par la disparition et l'enlèvement (résorption) de masse osseuse.

L'ostéoporose apparaît quand la résorption osseuse est plus grande que la formation osseuse. Les femmes les plus âgées sont particulièrement vulnérables à l'ostéoporose du fait du déclin des oestrogènes après la ménopause. D'autres facteurs qui conduisent à l'ostéoporose incluent un régime pauvre en calcium et en vitamine D ou le fait de fumer. Après des fractures, l'os commence un processus de réparation et la formation d'os à un taux plus élevé que la résorption osseuse. Ce processus demande beaucoup de temps. Le remodelage osseux prend de nombreux mois.

Le phénomène d'ostéoporose au niveau microscopique de la structure osseuse se traduit par une réduction des travées à l'intérieur de l'os [Guglielmi and Scalzo (2010)]. Les structures trabéculaires des os ostéoporotiques sont beaucoup plus fines que celle de l'os normal. La principale caractéristique radiographique de l'ostéoporose est l'amincissement cortical. La microtomographie par rayonnement synchrotron est utilisé dans la recherche sur les os pour l'analyse de la microstructure trabéculaire de l'os depuis longtemps [Nuzzo *et al.* (2002)b, Nuzzo *et al.* (2002)a]. En comparaison du système standard de microtomographie, le système de microtomographie synchrotron a plusieurs avantages [Flannery *et al.* (1987), Salomé *et al.* (1999)]. Il est basé sur un faisceau de rayons X réellement parallèles. L'intensité des rayons X est très forte et monochromatique pour l'énergie sélectionnée. ce qui permet d'éviter les artefacts de beam hardening et d'atteindre des résolutions spatiales très élevées. Le système développé sur la linge ID19 de l'ESRF [Salomé *et al.* (1999)] est de plus basé sur une géométrie parallèle 3D, ce qui permet également d'éviter les artefacts de reconstruction conique de la plupart des systèmes standards. Dans notre travail, nous avons considéré une géométrie parallèle car nous utilisons des données tomographiques issues de ce système.

### Chapitre 3: La reconstruction tomographique

La formation d'un image tomographique requiert l'acquisition de projections à partir de différents angles de vue [Peyrin and Douek (2013), Peter and Peyrin (2011), Jia *et al.* (2010), Sidky and Pan (2008), Ritschl *et al.* (2011), Duan *et al.* (2009)]. Un grand nombre de projections est requis pour reconstruire une image de haute qualité mais l'acquisition est alors associée à une dose importante dangereuse pour le patient. Un moyen efficace de diminuer la dose est de réduire le nombre d'angles de vues [Sidky and Pan (2006)]. Par conséquent, il est crucial de réduire le nombre de projections en imagerie dynamique ou quand la dose doit être réduite.

La reconstruction à partir d'un nombre limité de projections est un problème important en tomographie. Usuellement, le problème de reconstruction tomographique consiste à estimer un signal multidimensionnel  $f$  dans un espace de Hilbert  $H$  à partir de mesures de plus basse dimension de ses intégrale de ligne  $p$ . En tomographie discrète, la fonction à reconstruire prend un nombre discret de valeurs. La tomographie binaire est un cas particulier de la tomographie discrète, où l'object à reconstruire peut prendre seulement deux valeurs: 0 ou 1.

**Tomographie par rayons X** La tomographie par rayons X est une technique qui est d'une importance majeure dans les études sur le tissu osseux en fournissant une large gamme d'images biomédicales 3D avec différentes résolutions entre le millimètre jusqu'au nanomètre. Le principe fondamental de la tomographie par rayons X est basé sur l'atténuation des rayons X. L'imagerie par tomographie consiste à envoyer des rayons X sur un objet et à mesurer la décroissance de l'intensité des rayons X le long de chemins linéaires. Ce type de décroissance est caractérisé par la loi de Beer Lambert [Panetta (2016)].

La tomographie est très utile pour visualiser la structure à l'intérieur d'un object solide sans le détruire. Usuellement, le système de tomographie consiste en une source de rayons X, une géométrie de rotation par rapport à l'objet qui doit être imagé et une série de détecteurs qui sont utilisés pour mesurer l'intensité des rayons X transmis à travers l'object, mesure transformée en projection par un ordinateur. Alors, chaque projection correspond à la somme des valeurs de l'absorption le long du chemin des rayons X.

**Méthodes de reconstruction pour la tomographie** Soit  $\Omega \subset \mathbb{R}^2$  un domain ouvert et borné, le modèle mathématique pour la tomographie 2D est la transformée de Radon  $R$  [Natterer (1986)].

Il y a deux principales méthodes de reconstruction pour la tomographie:les méthodes analytiques et les méthodes itératives [Bruyant (2002)]. Usuellement, les algorithmes analytiques génèrent des images reconstruites précises seulement si un grand nombre de projections est disponible. Les algorithmes itératifs sont plus adaptés pour reconstruire des images à partir d'un nombre limité de projections, ce qui est très utile pour réduire la

dose de rayons X et diminuer le temps de collection des données. Cependant, ces schémas itératifs doivent être régularisés.

La première reconstruction analytique d'une image par rayons X a été proposée par Cormack en 1963 [Cormack (1963), Brooks and Di Chiro (1975)]. Les méthodes de reconstruction analytiques sont basées sur la considération des densités projetées avec les intégrales de ligne de rayons passant à travers l'object. Il existe de nombreuses méthodes pour déterminer les distribution de densité basées sur les transformées de Fourier, un développement en fonctions orthogonales [Cormack (1973), Inouye (1979), Mukundan *et al.* (2001)]. La méthode de reconstruction analytique la plus utilisée est la rétroprojection filtrée pour la tomographie parallèle 2D [Bruyant (2002), Zeng (2001), Kinahan and Rogers (1989)].

Dans le cadre des méthodes de reconstruction itératives, le système linéaire  $Rf = p^\delta$  reliant les données de projections et l'image à reconstruire est résolu itérativement. L'erreur quadratique moyenne  $E(f) = \|Rf - p^\delta\|^2$  entre les projections mesurées  $p^\delta$  et les projections de l'image  $f$  est calculée. Les méthodes de reconstruction algébriques (SIRT, ART, SART) [Gordon *et al.* (1970), Herman (2009), Batenburg and Sijbers (2009), Batenburg and Sijbers (2006), Kabiena (2015)] et les méthodes de régularisation (comme la variation totale (TV) [Rudin *et al.* (2013)], la régularisation par level-set (LS) donnent lieu à des algorithmes itératifs [Chan and Tai (2004), Chung *et al.* (2005), Fruhauf *et al.* (2005), DeCezaro *et al.* (2009), Sixou *et al.* (2013)]. Nous nous intéresserons surtout à des méthodes de régularisation TV et LS dans les chapitres suivants.

Dans le cas de la tomographie discrète, les images à reconstruire prennent un nombre fini de valeurs discrètes. Dans le processus de reconstruction, les valeurs des images sont discontinues. Il y a aussi deux types d'approches pour la tomographie discrète: analyse statistiques et analyse convexe des algorithmes de reconstruction. Les méthodes de reconstruction sont basées sur le principe de Bayes [Geman and Hwang (1986), Gindi *et al.* (1993)] et les champs de Markov aléatoires [Liao and Herman (2004), Nadabar and Jain (1996), Chalmond (1988), Weber *et al.* (2005)]. Le but principal de cette méthode est de maximiser la probabilité à posteriori  $P(f|p^\delta)$  [Tsui *et al.* (1991), Frieden (1972), Vu and Knuiman (2002), Bruyant (2002)]. Une autre approche possible pour résoudre le problème de tomographie discrète est de le formuler comme un problème convexe de projection sur un ensemble de domaines convexes ou avec une approche de différence de fonctions convexes et concaves (D.C. programming) [Schüle *et al.* (2005)b, Tao and An (1998), Schüle *et al.* (2005)c].

**Conclusion** En conclusion, ce chapitre présente les principes de tomographie par rayons X. La micro-tomographie avec le rayonnement synchrotron est un moyen utile pour l'analyse des travées au niveau microscopique de la structure hierachique de l'os. De nombreuses méthodes ont été proposées pour reconstruire une image de grande qualité avec une faible dose. Nous avons présenté les deux approches principales de reconstruction par des méthodes analytiques et algébriques. Une brève présentation des méthodes pour de reconstruc-

tion discrète est également donnée. A partir du prochain chapitre, nous nous concentrerons sur la reconstruction tomographique binaire de la microstructure de l'os avec un nombre limité de projections avec la Variation Totale et avec des méthodes de régularisation avec level-set.

## Partie II: Contribution

### Chapitre 4: La reconstruction tomographique binaire de microstructures de l'os à partir d'un nombre limité de projections

Dans ce chapitre, nous présentons deux méthodes de reconstruction binaires régularisées par Variation Totale ou par une méthode level-set ainsi que les détails de simulations et des résultats numériques.

**Tomographie binaire** Le problème de tomographie binaire peut s'écrire sous la forme d'un système linéaire sous-déterminé:

$$Rf = p^\delta \quad f = (f_1, \dots, f_n) \in \{0, 1\}^n \quad (1)$$

avec l'opérateur de Radon  $R$ , les valeurs de projections mesurées  $p^\delta$ , et les valeurs de pixels  $(f_i)_{i \leq i \leq n}$  de l'image avec la contrainte binaire  $f = (f_1, \dots, f_n) \in \{0, 1\}^2$ . C'est un problème inverse mal posé même si les valeurs des pixels ne sont pas continues. L'image reconstruite peut être très différente de l'image  $f$  en présence de bruit. Un moyen usuel de régulariser le problème de tomographie binaire consiste à constituer une fonctionnelle de régularisation  $E(f)$  avec un terme de fidélité aux données qui mesure l'accord entre les mesures et l'image reconstruite et un terme de régularisation  $J(f)$  qui impose un a priori sur la solution. Le terme d'attache aux données est usuellement basé sur la norme  $L_2$  et la fonctionnelle à minimiser peut être écrite comme:

$$E(f) = \frac{\mu}{2} \|Rf - p^\delta\|_{L_2}^2 + J(f) \quad (2)$$

Le paramètre  $\mu$  est le paramètre de régularisation qui équilibre la contribution du terme d'attache aux données et le terme de régularisation. Les projections mesurées bruitées  $p^\delta$  sont supposées bruitées avec un niveau de bruit  $\delta$ , satisfaisant  $\|p^\delta - p\|_2 \leq \delta$ .

**Méthodes** Ce chapitre considère la méthode de régularisation TV et la méthode de régularisation level-set pour le problème de tomographie discrète. Dans ce cas, l'opérateur direct est le projecteur de Radon.

**Méthode de Régulation TV** Nous partons de la régularisation TV sans et avec la contrainte convexe binaire sur la fonction à reconstruire [Becker *et al.* (2009), Chambolle and Pock (2011), Goldstein and Osher (2009)]. La régularisation isotrope TV basée sur un calcul de la norme  $L_1$  du gradient est définie par:

$$J_{TV}(f) = \int_{\Omega} |\nabla f(r)| dr = \int_{\Omega} \sqrt{f_x^2 + f_y^2} dx dy \quad (3)$$

$f_x$  et  $f_y$  sont les gradients sur les deux directions. La méthode de Lagrangien augmenté combinée avec la méthode Alternating Direction Minimization Method (ADMM) [Afonso

[*et al.* (2011), *Afonso et al.* (2010), *Ng et al.* (2010)] sont utilisées pour minimiser la fonctionnelle de régularisation  $E(f)$  pour obtenir l'image de reconstruction finale  $f$ . Le Lagrangien suivant est considéré:

$$\mathcal{L}(f, (g_i), (\lambda_i)) = \sum_i (\|g_i\|_2 - \lambda_i^t(g_i - D_i f) + \frac{\beta}{2} \|g_i - D_i f\|_2^2) + \frac{\mu}{2} \|p^\delta - Rf\|_2^2 \quad (4)$$

où  $\mu$  est le paramètre de régularisation ,  $\beta$  le paramètre Lagrangien.

Les multiplicateurs de Lagrange,  $(\lambda_i)_{1 \leq i \leq n}$  sont des vecteurs dans  $\mathbb{R}^{2n^2}$ . Pour chaque pixel  $i$ ,  $D_i f \in \mathbb{R}^2$  représente la différence finie au pixel  $i$  dans les directions horizontale et verticale,  $(g_i)_{1 \leq i \leq n}$  une inconnue auxiliaire associée au gradient. L'algorithme ADMM recherche le point selle du Lagrangien en itérant les équations suivantes:

$$\begin{aligned} g_i^{k+1} &= \arg \min_{g_i} \mathcal{L}(f^k, (g_i^k), (\lambda_i^k)) \\ f^{k+1} &= \arg \min_f \mathcal{L}(f, (g_i^{k+1}), (\lambda_i^k)) \\ \lambda_i^{k+1} &= \arg \min_{\lambda_i} \mathcal{L}(f^{k+1}, (g_i^{k+1}), (\lambda_i^k)) \end{aligned} \quad (5)$$

Dans ce travail, nous avons utilisé la norme TV isotrope et la norme  $L_2$  du gradient. Avec l'algorithme de minimisation alterné, les séquences  $(f^k, (g_i^k)_{1 \leq i \leq n}, (\lambda_i^k)_{1 \leq i \leq n})$  sont calculées avec le schéma suivant:

$$g_i^{k+1} = \max\left\{\|D_i f^k + \frac{1}{\beta}(\lambda_i^k)\| - \frac{1}{\beta}, 0\right\} \frac{D_i f^k + \frac{1}{\beta}(\lambda_i^k)}{\|D_i f^k + \frac{1}{\beta}(\lambda_i^k)\|} \quad (6)$$

Le nouveau itéré  $f^{k+1}$  est obtenu par le système linéaire suivant:

$$\left(\sum_i D_i^t D_i + \frac{\mu}{\beta} R^t R\right) f^{k+1} = \sum_i D_i^t \left(g_i^{k+1} - \frac{1}{\beta} \lambda_i^k\right) + \frac{\mu}{\beta} R^t p^\delta \quad (7)$$

Le multiplicateur de Lagrange  $(\lambda_i)$  est mise à jour avec:

$$\lambda_i^{k+1} = \lambda_i^k - \beta(g_i^{k+1} - D_i f^{k+1}) \quad (8)$$

La suite  $(f^k, (g_i^k), (\lambda_i^k))$  générée par l'algorithme ADMM converge vers un point de Kuhn-Tucker du problème  $E(f)$ ,  $(f^*, (g_i^*), (\lambda_i^*))$ , si  $(P)$  en a un . Si  $E(f)$  n'a pas de solution optimale, au moins l'une des suites diverge.

**Méthode de Level-set** Ensuite, une approche level-set avec un terme de régularisation  $H_1 - TV$  est aussi utilisée pour résoudre le problème nonlinéaire [*DeCezaro et al.* (2009), *DeCezaro et al.* (2013), *Sixou et al.* (2013), *Egger and Leitao (2009)*]. L'image  $f$  est alors représentée avec une distribution de Heaviside avec une fonction level-set  $\theta \in H_1(\Omega)$  comme  $f = H(\theta)$  égale à 1 si  $\theta > 0$  et 0 sinon. Par conséquent, la fonctionnelle de

régularisation peut s'écrire:

$$E(\theta) = \frac{\|p^\delta - RH(\theta)\|_2^2}{2} + \lambda F(\theta) \quad (9)$$

où  $F(\theta)$  est une fonctionnelle de régularisation pour la fonction level-set  $\theta$ . Dans ce travail, nous considérons une fonctionnelle de régularisation Total Variation- $H_1$ :

$$F(\theta) = \beta_1 |H(\theta)|_{TV} + \beta_2 \|\theta\|_{H_1}^2 = \beta_1 |H(\theta)|_{TV} + \beta_2 (\|\theta\|_{L_2}^2 + \|\nabla \theta\|_{L_2}^2) \quad (10)$$

Les paramètres de régularisation  $\beta_1, \beta_2$  déterminent les poids relatifs des différents termes de régularisation. Ensuite nous comparons les résultats et les erreurs de reconstruction obtenus avec la régularisation classique TV minimisée avec l'algorithme ADMM [Ng *et al.* (2010), Afonso *et al.* (2010), Afonso *et al.* (2011)] avec les deux méthodes de régularisation level-set. La comparaison entre les différentes méthodes est faite sur un simple disque et sur une section plus complexe d'os caractérisée par de larges régions homogènes mais aussi par des structures tubulaires.

Comme  $H$  est discontinue, il est nécessaire de considérer des minima généralisés de la fonctionnelle de régularisation dans l'implémentation numérique [Egger and Leitao (2009), DeCezaro *et al.* (2009)]. Dans ce travail, la fonction de Heaviside  $H$  est remplacée par l'approximation suivante:  $H_\epsilon$ :

$$H_\epsilon(x) = \frac{1+2\epsilon}{2}(\operatorname{erf}(x/\epsilon) + 1) - \epsilon \quad (11)$$

où  $\epsilon$  est une constante positive qui détermine l'échelle à laquelle la fonction est lissée. La fonctionnelle de régularisation lissée de Tikhonov est donnée par :

$$E_\epsilon(\theta) = \frac{\|RH_\epsilon(\theta) - p^\delta\|_2^2}{2} + \beta_1 |H_\epsilon(\theta)|_{TV} + \beta_2 \|\theta\|_{H_1}^2 \quad (12)$$

où  $|\cdot|_{TV}$  est la semi-norme de Variation Totale. Les minimiseurs des fonctionnelles de Tikhonov sont obtenus avec une condition d'optimalité du premier ordre pour la fonctionnelle lissée  $G(\theta) = 0$ , avec:

$$G(\theta) = H'_\epsilon R^*(RH_\epsilon(\theta) - p^\delta) + \beta_2(I - \Delta)(\theta) + \beta_1 \frac{\partial |H_\epsilon(\theta)|_{BV}}{\partial \theta} \quad (13)$$

où  $R^*$  est l'adjoint de l'opérateur de projection. La différentielle de  $|H_\epsilon(\theta)|_{TV}$  est donnée par [Tai and Chan (2004)]:

$$\frac{\partial |H_\epsilon(\theta)|_{TV}}{\partial \theta} = -\delta_D(\theta) \nabla \cdot \frac{\nabla \theta}{|\nabla \theta|} \quad (14)$$

où  $\delta_D$  est une distribution de Dirac.

Les solutions de la condition d'optimalité  $G(\theta) = 0$  sont obtenues avec une condition

de Gauss-Newton. A partir de  $\theta_k$ , la mise à jour  $\theta_{k+1} = \theta_k + \lambda\delta\theta$  est obtenue avec:

$$V_k^* V_k \delta\theta + \beta_2(I - \Delta)(\delta\theta) - \beta_1 \delta_D(\theta_k) \nabla \cdot \frac{\nabla \delta\theta}{|\nabla \theta_k|} = -G(\theta_k) \quad (15)$$

où  $V_k$  est l'opérateur  $V_k = RH'_\epsilon(\theta_k)$ . Ces systèmes linéaires symétriques sont résolus avec une méthode de gradient conjugué. Dans la formule précédente  $\lambda$  est un paramètre de relaxation.

**Simulations numériques** Dans nos simulations, l'opérateur de projection  $R$  est l'approximation discrète de la transformée de Radon, implémentée avec la Toolbox Matlab. Les méthodes de régularisation TV et LS sont appliquées à deux petites images de taille  $256 \times 256$  et à deux grandes images de taille  $512 \times 512$  avec une densité faible ou forte. La première image est un simple disque et les petites images d'os sont des coupes d'os reconstruites avec 400 projections avec l'algorithme FBP et ensuite seuillées. La comparaison des résultats de reconstruction sur le simple disque et sur la section d'os est utile pour comprendre l'effet de la complexité de la géométrie. Les grandes images sont reconstruites avec 729 projections. Dans les trois sections d'os, la taille pixel est  $15\mu\text{m}$ . Ces images sont considérées comme les images vraies.

Dans nos simulations, les images sont reconstruites à partir d'un nombre limité d'angles de projection  $M$  avec  $M = 20$  et  $M = 50$ . Des nombres de projection plus faibles comme  $M = 10$  ne sont pas considérés dans ce travail car les erreurs de reconstruction obtenues sur les frontières sont trop grandes. Pour toutes les images, les projections buitées  $p^\delta$  sont obtenues en ajoutant de bruit Gaussien avec un écart type  $\sigma_p$  aux projections non bruitées  $p$ . La distribution du bruit est caractérisée par une déviation standard  $\sigma_p$  ou par un rapport crête à crête signal sur bruit  $PPSNR$ . Ce niveau de bruit  $\delta$  peut être estimé avec  $\delta^2 = MN_r\sigma_p^2$  où  $N_r$  est le nombre de rayons X par angle de projection.

Les itérations sont stoppées quand la fonctionnelle de régularisation stagne. L'indice final des itérations  $m$  est déterminé par le critère d'arrêt  $\|f^{m+1} - f^m\|_2 / \|f^m\|_2 < 0.0001$ . Notre choix de l'indice optimal est basé sur le principe de discrepancy de Morozov [[Morozov \(1984\)](#)]. Pour la méthode de régularisation TV, il y a deux paramètres importants: le paramètre de régularisation  $\mu$  et le paramètre Lagrangien  $\beta$ . Le paramètre  $\beta$  contrôle la vitesse de convergence. L'image reconstruite  $f^m(\mu)$  obtenue à la fin du processus d'optimisation dépend seulement du paramètre de régularisation  $\mu$ . Dans nos simulations numériques, le paramètre de régularisation et le paramètre de Lagrange  $\beta$  sont sélectionnés quand la condition suivante est satisfaite  $\frac{\|Rf^m - p^\delta\| - \delta}{\delta} \leq \xi$ , with  $\xi = 0.01$ .

Dans l'algorithme level-set classique, la constante positive  $\epsilon$  qui contrôle la fonction de Heaviside lissée a été fixée à 0.03. Le paramètre de régularisation  $\beta_1$  a été fixé à 0 car le terme  $H_1$  domine le terme TV. De façon similaire à la méthodologie utilisée pour la régularisation TV, nous avons testés de nombreux paramètres pour l'algorithme level-set pour vérifier le principe de Morozov. Quand le minimum de terme d'attache aux données est bien au-dessus du niveau de bruit, le principe de Morozov ne peut être appliqué, mais une

bonne estimation des paramètres de régularisation optimaux est obtenue avec la méthode de la courbe en  $L$ .

**Résultats** Tout d'abord, les méthodes de régularisation isotrope et anisotrope TV avec une contrainte convexe additionnelle sont testées sur les images de section osseuse. En général, pour la régularisation TV avec contrainte convexe, il n'y a pas de différences entre les normes TV isotrope et anisotrope. Les résultats de reconstruction obtenus avec une norme isotrope sont parfois un peu meilleurs.

Pour l'image de disque, les résultats de reconstruction obtenus sans et avec une contrainte convexe sont très bons et sont presque les mêmes. La ligne de niveau 0 de l'image de disque est un cercle et est bien reconstruite par la régularisation TV qui tend à minimiser son périmètre [Aubert and Kornprobst (2006)]. Quand le niveau de bruit  $\sigma_p = 25.65$  est élevé, la régularisation TV sans contrainte convexe fonctionne mieux. Au contraire, pour le petite image d'os taille  $256 \times 256$ , avec une structure plus complexe, l'algorithme TV box donne une erreur normalisée  $E_m$  et un taux de misclassification  $MR_m$  minimales pour tous les niveaux de bruits étudiés.

Pour les petites images, les deux méthodes de régularisations TV donnent dans la plupart des cas les meilleurs résultats de reconstruction avec 20 ou 50 projections. Pour un faible nombre de projections, ( $M=20$ ) et un niveau de bruit élevé, l'approche LS peut dépasser la régularisation TV. Quand le problème est très mal posé et pour des structures complexes le terme TV qui favorise les structures en forme de disque n'est pas le plus efficace a priori.

La méthode de régularisation TV est la moins bonne pour de grandes images. La méthode TV fonctionne mal sur de grande sections avec des régions complexes et allongées. Des détails et des structures fines sont perdus avec l'a priori TV. La régularisation level-set inclut des contraintes qui favorisent les valeurs binaires et améliorent les résultats de reconstruction.

Tandis que la régularisation TV avec des contraintes convexes donne de meilleurs résultats de reconstruction que la régularisation TV sans contrainte sur les grosses images peu denses ou très denses. La méthode TV fonctionne mal sur les deux sections avec des structures complexes et des régions allongées.

**Conclusion** Dans ce chapitre, nous avons étudié le problème de la reconstruction en tomographie binaire de la microstructure de l'os à partir d'un nombre limité de projections en testant deux méthodes de régularisation: régularisation TV et méthode de régularisation avec level-set.

Pour les méthodes de régularisation TV, deux algorithmes ont été comparés. Le premier algorithme est la régularisation classique TV. Dans la seconde approche, une contrainte convexe a été ajoutée pour imposer la contrainte binaire. Les méthodes ont été implémentées avec l'algorithme ADMM. Pour la régularisation LS, la première méthode level-set est basée sur une représentation des fonctions à reconstruire avec une distribution

de Heaviside qui conduit à une formulation du problème de tomographie binaire comme un problème inverse non linéaire.

Les performances de ces algorithmes ont été comparées avec différents niveaux de bruits sur deux petites images (une image de disque et une image de coupe d'os obtenue par micro-CT) et deux grosses images (coupes peu denses et très denses d'images obtenue par micro-CT) avec différent nombres de projections. De bons résultats de reconstruction sont obtenus avec les méthodes de régularisation TV. Les résultats de reconstruction qui sont obtenus avec la méthode classique level-set et la méthode level-set constante par morceaux sont très similaires. La régularisation level-set dépasse la régularisation TV pour de larges images avec des structures complexes. Cependant, pour les méthodes de régularisation TV et LS, des erreurs de reconstruction sont encore présentes sur les frontières des images reconstruites et certaines régions sont perdues quand le nombre de projection est bas. La raison est que le problème de tomographie discrète est non convexe et l'image reconstruite correspond à un minimum local de la fonctionnelle non convexe de régularisation.

## Chapitre 5: Méthodes d'optimisation stochastiques pour la reconstruction de tomographie binaire

L'optimisation globale est un problème fréquent pour les problèmes inverses. Le but principal de ce chapitre est d'affiner les résultats de reconstruction obtenus avec TV ou LS méthodes déterministes. Il est très intéressant d'échapper à ce minimum local par des méthodes d'optimisation globale. La méthode de gradient stochastique est une méthode d'optimisation globale célèbre qui est bien connue dans le domaine de l'optimisation convexe [Bertsekas and Tsitsiklis (2000)]. L'idée principale de cette méthode est de combiner un flux de gradient et une perturbation stochastique pour échapper à l'un des minima locaux pour trouver les minima globaux [Gidas (1995), Parpas and Rustem (2009), Chow *et al.* (2009), T.S.Chiang and S.J.Shev (1987), Wang *et al.* (2014), Wang *et al.* (2015)].

La principale contribution de ce chapitre est d'utiliser des méthodes stochastiques level-set ou TV pour la tomographie binaire pour améliorer les images reconstruites obtenues avec le schéma déterministe correspondant.

**Méthodes** En premier lieu, les résultats de reconstruction obtenus avec la nouvelle méthode de régularisation level-set stochastique sont comparés avec ceux obtenus avec la méthode classique de recuit simulé [Cot *et al.* (1998), Catoni (1992)a, Azencott (1992)]. La méthode stochastique est basée sur la formulation de Stratanovitch en raison de l'évolution de la courbe frontière ou level-set zero qui est alors indépendante de la fonction level-set  $\theta$  utilisée pour la représenter [Prato and J.Zabczyk (1992)]. L'équation au dérivées partielles stochastique est:

$$d\theta(x, t) = \delta\theta(x, t) + \eta(t)|\nabla\theta(x, t)| \circ dW(t) \quad (16)$$

où  $\circ$  correspond à la convention de Stratanovitch et  $\delta\theta$  est le gradient de  $\theta$ . En utilisant la définition de l'intégrale de Stratanovitch, l'équation peut être transformée en l'équation différentielle stochastique de Itô suivante [Juan *et al.* (2006)]:

$$d\theta(x, t) = \delta\theta(x, t) + \eta(t)|\nabla\theta(x, t)|dW(t) + \frac{1}{2}\eta(t)(\Delta\theta(x, t) - |\nabla\theta(x, t)|\text{div}(\frac{\nabla\theta(x, t)}{|\nabla\theta(x, t)|})) \quad (17)$$

Ensuite une nouvelle approche TV stochastique est envisagé. Différents termes de bruits basés sur la régularisation stochastique TV sont comparés incluant un terme de bruit de frontière et une perturbation plus homogène basée sur le gradient du terme d'attache aux données de la fonctionnelle de régularisation. Dans cette partie, nous considérons un couplage entre ADMM et une diffusion stochastique:

$$df(t) = -\nabla\mathcal{L}(f, (g_i^{k+1}), h^{k+1}, (\lambda_i^k), \lambda_C^k)dt + \sigma(f(t), t)dW(t) \quad (18)$$

Nous introduisons dans la suite trois termes de bruit différents correspondant à des changements de forme et de topologie.

1) Un terme de bruit dépendant du gradient:

$$\sigma(f(t), t)dW(t) = \eta_1 \left( \frac{\partial f}{\partial x} dW_1(t) + \frac{\partial f}{\partial y} dW_2(t) \right) \quad (19)$$

où  $(W_k(t))_{k=1,2}$  sont des champs aléatoires indépendant de Wiener sur  $H$  avec une fonction de covariance continue  $C_k$  avec un noyau intégral borné  $r_k$ , et  $\eta_1$  une constante positive qui contrôle l'intensité du bruit.

2) Un bruit additif avec un opérateur de covariance adapté:

On considère un processus Wiener avec une fonction de covariance  $C$ ,  $W_C(t)$  avec la représentation suivante [Prato and J.Zabczyk (1992), Prévôt and Röckner (2007)]:

$$W_C(t) = \sum_{k=1}^{\infty} \sqrt{\eta_k} \omega_t^k \phi_k \quad (20)$$

où  $\{\omega_t^k\}$  est une séquence de mouvements Browniens unidimensionnels indépendant et identiques. Les fonctions propres  $\phi_k$  sont celles obtenues avec une décomposition en ondelette de la frontière. Les valeurs propres  $\{\eta_k\}_{k \in J}$  correspondent aux ondelettes de hautes fréquences utilisés pour la décomposition de la frontière sont fixées à une valeur constante  $\eta_2$ . Les autres valeurs propres de l'opérateur de covariance sont fixées à zero.

3) Un terme de bruit non linéaire dépendant du gradient est aussi considéré:

$$\sigma(f(t))dW(t) = \eta_3(1 - f(t))R^*(Rf(t) - p^n)dW(t) \quad (21)$$

où  $\eta_3$  est une constante positive et  $W(t)$  un champ aléatoire de Wiener avec un noyau borné. Ce terme de bruit est proportionnel au gradient des données de la fonctionnelle objectif.

En comparaison avec les méthodes de régularisation level-set stochastique qui modifient uniquement la forme des régions 0 et 1, l'originalité de la méthode stochastique TV est double. En premier lieu, le changement aléatoire de la frontière est mis en oeuvre d'une nouvelle façon avec le gradient de l'image ou avec des ondelettes. De plus, les changements aléatoires de topologie sont inclus pour mettre en évidence de nouvelles régions qui ne sont pas détectées avec des changements de forme. Les résultats numériques pour la méthode stochastique level-set et la régularisation TV sont illustrés sur des sections d'os pour différents niveaux de bruits et différents nombre de projections.

**Simulations numériques** Dans cette partie, l'opérateur de projection  $R$  est l'approximation discrète de la transformation de Radon implémentée avec la Matlab Image Toolbox. La méthode stochastique level-set et la méthode stochastique TV sont appliquées à deux petites images de taille  $256 \times 256$ . Pour les deux méthodes stochastiques, une diffusion intermittente est appliquée et les schémas déterministes et stochastiques sont appliqués successivement et de façon itérative. A la fin de chaque boucle déterministe ou stochastique, l'image est binarisée.

La méthode stochastique level-set a été testée sur l'image d'os de densité élevée pour  $M = 10$  et  $M = 15$  avec une déviation standard faible  $\sigma_p = 3$  and  $\sigma_p = 6.5$ . Le paramètre  $\epsilon$  est fixé à 0.03 pour une bonne précision. Le paramètre de régularisation  $\beta_1$  est fixé à 0 car le terme  $H_1$  domine le terme  $TV$ . Tout d'abord, un schéma de régularisatoin déterministe level-set est appliqué, partant d'une fonction level-set initiale  $\theta_0 = 0$  pour obtenir une image binaire reconstruite  $f_0$ . Les itérations sont stoppées quand les itérés stagnent  $\frac{\|f^{k+1} - f^k\|_2}{\|f^k\|_2} < 0.01$ . Les paramètres de régularisation sont choisis pour obtenir la meilleure décroissance de la fonctionnelle de régularisation. L'algorithme stochastique intermittent est ensuite appliqué à cette image initiale  $f_0$ . Le niveau de bruit  $\eta$  et le nombre d'itérations  $T$  sont choisis aléatoirement avec une distribution uniforme dans  $[0.01, 0.1]$  et  $[1, 100]$ . Quand la diffusion stochastique n'est pas appliquée, une méthode déterministe level-set est appliquée pendant 100 itérations.

La méthode stochastique TV est testée sur des images d'os de faible et haute densité avec une déviation standard  $\sigma_p = 20$  et  $\sigma_p = 20$ . Les images sont d'abord reconstituées avec une régularisation TV et avec un algorithme ADMM déterministe. Les itérations sont stoppées quand  $\|\frac{f^{k+1} - f^k}{f^k}\| < 0.01$ . Les images binaires finales obtenues à la fin du processus d'optimisation sont notées  $f_0$ . Les meilleurs paramètres  $(\mu, \beta)$  qui sont choisis satisfont le principe de Morozov [[Morozov \(1984\)](#)]. Le processus de Wiener de dimension infinie est approché par un champ Gaussien aléatoire sur une grille de l'image. La discréétisation des équations au dérivées partielles et du processus de Wiener sont mises en oeuvre avec des méthodes classiques de différence finie et avec la méthode de Euler-Maruyama [[Kloeden and Platen \(1992\)](#)]. L'algorithme stochasique est mise en oeuvre de façon alternative avec sa version déterministe sur des plages de temps aléatoire dans la gamme  $[0, T_{max}]$  avec  $T_{max} = 100$  et avec un bruit stochastique  $\eta_i$ , ( $i=1,2$  ou  $3$ ). Pour chaque type de bruit, les paramètres qui règlent la force du bruit  $\eta_1, \eta_2, \eta_3$  sont choisis par essais et erreur pour obtenir la meilleure décroissance du terme d'attache aux données  $\|Rf_b^k - p^\delta\|$ , où  $f_b^k$  est la binarisation de l'image en niveaux de bruit.

**Résultats** A la fin des simulations numériques du level-set stochastique, les erreurs sur la frontière de l'image sont beaucoup plus faibles. L'évolution continue de la frontière est plus efficace que l'approche par chaine de Markov. De meilleurs résultats de reconstruction sont obtenus avec un algorithme level-set stochastique plutôt qu'avec une minimisation par recuit simulé avec les mêmes conditions initiales et avec le même nombre d'itérations, pour tous les niveaux de bruit et tous les nombres de projections. Cependant, la méthode stochastique level-set correspond à une évolution de la forme et ne modifie pas la topologie des régions de 0 et de 1 des images reconstruites. L'amélioration de la reconstruction avec les méthodes stochastiques level-set n'est pas claire pour les images de faibles densité avec de nombreuses régions manquantes dans la première image reconstruite et aussi pour les niveaux de bruit les plus élevés.

De façon similaire aux résultats de reconstruction avec la méthode level-set déterministe, certaines erreurs sont encore présentes sur les frontières des régions de l'image

obtenues avec l'algorithme TV déterministe. En particulier, pour l'image d'os de faible densité, de grandes régions ont disparu de l'image restaurée. Pour les images denses, une amélioration importante a été obtenue pour la méthode stochastique TV qui concentre le bruit sur les frontières et les meilleurs résultats de reconstruction sont obtenus avec la méthode stochastique qui ajoute aussi du bruit proportionnel à la dérivée du gradient de l'image en niveaux de gris. Pour les images peu denses, de nombreuses structures d'os sont perdues dans la première image  $f_0$  obtenue avec la méthode TV déterministe. Ajouter simplement du bruit stochastique à la frontière semble inutile. La raison est que le bruit de frontière stochastique se concentre sur la dérivée de forme et n'est pas capable de trouver les régions perdues. Ajouter du bruit homogène en même temps conduit à une meilleure reconstruction. Des régions perdues sont retrouvées à la fin du processus d'optimisation global.

**Conclusion** Ce travail compare de nouvelles méthodes de diffusion pour améliorer les images reconstruites binaires de sections d'os avec un faible nombre de projections. Une première image reconstruite est obtenue avec les méthodes déterministes de régularisation level-set ou TV. Ensuite cette image est améliorée avec une diffusion intermittente. Dans l'algorithme stochastique level set, la restauration est améliorée avec une équation aux dérivées partielles stochastique basée sur une formulation de Stratanovitch. Dans la méthode TV stochastique, le bruit de frontière est implémenté avec une estimation du gradient par différences finies ou avec une décomposition en ondelette et avec un bruit homogène proportionnel au gradient du terme d'attache aux données. Les méthodes stochastiques basées sur la régularisation level-set et TV ont beaucoup amélioré les images reconstruites si elles sont adaptées aux différentes conditions. L'algorithme stochastique level-set conduit à une amélioration importante de la reconstruction sur les frontières entre les régions 0 ou 1. Cette méthode est très utilisée pour les faibles niveaux de bruit mais ne donne pas des reconstructions améliorées pour les niveaux de bruit les plus élevés et pour les images de faible densité. Pour les niveaux de bruit plus élevés, l'approche stochastique TV est plus efficace car elle conduit à une modification des frontières mais elle révèle aussi de nouvelles régions dans l'image quand deux types de bruit sont inclus.

## Chapitre 6: La reconstruction binaire avec l'algorithme de Variation Totale sur les images 3D

Nous avons étudié les performances, avantages et désavantages de la méthode de régularisation par Variation Totale et de la méthode level-set pour la reconstruction binaire à partir d'un nombre limité de projections pour des images 2D et comment améliorer les résultats de reconstruction avec un méthode stochastique dans les chapitre précédents. Nous tentons d'étendre ces méthodes à des volumes 3D pour voir si les méthodes proposées peuvent être utiles en 3 dimensions. Dans ce travail, nous avons choisi RTK (Reconstruction Toolkit) [Rit et al. (2014)] comme plateforme pour nos reconstruction 3D en raison de ses avantages. RTK est une plateforme en libre accès avec des méthodes de reconstruction pour une géométrie cône beam basées sur ITK (Insight Toolkit) et utilisant un code GPU. Il faut implémenter un algorithme de reconstruction sur RTK en utilisant un filtre constitué de plusieurs sous filtres dans une séquence correcte et insérant ce filtre dans une pipeline RTK. La tâche de calcul sera implémentée de façon automatique avec RTK et la sortie sera obtenue à la fin du processus de reconstruction.

**Méthode** Si nous voulons implémenter la régularisation TV avec une contrainte convexe (TVbox) sur RTK, la première chose importante est de décider de la suite des implémentations dans l'algorithme TV sur RTK. La seconde tâche importante est de concevoir un filtre TV-ADMM suivant la séquence des implémentations de l'algorithme TV avec les entrées: paramètre de régularisation  $\mu$ , paramètre Lagrangien  $\beta$ , données de projections bruitées  $p^\delta$ , volume initial 3D vide  $f_0$  et géométrie CBCT.

**Algorithme de régularisation TV regularization pour des volumes 3D** La fonctionnelle de régularisation TV avec une contrainte convexe  $E(f)$  pour des reconstructions 3D est la même que celle de la reconstruction 2D:

$$E(f) = \frac{\mu}{2} \|Rf - p^\delta\|_{L_2}^2 + J_{TV}(f) \quad s.t. \quad f \in [C_0, C_1]^n \quad (22)$$

$[C_0, C_1]$  est un set convexe. Le terme de régularisation isotrope TV  $J_{TV}(f)$  basé sur le calcul de la norme  $L_1$  du gradient des volumes discret 3D  $f$  est défini par:

$$J_{TV}(f) = \nabla f = \sum_{v=1}^V \sqrt{[\nabla_x f(v)]^2 + [\nabla_y f(v)]^2 + [\nabla_z f(v)]^2} \quad (23)$$

où  $v$  est la position du voxel et  $V$  le nombre total de voxels dans le volume  $f$ . Dans cette section, la méthode de Lagrangien augmenté avec la mise à jour méthode de minimization par Directions Alternées (ADMM) ) [Afonso et al. (2011), Afonso et al. (2010), Ng et al. (2010)] est utilisée pour minimiser la fonctionnelle de régularisation TV  $E(f)$  pour obtenir le volume final reconstruit  $f$ .

Le problème de trouver  $\arg \min_f E(f)$  est équivalent au problème sous contrainte:

$$\begin{aligned} \mathcal{L}(f, (g), h, (\lambda), \lambda_C) = & \sum_{v=1}^V (\|g_v\|_2 - \lambda^t(g - \nabla f) + \frac{\beta}{2}\|g - \nabla f\|_2^2) + \frac{\mu}{2}\|p^\delta - Rf\|_2^2 \\ & + I_C(h) + \frac{\beta}{2}\|h - f\|_2^2 - \lambda_C^t(h - f) \quad (24) \\ g &= \nabla f \\ h &= I_c(f) \in [C_0, C_1]^n \end{aligned}$$

**Filtre TVbox-ADMM avec RTK** La chose la plus importante pour constituer un filtre TV-ADMM sur RTK est la combinaison d'une suite de sous-filtres. Par conséquent, les étapes de chaque itération ADMM pour la recherche du point selle du Lagrangian augmenté sont cruciales:

- Etape1: minimisation  $\mathcal{L}(f, (g), h, (\lambda), \lambda_C)$  pour  $g^k$ ;
- Etape2: minimisation  $\mathcal{L}(f, (g), h, (\lambda), \lambda_C)$  pour  $h^k$ ;
- Etape3: mise à jour des multiplicateurs de Lagrange  $\lambda^k$  et  $\lambda_c^k$ ;
- Etape4: mise à jour de  $f^k$  avec un algorithme de gradient conjugué pour résoudre le problème inverse  $Af = b$ .

**Simulations numériques** Dans nos expériences, l'opérateur de projection  $R$  est l'approximation discrète de la transformée de Radon, qui est implémentée sur RTK. La méthode de régularisation TV avec une contrainte convexe est appliquée sur un phantôme Shepp-Logan de taille  $256 \times 256 \times 256$  et un volume trabéculaire 3D de  $627 \times 627 \times 32$  reconstruit avec l'algorithme FDK. Les volumes binaires ont été obtenus par une simple méthode de seuillage. Afin d'obtenir les meilleurs résultats de reconstruction, le choix des meilleurs paramètres de régularisation est aussi basé sur le principe de discrepancy de Morozov [Morozov (1984)], satisfaisant  $\|Rf - p^\delta\| \approx \delta$ , où  $\delta$  a été estimé par  $\delta = \sqrt{MN_r}\sigma_p$ . Les itérations sont stoppées quand la fonctionnelle de régularisation stagne. L'indice final  $m$  est déterminé par la condition d'arrêt des itérations  $\|f^{m+1} - f^m\| / \|f^m\|_2 < 0.0001$ .

La fantôme Shepp-Logan avec une taille  $256 \times 256 \times 256$  et une résolution de voxel de 2 mm a été reconstruit à partir de 400 angles de projections et leur origines localisent sur  $(-255, -255, -255)$ mm. La distance de la source de rayons X au détecter (SDD) est 1536mm, la distance de la source de rayons X au centre de l'objet (SID) est 1000mm pour la configuration de la géométrie du système CBCT.

Les données de projection réelle, de taille  $627 \times 32$  et avec une résolution de  $15 \mu\text{m}$ , ont été obtenues par découpe et sous-échantillonnée avec un facteur 2, à partir d'une donnée expérimentale de 3000 projection CBCT au format ESRF de taille  $1974 \times 1100$  acquis avec une résolution de  $7.5 \mu\text{m}$ . Le volume trabéculaire 3D de taille  $627 \times 627 \times 32$  a été reconstruit. Les origines du volume trabéculaire 3D localisent est sur  $(-0.47, -0.47, 0.39)$ cm. La distance de la source de rayons X au détecter (SDD) est 100.01m, la distance de la source de rayons X au centre de l'objet (SID) est 100m pour la configuration de la géométrie du système CBCT, le décalage de la source de rayons X à l' $x$  direction est -0.74cm.

Pour le fantôme de Shepp-Logan simple, la méthode TV box a été testée pour  $M = 10$ ,  $M = 15$  et  $M = 20$  projections également espacées et bruitées, avec  $N_r = 256 \times 256$  rayons par angle de projection, avec un bruit Gaussien ajouté aux projections. La distribution du bruit est caractérisée par la déviation standard du bruit  $\sigma_p = 6, 11, 23$  et le rapport signal sur bruit  $PPSNR = 13.6dB, 9.5dB, 5.25dB$ . De plus, l'algorithme TV box a aussi été appliqué à des volumes 3D trabéculaires avec une microstructure complexe pour vérifier l'efficacité de la méthode avec RTK. La méthode a été testée avec  $M = 200$  et  $M = 600$  projections bruitées et  $N_r = 627 \times 32$  rayons par projection.

**Résultats and Conclusion** En conclusion, il y a de claires corrélations entre la décroissance du terme de écart  $\|Rf - p^\delta\|$  et la décroissance du taux de mauvais classification  $MR$  et des erreurs de reconstruction  $\|f - f^*\|/\|f^*\|$  pour le Shepp-Logan et pour le volume osseux 3D.

Dans ce chapitre, nous avons montré à nouveau que la méthode de régularisation TV box est très intéressant pour obtenir des informations sur les bords d'une structure simple approximant une sphère. Pour le fantôme Shepp-Logan, quand le niveau de bruit est bas, seule quelques projections comme pour  $M = 20$  sont nécessaires pour obtenir un bon résultat de reconstruction. Pour des structures complexes, plus de projections sont nécessaires pour obtenir une reconstruction acceptable.

Avec la décroissance du nombre de projections ou l'augmentation du niveau de bruit sur les données de projections, de grandes erreurs de reconstruction sont obtenues sur les surfaces des volumes reconstruits. Une optimisation globale est nécessaire pour améliorer ces mauvais volumes reconstruits. A l'avenir, nous tentrons d'étendre la diffusion stochastique à des images 3D pour améliorer les résultats de reconstruction.

## Chapitre 7: La reconstruction multi-niveau à partir d'un nombre limité de projections

Usuellement, le problème de tomographie discrète est considéré pour le cas binaire [Wang et al. (2014), Wang et al. (2016), Sixou et al. (2013)]. Cependant, il y a peu d'études pour la reconstruction tomographique d'images ayant plus de deux niveaux de gris. Dans ce chapitre, nous considérons ce problème. Il est formulé comme un problème d'optimisation de forme avec plusieurs fonctions level-set et régularisé avec des termes de type Total-Variation-Sobolev. Les résultats de reconstruction obtenus avec la nouvelle approche level-set sont comparés avec ceux obtenus avec la méthode de régularisation TV ADMM. Les simulations sont appliquées sur un fantôme Shepp-Logan de taille  $128 \times 128$  avec plusieurs nombre de projections et deux bruits additifs Gaussiens sur les données de projection.I

**Méthode** Dans ce travail, nous considérons seulement le cas de trois niveaux  $f_1$ ,  $f_2$  et  $f_3$  pour la fonction  $f$ . Nous supposons que l'image  $f$  à reconstruire peut être représentée par deux fonctions level set  $\theta_1$  et  $\theta_2$ :

$$f = f_1(1 - H(\theta_1))(1 - H(\theta_2)) + f_2H(\theta_1)H(\theta_2) + f_3H(\theta_2)(1 - H(\theta_1)) \quad (25)$$

où les deux fonctions level-set  $\theta_1$  et  $\theta_2$  appartiennent à l'espace de Sobolev du premier ordre. Par rapport à  $\theta_1$  and  $\theta_2$ , le problème de reconstruction devient non linéaire. La fonctionnelle de régularisation à minimiser peut s'écrire:

$$E(\theta_1, \theta_2) = \frac{\|RH(\theta_1, \theta_2) - p^\delta\|_2^2}{2} + \alpha(F(\theta_1, \theta_2)) \quad (26)$$

où  $F$  est le terme de régularisation pour les fonction level-set. Dans ce travail, nous avons considéré une fonctionnelle de régularisation Total Variation- $H_1$  pour chaque fonction level set [Egger and Leitao (2009), DeCezaro et al. (2009)]:

$$F(\theta_1, \theta_2) = \beta_1|H_\epsilon(\theta_1)|_{TV} + \beta_2\|\theta_1\|_{H_1}^2 + \gamma_1|H_\epsilon(\theta_2)|_{TV} + \gamma_2\|\theta_2\|_{H_1}^2 \quad (27)$$

Dans l'implémentation numérique, il est nécessaire de remplacer la fonction de Heaviside  $H$  et la fonction de Dirac  $\delta$  par des approximations lissées. L'approximation suivante est aussi utilisée pour la méthode multi-level:

$$H_\epsilon(x) = \frac{1+2\epsilon}{2}(erf(x/\epsilon) + 1) - \epsilon \quad (28)$$

où  $\epsilon$  est une constante réelle positive. Nous avons donné des valeurs identiques aux paramètres  $\epsilon_1$ ,  $\epsilon_2$  pour  $\theta_1$ ,  $\theta_2$ . La fonctionnelle de régularisation lissée est donnée par:

$$E_\epsilon(\theta) = \frac{\|Rf(\theta_1, \theta_2) - p^\delta\|_2^2}{2} + \beta_1|H_\epsilon(\theta_1)|_{TV} + \beta_2\|\theta_1\|_{H_1}^2 + \gamma_1|H_\epsilon(\theta_2)|_{TV} + \gamma_2\|\theta_2\|_{H_1}^2 \quad (29)$$

où  $|.|_{TV}$  est le terme de Variation Totale. Les minimiseurs des fonctionnelles de Tikhonov

sont obtenus par une condition d'optimalité pour les deux fonctions level-set pour les deux fonctionnelles lissées,  $\frac{\partial F_\epsilon}{\partial \theta_1} = G_1(\theta_1, \theta_2) = 0$  and similarly  $G_2(\theta_1, \theta_2) = 0$ , with:

$$G_1(\theta_1, \theta_2) = \frac{\partial f}{\partial \theta_1} R^*(Rf(\theta_1, \theta_2) - p^\delta) + \beta_2(I - \Delta)(\theta_1) + \beta_1 \frac{\partial |H_\epsilon(\theta_1)|_{TV}}{\partial \theta_1} \quad (30)$$

Les dérivées par rapport à  $\theta_1$  and  $\theta_2$  peuvent s'écrire:

$$\begin{aligned} \frac{\partial f}{\partial \theta_1} &= (f_2 - f_3)H(\theta_2)H'(\theta_1) - f_1H'(\theta_1)(1 - H(\theta_2)) \\ \frac{\partial f}{\partial \theta_2} &= f_2H'(\theta_2)H(\theta_1) + f_3H'(\theta_2)(1 - H(\theta_1)) - f_1(1 - H(\theta_1))H'(\theta_2) \end{aligned} \quad (31)$$

où  $H'$  est évaluée sur l'approximation lissée  $H_\epsilon$ .

La différentielle  $|H_\epsilon(\theta_1)|_{TV}$  est:

$$\frac{\partial |H_\epsilon(\theta_1)|_{TV}}{\partial \theta_1} = -\delta(\theta_1^k) \frac{\nabla \theta_1}{|\nabla \theta_1|} \quad (32)$$

A partir de  $\theta_1^k$ , la mise à jour  $\theta_1^{k+1} = \theta_1^k + \delta\theta$  est obtenue avec une méthode de Gauss-Newton avec une linéarisation de la condition  $G_1(\theta_1^k + \delta\theta) = 0$ .

$$V_k^* V_k \delta\theta + \beta_2(I - \Delta)(\delta\theta) - \beta_1 \delta(\theta_1^k) \nabla \cdot \frac{\nabla \delta\theta}{|\nabla \theta_1^k|} = -G(\theta_1^k) \quad (33)$$

où  $V_k$  est l'opérateur  $V_k = R \frac{\partial f}{\partial \theta_1}(\theta_1^k)$ . Une formule identique est utilisée pour  $\theta_2$ . Ces systèmes sont résolus avec des méthodes de gradient conjugué.

**Simulations numériques** Les méthodes TV et level-set ont été appliquées sur un fantôme de Shepp-Logan 2D simple avec trois niveaux de gris de taille  $128 \times 128$ . Deux bruits Gaussiens différents ont été ajoutés aux données de projections  $p$  avec une déviation standard  $\sigma_p = 3$  et  $\sigma_p = 6.5$  correspondant à des rapport signal sur bruit de  $18dB$  et  $12dB$ . Les méthodes de régularisation TV et level-set ont été testés sur un nombre limité de vues,  $M$ , avec  $M = 20, 30$  ou  $50$ . Dans notre travail, les détails de simulations sont les même qu'au chapitre 4. Dans la méthode de level-set proposé, les meilleures fonctions level-set proposées sont  $\theta_1$  et  $\theta_2$  qui sont fixées à zero. Dans nos simulations, la constante positive  $\epsilon$  est fixée à  $11$ . A la fin du processus de reconstruction, les images en niveaux de gris reconstruites sont projetées sur les valeurs discrètes  $f = 0, 1, 2$  avec les seuils  $0.5$  et  $1.3$ .

**Résultats** Dans les deux cas, les erreurs de reconstruction sont situées sur les frontières. Pour l'approche level-set, de nombreuses erreurs sont situées sur la jonction entre les régions avec différentes valeurs. Avec l'augmentation du nombre d'angles de projections, la variance des valeurs de images en niveaux de gris diminue. Quand le niveau de bruit est élevé  $\sigma_p = 6.5$ , et le nombre de projection bas  $M = 20$ , il y a beaucoup de points isolés

sur les images.

Les résultats de reconstruction obtenus avec l'algorithme TV ADMM sont meilleurs que ceux obtenus avec la méthode level-set. La méthode de régularisation TV est bien connue pour préserver les bords des images et fournir de bonnes images de reconstruction avec peu d'angles de vue. La ligne de niveau zero du Shepp-Logan est bien restorée avec le terme de régularisation qui tend à minimiser son périmètre. Les frontières des images reconstruites obtenues avec la régularisation TV sont plus lisses.

**Conclusion** Dans ce chapitre, deux méthodes de reconstruction pour la tomographie discrète multi-level avec un nombre limité de projections sont comparés. La première méthode est basée sur une représentation de la fonction à reconstruire avec plusieurs fonctions level-set qui conduit à un problème inverse non linéaire. La seconde méthode est l'approche classique de régularisation TV. La solution optimale est obtenue avec l'algorithme de régularisation TV. Des test simples faits sur une image Shepp-Logan montrent que la régularisation TV dépasse les méthodes level-set dans la plupart des cas. Des expériences sur des objets plus complexes sont nécessaires pour évaluer la méthode level-set proposée.

## Chapitre 8: Conclusions et perspectives

**Conclusions** Dans cette thèse, nous avons étudié des méthodes de reconstruction tomographies discrètes à partir d'un nombre limité de projections pour l'imaginaire de la microstructure de l'os trabéculaire. Le principal but de cette thèse est d'obtenir des images reconstruites de haute qualité avec une dose faible et un temps de d'acquisition faible.

En premier lieu, nous nous sommes intéressés à des méthodes de régularisation level-set et TV. Les deux méthodes ont été comparées avec différents niveaux de bruit et différents nombres de projections sur deux petites images et deux grosses images d'os trabéculaire. Nous partons d'une régularisation TV avec et sans contrainte sur la fonction à reconstruire. La fonctionnelle de régularisation TV est minimisée avec l'algorithme Alternate Direction of Minimization method (ADMM). Ensuite, la méthode level-set avec la régularisation  $H_1$ -TV est aussi utilisée pour résoudre ce problème non linéaire. La méthode de régularisation TV avec des contraintes convexes donne de meilleurs résultats de reconstruction. La régularisation TV sans contrainte convexe est moins efficace pour les grosses images que la régularisation level-set. Cependant, les erreurs de reconstruction sont localisées sur la frontière de toutes les images reconstruites quand le nombre de projection est faible et le niveau de bruit élevé. Des minima locaux sont obtenus.

Ensuite un algorithme level-set avec une régularisation  $H_1$ -TV est utilisé pour résoudre ce problème non linéaire. La régularisation TV avec une contrainte convexe donne de meilleurs résultats de reconstruction. La régularisation TV sans contrainte convexe est moins efficace pour les grandes images que la méthode level-set. Cependant, des erreurs de reconstruction sont localisées sur les frontières de toutes les images reconstruites quand le nombre de projection est faible et en présence d'un bruit élevé.

Ensuite, nous essayons d'échapper au minima locaux et de trouver un optimum local. Une perturbation stochastique est utilisée pour échapper à ces minima locaux. Nous utilisons une méthode level-set stochastique et une méthode TV stochastique pour améliorer les mauvaises images reconstituées obtenues avec les schémas déterministes. Les résultats numériques pour les méthodes stochastique level-set et TV sont illustrés sur les sections tomographiques d'os avec différents niveaux de bruit et différents nombre de projections.

- Les images reconstruites obtenues avec la méthode level-set stochastique sont comparées avec celles obtenues avec la méthode de recuit simulé. La méthode stochastique level-set converge plus vite. Cependant, avec cette méthode, seulement la frontière entre les régions 0 et 1 est modifiée. Aucune région nouvelle n'est mise en évidence et cette méthode n'est pas applicable pour les niveaux de bruit élevés et pour les images de section osseuse de faible densité.
- Dans une seconde étape, une nouvelle approche stochastique est présentée basée sur la régularisation TV et sur la méthode ADMM. Différents termes de bruit basés sur la régularisation TV sont comparés incluant un terme de bruit de frontière et une

perturbation plus homogène basée sur le gradient du terme d'attache aux données de la fonctionnelle de régularisation. Comparé avec les méthodes stochastique level-set qui modifient seulement la forme des régions 0 et 1, l'avantage de la méthode stochastique TV est double. Un changement aléatoire de la frontière entre les régions 0 et 1 est mis en oeuvre d'une nouvelle manière avec des ondelettes ou le gradient de l'image. De plus, des changements topologiques aléatoires sont inclus pour révéler de nouvelles régions qui ne sont pas détectées avec les changements de forme.

Le chapitre suivant s'est intéressé à la reconstruction de volumes 3D. Dans cette partie, la méthode de régularisation TV est appliquée à une image Shepp-Logan et à des données réelles avec des structures trabéculaires. Pour cela, la méthode TV a été implémenté dans le logiciel RTK développé dans l'équipe (reconstruction toolkit). Les résultats de reconstruction montrent que la méthode TV est intéressante pour les volumes 3D.

Le dernier chapitre vise à étendre l'algorithme level-set du cas binaire au cas multi-niveau. La fonction à reconstruire est représentée avec plusieurs fonctions level-set ce qui conduit à un problème inverse non linéaire. Dans l'implémentation, les images en niveau de gris reconstruites sont projectées sur des niveaux discrets avec un seuillage.

Pour résumer, cette thèse travaille sur les problèmes de reconstruction binaire sur des images 2D et tente d'étendre les méthodes correspondantes à des volumes 3D et à des images reconstruites multi-level. Nous nous sommes concentrés sur deux méthodes de régularisation: TV et LS. Les deux méthodes ont été appliquées sur différentes images CT binaires avec différentes structures, taille d'images, fraction osseuses et avec différents niveaux de bruit et nombre de projections pour vérifier l'efficacité et les limites de deux méthodes. Nous avons montré que la méthode LS est une bonne méthode de reconstruction en comparaison de la méthode TV quand le niveau de bruit est faible. La méthode TV est plus intéressante pour reconstruire une image avec un niveau de bruit plus élevé. Nous avons utilisé un nombre très limité de projections et de nombreuses erreurs de reconstruction se trouvent sur les frontières des images reconstruites. C'est pourquoi nous essayons d'utiliser une méthode d'optimisation globale pour raffiner les résultats de reconstruction obtenus avec les méthodes TV et LS. Dans ce travail, nous choisissons des diffusions stochastiques car cette méthode combine les avantages d'un flux de gradient avec des perturbations stochastiques pour échapper aux minima locaux. A la fin de ces processus d'optimisation, de grandes améliorations ont été obtenues. Nous avons étendu la méthode de régularisation TV à un simple Shepp-Logan et à un volume osseux complexe 3D. Nous avons aussi utilisé la méthode LS pour reconstruire une image simple avec trois niveaux de gris. De bons résultats de reconstruction sont obtenus.

**Perspectives** Cette thèse est un travail préliminaire sur la reconstruction binaire et multi-level sur des images 2D et 3D. De nombreux aspects seront étudiés dans le futur:

Dans la partie sur les volumes 3D réels, seule la régularisation TV box a été testée sur

de petits volumes de taille  $627 \times 627 \times 32$ . Toutes les méthodes développées dans cette thèse pour de petites sections osseuses peuvent être appliquées et comparées pour des volumes 3D réels. Des volumes avec différentes densités et des structures plus ou moins complexes peuvent être étudiés et testés dans le futur. En premier lieu, les algorithmes level-set devraient aussi être étendus à des volumes 3D de données réelles. Ce type de méthode peut être étendu au cas binaire où au cas multi-level. Les algorithmes TV et TV box peuvent aussi être comparés de façon détaillée sur des volume 3D réels. De plus, des perturbations stochastiques devraient aussi être utilisées pour améliorer les mauvais résultats de reconstruction obtenus avec les méthodes correspondantes déterministes quand le nombre de projection est bas et le bruit élevé. Elles peuvent être utiles pour diminuer les erreurs situées sur des frontières irrégulières aussi pour des volumes 3D. Les méthodes stochastiques level-set et les méthodes stochastiques basées sur la méthode TV devraient être généralisées et testées sur des volumes 3D. Des études méthodologiques et le développement de nouveaux algorithmes peuvent aussi être intéressant. L'idée du travail futur est de trouver de nouvelles méthodes pour inclure les contraintes binaires ou multi-level et d'utiliser les méthodes stochastiques pour échapper au minima locaux liés à la non convexité du problème. En suivant les idées de la méthode DART, nous pourrions faire évoluer la fonctionnelle de régularisation. Nous pourrions étudier en détail les différentes approches stochastiques pour le problème de reconstruction multi-level et différents types de bruit pourraient être étudiés. Nous pourrions remplacer la contrainte convexe utilisée pour TV par une contrainte non convexe pour favoriser l'évolution des valeurs de la fonction reconstruite vers 0 et 1. De nombreux algorithmes peuvent être étudiés, certains similaires à l'approche par différence de fonctions convexes mentionnée dans la partie bibliographique. Les versions stochastiques correspondantes pourraient être étudiées en détail.



# Abbreviations and Symbols

## Abbreviations

BMD	Bone Mineral Density
DXA	Dual-energy X-ray Absorptionmetry
CT	Computed Tomography
SR micro-CT	Synchrotron Radiation micro-CT
ESRF	European Synchrotron Radiation Facility
FBP	Filtered BackProjection
ART	Algebraic Reconstruction Technique
SIRT	Simultaneous Iterative Reconstruction Technique
SART	Simultaneous Algebraic Reconstruction Technique
ME-EL	Maximum Likelihood- Expectation Maximization
ICM	Iteration Conditional Models
DART	Discrete Algebraic Reconstruction Technique
TV	Total Variation
ADMM	Alternate Direction of Minimization Method
LS	Level-Set
PCLS	Piecewise Constant Level-Set
FDK	Feldkamp David Kress
ID	Intermittent Diffusion
RTK	Reconstruction ToolKit
IDE	Integrated Development Environment

## Notations

$I_0$	initial X-ray intensity
$I$	transmitted X-ray intensity
$R$	Radon transform operator
$\Omega$	bounded open domain
$f$	image to be reconstructed
$f^*$	ground-truth image

$f^m$	reconstructed image at iterate $m$
$f_0$	initial reconstructed image with deterministic TV or LS method
$M$	number of projection angles
$N_r$	X-ray number per projection angle
$L(\phi, s)$	line integral of X-ray
$\phi$	polar angle with $\phi \in [0, \pi]$
$s$	distance from the X-ray line to the origin
$\sigma_p$	the standard derivation of Gaussian noise on raw projection data
$\delta$	noise level of projection data, $\delta = \sqrt{M N_r} \sigma_p$
$p$	raw projection data
$p^\delta$	noisy projection data
$E_\delta$	Data term $E_\delta = \ Rf - p^\delta\ $
$E_m$	minimum error $E_m = \ f^m - f\ $
$TH$	threshold value
$MR$	misclassification rate
$pMR$	positive misclassification rate
$nMR$	negative misclassification rate
$MR_m$	misclassification rate of $f^m$
$f_D$	difference map
$PPSNR$	Peak to Peak Signal to Noise Ratio
$\mu$	regularization parameter
$\beta$	Lagrangian parameter
$C$	convex constraints of TV with $f \in C = [0, 1]^n$
$D_i f$	first-order finite difference of $f$ in all directions
$\mathcal{L}(\cdot)$	augmented Lagrangian equation
$E(\cdot)$	TV or LS regularization functional to minimize
$\lambda$	Lagrange multiplier in augmented Lagrangian equation $\mathcal{L}(\cdot)$
$J_{TV}(f)$	TV regularization term
$\theta$	level-set function
$F(\theta)$	LS regularization term
$H(\theta)$	Heaviside distribution function
$H_\epsilon(theta)$	smooth approximation of Heaviside distribution function
$\epsilon$	real positive constant to control the scale of smoothed Dirac
$W$	$m$ -dimensional Brownian motion $W = (W_1(t), \dots, W_m(t))$
$\nu$	normalized eigenfunction (wavelet base)
$\eta$	stochastic noise coefficient
$X(t)$	random trajectory
$T$	time interval
$\sigma(f(t), t)dW(t)$	stochastic noise term based on TV regularization method
$\theta^*$	X-ray projection direction
$\bar{n}(x)$	exterior normal of boundary at point $x$
$\hat{A}$	the angle between $(\bar{n})$ and $\theta^*$

# I Background

---



# Chapter 1

---

## Introduction

---

### 1.1 Overview

Osteoporosis is a kind of bone disease leading to fractures. According to a survey of the International Osteoporosis Foundation, it is reported that osteoporosis causes more than 8.9 million fractures annually, resulting in an osteoporotic fracture every 3 seconds. Osteoporosis is characterized by a bone loss and the alteration of bone microarchitecture. Therefore the assessment of trabecular bone microarchitecture is important in the diagnosis of osteoporosis.

The structure of trabecular bone can be imaged in X-ray CT techniques, but the expected progresses are to reduce radiation dose and/or decrease scanning time. A good way to reduce the radiation dose is reducing the projection angles. It means we should reconstruct a CT image with a limited number of projections, which makes the reconstruction with a finite number of intensity levels (2 levels for binary image) to be a highly ill-posed inverse problem.

In this work, we investigated Level-set and Total Variation regularization methods to solve this problem. Our tests showed that reconstruction errors were located on the boundaries of the reconstructed images, and that some regions were lost sometimes. Local minima were obtained. Therefore, it seems interesting to escape the local minima and find global optima. A global optimization method was introduced into the reconstruction problem. In this work, it was proved that a stochastic perturbation can be a useful way to escape local minima and find global optima.

## 1.2 Thesis Objective

The main aim of this thesis focus on the following three aspects: 1) Develop suitable binary reconstruction methods (Leve-set (LS) and Total Variation (TV) regularization methods) from a limited number of projections for bone cross-section images; 2) Investigate global optimization with a stochastic method to improve the reconstruction results with LS and TV regularization methods, especially when a high noise exists in the raw projection data. 3) Extend TV regularization method from 2D images to 3D volumes.

## 1.3 Structure of the Thesis

The manuscript is organized as follows:

- Background: This part includes 3 chapters, introducing the background, basic knowledge about human bone, X-ray Computed Tomography and the mainly existed reconstruction methods of CT images.
  - Chapter 1 introduces briefly the general background, the main aim of this thesis and the structure of this manuscript.
  - Chapter 2 describes the hierarchical structure, basic functionality, and the remodeling, the relationships between human bone tissue and the bone disease:osteoporosis. At the same time, the advantages of synchrotron micro-CT compared with traditional micro-CT is introduced.
  - Chapter 3 explains the basic principles of X-ray Computed Tomography (CT) reconstruction. At the end of this chapter, we focused on the existing reconstruction methods for CT images.
- Contributions: This part presents our main contribution in binary tomography reconstruction of bone microstructure from a limited number of projections.
  - Chapter 4 focuses on two regularization reconstruction methods: level-set and total variation regularization methods. Both regularization methods are compared under different noise levels on two small and two big images with different number of projections.
  - Chapter 5 tries to improve the reconstruction results obtained in Chapter 4 using a stochastic optimization method. And it was proved the stochastic methods are very useful for a poor first reconstruction obtained with a small projection number and high noise level with deterministic LS or TV methods.
  - Chapter 6 extends 2D images to 3D volumes with TV regularization methods. This method was implemented on Reconstruction toolkit (RTK) an open source software developed by the laboratory CREATIS.

- chapter 7 tries to extend the level-set algorithm from binary case to multi-level case. The main aim of this extension is to present more details inside the reconstructed image.
- Conclusions and perspectives:
  - Chapter 8 summarizes the contributions of this manuscript and gives a perspective for the future works.
- Annexes and Bibliography.



## Chapter 2

---

# Bone Medical Contexts and X-Ray Imaging

---

### 2.1 Human Bones and Osteoporosis

A human bone is a rigid organ which is relatively hard, light and with a high strength. As a system, there are 206 separate bones in the adult, and these bones are connected by tendons and ligaments attached to the ends of bones [Folkens *et al.* (2002)]. Human bones support and protect the vital organs of the body, produce red and white blood cells and store minerals. Human bones have a variety of shapes and sizes, with complex external and internal structures. There are five types of bones in the human body: long bones, flat bones, irregular bones, short bones and sesamoid bones.

Osteoporosis is a kind of bone disease which decreases bone strength and increases the risk of a broken bone, such as bone fractures [Kanis *et al.* (1994), Golob and Laya (2015)]. Bones that commonly break as the normal complication of osteoporosis include long bones (such as the bones of the forearms, the bones of the ossa cruris), flat bones (such as hip, rib) and irregular bones (such as lumber vertebrae) [MELTON *et al.* (1989), Golob and Laya (2015)] as shown in Fig.2.1.

The main reason of osteoporosis is due to greater than normal bone loss, leading to a lower "peak bone mass" [Bonjour *et al.* (1994), Heaney *et al.* (2000)] and to the deterioration of the microarchitecture of bone tissue. For instance, when the normal thoracic vertebrae is affected by osteoporosis, it will gradually collapse. This results in kyphosis, an excessive curvature of the thoracic region. Fig.2.2 shows the normal postures

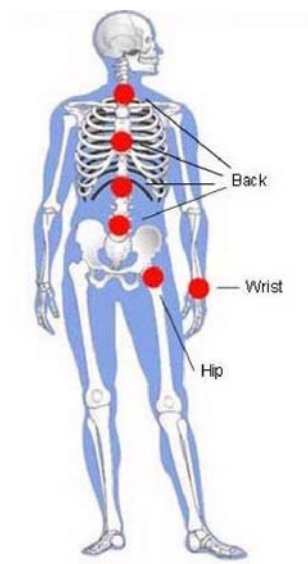


Figure 2.1: Common fracture sites for osteoporosis . <http://www.health24.com>

at age 40 and the osteoporotic changes at age 60 and 70 years, leading a loss of as much as 6 to 9 inches in height.

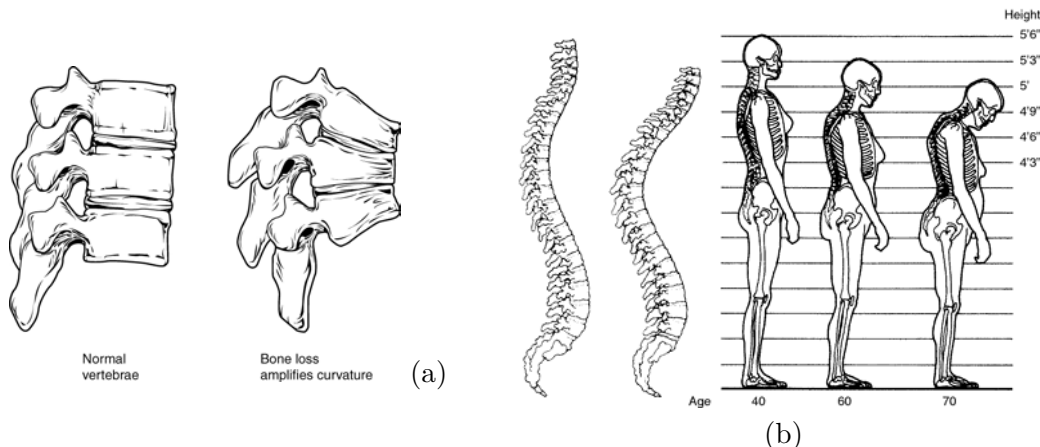


Figure 2.2: (a) Normal and diseased thoracic vertebrae, (b) Normal and osteoporosis standing postures. <https://en.wikipedia.org/wiki> and <http://medical-dictionary.thefreedictionary.com/osteoporosis>

One way for the diagnosis of osteoporosis is measuring the bone mineral density (BMD) [Guglielmi and Scalzo (2010)]. The osteoporosis is diagnosed when the bone mineral density is 2.5 standard deviations lower than the normal one (average of young, healthy adults). The most trusted method of measuring BMD is dual-energy X-ray absorptiometry (DXA).

The main radiographic features of osteoporosis is that cortical bone becomes thinning. Although radiography is relatively insensitive to detection of early disease and requires a substantial amount of bone loss (about 30 %) to be apparent on X-ray images, the conventional radiography is still useful, both by itself and in conjunction with CT or MRI,

for detecting the decrease of bone mass.

## 2.2 Bone Tissue and Bone Dynamics

### 2.2.1 Hierarchical structure of bone

Bone tissue is a type of dense connected tissue. Bone tissue is not simple and solid, but a dynamic structure composed of both living tissues, such as bone cells, fat cells, blood vessels, and nonliving materials, including water and minerals [Dorozhkin (2010), Barkaoui and Hamblin (2011)]. In order understand biological and mechanical functions of bones, a multiscale modeling is required [Barkaoui *et al.* (2014)]. Five levels of hierarchical bone structures have been distinguished in [Sato and Webster (2004), Jung and Kleinheinz (2013)] which are shown in Fig.2.3: (i) macrostructure level (organ level), consisting of cortical and cancellous bones; (ii) microstructure level, at an observation scale from  $10 \mu\text{m}$  to  $500 \mu\text{m}$ , consisting of osteons and single trabeculae. (iii) sub-micro level from  $1 \mu\text{m}$  to  $10 \mu\text{m}$ , with the material building up the structures of both osteons and trabeculae (iv) nano-level from hundreds of nanometers to  $1\mu\text{m}$ , containing collagen fibers. (v) sub-nano level below  $0.5 \mu\text{m}$ , including molecules of bone.

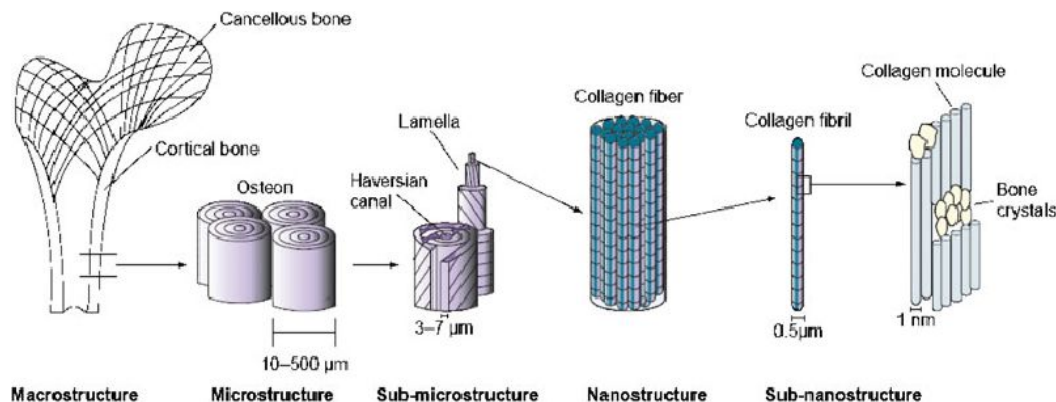


Figure 2.3: Hierarchical structure of human bone. (Image from [Sato and Webster (2004)])

Because of the complex and elaborate structures of bone, the mechanical properties of bone, in particular those at the micro- and nano- structure level, remain poorly understood [Rho *et al.* (1998)]. Therefore, many investigations have been done to study the characteristics of human bone at the two levels. And the main studies of this thesis focus on the structures of trabecular, which is related to the diagnosis of osteoporosis, on the second microstructure level with an observation scale from  $10 \mu\text{m}$  to  $500 \mu\text{m}$ .

### 2.2.2 Microstructure of bone tissue

Bones are made up of bone tissue as well as marrow, blood vessels, nerves and epithelium, while bone tissue refers to the bone mineral matrix that forms the rigid sections of the organs and the bone cells within it. At the microlevel of bone microstructure, hu-

man bone is made of two morphological distinctive parts: cortical bones and cancellous (trabecular or spongy) bones [Schaffler and Burr (1988)]. The detailed structure of bone tissue (a femur) is presented in Fig.2.4.

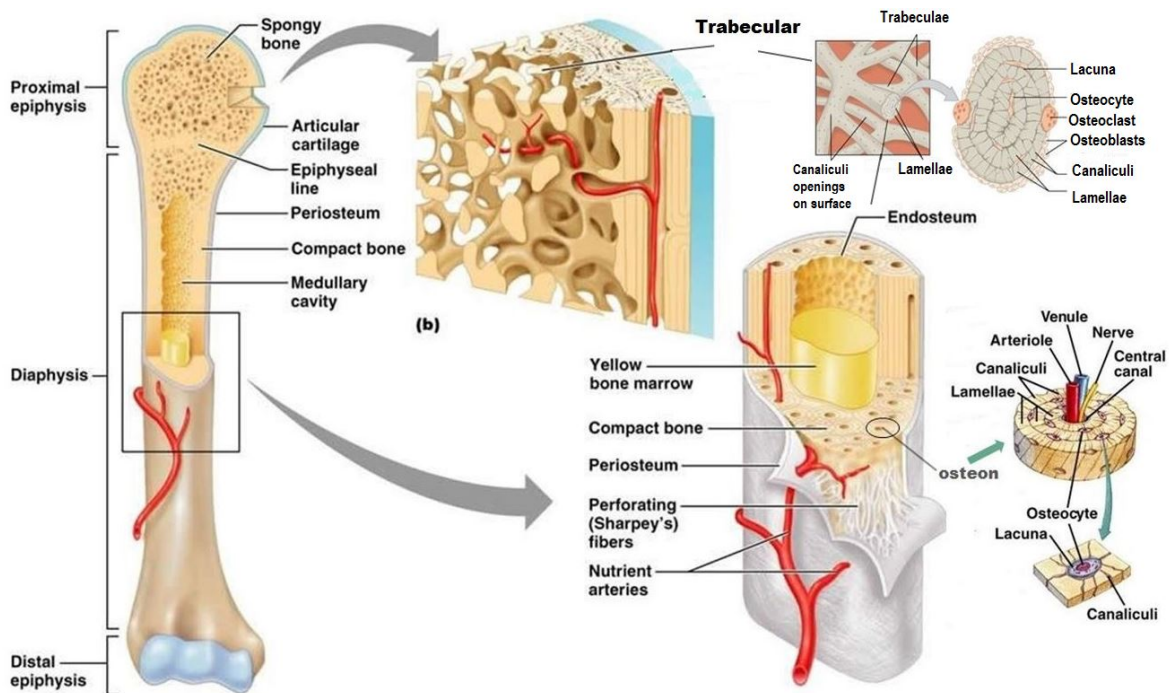


Figure 2.4: Structure of bone tissue. <http://classes.midlandstech.edu/carterp/Courses/bio210/chap06/lecture1.html>

The cortical bone is called compact bone, forming the shell of the human bone and ensuring a mechanical function of support and protection. The compact bone is the densest part of human bone and contributes to 80% of the total mass of the skeleton. The basic unit of the compact bone is an "osteon" and each unit has a cylindrical structure composed by concentric tubes of bone matrix (the lamellae) surrounding a Haversian canal that serves as a passage way for blood vessels and nerves. The compact bone is really hard and dense and surgeons must use a saw to cut through it. Its porosity is less than 15% [Schaffler and Burr (1988)]. The trabecular bone forms the inner spongy bone found most commonly at the ends of long bones, such as the femur, as well as in flat and irregular bones such as hip and vertebrae [Launey *et al.* (2010)]. Trabecular bone is a complex sponge-like network structure made up with trabeculae, a kind of rod-like and plate-like structures [Shi *et al.* (2010)] with thicknesses in the order of 100-300  $\mu\text{m}$  [Launey *et al.* (2010)]. The inter-space of network structure is filled with bone marrow. In contrary to the cortical bone, the structure of the cancellous bone is irregular, sinuous and furcal. The porosity of the cancellous bone is approximately more than 70% [Schaffler and Burr (1988)].

Fig.2.5 is illustrating the decrease of bone mass and the change of trabecular bone in the case of osteoporosis. As we can see, because of the reduction of bone mass and loss of connectivity of bone, the trabecular structures of the osteoporosis bones are much

sparser than that of a normal bone, leading to a high probability of fractures. The risk of osteoporosis arises when pain in the special regions (Fig.2.1) is suffered by a patient. It is strongly recommended to make a clinic diagnosis.

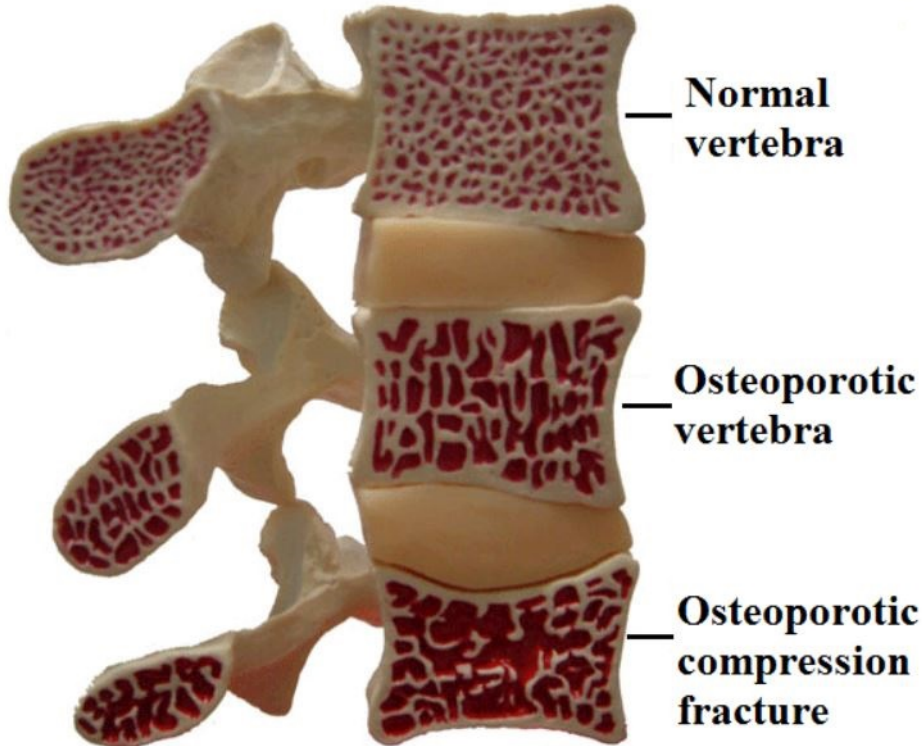


Figure 2.5: Stages of vertebral osteoporosis (top to bottom). Osteoporotic bone loss a lot of bone mass and connectivity. <http://www.neuros.net>

### 2.2.3 Bone dynamics

Bone changes its mass and structure constantly during life through three biological mechanisms: growth, modeling and remodeling. The process in which woven bone is replaced by lamellar bone plays an very important role in the three biological mechanisms and in the bone repair that occurs after the fractures because of osteoporosis. Bone begins to form before we are born, and bones continue to grow throughout childhood and adolescence. Bone growth expands the sizes of bone in the longitudinal and radial (in width) directions mainly by the bone modeling mechanism which changes the bone mass and its form. Bone remodeling is a lifelong process where old bone tissue is replaced by new bone, micro-damaged bone with newer, healthier bone and calcium and phosphate homeostasis to maintain the bone mass [Clarke (2008), Hadjidakis and Androulakis (2006)]. In the first year of life, almost 100% of the skeleton is replaced. In adults, remodeling proceeds at about 10% per year [Bon (2016)]. In adult skeletons, bone remodeling is balanced by bone deposit and removal. While bone deposit occurs at a greater rate when bone is injured (for example fracture). The bone remodeling process can be divided into

five stages: activation, resorption, reversal, formation and quiescence involving different kinds of bone cells as shown in Fig.2.6 and Fig.2.7. The total process takes about 3 to 6 months [Misch and Bortolotti (2009)].

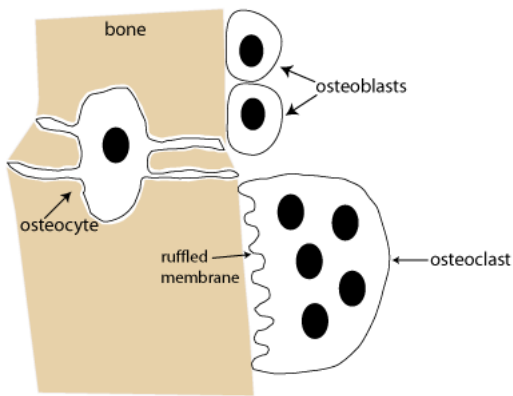


Figure 2.6: Bone cells related to remodeling cycle. <https://courses.washington.edu/conj/bess/bone/bone2.html>

There are three kinds of bone cells related to the bone remodeling cycle: osteoblasts, osteocytes and osteoclasts [Rodan (1992)]. Osteoblasts are bone-forming cells. They are attached to the surface of bone. They can be stimulated to proliferate and differentiate as osteocytes. Osteocytes are bone cells formed from osteoblasts. They send out long tendrils (ruffled membrane) to connect numerous osteocytes to each other. While osteoblasts and osteocytes have the same source, are the different stages of the same cells. Osteoclasts' job is breaking down the composite material in bones in the resorption process that send the calcium in the bones acted on by osteoclasts back into the bloodstream. Osteoclast cells are produced when more blood calcium is needed, and suppressed when there is no deficiency of calcium in the body. They are also vital in repairing mechanical breaks (fractures) to the bone. During

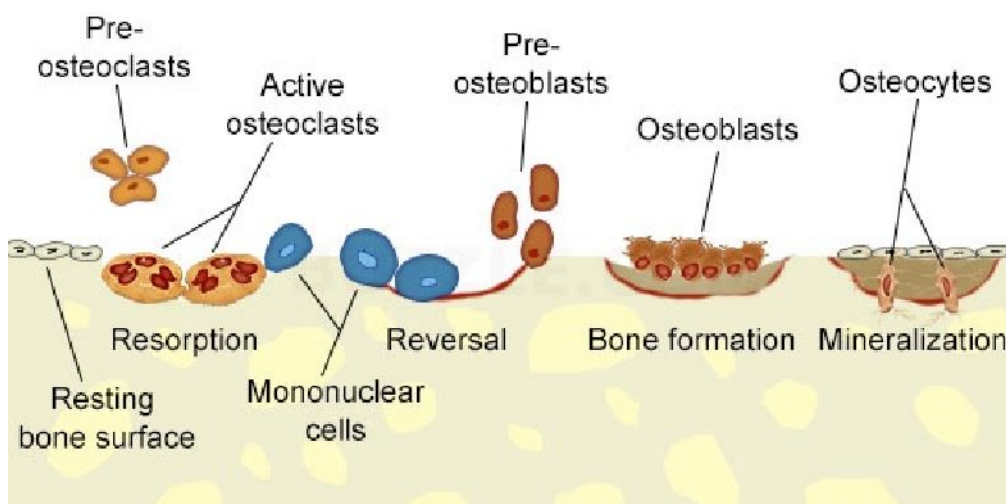


Figure 2.7: Bone remodeling cycle <http://www.buzzle.com/articles/osteoblast-vs-osteoclast-vs-osteocyte.html>

the activation phase, preosteoclasts are stimulated and differentiate under the influence of cytokines and growth factors. The mature osteoclasts then migrate and attach to the exposed surface. Osteoclasts digest mineral matrix of the old bone in the resorption period;

In the reversal period, resorption stop and the next formation start through the action of osteoblasts. Then osteoblasts synthesize the new bone matrix in the fourth stage and gradually differentiate into bone-lining cells and the bone turn into a quiescence phase.

An imbalance of the resorption and bone formation processes in the bone remodeling cycle will lead to many bone diseases. For example, osteoporosis occurs when the bone resorption rate is greater than that of bone formation. Older women are especially vulnerable to osteoporosis and loss the bone mass, due to the decline in estrogen after menopause. Other factors that lead to osteoporosis include a small body form, a diet poor in calcium and vitamin D, smoking, certain hormone-related conditions and so on.

## 2.3 X-Ray Imaging of Bone

### 2.3.1 Radiography images of osteoporotic bone

The main reason of osteoporosis is the greater than normal bone loss, leading lower "peak bone mass", which can be defined as the amount of bony tissue present at the end of the skeletal maturation. This is an important determinant of osteoporotic fracture risk [Heaney *et al.* (2000)]. At the microlevel, the main radiographic features of generalized osteoporosis is the reduction of trabecular bone. For example, images in Fig.2.8 were acquired in existed specimens from sham-operated (a,c) and ovariectomized (b,d) rats using a micro-CT system. We can see in the Images (Fig.2.8), the trabecular is just hanging there, losing connections and offering no strengths to the bones.

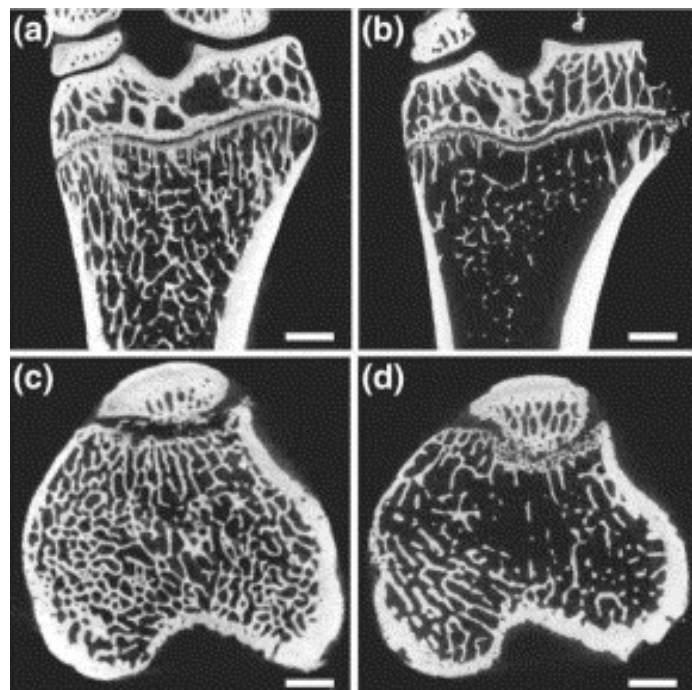


Figure 2.8: Cross-sectional micro-CT images of existed rat limbs at a  $14 \mu\text{m}$  isotropic voxel spacing [Holdsworth and Thornton (2002)].

Although radiography is relatively insensitive to detection of early disease and requires a substantial amount of bone loss (about 30 %) to be apparent on X-ray images, The computer aided diagnosis (CAD) is still useful. X-ray scans will show any low density bones, as well as osteoporotic fractures.

### 2.3.2 X-Ray Computed Tomography (CT)

X-ray radiography is the oldest and simplest medical imaging technique, although it does not generate a 3D image of bone structure [Peter and Peyrin (2011)]. X-ray computed tomography (CT) was developed in the early 1970's by Hounsfield G. N. [Hounsfield (1973)]. It is very effective for visualizing the inside features of a solid object without destruction and it has revolutionized medical imaging technology by producing anatomical images of high accuracy and with much clinical details [Wellington and Vinegar (1987)]. After decades of developments, CT has become a major analysis and diagnosis tool in bone biology by providing a wide range of 3D biomedical images with different density resolution between millimeters down to nanometers.

Clinical CT is well adapted for imaging bone with a low resolution (200-500  $\mu\text{m}$ ), which is very limited to the research for trabecular bone. And some high-resolution CT has been used to evaluate trabecular microarchitecture in *in vivo* human bone imaging studies and provided quantitative measures of bone structures [Burghardt *et al.* (2011)].

### 2.3.3 Dual X-ray Absorptiometry (DXA)

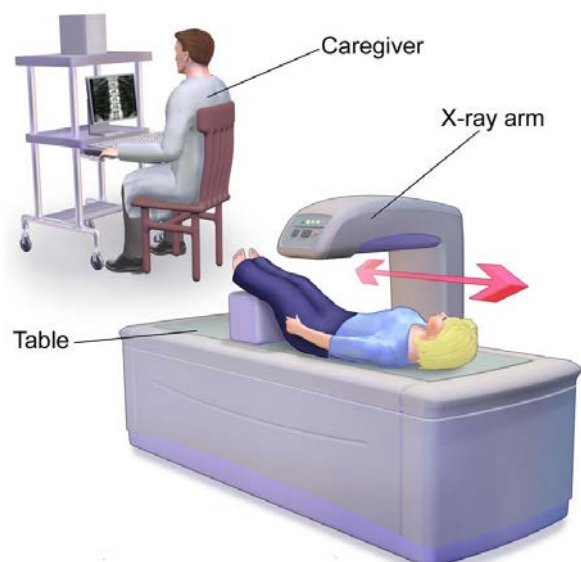


Figure 2.9: A DXA scanner used to measure bone density (BMD). <http://en.wikipedia.org>

Bone Mineral Density (BMD) is an important indicator of osteoporosis and of the risk of fractures. It refers to the mass of mineral per volume of bone . Clinically it is measured approximately by optical density per  $\text{cm}^2$  of bone surface [Laskey (1996)]. DXA is currently the most widely used BMD tests method because it is cheap, easy to use and can provide a high accuracy of BMD estimates in adults. What's more, DXA scanning is very small, therefore, it is a simple and safe

technique that can be used for children [Gilsanz (1998)]. In a DXA scanner (Fig.2.9), two X-ray beams with different energies are transmitted through patient's bone, the BMD

can be determined by the absorptions of each beam by bone after subtracting the absorption by soft tissues.

### 2.3.4 Micro-CT and Synchrotron Radiation (SR) micro-CT

#### Micro-CT

Micro-CT enables a non-invasive inspection to see anatomical changes in small objects [Li *et al.* (2008)]. The first micro-CT scanner which has been used for the evaluation of the three-dimensional micro-structure of trabecular bone has been proposed in 1989 by Feldkamp [Feldkamp *et al.* (1989)]. After this first scanner, the first commercialized bone micro-CT scanner was available in 1994 [Müller and Rüegsegger (1994)], Micro-CT technique started to become a standard in bone research fields with a high resolution. Currently most Micro-CT system are based on a cone beam geometry. Usually, the X-ray tomography system consists of an X-ray source, a rotational geometry with respect to the object being imaged and a series of detectors which are used to measure X-ray energy deposition to be transformed into X-ray projection by a computer. The emitting material and the X-ray energy of the tube determine the X-ray spectrum, which impacts the X-ray intensity. The majority of detectors use scintillators with iodide, gadolinium oxysulfide, and sodium tungstate [Wikipedia (2016)] to convert X-ray energy deposition into electronic signals which can be recognized by a computer. For example, a typical Cone-Beam CT setup is shown Fig.2.10.

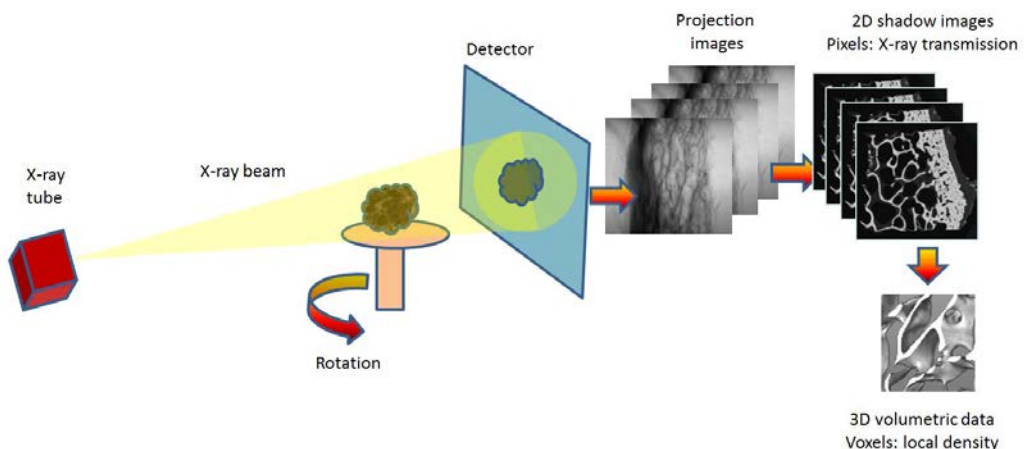


Figure 2.10: Scanning geometry for Cone-Beam CT setup with a rotational bed. A number of projections with different angles can be acquired to obtain a reconstructed image.

#### SR micro-CT

Synchrotron Radiation (SR) micro-CT has interesting properties in bone research for the analysis of the trabecular bone micro-structure in bone research [Nuzzo *et al.* (2002)b, Nuzzo *et al.* (2002)a]. The use of SR micro-CT compared to a standard X-ray micro-CT

has several significant advantages [Flannery *et al.* (1987), Salomé *et al.* (1999)]. Firstly, the intensity of X-ray beam of SR micro-CT is very high which provides a high Signal to Noise Ratio (SNR) even at very high spatial resolution to offer better image quality and reducing the acquisition time. Secondly, the SR micro-CT generally uses monochromatic x-ray beam for a selected energy, avoiding beam hardening.

The European synchrotron radiation facility (ESRF) is one of the three third-generation large-scale synchrotron X-ray source with powerful (6 GeV) electron energy in the world [Syn (2016)]. It was set up in Grenoble and consists of a linear accelerator (Linac), a booster synchrotron and a storage ring which is connected to beamlines, Fig.2.12.

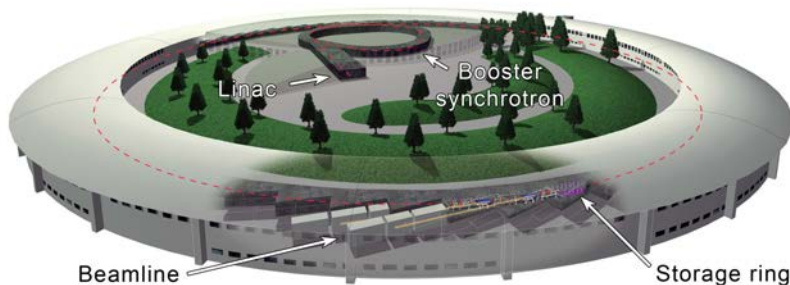


Figure 2.11: The European Synchrotron Radiation Facility <http://www.esrf.eu>

Especially, the beamline ID19 of ESRF is a long imaging beamline, designed for full-field parallel-beam imaging techniques. The principle of the micro-CT on ID19 is to acquire 2D parallel radiographies of a sample in for different angles spanning 180° or 360° [Salomé *et al.* (1999)]. A typical experimental configuration for SR micro-CT at ID19 is shown in Fig.2.11, which is similar to a standard micro-CT expect that it uses a 3D parallel beam, which avoids the reconstruction artifacts from most standard systems.

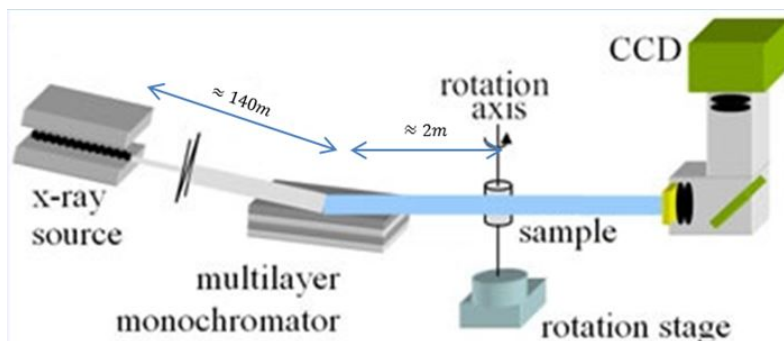


Figure 2.12: (A SR micro-CT setup at beamline ID19 with monochromatic beam for computed tomography <http://www.esrf.eu>

For example, two reconstructed human bone cross-sections size of  $1024 \times 1024$  are displayed in Fig. 2.13, acquiring with the synchrotron micro-CT at beamline ID19 at ESRF [Apostol *et al.* (2006)], We will do our simulations with this two reconstructed images.

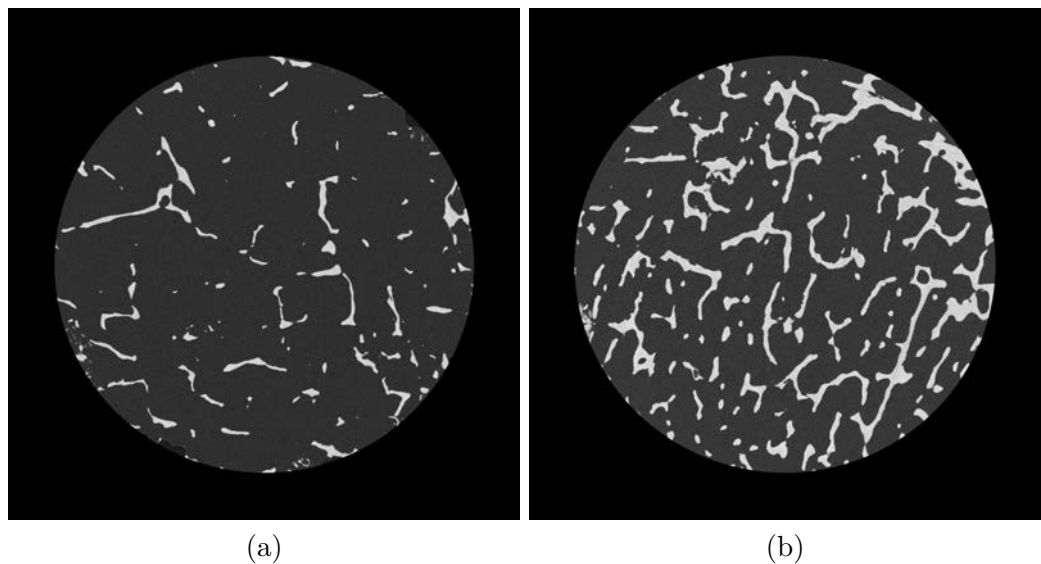


Figure 2.13: Two reconstructed bone cross-section with FBP algorithm size of  $1024 \times 1024$ , acquired with synchrotron radiation micro-CT on beamline ID19 at the ESRF (pixel size  $15 \mu\text{m}$ ). (a) Bone cross-section with osteoporosis; (b) Normal bone cross-section.

## 2.4 Conclusion

In this chapter, a brief review about bone medical context and a short presentation of X-ray CT imaging of bone were given. Osteoporosis is a kind of common disease which leads to bone fragility. An osteoporotic bone at micro-level is losing a lot of trabecular bone and the connectivity. X-ray CT imaging is a useful and non-destructive method for the diagnosis of osteoporosis. Clinical CT or DXA are useful ways to measure the bone density with a good accuracy but they are limited for the trabecular bone because of their low resolution. High-resolution CT imaging techniques like micro-CT, SR micro-CT provides high-quality X-ray images of the microstructure of human bone and expands the methods of diagnosis and therapy for osteoporosis.



# Chapter 3

---

## Tomography Reconstruction Methods

---

This chapter focus on the "X-ray Computed Tomography (CT) reconstruction". Firstly, the basic physical principles of X-ray tomography reconstruction are presented. Then some classical existing reconstruction methods are presented and their advantages/disadvantages are discussed briefly.

### 3.1 Physical Principle of X-Ray CT Reconstruction

#### 3.1.1 X-Ray attenuation

The intensity of X-ray will decrease after passing through an uniform object. This decrease is described by Beer's Law with a intensity reduction function of X-ray energy, path length and material attenuation coefficient  $\alpha$ . A basic model of Beer's law for a monochromatic X-ray beam entering a homogeneous object is [Panetta (2016)]:

$$I = I_0 e^{-\alpha l} \quad (3.1)$$

where  $I_0$  is the initial X-ray intensity and  $I$  is the transmitted X-ray intensity after passing through this homogeneous object with thickness  $l$ . If there are multiple materials, then the final continuous attenuation function is given by:

$$I = I_0 e^{- \int \alpha(x,y) dl} \quad (3.2)$$

where  $\int \alpha(x, y)dl$  is the integral of attenuation coefficient function  $\alpha(x, y)$  on the pass line  $l$ . For a discrete model, the attenuation function is given by:

$$I = I_0 e^{\sum_i -\alpha_i l_i} \quad (3.3)$$

where  $i$  is the material index with an attenuation coefficient  $\alpha_i$  and with a linear path  $l_i$ .

Photoelectric absorption and Compton scattering are two prevailing physical processes which are responsible for X-ray attenuation. The former occurs when the total energy of the incoming X-ray is transferred to the inner electrons, while the later occurs when the incoming X-ray interacts with an outer electron of an atom, losing a part of its energy and changing its direction. Therefore, the linear attenuation coefficient  $\alpha$  mainly depends on both electron density  $\rho$  and the atomic number  $Z$  [Jacobs *et al.* (1995)].

$$\alpha = \rho(a + bZ^{3.8}/E^{3.2}) \quad (3.4)$$

where  $a$  is the nearly energy-independent Klein-Nishina coefficient and  $b$  is a constant. Generally, the photoelectric absorption predominates over the X-ray attenuation for low X-ray energy, approximately up to 100 keV, while Compton scattering is the main physical process for X-ray attenuation when X-ray energy is above this level.

### 3.1.2 CT projections

The tomographic reconstruction problem consists in the estimation of the X-ray linear attenuation coefficient from a set of its line integrals. According to the reconstruction theory developed by J.Radon in 1917, a CT cross-section image can be reconstructed from a number of projections at many different angles (Fig. 3.1) by computing the attenuation coefficients for each voxel corresponding to a given material, such as bone, fat, tissue or water for example.

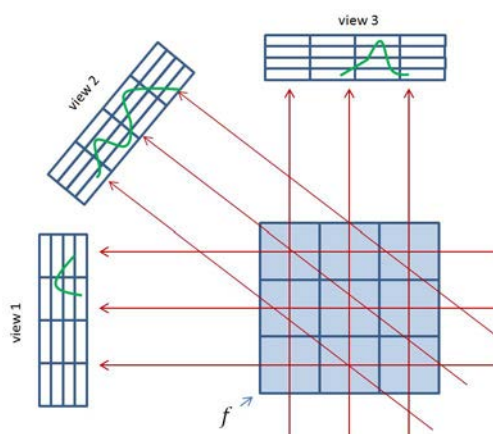


Figure 3.1: CT projections. The X-ray source is sequentially rotated and new projections are acquired.

Computed tomography acquires a series of projections and then reconstructs the corresponding image. Each view's projection corresponds to the sum of the image absorption values along the X-ray path. Typically, a CT scan uses thousands of views with different projection angles. Usually, a CT cross-section image is called a **slice**, corresponding to a plane with a small thickness. The grey levels in 2D image corresponds to the X-ray attenuation, which reflects the X-ray absorption or scattering when the X-ray passes through the voxels.

### 3.1.3 Radon transform and tomography reconstruction

In our work, the X-ray beam of the SR micro-CT setup is parallel, therefore, we consider here a simple parallel geometry, shown in Fig.3.2, and the direct operator is the Radon projection operator described below [Natterer (1986)].

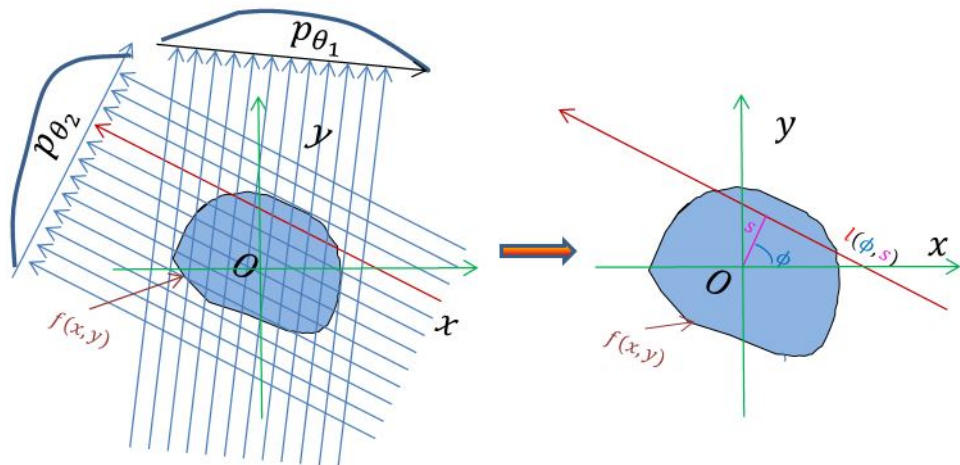


Figure 3.2: Principle of the parallel tomographic acquisition and Radon Transform.

Let  $\Omega \subset \mathbb{R}^2$  be a bounded open domain, the mathematical model for 2D-tomography is the Radon transform  $R$  [Natterer (1986), E.T.Qinto (1993)]. Let  $L(\phi, s)$  be the line defined by  $L(\phi, s) = \{\tau\Phi^* + s\Phi : \tau \in \mathbb{R}\}$ , with  $\Phi = (\cos(\phi), \sin(\phi))$  and  $\Phi^* = (-\sin(\phi), \cos(\phi))$ ,  $\phi \in [0, \pi]$  is the polar angle, and  $s \in [-a, a]$  is the distance from the line to the origin  $O$ , Fig.3.2. The Radon transform for  $f \in L^1(\Omega)$  is the set of line integrals  $s$  on  $L(\phi, s)$  defined by:

$$Rf(\phi, s) = \int f(s\cos(\phi) - \tau\sin(\phi), s\sin(\phi) + \tau\cos(\phi)) d\tau \quad (3.5)$$

with:

$$p(\phi, s) = Rf(\phi, s) \quad (3.6)$$

where  $(s\cos(\phi) - \tau\sin(\phi), s\sin(\phi) + \tau\cos(\phi))$  is the spatial position in the Cartesian coordinate system.

The standard Radon transform is continuous. The continuous problem must be discretized to obtain a numerical solution. In the discretized tomography reconstruction, the

set of all projections rays generate the linear system:

$$Rf = p^\delta \quad f = (f_1, f_2, \dots, f_n) \quad (3.7)$$

where  $R$  is the projection matrix,  $(f_i)_{1 \leq i \leq n}$  represents the pixel values to be reconstructed and  $p^\delta$  the noisy projections.

## 3.2 Reconstruction Methods for Continuous Tomography

There are many different existing algorithms for X-ray CT reconstructions. In this section, we will present the two main reconstruction methods for continuous tomography: the analytical and iterative reconstruction approaches [Bruyant (2002)]. The most widely used analytical image reconstruction method is Filtered BackProjection Method (FBP) [Kinahan and Rogers (1989)]. With the development of computer hardware, iterative reconstruction methods have been popular because it is easy to model and handle the noises existing in raw projections [Zeng (2001), Beister *et al.* (2012)]. Especially, regularization methods which integrate prior information into the image to be reconstructed was developed recently [Sidky and Pan (2006), Sidky and Pan (2008), Sidky *et al.* (2012), Ritschl *et al.* (2011), Defrise *et al.* (2011)].

### 3.2.1 Analytical image reconstruction methods

The first analytical reconstruction method of an X-ray image was proposed by Cormack in 1963 [Cormack (1963)]. The analytical reconstruction methods are based on considering the projected densities with the line integrals along the X-ray beams passing through the object. In this section, the most widely used analytical reconstruction method: a filtered backprojection (FBP) for 2D parallel tomography [Peyrin and Engelke (2012)] is presented.

#### Filtered backprojection method

The Fourier Slice theorem is fundamental in analytical tomography reconstruction methods, however its direct discretization poses a number of interpolation problems in Fourier space. The introduction of the back-projection operator allows to obtain a convenient reconstruction formula, known as Filtered BackProjection (FBP). The inversion formula is based on the back-projection operator  $\mathcal{B}$  defined as [Bruyant (2002), Zeng (2001), Kinahan and Rogers (1989)]:

$$\mathcal{B}(p)(x, y) = \int_0^\pi p(\phi, x\cos\phi + y\sin\phi) d\phi \quad (3.8)$$

This operator is the adjoint of the Radon Transform, and it can be understood as the accumulation of the X-ray beams passing by the point  $(x, y)$ . The reconstructed image

can be obtained by:

$$\hat{f}(x, y) = \mathcal{B}\mathcal{K}p(x, y) = \mathcal{B}\mathcal{K}Rf(x, y) \quad (3.9)$$

$\mathcal{K}$  denotes the ramp filtering operator. The discretization of the FBP reconstruction formula provides a reliable estimation of the image only if a large number of projection angles are available.

### 3.2.2 Iterative image reconstruction methods

The continuous tomography reconstruction problem can be discretized and associated with a linear system  $p = Rf$ . If there was no noise existing, it seems that the image  $f$  would be obtained by:

$$f = R^{-1}p \quad (3.10)$$

In fact the inverse of the matrix  $R$  is not well-defined. But in a real system, noise can not be avoided. The acquired projection data  $p^\delta$  contained the real projection data  $p$  and the noise signal  $\delta$ :

$$p^\delta = p + \delta \quad (3.11)$$

Very often, the noise is assumed to be Gaussian and the noisy projections  $p^\delta$  and projections without noise  $p$  are assumed to be such that  $\|p^\delta - p\|_{L_2} \approx \delta$ , where  $\delta$  is the noise level [Morozov (1984)].

In the framework of iterative image reconstruction, the linear system  $p = Rf$  relating the projections and the image is solved iteratively. Generally speaking, all the algebraic methods (ART, SIRT et al.) can be written as [Gordon *et al.* (1970), Herman (2009)]:

$$f^{n+1} = f^n + \lambda SR^T(p^\delta - Rf^n) \quad (3.12)$$

where  $S$  is a diagonal matrix and  $R^T$  the adjoint of the Radon transform [Benhali and Peyrin (2002)].

**Algebraic Reconstruction Techniques (ART)** The ART is frequently used in tomography reconstruction, and it was proposed in 1984 [Andersen and Kak (1984)]. This algorithm starts with an initial guess  $f^0 = 0$ , and the current reconstruction image is updated with each line of the system. It is easy to incorporate prior knowledge into the reconstruction process. The algorithm could be expressed as follows:

$$f_i^{n+1} = f_i^n + \lambda_n \frac{(p_i^\delta - \langle r_i, f^n \rangle)}{\|r_i\|^2} r_i^T \quad (3.13)$$

where  $\lambda_n$  is a relaxation parameter and  $r_i$  the  $i$ -th line of the projection matrix. In each iteration, a single projection matrix  $R$  is used. It is possible to use blocks inside the matrix  $R$  instead of line. If a block corresponds to a projection, the SART (Simultaneous ART)

is obtained.

### Simultaneous Iterative Reconstruction Techniques (SIRT)

The SIRT algorithm is based on the least square methods [Benhali and Peyrin (2002)]. In this method, every pixel  $f_j$  is iterative corrected, using all the X-rays passing through  $f_j$ . The main iterative relation is expressed as:

$$f_j^{n+1} = f_j^n + \lambda \frac{\sum_{i=1}^N (p_i^\delta - \langle r_i, f^n \rangle) r_{ij}}{\sum_{i=1}^N \sum_{q=1}^M r_{iq} r_{ij}} \quad (3.14)$$

where  $r_i$  is the  $i$ -th row of the matrix  $R$ , and  $r_{ij}$  is the factor in the  $i$ -th row and  $j$ -th column of matrix  $R$ .

SIRT is less sensitive to the errors of the measurement projection data  $p^\delta$ , therefore, it can generate high quality reconstruction images, and what is more, it always converges. However, the main disadvantage of SIRT is that its convergence speed is low. If you want to get a more precise reconstruction image, you should perform more iterations.

These reconstruction algorithms are unstable when noise is present in the projection data  $p$  and we have to use regularization methods to obtain stable solutions.

### 3.2.3 Regularized reconstruction methods

The former methods are not regularized and can lead to very high reconstruction errors when noisy data are considered or when the number of projections decrease. In this section, we present some regularization methods that will be used in this work. Regularization method have been widely used in inverse problems [Wik (2015)]. These approaches refer to the introduction additional information in order to solve an ill-posed problem like  $E(f) = \|p^\delta - Rf\|^2$ . A common approach is to construct a regularization functional which can be written as:

$$E(f) = \|p^\delta - Rf\|^2 + \lambda J(f) \quad (3.15)$$

where  $\lambda$  is a regularization parameter used to control the weight of this prior  $J(f)$ . The classical Tikhonov regularization [Tikhonov (1977), Tikhonov *et al.* (2013)] is given by  $J_{TH}(f) = \|Df\|_2^2$ , where  $D$  is a differential operator.

#### Total Variation (TV) regularization Method

Total Variation Regularization Method was proposed by Rudin in 1992 [Rudin *et al.* (2013)]. Let  $\Omega$  be a bounded open subset of  $\mathbb{R}^2$ , and a image  $f$  belongs to the first-order Sobolev space:  $f \in H_1(\Omega)$ , the TV regularization is defined as:

$$J_{TV} = \int_{\Omega} |\nabla f(r)| dr = \int_{\Omega} \sqrt{f_x^2 + f_y^2} dx dy \quad (3.16)$$

and the anisotropic TV regularization is defined as:

$$J_{TV} = \int_{\Omega} |\nabla f(r)| dr = \int_{\Omega} \sqrt{|f_x| + |f_y|} dx dy \quad (3.17)$$

The TV norm has been described in the literature as a method for reducing noise in two-dimensional images while preserving edges, without introducing ringing or edge artifacts [Chan *et al.* (2000), Chung *et al.* (2005), Borsic *et al.* (2010), Wang *et al.* (2016)].

### Level-set (LS) regularization method

The key feature of the scheme is to use level-set functions to represent the image domains with different pixel values [Chan and Tai (2004), Chung *et al.* (2005), Fruhauf *et al.* (2005), DeCezaro *et al.* (2009), Sixou *et al.* (2013)]. For simplicity, we just assume the image  $f$  to be reconstructed is piecewise constant and only has two pixel values 0 and 1 on two disjoint measurable subsets with  $\Omega = \Omega_0 \cup \Omega_1$ . Therefore,  $f$  is the indicator function of the set  $\Omega_1$ . The image  $f$  can be represented with the Heaviside distribution with a level-set function  $\theta \in H_1(\Omega)$  as  $f = H(\theta)$  equal 1 if  $\theta > 0$  and 0 otherwise. Therefore, the regularization function 3.15 can be represented as:

$$E(\theta) = \frac{\|p^\delta - RH(\theta)\|_2^2}{2} + \lambda F(\theta) \quad (3.18)$$

where  $F(\theta)$  is a regularization functional for the level-set function  $\theta$ .

This variational regularization functionals have been presented in a continuous framework. For their minimization, a discretization is necessary and iterative methods are very often used to obtain the minimizer.

## 3.3 Reconstruction Methods for Discrete Tomography

A number of reconstruction methods have been proposed to address the discrete tomography, when only a limited number of pixel (voxel) values in the image (volume) to be reconstructed is considered. These methods are generally iterative and rely on a sparsity prior which may be applied in the image domain or after a sparse transform such as a wavelet transform [Yu and Wang (2010)]. Some methods are based on discrete algebraic reconstruction techniques [Batenburg and Sijbers (2009), Cai and Ma (2010)]. Markov random fields have also been much used [Liao and Herman (2004)]. Some methods minimize a functional that incorporates a data term and a binary constraint, with stochastic techniques [Rusko and Kuba (2005)] or convex analysis optimization [Capricelli and Combettes (2007), Schüle *et al.* (2005)b]. Belief Propagation reconstruction approach has been proposed [Gouillart *et al.* (2013)]. In this section, the main discrete reconstruction methods investigated in the literature are described in briefly.

### 3.3.1 Discrete Algebraic Reconstruction Technique(DART)

Based on algebraic reconstruction technique (ART), a discrete reconstruction method [Batenburg and Sijbers (2009), Batenburg and Sijbers (2011)] has been proposed to reconstruct a binary image  $f_b$ . A reconstruction image is obtained with ART, and then a threshold is used to segment the reconstructed image  $f_b$  and detect the boundary region  $U$ . All the pixels who are not in region  $U$  keep their pixel values and the pixels in region  $U$  are updated by ART once again. The algorithm will be iterated until the stopping criterion is achieved. The scheme used with DART is shown in Fig.3.3: In a DART step, each boundary pixel

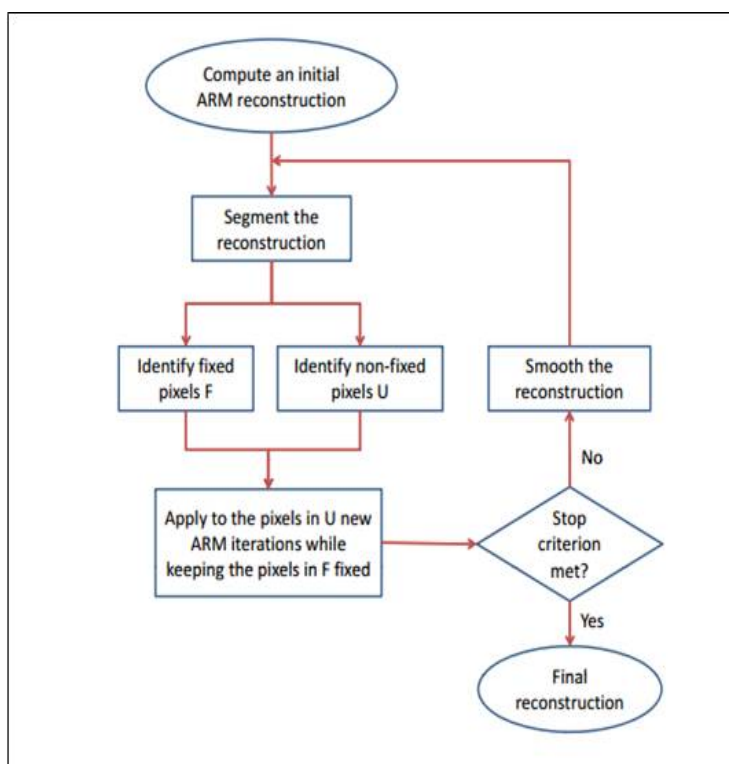


Figure 3.3: The flow chart of DART method [Batenburg and Sijbers (2011)]

is allowed to vary independently, which may result in large local variations of pixel values, therefore, smoothing is necessary after each step. The DART gives good results for binary reconstruction. And DART algorithm is not much sensitive to the noise in projection data. However, DART is an heuristic algorithm without guaranteed convergence properties. It is based on the choice of several parameters that may change the reconstruction errors. The DART algorithm has been implemented in a Toolbox, the ASTRA Toolbox [Palenstijn *et al.* (2013)]. Recently, a new discrete tomography reconstruction named Total Variation Regularized Discrete Algebraic Reconstruction Technique (TVR-DART) has been proposed in [Zhuge *et al.* (2015)]. Compared with the old method, the new method is more robust and automated.

### 3.3.2 Statistical reconstruction methods

Statistical reconstruction methods consider that the image  $f$  is a random field. By knowing the data and assuming a prior model of  $f$ , it is possible to obtain an estimation of  $f$  based on bayesian theory. We recall it below for the case of Markov random fields and Gibbs distribution.

#### Basic theories

**Markov random fields and Gibbs distribution** Markov random fields have also been much used in discrete tomography reconstruction [Liao and Herman (2004), Nadabar and Jain (1996), Chalmond (1988), Weber *et al.* (2005)]. Suppose  $S$  is the set of site  $s$  and  $F_s$  is a random field. For every site  $s \in S$ ,  $f_s$  is the value of  $F_s$ , with the configuration  $\{F_s = f_s, s \in S\}$ . Markov random field could be defined as:

$$\forall s \in S, P(F_s = f_s | f_t, t = S - \{s\}) = P(f_s | f_t, t \in N_s) \quad (3.19)$$

where  $N_s$  is the neighbourhood of pixel  $s$ . the positions of pixel  $s$  and of its 2-order neighbours are shown in Fig.3.4

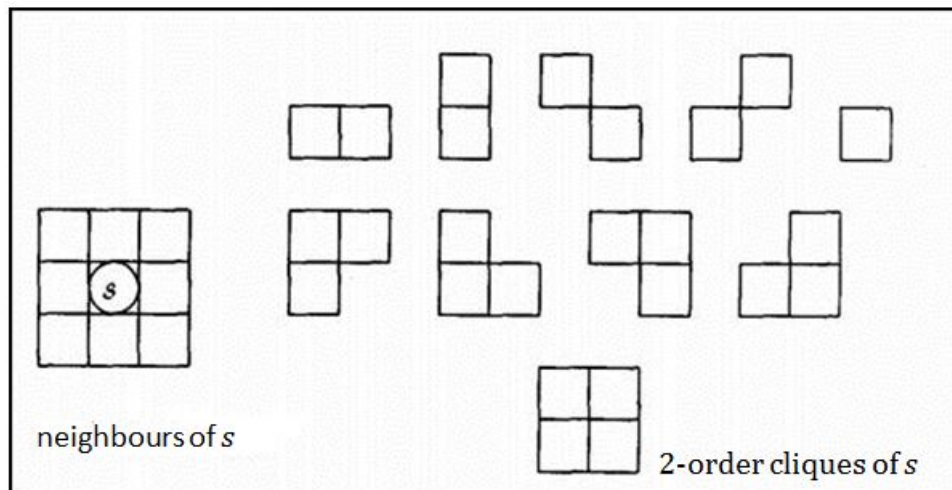


Figure 3.4: 2-order cliques of  $s$ ,  $s$  is in a 8-neighbours system.

The Markov random field can be expressed as a Gibbs distribution [Liao and Herman (2001), Geman and Geman (1993), Geman and Geman (1984)]:

$$P(F_s) = \frac{1}{Z_s} \exp(-\sum_{c \in C} V_c(f_c)) \quad (3.20)$$

and  $U(f) = \sum_{c \in C} V_c(f_c)$  is the energy function,  $Z_s = \sum_{z \in \Omega} \exp\{-U(f)\}$  is the partition function,  $C$  is the set of “cliques” which is used to describe the interactions among the pixels,  $V_c$  is the potential function.

**Bayesian equation** Let  $f$  is the image to be reconstructed with  $p^\delta = Rf + \delta$  and  $U(f)$  is a cost function, the best estimate of  $f$  is that  $f$  maximizes the a posteriori conditional probability of image  $f$  under a given measurement  $p^\delta$ . The Bayesian rule gives the posterior probability [Geman and Geman (1984), Gindi *et al.* (1993)]

$$P(f|p^\delta) = \frac{P(p^\delta|f)P(f)}{P(p^\delta)} \quad (3.21)$$

in terms the conditional probability of measurement  $p^\delta$  of given  $f$ , and  $P(f)$  and  $P(p^\delta)$  are priori probability distributions of  $f$  and  $p^\delta$  separately.

If  $p^\delta$  is Gaussian distribution with the mean  $Rf$ , We have

$$P(p^\delta|f) \propto \exp(-(p^\delta - Rf)^T(p^\delta - Rf)) \quad (3.22)$$

and

$$P(f) \propto \exp(-U(f)) \quad (3.23)$$

Therefore, the maximum a posteriori (MAP) probability can be obtained as:

$$P(f|p^\delta) \propto \exp(-(\|p^\delta - Rf\|^2 + U(f))) \quad (3.24)$$

If we want to maximize the posterior probability  $P(f|p^\delta)$ , we should minimize the  $J(f) = (\|p^\delta - Rf\|^2 + U(f))$ .

$$\hat{f} = \arg \min_f J(f) \quad (3.25)$$

### Non-local regularization

Different type of prior based on Markov chains can be used for the binary tomography problem. In the objective function a smoothness term that will promote the spatial homogeneity of the reconstructed image. A standard smoothness prior based on the Laplacian is defined as:

$$\langle f, Lf \rangle = \sum_{i=1}^n \sum_{j \in N(i)} (f_i - f_j)^2 \quad (3.26)$$

with  $N(i)$  is the 4-neighbourhood of  $i$ .

A non-local regularization could be defined with an undirected graph  $G = (V, E, \omega)$ , which consists of a set of vertices  $V$ , a set of edges  $E \in V \times V$  and a weight function  $\omega$  [Sixou and Peyrin (2012), Peyré *et al.* (2011)]. Given a vertex  $u$  and an edge  $uv$  in this undirected Graph  $G$ , the gradient function  $\partial_v f(u)$  could be defined as:

$$\partial_v f(u) = \sqrt{\omega(u, v)}(f(u) - f(v)) \quad (3.27)$$

and the gradient operator is the vector defined by  $\nabla_\omega = (\partial_{v1} f(u), \partial_{v2} f(u), \dots, \partial_{vk} f(u))$ , where  $v1, v2, \dots, vk$  belong to the neighbourhood  $N(u)$  of the vertex  $u$ ,  $\omega(u, v)$  is the weight vector.

The regularization functional associated to the  $L_2$  of the graph gradient is:

$$R(f, \omega) = \frac{\sum_u \sum_{v \in N(u)} \omega(u, v)(f(u) - f(v))^2}{2} \quad (3.28)$$

The weight function may be defined as:

$$w(u, v) = \frac{1}{\|u - v\|^2} \exp\left(-\frac{f(u) - f(v)}{2\delta^2}\right) \quad (3.29)$$

where  $\delta$  is a positive parameter.

## Algorithms

Some typical algorithms based on Markov chains and Bayesian equations are presented in the following section.

### Maximum Likelihood - Expectation Maximization (ML-EM)

It is possible to use the same Bayesian approach for Poisson noise. Assuming that the measured projection data  $p_i^\delta$  are Poisson independent random variables, the iterative expectation-maximization (EM) algorithm was used to estimate the image  $f$  by maximizing the maximum-likelihood (ML) function, which is the probability that the image  $f$  generates the measured projection data [Tsui *et al.* (1991), Frieden (1972), Vu and Knuiman (2002), Bruyant (2002)]:

$$L(f) = P(p^\delta | f) = \prod_i P(p_i^\delta | f) = \prod_i \frac{e^{-R_i \cdot f} (R_i \cdot f)^{p_i^\delta}}{p_i^\delta!} \quad (3.30)$$

Then the ML-EM algorithm can be written as:

$$f_j^{n+1} = f_j^n \cdot \frac{1}{\sum_j R_{ij}} \cdot \sum_j R_{ij} \frac{p_j^\delta}{\sum_k R_{kj} f_k^n} \quad (3.31)$$

This method starts from an initial guess  $f^0 = 0$ . The pixel values obtained with the reconstructed images are always positive.

### Iteration Conditional Models (ICM)

The main idea of ICM is to update pixel value one by one based on Markov Random Field and Bayesian estimation [Besag (1986), Retraint *et al.* (1998)]. The total projection data generated by all the X-ray passing by the pixel  $f_j$  is defined as:

$$J^k(f_j) = \sum_i (p_i^\delta - \sum_{l \neq j} (R_{il} f_i - R_{lj} f_j)) \quad (3.32)$$

The ICM for discrete reconstruction is defined as:

$$f_j^{k+1} = \begin{cases} f_j^k & J^{k+1}(\bar{f}_j) \geq J^k(f_j) \\ \bar{f}_j^k & J^{k+1}(\bar{f}_j) < J^k(f_j) \end{cases} \quad (3.33)$$

where  $\bar{f}$  is the complement of  $f$ .

### Multi-scale optimization methods

The algorithms based on Markov Random Fields within the framework of Bayesian estimation are generally greedy methods, therefore, multiresolution method is used to speed up the convergence rate and obtain good estimates [Pérez and Heitz (1992)].

As proved in section 3.3.2, maximizing the probability  $P(f/p^\delta)$  is equivalent to minimize  $J(f) = \|p^\delta - Hf\|^2 + U(f)$ .

$$\hat{f} = \arg \min_f J(f) \quad (3.34)$$

In a multi-resolution problem, suppose the configuration space  $\Omega$  could be decomposed as:

$$\Omega^n \subset \Omega^{n-1} \subset \Omega^{n-2} \subset \dots \subset \Omega \quad (3.35)$$

In the  $j$ -th configuration space, we could obtain:

$$\hat{f}^j = \arg \min_{f \in \Omega^j} J(f) \quad (3.36)$$

Assuming the projection image has a size  $2^m \times 2^m$ ,  $N_j$  is the total number of blocks of size  $2^{m^j} \times 2^{n^j}$  ( $m^j < m, n^j < n$ ) and  $B_k^j$  ( $k < N_j$ ) is the  $k$ -th block of the  $j$ -th configuration. For a clique  $c$ , its possible position among blocks are shown in Fig.3.5:

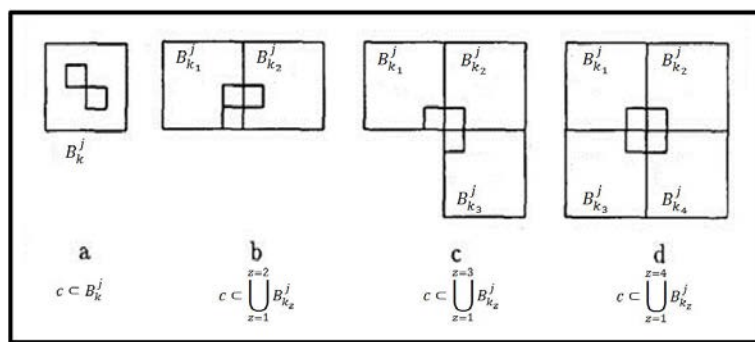


Figure 3.5: the positions of a clique  $c$  among blocks ,  $c$  is cliques of  $s$  in a 8-neighbours system [Pérez and Heitz (1992)].

The configuration for level  $j$  is shown in Fig.3.6. The  $f^j$  should be estimated first, then the initial estimation for the next resolution is obtained by interpolation by repetition. For

each resolution level  $j$ , we have to minimize the functional:

$$J(f^j) = \sum_{B_s^j \in B^j} \sum_{r \in B_s^j} \|p_r^\delta - h_r f_r^j\|^2 + U^j(f^j) \quad (3.37)$$

According to [Pérez and Heitz (1992)], the multi-scale optimization speed up the convergence effectively, and it is a very interesting method that we will try to extend to our discrete CT reconstruction problem. Some methods based on Belief Propagation have been developed recently [Gouillart *et al.* (2013)]. They will not be discussed here.

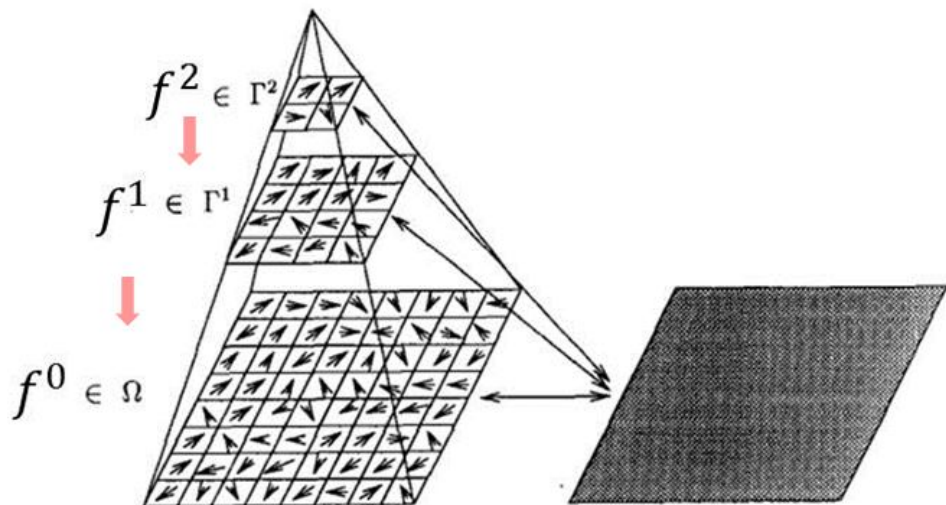


Figure 3.6: The sketch of pyramid structure [Pérez and Heitz (1992)].

### 3.3.3 Convex analysis methods

#### Binary tomography problem and feasibility problem

Another approach for solving the discrete tomography problem is to formulate it as a convex feasibility problem [Capricelli and Combettes (2005), Kamphuis and Beekman (1998), Schüle *et al.* (2005)b, Tao and An (1998), Schüle *et al.* (2005)c]:

$$\text{Find } \bar{f} \in S = \bigcap_{i=1}^m S_i \quad \text{and } \min \varphi(\bar{f}) = \varphi(S) \quad (3.38)$$

Where  $(S_i)_{1 \leq i \leq m}$  are closed convex sets in Euclidean space  $\mathbb{R}^N$  extracted from prior knowledges such as bounds on the image  $f$  and  $\varphi : \mathbb{R}^N \rightarrow ]-\infty, +\infty]$  is a convex function. In [Capricelli and Combettes (2005)], a quadratic function is used:

$$\varphi : \mathbb{R}^N \rightarrow \mathbb{R} : f \mapsto \langle Rf - r | Rf - r \rangle \quad (3.39)$$

and the constraint sets  $(S_i)_{1 \leq i \leq m}$  are defined as:

$$(\forall i \in \{1, \dots, m\}) \quad S_i = \{f \in \mathbb{R}^N \mid h_i(f) \leq \delta_i\} \quad (3.40)$$

Where  $(h_i)_{1 \leq i \leq m}$  are convex functions from  $\mathbb{R}^N$  to  $\mathbb{R}$  and  $(\delta_i)_{1 \leq i \leq m} \in \mathbb{R}^m$  are the constraints. Under this assumptions, for every  $f \in \mathbb{R}^N$ ,  $h_i$  has at least one subgradient at  $f$ :

$$(\forall y \in \mathbb{R}^N) \quad \langle y - f | g_i \rangle + h_i(f) \leq h_i(y) \quad (3.41)$$

This means  $g_i$  belongs to the subdifferential at  $f$ , and the set of all subgradients of  $h_i$  is expressed as  $\partial h_i(f)$ . The subgradient projection  $G_i f$  of  $f$  onto  $S_i$  is obtained by selecting an arbitrary  $g_i \in \partial h_i(f)$ :

$$G_i f = \begin{cases} f + \frac{\delta_i - h_i(f)}{\|g_i\|^2} g_i & h_i(f) > \delta_i \\ f & h_i(f) \leq \delta_i \end{cases} \quad (3.42)$$

It is noticed that computing  $G_i f$  only need one subgradient of  $h_i(f)$  at  $f$ . This method is able to perform parallel processing of variable blocks of constraints, and it uses subgradient projections onto the constraints sets. It is similar to the proximal algorithms much investigated in the literature.

### Convex-concave methods and Difference of Convex functions (D.C.) programs

The discrete tomography problem is associated with an under-determined linear system with limited number of pixel values. The binary case is defined as:

$$Rf = p^\delta \quad f = (f_1, f_2, \dots, f_n) \in \{0, 1\} \quad (3.43)$$

where  $R$  is projection matrix;  $f$  are pixel values and  $p^\delta$  the projection values. This problem is non convex and it can be formulated as the minimization of the difference of two convex functions. Taking account of the binary constraints, the following objective function can be considered: [Weber *et al.* (2005), Sixou and Peyrin (2012)]:

$$E(f, \alpha, \beta) = \frac{\|Rf - p^\delta\|^2}{2} + \frac{\alpha}{2} \langle f, Lf \rangle + \beta \frac{\langle f, (e - f) \rangle}{2} \quad (3.44)$$

where  $\alpha, \beta$  are the regularization parameters;  $L$  is a smoothness matrix;  $e = (1, 1, \dots, 1)$ . This objective function contains three terms: the first one is projection error; the second one is a smoothness term which will promotes the spatial homogeneity; and the last one is a concave function enforcing binary values.

Then the objective function can be written as:

$$E(f, \alpha, \beta) = \frac{\langle f, Qf \rangle}{2} + \langle q, f \rangle + \beta \frac{\langle f, (e - f) \rangle}{2} \quad (3.45)$$

with  $Q = R^T R + \alpha L$ ,  $q = -R^T p^\delta$ . The main propose of D.C program is to obtain a minimum of this functional [Schüle *et al.* (2005)b, Tao and An (1998), Schüle *et al.* (2005)c]. Let  $h_1, h_2: \mathbb{R}^n \rightarrow \bar{\mathbb{R}}$ , lower-semicontinuous and convex,  $\text{dom } h_1 \subset \text{dom } h_2$ ,  $\text{dom } h_2^* \subset \text{dom } h_1^*$  and  $f = h_1 - h_2$ . Consider the optimization problem:

$$\inf\{E(f) = h_1(f) - h_2(f); f \in \mathbb{R}^n\} \quad (3.46)$$

The algorithm for this kind of non-convex optimization problem can be expressed by Fig. 3.7: where the subdifferential of the functions  $h_1$  and  $h_2^*$  have to be calculated.

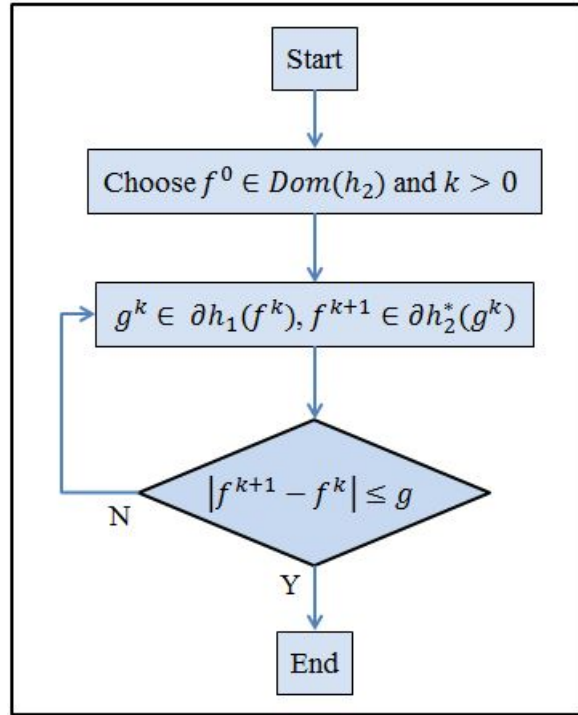


Figure 3.7: The flow chart of D.C program

Therefore, the objective function  $E(f, \alpha, \beta)$  could be decomposed by D.C program as:

$$E(f, \alpha, \beta) = h_1(f, \alpha) - h_2(f, \beta) \quad (3.47)$$

and:

$$h_1 = \frac{\langle f, \lambda I f \rangle}{2} + l_c(f) \quad (3.48)$$

$$h_2 = \frac{\langle f, [(\lambda + \beta)I - Q]f \rangle}{2} - \langle q + \frac{\beta e}{2}, f \rangle \quad (3.49)$$

where  $l_c$  is the indicator function of the set  $C = [0, 1]^n$ ,  $\lambda$  is the upper bound of the largest eigenvalue of  $Q$ . The update rules of equation (3.48) and (3.49) are:

$$g^k = [(\lambda + \beta)I - Q]f^k \quad (3.50)$$

$$f_i^{k+1} = \begin{cases} 0 & g_i^k \leq 0 \\ 1 & g_i^k \geq \lambda \\ g_i^k / \lambda & \text{otherwise} \end{cases} \quad (3.51)$$

This algorithm was applied to binary tomography problems and good reconstruction results have been obtained [Weber *et al.* (2005), Sixou and Peyrin (2012)].

### 3.4 Conclusion

In this chapter, a brief review on the principles of the X-ray computed tomography (CT) was presented. We have described the basic theory and methods for tomography reconstruction.

There are two main classes of reconstruction methods in tomography: analytical and iterative reconstruction algorithms. Usually, the analytical algorithms will generate precise reconstructed image only when a large number of projection data are considered. The iterative algorithms can be useful to reconstruct images from a limited number of projections, which is very useful to reduce the X-ray dose and shorten the data collection time. Yet, these iterative schemes must be regularized in the presence of noisy data.

In the discrete tomography problem, the image to be reconstructed has only several pixel values. Especially, there are only two intensity levels that are considered in binary tomography. In the reconstruction process, the image values are discontinuous. Some discrete CT reconstruction methods such as DART have been detailed in this chapter. Other discrete reconstruction methods such as statistical methods based on Markov chains and Bayesian equation and convex analysis methods are also presented in this chapter.

In the next chapter, our main work will focus on binary tomography from a limited number of projections with TV and LS regularization methods.

## II Contribution

---



## Chapter 4

---

# Binary Tomography Reconstruction of Bone Microstructure from a Limited Number of Projections

---

### 4.1 Introduction

In this chapter, we will focus on the topic of binary tomography reconstruction of bone microstructure from a limited number of projections. Reducing the number of projections is an important issue in X-ray Computed Tomography, and it is particularly crucial when imaging a moving organ, such as the beating heart or when the irradiation dose has to be reduced as for *in vivo* investigation of the bone microstructure. Therefore, it is interesting to study new optimization schemes to reconstruct images from a limited number of projections. Binary tomography methods may be proposed to set a simpler inverse problem [Herman and Kuba (2007)]. The binary tomography problem is associated with an under-determined linear system of equations with the linear Radon projections operator  $R$  and binary constraints:

$$Rf = p^\delta \quad f = (f_1, \dots, f_n) \in \{0, 1\}^n \tag{4.1}$$

with the Radon operator  $R$ , the measured projection values  $p^\delta$ , and the pixel values  $(f_i)_{i \leq i \leq n}$  of the image with binary constraints  $f = (f_1, \dots, f_n) \in \{0, 1\}^2$ .

The binary tomography problem that reconstructing from a limited number of projections is highly ill-posed and must be regularized. Recently, with the development of

compressive sensing approaches, a number of algorithms based on Total Variation (TV) regularization scheme have been investigated for CT [Sidky and Pan (2006), Sidky and Pan (2008), Sidky *et al.* (2012), Ritschl *et al.* (2011), Defrise *et al.* (2011)]. The TV is well-known to preserve edge and it provides good reconstruction images with sparse view sampling. While it is not clear whether TV is appropriate to reconstruct trabecular bone images due to its fine structures and multi-scale details inside. Level-set (LS) regularization methods have also been studied recently to reconstruct solutions of inverse problems with non-smooth and piecewise constant solutions [Egger and Leitao (2009), DeCezaro *et al.* (2009), Tai and Chan (2004), DeCezaro *et al.* (2013)]. Yet, LS methods have not been applied to binary tomography problem. These methods improve the classical Tikhonov regularization which gives poor results for the reconstruction of non-smooth solutions. They can be extended to the general discrete case in which the image to be reconstructed can take several discrete values.

The main contribution of this chapter is to use the TV regularization method and the Level-set regularization methods for binary tomography problem. In this case, the direct operator is the Radon projector. We start from the TV regularization without and with the binary convex constraints on the image function to be reconstructed. A LS scheme with  $H_1 - TV$  regularization [DeCezaro *et al.* (2009)] and a Piecewise Constant Level-set (PCLS) approach with an augmented Lagrangian approach are also used to solve this nonlinear problem [DeCezaro *et al.* (2013)]. Then we compare the results and reconstruction errors obtained with the classical TV regularization functional minimized by the Alternate Direction of Minimization Method (ADMM) algorithm and with the two level-set regularization methods. The comparison of these inverse schemes is performed on a simple disk and on two more complex CT cross-sections of trabecular bone with different bone density.

This chapter is structured as follows. After the introduction, the second section deals with the TV regularization method and the ADMM minimization methodology. Then, the nonlinear level-set formulation of the binary tomography is presented together with a piecewise constant level-set method and an augmented Lagrangian approach in the third section. Some criteria were introduced to evaluate the reconstruction qualities in the fourth section. The numerical results obtained on a simple disk or on noisy bone CT cross-section images of various size selected on Fig.2.13 are reported and discussed in the last section. At the end of this chapter, we then give the main conclusions and perspectives of our work.

## 4.2 Total Variation (TV) regularization and ADMM approach

As mentioned in Eq.3.15, a common way to regularize the binary tomography problem is to construct a regularization functional  $E(f)$  with a data fidelity term that measures the consistency between the estimates and the measurements and a regularization term

$J(f)$  that imposes an a priori constraint on the solution. The data-fitting term is usually based on the  $L_2$  norm and the regularization functional can then be written as:

$$E(f) = \frac{\mu}{2} \|Rf - p^\delta\|_{L_2}^2 + J(f) \quad (4.2)$$

The parameter  $\mu$  is the regularization parameter balancing the contribution of the data fidelity term and the regularization term. The measured projection data  $p^\delta$  is the approximation of the real projection data  $p$ , corresponding to the true solution  $f^*$  with  $Rf^* = p$ . The noisy data  $p^\delta$  are assumed to be corrupted by noise with a noise level  $\delta$ , satisfying  $\|p^\delta - p\|_2 \leq \delta$ .

In Section. 3.2.3, the isotropic TV regularization based on computing the  $L_1$  norm of the gradient is defined:

$$J_{TV}(f) = \int_{\Omega} |\nabla f(r)| dr = \int_{\Omega} \sqrt{f_x^2 + f_y^2} dx dy \quad (4.3)$$

The reconstruction results obtained with the isotropic TV were very similar or slightly better than the ones achieved with the anisotropic TV for most cases investigated. We will mainly present the results obtained with the isotropic norm in this work.

The binary constraints lead to a non-convex inverse problem. Convexified models obtained by relaxation of the binary constraint have often been considered for segmentation tasks [Bresson *et al.* (2007), Brown *et al.* (2012)]. In this study, we use the same type of methods and then function  $f$  to be reconstructed is thus allowed to take values continuously from  $[0, 1]$ . The convex constraints can be included in the regularization functional [Afonso *et al.* (2011), Afonso *et al.* (2010)]. The following optimization problems without and with convex constraints  $f \in C = [0, 1]^n$  have been considered as problems  $(P_1)$  and  $(P_2)$ :

$$\begin{aligned} (P_1) \quad & \text{minimize } \frac{\mu}{2} \|p^\delta - Rf\|_2^2 + J_{TV}(f) \\ (P_2) \quad & \text{minimize } \frac{\mu}{2} \|p^\delta - Rf\|_2^2 + J_{TV}(f) \quad s.t. \quad f \in [0, 1]^n \end{aligned} \quad (4.4)$$

Various numerical methods have been used to solve the TV regularized deconvolution problem including partial differential equations, splitting or primal dual methods [Becker *et al.* (2009), Chambolle and Pock (2011), Goldstein and Osher (2009)]. Results of extensive numerical experiments show that algorithms based on the ADMM and an augmented Lagrangian function are among the state-of-the-art methods to minimize the TV regularization functional [Ng *et al.* (2010), Afonso *et al.* (2011), Afonso *et al.* (2010)]. Algorithms based on the ADMM (SALSA and C-SALSA) have been proposed to solve a number of image processing tasks, such as image inpainting and deblurring [Afonso *et al.* (2011), Afonso *et al.* (2010)]. Our problem is thus formulated as a minimization problem of the ADMM form with a series of linear constraints. In order to include convex constraints,

$f \in C = [0, 1]^n$ , the following augmented Lagrangian equation is considered:

$$\begin{aligned} \mathcal{L}(f, (g_i), h, (\lambda_i), \lambda_C) = & \sum_i (\|g_i\|_2 - \lambda_i^t(g_i - D_i f) + \frac{\beta}{2}\|g_i - D_i f\|_2^2) + \frac{\mu}{2}\|p^\delta - Rf\|_2^2 \\ & + I_C(h) + \frac{\beta}{2}\|h - f\|_2^2 - \lambda_C^t(h - f) \end{aligned} \quad (4.5)$$

where  $\mu$  is the regularization parameter,  $\beta$  the Lagrangian parameter and  $I_C$  the indicator function of the convex set  $C$ :

$$I_C(x) = \begin{cases} 0 & \text{if } x \in C \\ \infty & \text{otherwise} \end{cases} \quad (4.6)$$

The Lagrange multipliers  $(\lambda_i)_{1 \leq i \leq n}$ ,  $\lambda_C$  are vectors in  $\mathbb{R}^{2n}$  and  $\mathbb{R}^n$ . For each pixel  $i$ ,  $D_i f \in \mathbb{R}^2$  represents the first-order finite difference at pixel  $i$  in both horizontal and vertical directions,  $(g_i)_{1 \leq i \leq n}$  and  $h$  are the auxiliary unknowns corresponding to the gradient and the convex constraint. The ADMM algorithm searches for the saddle point of the augmented Lagrangian by iterating the following equations successively:

$$\begin{aligned} g_i^{k+1} &= \arg \min_{g_i} \mathcal{L}(f^k, (g_i^k), h^k, (\lambda_i^k), \lambda_C^k) \\ h^{k+1} &= \arg \min_h \mathcal{L}(f^k, (g_i^{k+1}), h^k, (\lambda_i^k), \lambda_C^k) \\ f^{k+1} &= \arg \min_f \mathcal{L}(f^k, (g_i^{k+1}), h^{k+1}, (\lambda_i^k), \lambda_C^k) \\ \lambda_i^{k+1} &= \arg \min_{\lambda_i} \mathcal{L}(f^{k+1}, (g_i^{k+1}), h^{k+1}, (\lambda_i^k), \lambda_C^k) \\ \lambda_C^{k+1} &= \arg \min_{\lambda_C} \mathcal{L}(f^{k+1}, (g_i^{k+1}), h^{k+1}, (\lambda_i^{k+1}), \lambda_C^k) \end{aligned} \quad (4.7)$$

In this work, we have used the isotropic TV and the  $L_2$  norm of the gradient. With the alternating minimization algorithm, the sequences  $(f^k, (g_i^k)_{1 \leq i \leq n}, h^k, (\lambda_i^k)_{1 \leq i \leq n}, \lambda_C^k)$  are constructed with the following iterative scheme:

For each pixel  $i$ :

$$g_i^{k+1} = \max\{\|D_i f^k + \frac{1}{\beta}(\lambda_i^k)\| - \frac{1}{\beta}, 0\} \frac{D_i f^k + \frac{1}{\beta}(\lambda_i^k)}{\|D_i f^k + \frac{1}{\beta}(\lambda_i^k)\|} \quad (4.8)$$

The  $h^k$  update is:

$$h^{k+1} = \pi_C(f^k + \frac{\lambda_C^k}{\beta}) \quad (4.9)$$

where  $\pi_C$  is the projection on the convex set  $C$ . The new iterate  $f^{k+1}$  is obtained from the following linear system:

$$(\sum_i D_i^t D_i + \frac{\mu}{\beta} R^t R + I) f^{k+1} = \sum_i D_i^t (g_i^{k+1} - \frac{1}{\beta} \lambda_i^k) + \frac{\mu}{\beta} R^t p^\delta + h^{k+1} - \frac{\lambda_C^k}{\beta} \quad (4.10)$$

where  $I$  is the identity operator. The Lagrange multipliers  $(\lambda_i), \lambda_C$  are updated with:

$$\lambda_i^{k+1} = \lambda_i^k - \beta(g_i^{k+1} - D_i f^{k+1}) \quad (4.11)$$

$$\lambda_C^{k+1} = \lambda_C^k - \beta(h^{k+1} - f^{k+1}) \quad (4.12)$$

The sequence  $(f^k, (g_i^k), h^k, (\lambda_i^k), \lambda_C^k)$  which is generated by the ADMM algorithm converges to a Kuhn-Tucker point of problem  $(P_2)$ ,  $(f^*, (g_i^*), h^*, (\lambda_i^*), \lambda_C^*)$ , if  $(P_2)$  has one. If  $(P_2)$  does not have an optimal solution, then at least one of the sequences diverges. If the additional convex constraint is not included in the regularization functional, the additional unknowns  $h$  and  $\lambda_C$  are not used and Eq.4.9 and Eq.4.12 are not considered.

## 4.3 Level-set Regularization Algorithm of the Binary Tomography

### 4.3.1 Level-set formulation of the binary tomography problem

Our new level-set tomography method is based on a formulation of the reconstruction as a nonlinear inverse problem [Sixou *et al.* (2013)]. As defined in Section 3.2.3, the level-set regularization function to be minimized is defined as:

$$E(\theta) = \frac{\|p^\delta - RH(\theta)\|_2^2}{2} + \lambda F(\theta) \quad (4.13)$$

where  $F(\theta)$  is a regularization function and the Heaviside distribution function  $H(\theta)$  with a level-set function  $\theta \in H_1(\Omega)$  equals 1 if  $\theta > 0$  and 0 otherwise (Fig.4.1). With respect to  $\theta$ , the reconstruction problem becomes nonlinear and consists in determining the level-set function  $\theta$  such that  $RH(\theta) = p^\delta$ . In this work, we considered a Total Variation- $H_1$  regularization functional [Egger and Leitao (2009), DeCezaro *et al.* (2009)]:

$$F(\theta) = \beta_1|H(\theta)|_{TV} + \beta_2\|\theta\|_{H_1}^2 = \beta_1|H(\theta)|_{TV} + \beta_2(\|\theta\|_{L_2}^2 + \|\nabla\theta\|_{L_2}^2) \quad (4.14)$$

The regularization parameters  $\beta_1, \beta_2$  determine the relative weights of the stabilizing terms. And the Total Variation (TV) seminorm is given by:

$$|H(\theta)|_{TV} = \int |\nabla H(\theta)| dx \quad (4.15)$$

It penalizes the length of the Hausdorff measure of the boundary of the set  $\Omega_1$ . This contour regularization term is included in the Chan-Vese functional to prevent the zero level curves becoming oscillatory [Chan and Vese (2001), Tai and Chan (2004)].

Since  $H$  is discontinuous, it is necessary to consider generalized minimizers of the regularization functional [Egger and Leitao (2009), DeCezaro *et al.* (2009)] in the numerical implementation. In this work, the Heaviside function  $H$  is replaced by the following

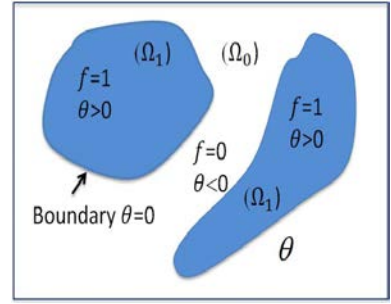


Figure 4.1: The sketch of level-set function.

smoothed approximations  $H_\epsilon$ :

$$H_\epsilon(x) = \frac{1+2\epsilon}{2}(\operatorname{erf}(x/\epsilon) + 1) - \epsilon \quad (4.16)$$

where  $\epsilon$  is a real positive constant that controls the scale of the smoothed Dirac. The smoothed Tikhonov regularization functional is given by:

$$E_\epsilon(\theta) = \frac{\|RH_\epsilon(\theta) - p^\delta\|_2^2}{2} + \beta_1|H_\epsilon(\theta)|_{TV} + \beta_2\|\theta\|_{H_1}^2 \quad (4.17)$$

where  $|\cdot|_{TV}$  is the Total Variation semi-norm. The minimizers of the Tikhonov functionals are found with a first-order optimality condition for the smoothed functionals,  $G(\theta) = 0$ , with:

$$G(\theta) = H'_\epsilon R^*(RH_\epsilon(\theta) - p^\delta) + \beta_2(I - \Delta)(\theta) + \beta_1 \frac{\partial|H_\epsilon(\theta)|_{BV}}{\partial\theta} \quad (4.18)$$

where  $R^*$  denotes the adjoint of the forward projection operator. The differential of  $|H_\epsilon(\theta)|_{TV}$  is given by [Tai and Chan (2004)]:

$$\frac{\partial|H_\epsilon(\theta)|_{TV}}{\partial\theta} = -\delta_D(\theta)\nabla \cdot \frac{\nabla\theta}{|\nabla\theta|} \quad (4.19)$$

where  $\delta_D$  is a Dirac distribution.

The solutions of the optimality condition  $G(\theta) = 0$  are obtained with a Gauss-Newton method. From the current estimate  $\theta_k$ , the update  $\theta_{k+1} = \theta_k + \lambda\delta\theta$  is obtained with:

$$V_k^*V_k\delta\theta + \beta_2(I - \Delta)(\delta\theta) - \beta_1\delta_D(\theta_k)\nabla \cdot \frac{\nabla\delta\theta}{|\nabla\theta_k|} = -G(\theta_k) \quad (4.20)$$

where  $V_k$  is the operator  $V_k = RH'_\epsilon(\theta_k)$ . These symmetric linear systems are solved by a conjugate gradient method. In the above formula,  $\lambda$  is a relaxation parameter.

### 4.3.2 Piecewise Constant Level-set (PCLS) with an augmented Lagrangian approach

In the framework of the Piecewise Constant Level-set (PCLS) approach [Tai *et al.* (2007), DeCezaro *et al.* (2013)], the unknown function  $f$  is represented with a smooth operator  $P : L_2(\Omega) \rightarrow L_2(\Omega)$  and a piecewise constant function  $\phi \in L_2(\Omega)$  as  $f = P(\phi)$ . In the binary tomography problem, the solution  $f$  takes the values 0 and 1, and thus it can be parametrized as  $f = \phi$ . In the discretized version, the assumption that the function  $\phi$  is piecewise constant with value 0 and 1 corresponds to the constraint:

$$K(\phi) = \phi(\phi - 1) = 0 \quad (4.21)$$

where  $K:L_2(\Omega) \rightarrow L_2(\Omega)$  is a smooth nonlinear operator. The binary tomography inverse problem can be formulated as:

$$R\phi = p^\delta \quad \text{where} \quad \phi \in \{L_2(\Omega) \mid K(\phi) = 0\} \quad (4.22)$$

Therefore, the regularization function Eq.4.13 can be rewritten as:

$$E(\phi) = \frac{\mu \|R\phi - p^\delta\|_2^2}{2} + |\phi|_{TV} \quad s.t. \quad \phi \in \{L_2(\Omega) \mid K(\phi) = 0\} \quad (4.23)$$

where  $\mu$  is the regularization parameter, the former constrained optimization problem is associated with an augmented Lagrangian functional:

$$L(\phi, \lambda) = \frac{\mu \|R\phi - p^\delta\|_2^2}{2} + \beta \frac{\|K(\phi)\|_{L_2(\Omega)}^2}{2} + \int \lambda K(\phi) + |\phi|_{TV} \quad (4.24)$$

where  $\beta$  is the Lagrange parameter,  $\lambda \in L_2(\Omega)$  is a Lagrange multiplier. The solutions  $(f^*, \lambda^*)$  is obtained as the saddle point of the algorithm. For a given penalty factor  $\beta$ , and starting from an initial guess  $(\phi_0, \lambda_0)$  the solutions  $(\phi^*, \lambda^*)$  are obtained by the optimality conditions:

$$\frac{\partial L}{\partial \phi} = 0 \quad , \quad \frac{\partial L}{\partial \lambda} = 0 \quad (4.25)$$

The level-set function and the Lagrange multiplier are updated iteratively. The updated level-set function is obtained through the minimization of the Lagrangian functional  $\phi_{k+1} = \arg \min_\phi L(\phi, \lambda_k)$ . The gradient  $\frac{\partial L}{\partial \phi}$  of the Lagrangian w.r.t  $\phi$  is given by:

$$\mu R^*(R\phi - p^\delta) + \beta K'^*(\phi)(K(\phi)) + K'^*(\phi)(\lambda) + \operatorname{div}\left(\frac{\nabla \phi}{|\nabla \phi|}\right) \quad (4.26)$$

where  $K'^*(\phi)$  is the adjoint of the Fréchet derivative of  $K$ . The iterate  $\phi_{k+1}$  is obtained with a gradient step:

$$\phi_{k+1} = \phi_k - \frac{\partial L}{\partial \phi^k} \quad (4.27)$$

The Lagrange multiplier is updated with:

$$\lambda_{k+1} = \lambda_k - K(\phi^{k+1}) \quad (4.28)$$

## 4.4 Quantification and Error Criteria of the Binary Reconstructed Images

At the end of reconstruction process, in order to evaluate the quality of reconstruction image  $f$ , some criteria are used which are defined in this section.

**Data term  $E_\delta$**  In the following , the Morozov [Morozov (1984)] discrepancy principle is often used to choose the best reconstructed image  $f$  which will satisfy  $\| Rf - p^\delta \| \approx \delta$ . Therefore, the noise error  $E_\delta$  between the measured projection data  $p^\delta$  and the simulated projection data of the reconstructed image  $f$  is defined as:

$$E_\delta = \| Rf - p^\delta \| \quad (4.29)$$

where  $f$  is the grey-level reconstructed image obtained at the end of reconstruction process.

**Minimum error  $E_m$**  The minimum error  $E_m$  will denote the error between the grey-level reconstructed image  $f^m$  at the final iteration  $m$  and the ground-truth image  $f^*$ . It is defined as:

$$E_m = \| f^m - f^* \| / \| f^* \| \quad (4.30)$$

The criterion  $E_m$  is used to evaluate the quality of grey-level reconstructed image.

**Misclassification rate  $MR$**  At the end of the reconstruction process, the reconstructed image  $f$  will be discretized with suitable thresholds. The misclassification rate  $MR$  is used to estimate the error between the final discrete image  $f_b$  and the ground-truth image  $f^*$ . It is defined as:

$$MR = \frac{\sum |f_b(i) - f^*(i)|}{N^2} \times 100\% \quad (4.31)$$

where  $f_b$  is the binarized version of the reconstructed image,  $f^*$  is the ground truth, and  $N$  the total number of pixels.

**Difference Map  $f_D$**  The difference map is defined as:

$$f_D = |f_b - f^*| \quad (4.32)$$

In the reconstruction process,  $E_m$  will denote the minimum error for grey-level reconstructed image  $f$ . The misclassification rate is useful to estimate the quality of the corresponding binary reconstructed image  $f_b$ . And the difference map provides a visual standard judgment of the difference between the final binary image  $f_b$  and the ground-truth  $f^*$ .

Even in the real world, it is impossible to have a ground-truth image, and we don't know the misclassification rate and difference map, they still provide some ways to judge the effect of the reconstruction algorithms.

## 4.5 Simulations and Discussions

In this section, we present the simulation details and the results obtained with the Total Variation (TV) and Level-set (LS) regularization methods.

### 4.5.1 Simulation details

In our experiments, the projection operator  $R$  is taken as the discrete approximation of the Radon transform, which is implemented on Matlab Image Toolbox. The TV and LS regularization methods were applied to two small images of size  $256 \times 256$ , which are shown in Fig.4.2, and to two big images of size  $512 \times 512$  with low and high bone density, which are shown in Fig.4.3 [Apostol *et al.* (2006), Bouxsein *et al.* (2010)]. The first small image is a simple disk image and the small bone image is an experimental bone cross-sections reconstructed with 400 projections from FBP (Filtered Back Projections) algorithm and subsequently thresholded. The comparison of the reconstruction results obtained on the simple disk image and on the bone cross-section is useful to understand the effect of the complexity of the geometry. The large images are reconstructed with 729 projections. In the three bone cross-section images, the pixel size is  $15\mu\text{m}$ . These images are regarded as the ground-truth images.

In our simulations, the images were reconstructed from a limited number of projection angles  $M$ , with  $M = 20$  and  $50$ . Lower projection numbers such as  $M = 10$  were not considered in this work since the reconstruction errors obtained on the boundaries are very large. For all images, the noisy projections  $p^\delta$  were obtained by adding a Gaussian noise with standard deviation  $\sigma_p$  to the raw projection data  $p$ . The noise distribution can be characterized by the standard deviation of the noise  $\sigma_p$  or peak to peak signal to noise ratio  $PPSNR$ :

$$PPSNR = 20\log\left(\frac{f_{max}}{n_{max}}\right) \quad (4.33)$$

where  $f_{max}$  and  $n_{max}$  are the maximum signal and noise amplitude respectively.

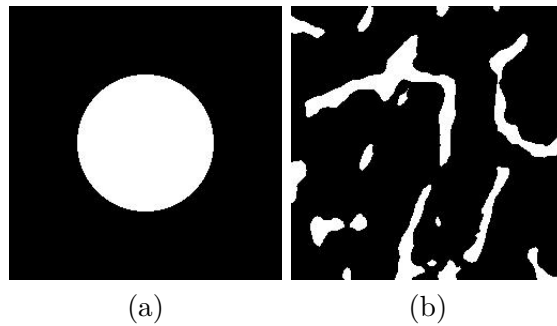


Figure 4.2: Small images of size  $256 \times 256$ : (a) Disk image;(b) Bone cross-section image, a central region of size  $256 \times 256$  of Fig.2.13.(b)

This noise level  $\delta$  can be estimated with  $\delta^2 = MN_r\sigma_p^2$ , where  $N_r$  is the number of X-rays per projection. The  $\sigma_p$  values, the peak to peak signal to noise ratio  $PPSNR$  values and the noise levels  $\delta$  are summarized in Table. 4.1 and Table. 4.2 for the small and large images respectively.

The iterations were stopped when the regularization functional stagnates. The final iteration index  $m$  is determined by the stopping condition:  $\|f^{m+1} - f^m\|_2 / \|f^m\|_2 < 0.0001$ .

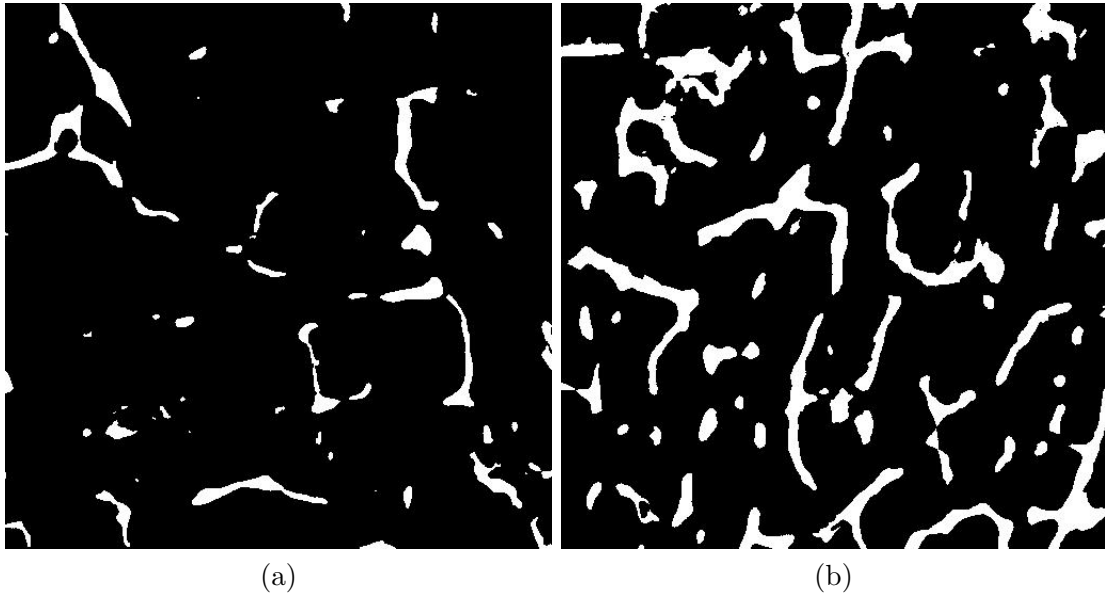


Figure 4.3: Large bone cross-section images of size  $512 \times 512$ , central regions of Fig.2.13:  
 (a) Sparse bone cross-section image;(b) Dense bone cross-section image.

Table 4.1: Noise standard deviation  $\sigma_p$ ,  $PPSNR$  and  $\delta$  values for small disk and bone images with 20 or 50 projections.

$\sigma_p$	Small Disk image		$\sigma_p$	Small bone image	
	M=20	M=50		M=20	M=50
	$\delta = 732.4$ $PPSNR = 15$	$\delta = 1158.1$ $PPSNR = 15$		$\delta = 562.8$ $PPSNR = 14$	$\delta = 889.4$ $PPSNR = 14$
8.55	$\delta = 1098.6$ $PPSNR = 12$	$\delta = 1737.2$ $PPSNR = 12$	6.57	$\delta = 844.2$ $PPSNR = 11$	$\delta = 1334.1$ $PPSNR = 11$
12.83	$\delta = 2197.3$ $PPSNR = 7$	$\delta = 3474.4$ $PPSNR = 7$	9.85	$\delta = 1688.4$ $PPSNR = 6$	$\delta = 2668.3$ $PPSNR = 6$
25.65			19.71		

In order to obtain the best reconstruction results, it is necessary to choose optimal regularization parameters. We have made an extensive sweeping of the values of the regularization parameters. Our choice of the optimal ones is based on the Morozov discrepancy principle [Morozov (1984)]. In most cases, the parameters which are chosen such as the final iterate,  $f^m$ , satisfies the condition:

$$\|Rf^m - p^\delta\| \approx \delta \quad (4.34)$$

where  $\delta$  is the noise level. For the TV regularization method, there are two important parameters: the regularization parameter  $\mu$  and Lagrangian parameter  $\beta$ . The  $\beta$  parameter

Table 4.2: Noise standard deviation  $\sigma_p$ ,  $PPSNR$  and  $\delta$  values for the big sparse and dense images with 20 projections.

$\sigma_p$	Big images	
	Sparse	Dense
3	$\delta = 365.6$ $PPSNR = 19$	$\delta = 368.02$ $PPSNR = 25$
6	$\delta = 731.16$ $PPSNR = 14$	$\delta = 736.16$ $PPSNR = 19$

controls the speed of convergence. The reconstructed image  $f^m(\mu)$  obtained at the end of the optimization process depends only on the regularization parameter  $\mu$ . In order to find the best combination of these parameters, we have tested many values of  $\beta$  and  $\mu$ . In our numerical simulations, the regulation parameter  $\mu$  and the Lagrange parameter  $\beta$  are selected when they satisfy the condition:  $\frac{\|Rf^m - p^\delta\| - \delta}{\delta} \leq \xi$ , with  $\xi = 0.01$ . In the classical level-set algorithm, the real positive constant  $\epsilon$  which controls the smoothed Heaviside function was set to 0.03. The regularization parameter  $\beta_1$  was set to 0 because the  $H_1$  term dominates the TV term [DeCezaro *et al.* (2009), Egger and Leitao (2009)]. Similarly to the methodology used for the TV regularization, we tested many parameters for the level-set algorithms to satisfy the Morozov principle. When the minimum of the data term is well-above the noise level, the Morozov principle can not be applied, but a good estimate of the optimal regularization parameters was obtained with the L-curve method [Hansen (2001)]. Finally, the misclassification rate  $MR$  and the difference map image  $f_{Diff}$  (defined in Section. 4.4) are used to evaluate the quality of binary images.

#### 4.5.2 Numerical results

##### Total Variation (TV) regularization method

In this section, we compare the reconstruction results obtained with TV regularization method. The minimization of the regularization functionals (Eq.4.4) is performed with an ADMM algorithm.

**Isotropic and anisotropic TV norms** First, the isotropic and anisotropic TV regularization methods without and with an additional box convex constraint are tested on these bone cross-section images. Generally, for TV regularization with a box constraint (TVbox) method, there are no obvious difference between the two norms. The reconstruction results obtained with isotropic norm are sometimes a little better. The reconstruction results with TVbox method for the big image with  $\sigma_p = 6$  and  $M = 20$  projections are displayed in Fig.4.4 and Fig.4.5;

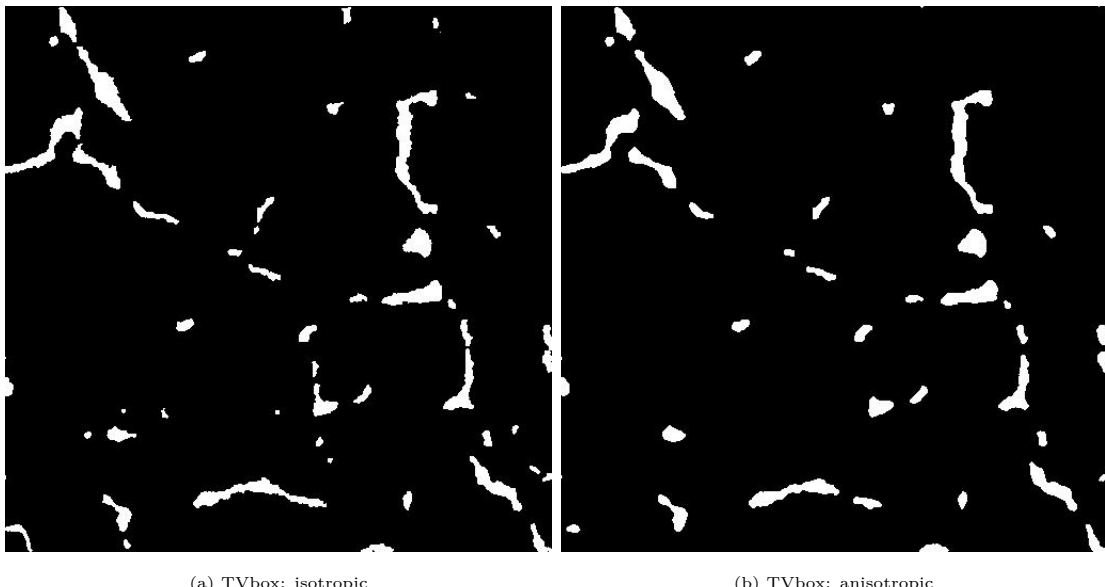


Figure 4.4: Binary sparse bone reconstructed images with TVbox method with 20 projection angles and 729 X-rays per projection with  $\sigma_p = 6$ . (a) isotropic TVbox:  $MR_m = 0.97\%$ ; (b) anisotropic TVbox:  $MR_m = 1.36\%$ .

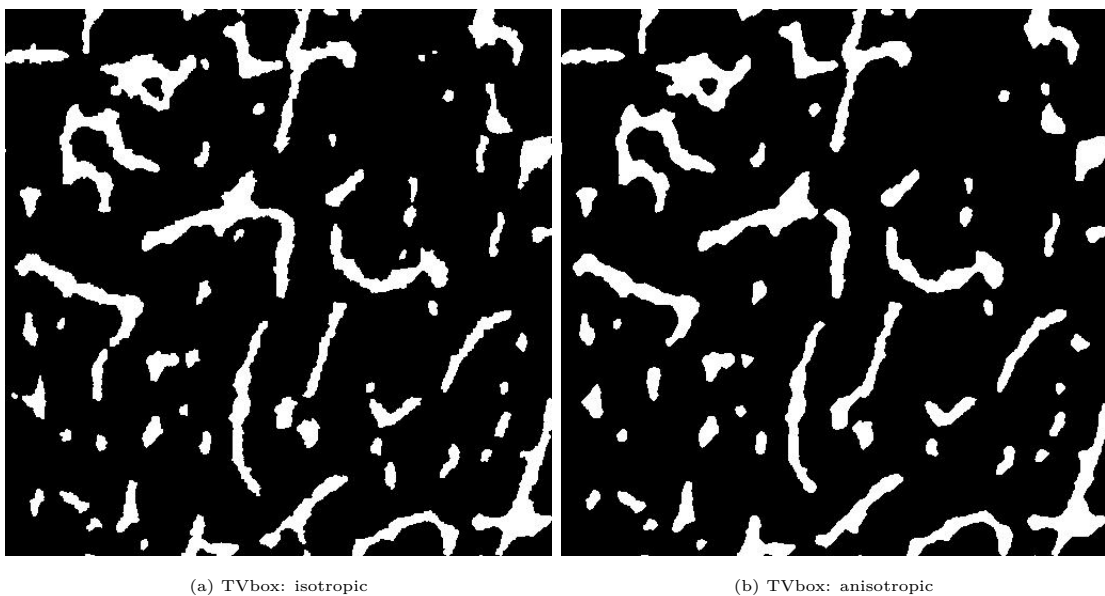


Figure 4.5: Binary dense bone reconstructed images with TVbox method with 20 projection angles and 729 X-rays per projection with  $\sigma_p = 6$ . (a) isotropic TV box:  $MR_m = 2.63\%$  ; (b) anisotropic TV box:  $MR_m = 3.39\%$  .

For the TV regularization (TV) method, the results obtained with the small images are similar to the ones obtained with the TV box method. The reconstruction results obtained with anisotropic TV are better than the ones for isotropic TV norm only for the big images. This special case is summarized in Table 4.3 and the reconstructed images with the two TV regularization with big bone cross-section images with  $\sigma_p = 6$  are shown

in Fig. 4.6 and Fig.4.7.

Table 4.3: Minimum error  $E_m$  and misclassification rate  $MR_m$  with isotropic and anisotropic TV regularizations for the big sparse and dense images with 20 projections.

$\sigma_p$ <b>M = 20</b>	Sparse image		Dense image	
	isotropic	anisotropic	isotropic	anisotropic
<b>3</b>	$E_m = 0.1320$ $MR_m = 2.33\%$	$E_m = 0.1032$ $MR_m = 1.23\%$	$E_m = 0.2299$ $MR_m = 5.61\%$	$E_m = 0.2181$ $MR_m = 4.53\%$
<b>6</b>	$E_m = 0.1342$ $MR_m = 2.35\%$	$E_m = 0.1098$ $MR_m = 1.41\%$	$E_m = 0.2332$ $MR_m = 5.59\%$	$E_m = 0.2195$ $MR_m = 4.61\%$

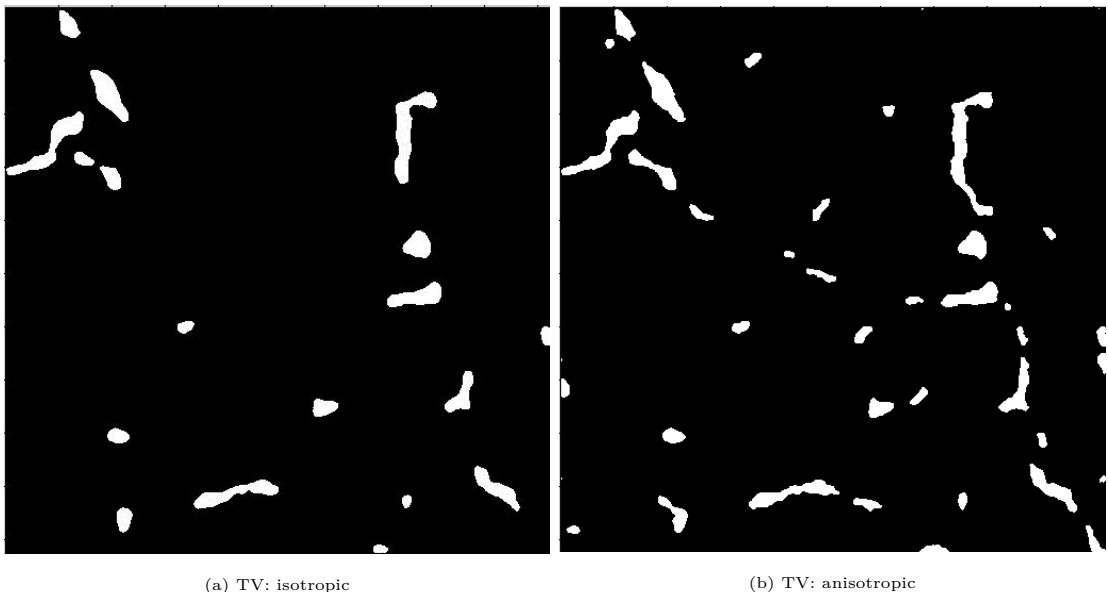


Figure 4.6: Binary sparse bone reconstructed images with 20 projection angles and 729 X-rays per projection with  $\sigma_p = 6$ . (a) isotropic TV:  $MR_m = 2.35\%$ ; (b) anisotropic TV:  $MR_m = 1.41\%$ .

In conclusion, the minimum error  $E_m$  and the misclassification rate  $MR_m$  of the reconstruction results obtained with isotropic TV were similar and even slightly better than the ones obtained with anisotropic TV for most cases investigated. Therefore, we only use isotropic TV norm in our simulations for the following work.

**TV regularization method without and with a box constraint** The discrete algebraic reconstruction technique (DART) [Batenburg and Sijbers (2009)] is an heuristic method with several adjustable parameters and it has been shown to give good results with enough SART iterations. Therefore, DART algorithm was applied to the three bone

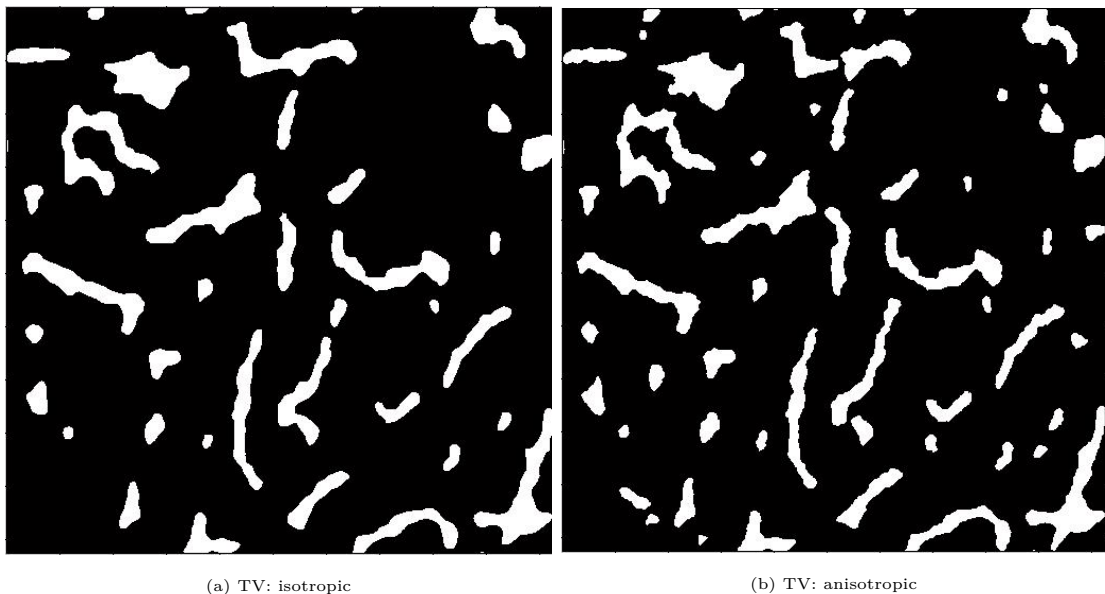


Figure 4.7: Binary dense bone reconstructed images with TV method with 20 projection angles and 729 X-rays per projection with  $\sigma_p = 6$ . (a) isotropic TV:  $MR_m = 5.59\%$  ; (b) anisotropic TV:  $MR_m = 4.61\%$  .

cross-section images for comparison. The basic idea of DART is described in Section 3.3.1. In our simulations, a first reconstructed image is obtained as a starting point using ART with 10000 iterations. Then a number of DART loops were performed, until the data term is very close to the noise level  $\delta$ . then, the DART algorithm is stopped. In each inner iteration, 3 SART iterations were performed, updating only the pixels in the boundary region  $U$ . The reconstructed image was smoothed at each step with a Gaussian filter. DART algorithm was implemented with the ASTRA tomography toolbox [Palenstijn *et al.* (2013), Van Gompel *et al.* (2010)]. The missclassification rate obtained at the end of the DART process is estimated from the binarized images. Comparing to TV, DART is more an heuristic method with more adjustable parameters but it has been shown to give good results with enough SART iterations.

**Small images** As an example of the reconstruction results obtained, the binary reconstructed images with 20 projection angles for TV regularization without and with box constraints are shown in Fig.4.8, Fig.4.9 and Fig.4.10, Fig.4.11 for the disk and the bone images respectively. We can see on the difference maps that the reconstruction errors are localized on the boundaries.

The evolution curves of data term ( $\|Rf^k - p^\delta\|$ ), and missclassification rate ( $MR(k)$ ) with the iteration number  $k$  for small bone image with 20 projection angles are shown in Fig.4.12. The evolution curves obtained with TV algorithm with convex constraints decrease faster and converge to smaller values than those without convex constraints.

Table.4.4, Table.4.5 summarize the minimum error  $E_m$  and missclassification rate

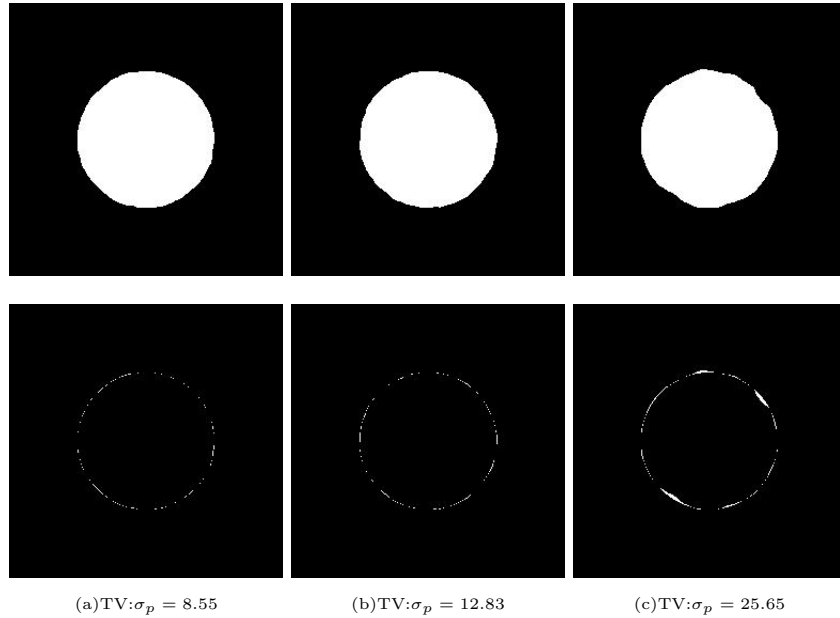


Figure 4.8: Binary Disk reconstructed images and difference maps with TV regularization method with 20 projection angles and 367 X-rays per projection.

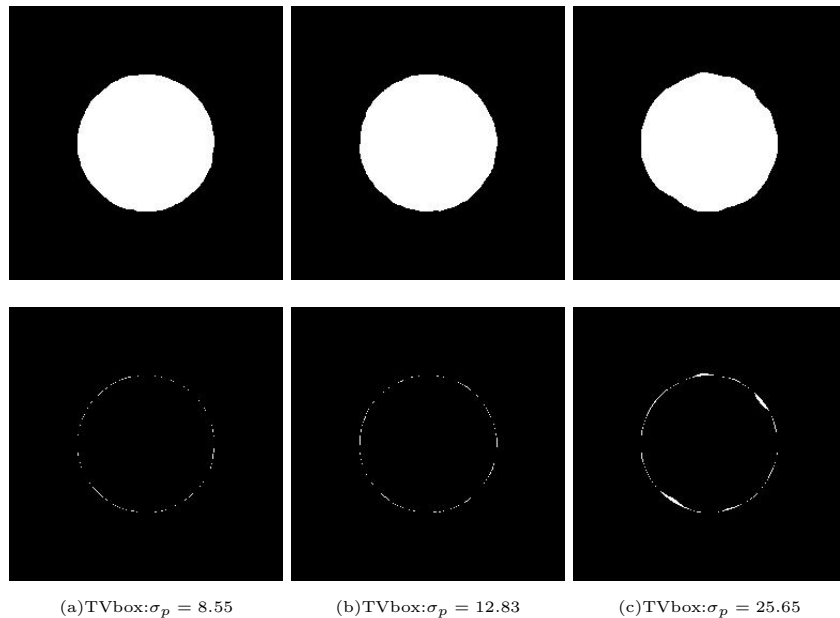


Figure 4.9: Binary Disk reconstructed images and difference maps with TV box regularization method with 20 projection angles and 367 X-rays per projection.

$MR_m$ , for disk and bone image respectively, for each noise level with 20 and 50 projections obtained with the TV regularization without or with the convex constraints. The values obtained with the DART algorithm for the small bone image are also given.

For the small disk image, the reconstruction results obtained without or with convex constraints are very good and they are almost the same. The level line of the disk image

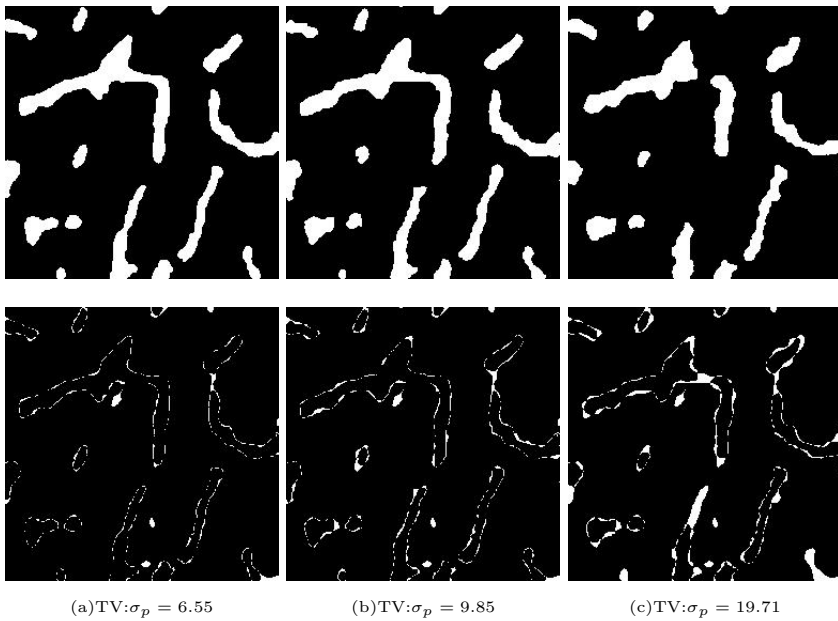


Figure 4.10: Binary small bone reconstructed images and difference maps with TV regularization method with 20 projection angles and 367 X-rays per projection.

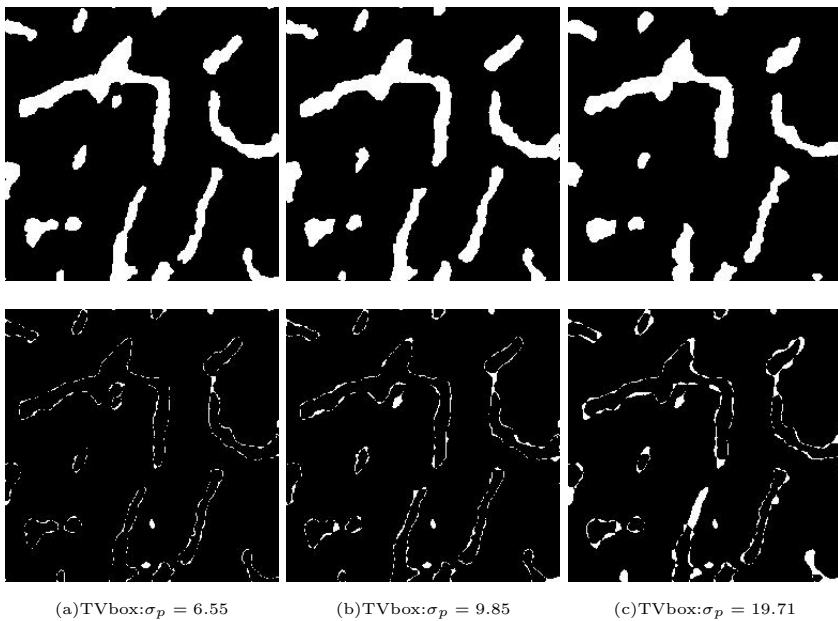


Figure 4.11: Binary small bone reconstructed images and difference maps with TV box regularization method with 20 projection angles and 367 X-rays per projection.

is circle and well restored by the TV regularization term which tends to minimize its perimeter. When the noise level  $\sigma_p = 25.65$  is high, TV without convex constraints performs better. On the contrary, for the bone image, with a more complex structure, the TV box algorithm gives the minimum normalized error  $E_m$  and misclassification rate  $MR_m$  for all the noise levels investigated. When the noise level is low, the TV and TV

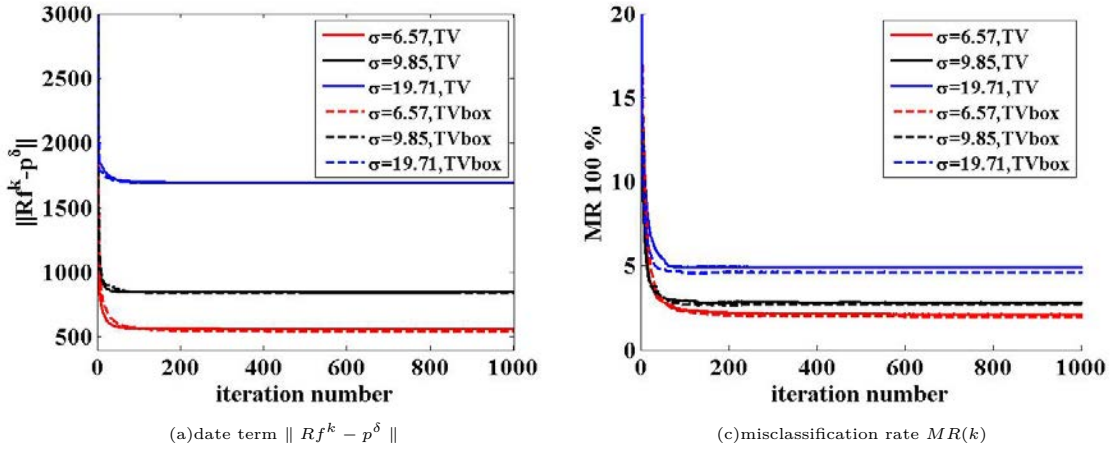


Figure 4.12: Evolution curves of data term and misclassification rate with the iteration number for small bone image with 20 projection angles

Table 4.4: Minimum errors  $E_m$  and missclassification rate  $MR_m$  for disk image for TV regularization without and with box convex constraints.

$\sigma_p$	TV		TV box	
	M=20	M=50	M=20	M=50
8.55	$E_m = 0.0505$ , $MR_m = 0.15\%$	$E_m = 0.0436$ , $MR_m = 0.093\%$	$E_m = 0.0505$ , $MR_m = 0.14\%$	$E_m = 0.0437$ , $MR_m = 0.095\%$
12.83	$E_m = 0.0535$ , $MR_m = 0.18\%$	$E_m = 0.0481$ , $MR_m = 0.14\%$	$E_m = 0.0535$ , $MR_m = 0.18\%$	$E_m = 0.0481$ , $MR_m = 0.14\%$
25.65	$E_m = 0.0737$ , $MR_m = 0.42\%$	$E_m = 0.0563$ , $MR_m = 0.27\%$	$E_m = 0.0739$ , $MR_m = 0.43\%$	$E_m = 0.0593$ , $MR_m = 0.32\%$

Table 4.5: Minimum errors  $E_m$  and missclassification rate  $MR_m$  for bone image for TV regularization without and with box convex constraints.

$\sigma_p$	TV		TV box		DART	
	M=20	M=50	M=20	M=50	M=20	M=50
6.55	$E_m = 0.1476$ , $MR_m = 2.11\%$	$E_m = 0.1041$ , $MR_m = 1.01\%$	$E_m = 0.1379$ , $MR_m = 1.95\%$	$E_m = 0.1026$ , $MR_m = 1.03\%$	$E_m = 0.1558$ , $MR_m = 2.71\%$	$E_m = 0.1223$ , $MR_m = 1.50\%$
9.85	$E_m = 0.1714$ , $MR_m = 2.82\%$	$E_m = 0.1292$ , $MR_m = 1.58\%$	$E_m = 0.1639$ , $MR_m = 2.69\%$	$E_m = 0.1278$ , $MR_m = 1.55\%$	$E_m = 0.1564$ , $MR_m = 2.71\%$	$E_m = 0.1230$ , $MR_m = 1.50\%$
19.71	$E_m = 0.2128$ , $MR_m = 4.90\%$	$E_m = 0.1660$ , $MR_m = 2.58\%$	$E_m = 0.2054$ , $MR_m = 4.63\%$	$E_m = 0.1610$ , $MR_m = 2.56\%$	$E_m = 0.1559$ , $MR_m = 2.70\%$	$E_m = 0.1201$ , $MR_m = 1.42\%$

box approaches perform better than DART. When the noise level  $\sigma_p = 19.71$  is high, the DART method achieves better reconstruction results.

**Big images** The TV algorithms without and with box constraints were also compared on big bone cross-sections images of size  $512 \times 512$ . We will present the reconstruction results in this section.

### *Reconstruction with $M=20$ projections*

For instance, the binary reconstructed images with TV regularization method without and with box constraints with  $\sigma_p = 3$  and  $M = 20$  projection angles are shown in Fig.4.14 and Fig.4.13 for low and high bone density images respectively. Similarly to the reconstruction results for the small images, the reconstruction errors are localized on the boundaries.

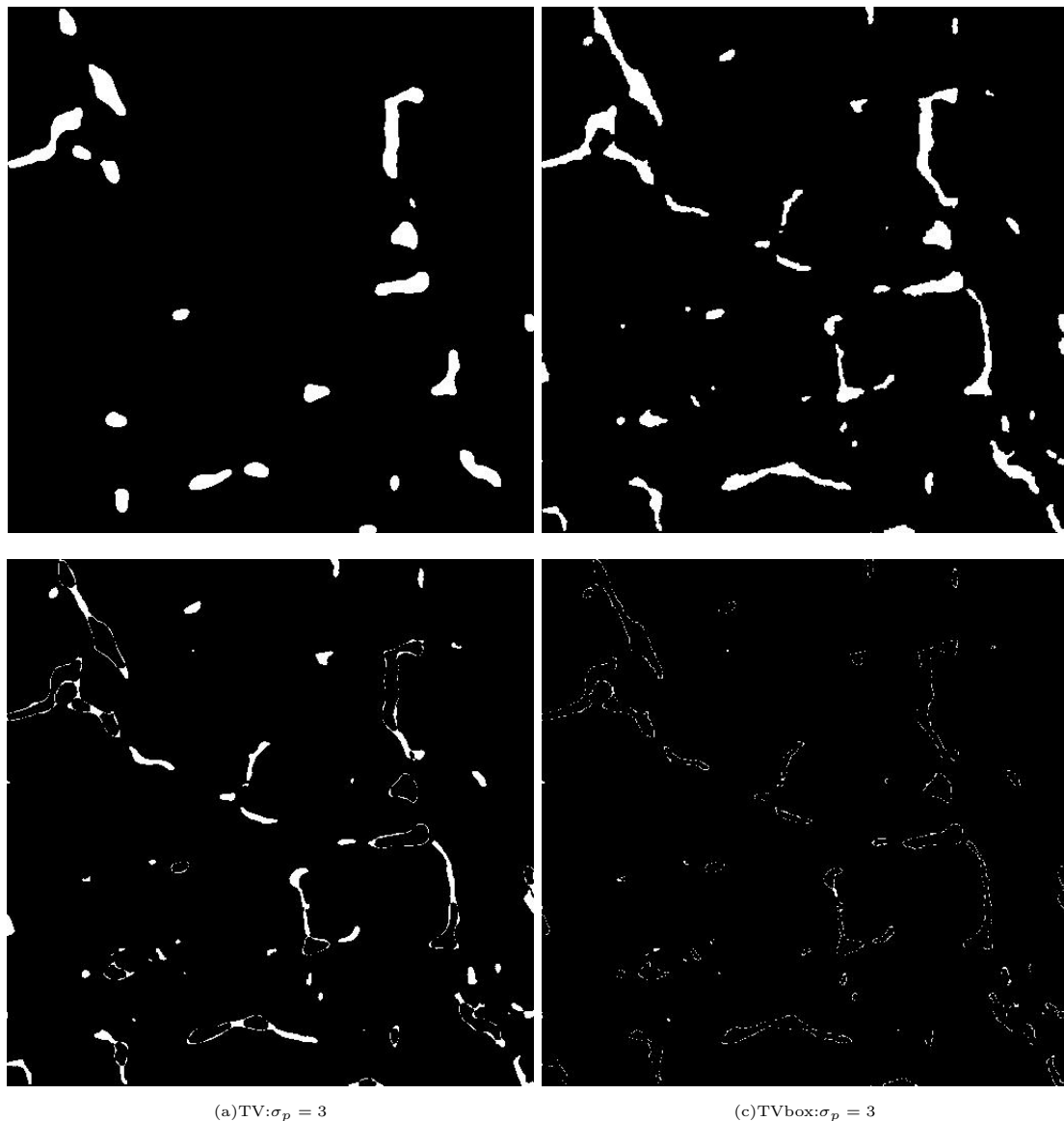


Figure 4.13: Binary sparse bone reconstructed images and difference maps with  $\sigma_p = 3$  and  $M=20$  projection angles and 729 X-rays per projection.

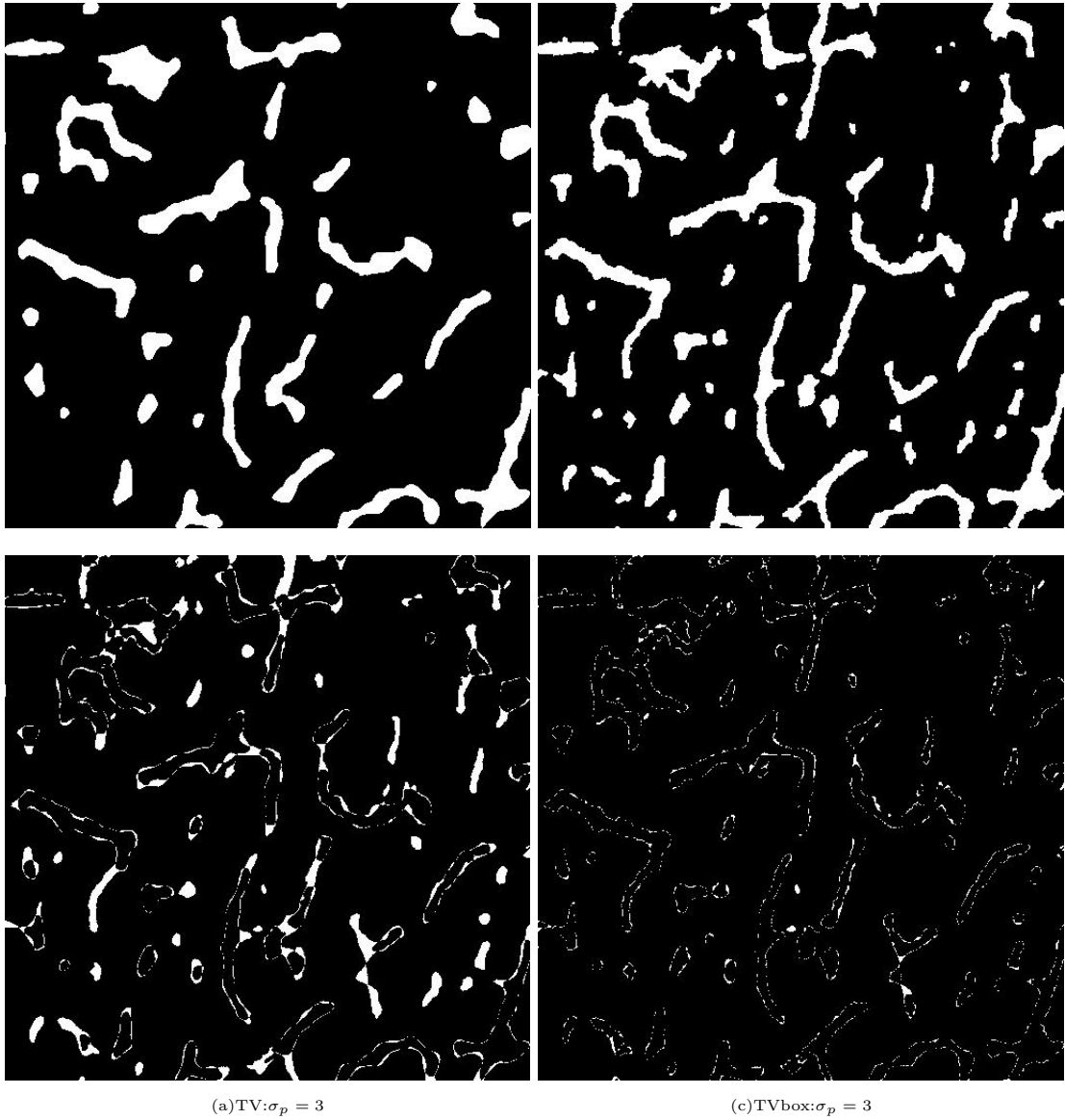


Figure 4.14: Binary dense bone reconstructed images and difference maps with  $\sigma_p = 3$  and M=20 projection angles and 729 X-rays per projection.

The evolution curves of data term  $\|Rf^k - p^\delta\|$  and misclassification rate ( $MR(k)$ ) with the iteration number are shown in Fig.4.15 and Fig.4.16 for the big sparse and dense bone image with 20 projection angles respectively.

In conclusion, the evolution curves of the data term  $\|Rf^k - p^\delta\|$  and misclassification rate  $MR(k)$  for TV algorithm with convex constraints decrease faster and give smaller values than without convex constraints. It was not possible to find a regularization parameter  $\mu$  and a Lagrange parameter  $\beta$  to make the data term  $\frac{\|Rf^m - p^\delta\| - \delta}{\delta} \leq \xi$ , with  $\xi = 0.01$  for TV algorithm without convex constraints because a good approximate solution can not be obtained with this regularization method. In our simulations, the smallest constant  $\xi$  which satisfies this relation is  $\xi = 0.5$ .

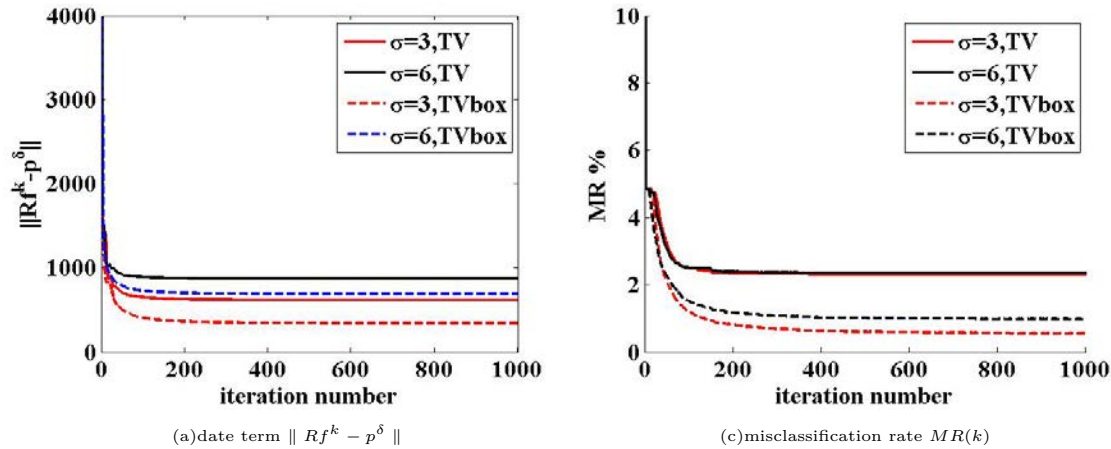


Figure 4.15: Evolution curves of data term and misclassification rate with the iteration number for big sparse bone image with 20 projection angles

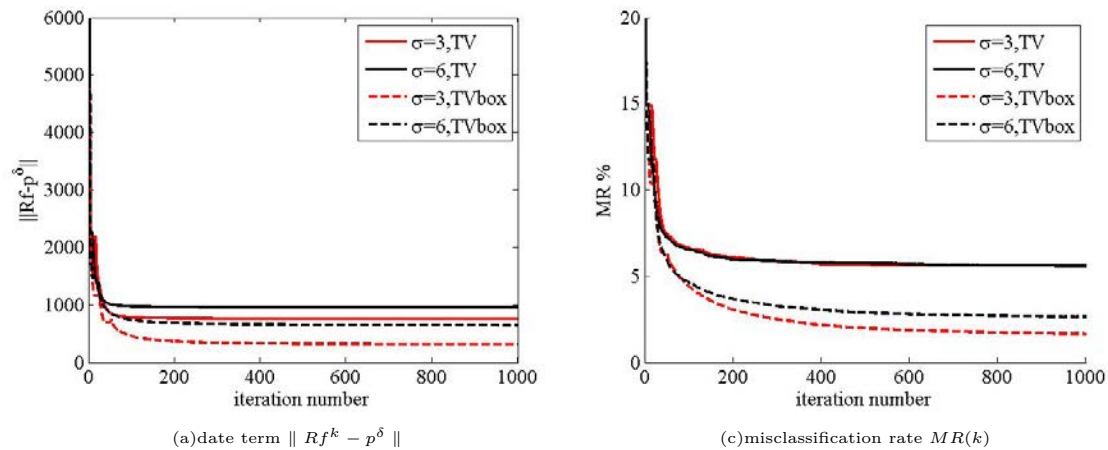


Figure 4.16: Evolution curves of data term and misclassification rate with the iteration number for big dense bone image with 20 projection angles

Table 4.6 summarizes the minimum error  $E_m$  and misclassification rate  $MR_m$  obtained for sparse and dense bone cross-section images with 20 projections. The values achieved with the DART algorithm are also given for comparison.

From Table 4.6, we see that the TV with box constraints algorithm gives better reconstruction results than the TV regularization method without any constraints on both big sparse and dense bone cross-section images. The TV method performs poorly on both bone cross-section images with complex structures and elongated regions. For the two bone cross-sections, the DART method is the worst method.

These big bone cross-sections are very challenging because of the fine structures inside of the images. For a subset  $A \subset \mathbb{R}^N$ , it is well-known that the total variation of the characteristic function of the subset is equal to its perimeter [Aubert and Kornprobst (2006)], and the TV regularization is thus not the most efficient approach for complex morphologies.

Table 4.6: Minimum errors  $E_m$  and missclassification rate  $MR_m$  for sparse bone images with 20 projections for TV regularization without with box convex constraints.

$\sigma_p$	Sparse Image			Dense Image		
	TV	TV box	DART	TV	TV box	DART
3	$E_m = 0.1320,$ $MR_m = 2.33\%$	$E_m = 0.0723,$ $MR_m = 0.55\%$	$E_m = 0.1574,$ $MR_m = 2.86\%$	$E_m = 0.2299,$ $MR_m = 5.61\%$	$E_m = 0.1351,$ $MR_m = 1.64\%$	$E_m = 0.2668,$ $MR_m = 7.80\%$
6	$E_m = 0.1342,$ $MR_m = 2.35\%$	$E_m = 0.0933,$ $MR_m = 0.97\%$	$E_m = 0.1560,$ $MR_m = 2.82\%$	$E_m = 0.2332,$ $MR_m = 5.59\%$	$E_m = 0.1623,$ $MR_m = 2.63\%$	$E_m = 0.2670,$ $MR_m = 7.93\%$

On the contrary, the TV regularization scheme with box constraints performs efficiently and it is able to extract many details and fine structures, when the parameter is chosen according to the Morozov principle. The reconstruction errors on the boundaries are much decreased.

### *Reconstruction with more projections*

Because of the complex and fine structures, there are still a lot of reconstruction errors located on the boundaries with  $M = 20$  projections for the big bone cross-sections with TV and TV box regularization methods. In this part, more projections are used, and we want to be sure whether a lower projection number such as  $M = 20$  or  $M = 50$  is suitable for a TV or TV box reconstruction or not. As mentioned in section 3.2.1, an exact FBP reconstruction needs a lot of projections. Therefore, FBP algorithm is applied on the two big bone cross-section images for comparison to study the effect of increasing projection number that acts on the reconstruction results with TV and TV box regularization methods.

Table 4.7 and Table 4.8 summarize the minimum error  $E_m$  and misclassification rate  $MR_m$  for  $\sigma_p = 3$  and  $\sigma_p = 6$  respectively, for the two big images with  $M = 50$ ,  $M = 100$  and  $M = 200$  projections. The values obtained with FBP algorithm are also given.

Table 4.7: Minimum errors  $E_m$  and missclassification rate  $MR_m$  for sparse bone images with  $\sigma_p = 3$  for TV regularization without with box convex constraints.

M	Sparse Image			Dense Image		
	TV	TV box	FBP	TV	TV box	FBP
50	$E_m = 0.1183,$ $MR_m = 1.75\%$	$E_m = 0.0543,$ $MR_m = 0.27\%$	$E_m = 0.2644,$ $MR_m = 6.65\%$	$E_m = 0.1712,$ $MR_m = 2.71\%$	$E_m = 0.0853,$ $MR_m = 0.61\%$	$E_m = 0.03382,$ $MR_m = 9.73\%$
100	$E_m = 0.1159,$ $MR_m = 1.72\%$	$E_m = 0.0498,$ $MR_m = 0.23\%$	$E_m = 0.1157,$ $MR_m = 1.27\%$	$E_m = 0.1616,$ $MR_m = 2.40\%$	$E_m = 0.0728,$ $MR_m = 0.34\%$	$E_m = 0.1586,$ $MR_m = 2.14\%$
200	$E_m = 0.1157,$ $MR_m = 1.68\%$	$E_m = 0.0468,$ $MR_m = 0.13\%$	$E_m = 0.0405,$ $MR_m = 0.16\%$	$E_m = 0.1604,$ $MR_m = 2.32\%$	$E_m = 0.0620,$ $MR_m = 0.18\%$	$E_m = 0.0627,$ $MR_m = 0.33\%$

Table 4.8: Minimum errors  $E_m$  and missclassification rate  $MR_m$  for sparse bone images with  $\sigma_p = 6$  for TV regularization without with box convex constraints.

M	Sparse Image			Dense Image		
	TV	TV box	FBP	TV	TV box	FBP
50	$E_m = 0.1194$ , $MR_m = 1.72\%$	$E_m = 0.0734$ , $MR_m = 0.57\%$	$E_m = 0.4537$ , $MR_m = 19.58\%$	$E_m = 0.1719$ , $MR_m = 2.78\%$	$E_m = 0.1148$ , $MR_m = 1.16\%$	$E_m = 0.4963$ , $MR_m = 20.95\%$
100	$E_m = 0.1162$ , $MR_m = 1.71\%$	$E_m = 0.0661$ , $MR_m = 0.43\%$	$E_m = 0.3374$ , $MR_m = 10.83\%$	$E_m = 0.1628$ , $MR_m = 2.46\%$	$E_m = 0.0978$ , $MR_m = 0.82\%$	$E_m = 0.3701$ , $MR_m = 11.65\%$
200	$E_m = 0.1162$ , $MR_m = 1.64\%$	$E_m = 0.0633$ , $MR_m = 0.32\%$	$E_m = 0.1990$ , $MR_m = 3.77\%$	$E_m = 0.1606$ , $MR_m = 2.38\%$	$E_m = 0.0902$ , $MR_m = 0.62\%$	$E_m = 0.2215$ , $MR_m = 4.17\%$
300	—	—	$E_m = 0.1276$ , $MR_m = 1.55\%$	—	—	$E_m = 0.1493$ , $MR_m = 2.76\%$
500	—	—	$E_m = 0.0619$ , $MR_m = 0.37\%$	—	—	$E_m = 0.0852$ , $MR_m = 0.62\%$

On the one hand, when there are only  $M = 50$  projections, the FBP reconstruction results are very bad. With the increase of projection number ( $M \geq 100$ ), the FBP reconstruction has been improved. For the low noise level  $\sigma_p = 3$ , FBP algorithm leads to similar reconstruction results than TV and TV box regularization methods when the projection number is high such as  $M = 100$  or  $M = 200$ . While for a higher noise level  $\sigma_p = 6$ , for FBP algorithm, more projections are needed to obtain a similar reconstruction results than with TV regularization methods.

On the other hand, the TV and TV box regularizations give much better reconstruction results with the rise of the projection number. The improvement is not as obvious with the FBP algorithm. The TV and TV box reconstruction method can give good reconstruction results with a lower projection number such as  $M = 50$ . They are effective for reconstructions from a limited number of views, especially when a high noise level exists in the raw projection data.

### Level-set regularization method

**L-curves** In our simulations, for the classical level-set method, the regularization parameter  $\beta_1$  is set to 0 because of the  $H_1$  term dominates the TV term (Section 4.5.1). Similarly to the methodology used for TV algorithms, we tested many regularization parameters. The best parameter  $\beta_2$  was selected according to Morozov principle. When the minimum data term  $\|Rf - p^\delta\|$  is well above the noise level  $\delta$ , the Morozov principle can not be used to estimate the best regularization parameter. A good way to solve this problem is to use L-curve method [Hansen (2001)].

In this method, for a grey-level reconstructed image  $f$ , the data term and the  $H_1$

regularization terms are calculated and the curve:

$$(\log \|Rf - P^\delta\|, \log \|\theta\|_{H_1}) \quad (4.35)$$

is plotted. We should choose the regularization parameter with the highest curvature of the L-curve.

The L-curve obtained with the big dense image with  $M = 20$  and  $\sigma_p = 3$  and the evolution curves of data term and misclassification rate is displayed in Fig.4.17. The data term is well above the noise level (green line). A good estimate of the optimal regularization parameter is obtained with the L-curve.

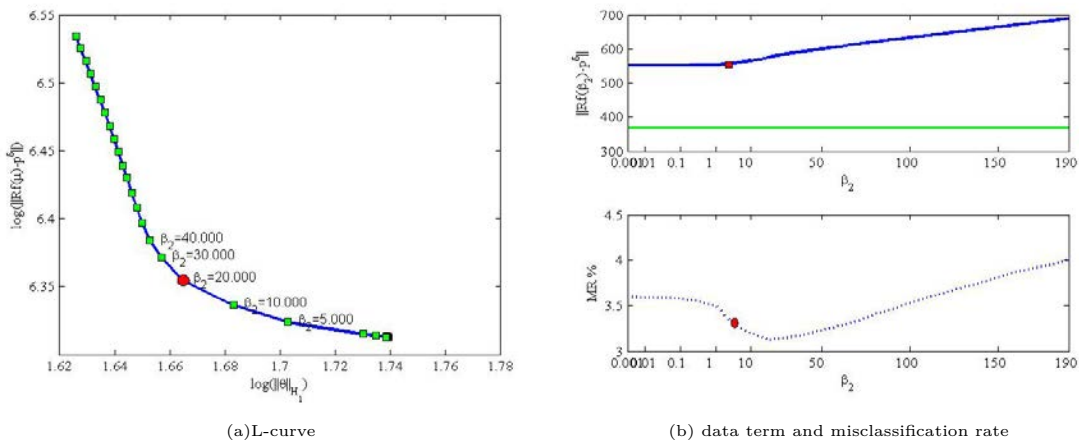


Figure 4.17: L-curve and evolution curves of the data term, the misclassification rate with the iteration number for big dense image with  $\sigma_p = 3$ , 20 projection angles.

**LS and PCLS reconstruction results** In this part, we present the the reconstruction results obtained with Level-set (LS) and Piecewise Constant Level-set (PCLS) regularization methods. and TV regularization method is used for comparison.

**Small images** The small disk reconstruction images ( $\sigma_p = 12.83$ ) and the small bone cross-section reconstruction images ( $\sigma_p = 9.85$ )obtained with LS and PCLS methods are displayed in Fig.4.18 and Fig.4.19 respectively.

The evolution curves of data term ( $\|Rf^k - p^\delta\|$ ) and misclassification rate ( $MR(k)$ ) with the iteration number are shown in Fig.4.20 and Fig.4.21 for the small bone image with  $\sigma_p = 9.85$ , 20 and 50 projection angles.

Table.4.9, Table.4.10 summarize the minimum error  $E_m$  for each image and noise level with 20 and 50 projections, together with the minimum misclassification rate  $MR_m$  obtained, by using TV regularization, level-set regularization and PCLS method respectively.

From these tables, we can infer that for small images, the TV regularization algorithm

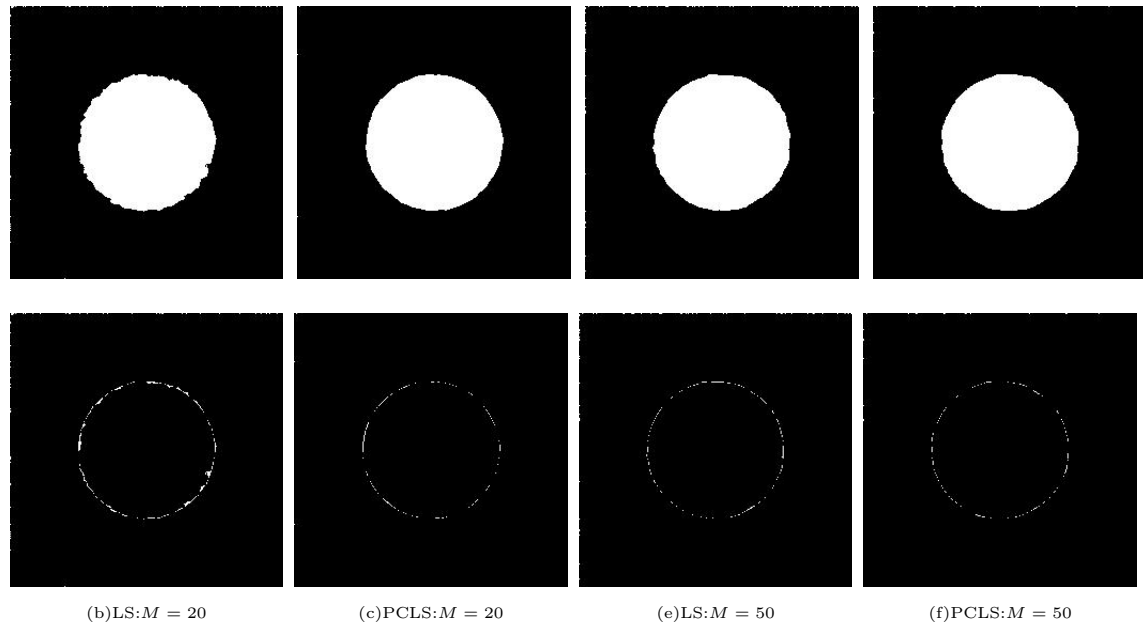


Figure 4.18: Binary disk reconstruction images and difference maps with LS and PCLS regularization methods with  $\sigma_p = 12.83$ , 20 and 50 projection angles, 367 X-rays per projection.

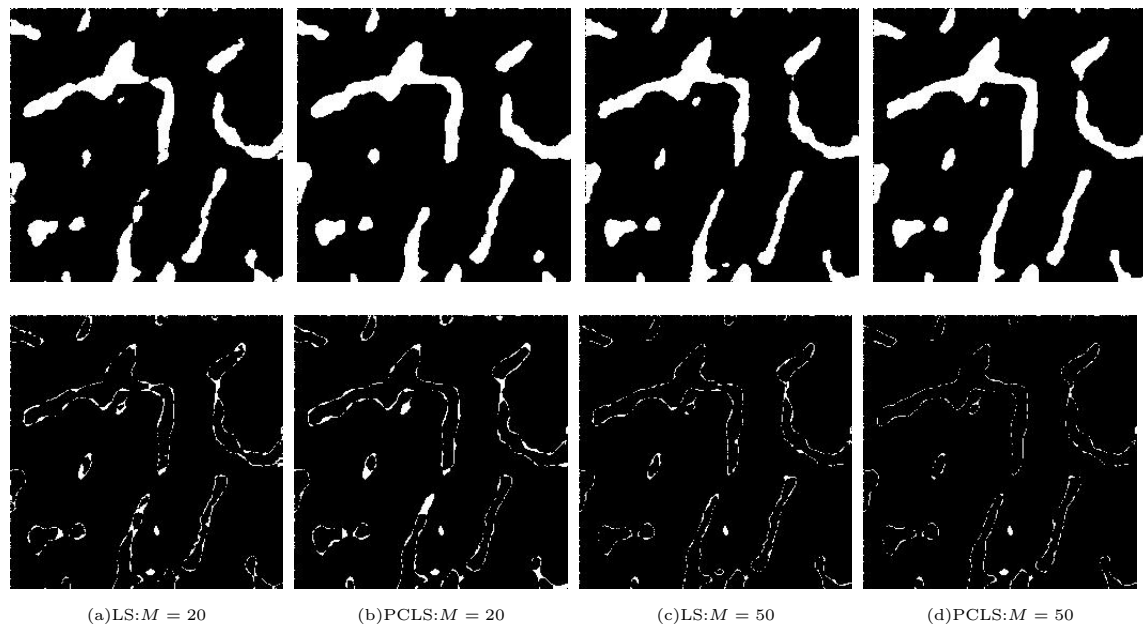


Figure 4.19: Binary bone reconstruction images and difference maps with LS and PCLS regularization methods with  $\sigma_p = 9.85$ , 20 and 50 projection angles, 367 X-rays per projection.

gives in most cases the best reconstruction results with 20 and 50 projections. For the simple disk image, PCLS method works better than LS algorithm. While for the small

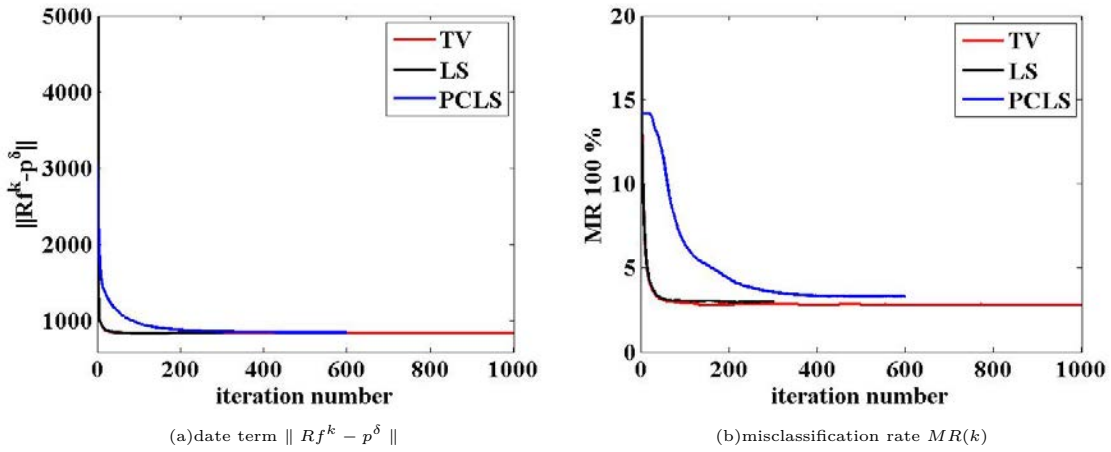


Figure 4.20: Evolution curves of the data term and of the misclassification rate with the iteration number for small bone image with  $\sigma_p = 9.85$ , 20 projection angles.

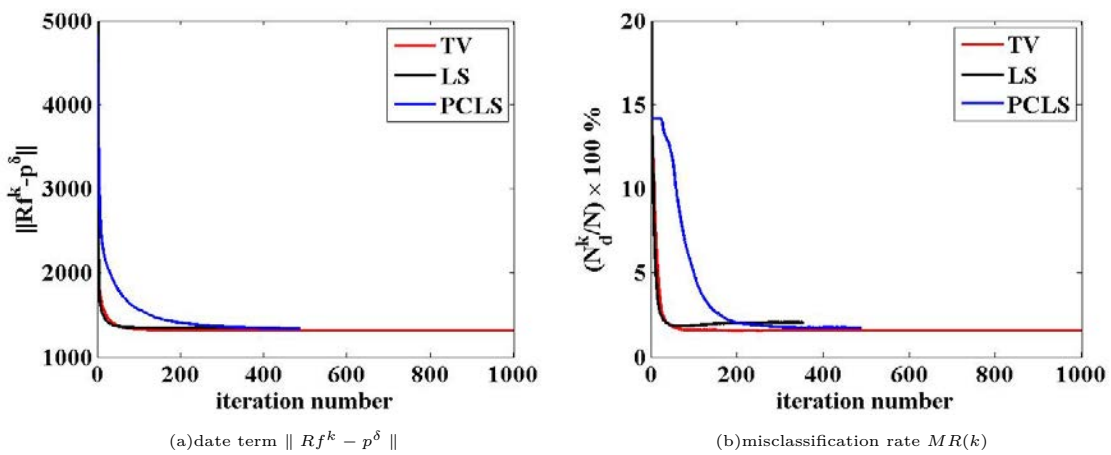


Figure 4.21: Evolution curves of the data term, of the normalized error and of the misclassification rate with the iteration number for small bone image with  $\sigma_p = 9.85$ , 50 projection angles.

bone image, the LS method works better than PCLS algorithm for few projection. For a low number of projections ( $M=20$ ) and a high noise level, the LS approach may outperform the TV regularization. When the problem is very ill-posed and for complex structure the TV term which favors disk like structures is not the most efficient a priori.

**Big images** The three algorithms were also compared on bone cross-sections images of size  $512 \times 512$ , and two noise levels  $\sigma_p = 3$ ,  $\sigma_p = 6$  have been tested. The binary reconstruction obtained with  $\sigma_p = 3$  for sparse and dense images are shown in Fig.4.22, Fig.4.23 respectively for level-set method (LS) and (PCLS) method.

The evolution curves of data term ( $\|Rf^k - p^\delta\|$ ) and misclassification rate ( $MR(k)$ )

Table 4.9: Minimum errors  $E_m$  and misclassification rate  $MR_m$  for small disk image with 20 and 50 projections.

$\sigma_p$	TV		LS		PCLS	
	M=20	M=50	M=20	M=50	M=20	M=50
8.55	$E_m = 0.0505$ $MR_m = 0.15\%$	$E_m = 0.0436$ $MR_m = 0.093\%$	$E_m = 0.0603$ $MR_m = 0.29\%$	$E_m = 0.0525$ $MR_m = 0.2\%$	$E_m = 0.1060$ $MR_m = 0.19\%$	$E_m = 0.0463$ $MR_m = 0.11\%$
12.83	$E_m = 0.0535$ $MR_m = 0.18\%$	$E_m = 0.0481$ $MR_m = 0.14\%$	$E_m = 0.0702$ $MR_m = 0.43\%$	$E_m = 0.0612$ $MR_m = 0.31\%$	$E_m = 0.1134$ $MR_m = 0.2\%$	$E_m = 0.0664$ $MR_m = 0.22\%$
25.65	$E_m = 0.0737$ $MR_m = 0.42\%$	$E_m = 0.0563$ $MR_m = 0.27\%$	$E_m = 0.1198$ $MR_m = 1.13\%$	$E_m = 0.0862$ $MR_m = 0.66\%$	$E_m = 0.1626$ $MR_m = 0.79\%$	$E_m = 0.1103$ $MR_m = 0.57\%$

Table 4.10: Minimum errors  $E_m$  and misclassification rate  $MR_m$  for small bone image with 20 and 50 projections.

$\sigma_p$	TV		LS		PCLS	
	M=20	M=50	M=20	M=50	M=20	M=50
6.57	$E_m = 0.1476,$ $MR_m = 2.11\%$	$E_m = 0.1041,$ $MR_m = 1.01\%$	$E_m = 0.1442,$ $MR_m = 2.32\%$	$E_m = 0.1192,$ $MR_m = 1.68\%$	$E_m = 0.2088,$ $MR_m = 3.44\%$	$E_m = 0.1324,$ $MR_m = 1.11\%$
9.85	$E_m = 0.1714$ $MR_m = 2.82\%$	$E_m = 0.1292$ $MR_m = 1.58\%$	$E_m = 0.1634$ $MR_m = 2.99\%$	$E_m = 0.1346$ $MR_m = 2.05\%$	$E_m = 0.1976$ $MR_m = 3.33\%$	$E_m = 0.1370$ $MR_m = 1.69\%$
19.71	$E_m = 0.2128$ $MR_m = 4.9\%$	$E_m = 0.0258$ $MR_m = 2.58\%$	$E_m = 0.2046$ $MR_m = 4.63\%$	$E_m = 0.1657$ $MR_m = 3.05\%$	$E_m = 0.2446$ $MR_m = 6.23\%$	$E_m = 0.1814$ $MR_m = 2.80\%$

with the iteration number are shown in Fig.4.24 and Fig.4.25 for the big sparse bone image with  $\sigma_p = 3$  and  $\sigma_p = 6$ , and 20 projection angles. The evolution curves for the big dense bone images are very similar.

Table 4.11 summarizes the minimum error  $E_m$  and minimum misclassification rate  $MR_m$  obtained for low density and high density bone cross-section images with 20 projections.

Table 4.11: Minimum errors  $E_m$  and misclassification rate  $MR_m$  for big bone image with 20 and 50 projections.

$\sigma_p$	Sparse Image			Dense Image		
	TV	LS	PCLS	TV	LS	PCLS
3	$E_m = 0.1320$ $MR_m = 2.33\%$	$E_m = 0.1015$ $MR_m = 1.27\%$	$E_m = 0.1016$ $MR_m = 1.22\%$	$E_m = 0.2299$ $MR_m = 5.61\%$	$E_m = 0.1739$ $MR_m = 3.09\%$	$E_m = 0.1580$ $MR_m = 2.71\%$
6	$E_m = 0.1342$ $MR_m = 2.35\%$	$E_m = 0.1117$ $MR_m = 1.6\%$	$E_m = 0.1365$ $MR_m = 2.26\%$	$E_m = 0.2332$ $MR_m = 5.59\%$	$E_m = 0.1854$ $MR_m = 3.81\%$	$E_m = 0.2202$ $MR_m = 4.85\%$

From this table, it is obvious that TV regularization method is the worst reconstruction

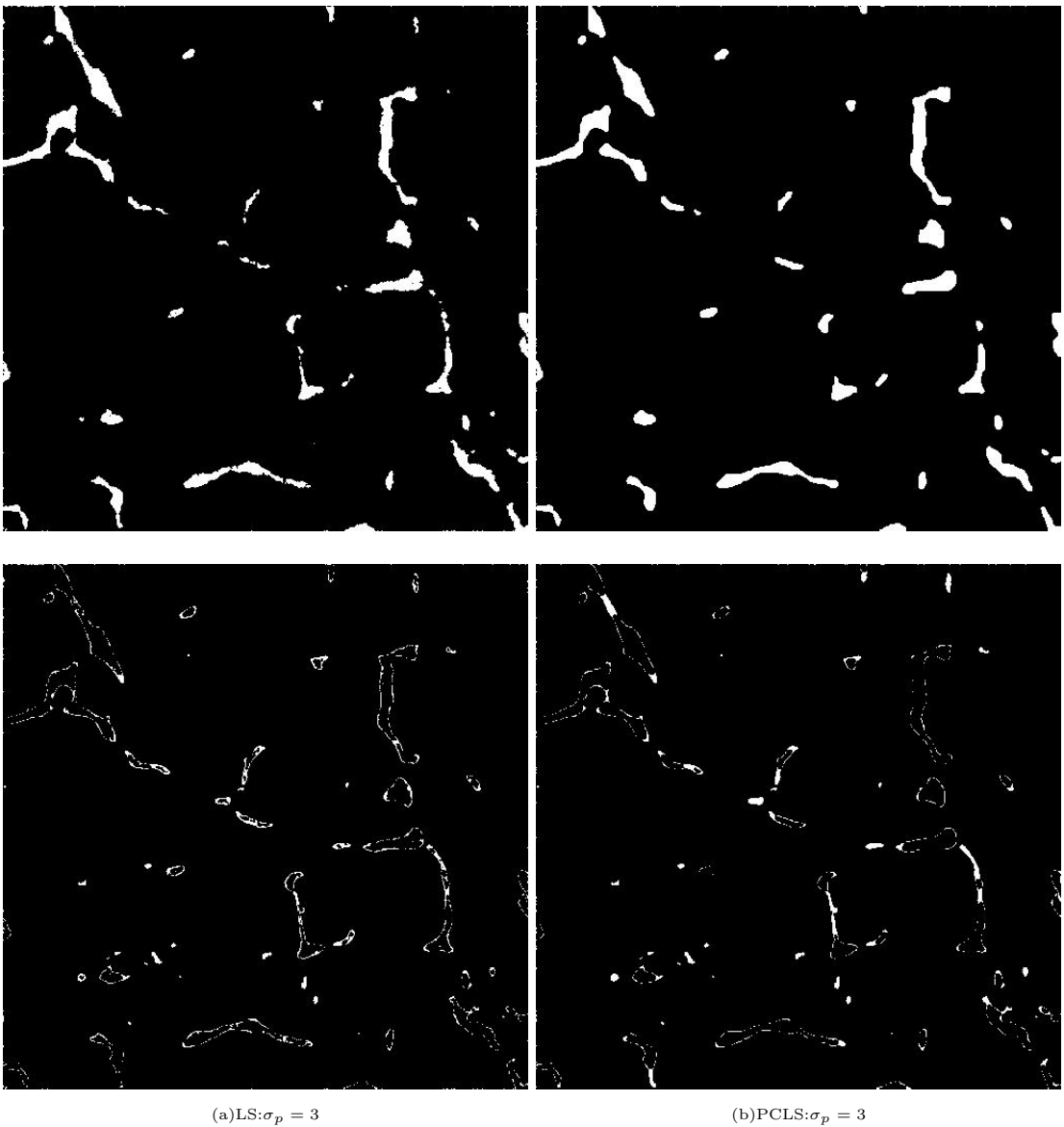


Figure 4.22: Binary dense bone reconstructed images and difference maps with  $\sigma_p = 3$ , 20 projection angles and 729 X-rays per projection.

method for large images. It is impossible to find a regularization parameter  $\mu$  and a Lagrange parameter  $\beta$  to make the data term  $\frac{\|Rf^m - p^\delta\| - \delta}{\delta} \leq \xi$ , with  $\xi = 0.01$  for TV algorithm. In our simulations, the smallest constant  $\xi$  which satisfies this relation is  $\xi = 0.5$ . The PCLS method is a little better than LS algorithm when the noise level  $\sigma_p = 3$  is low. The TV method performs poorly on large bone cross-sections with complex and elongated regions. Some details and fine structures are lost with the TV priori which minimize the perimeters of the boundaries. The level-set regularization includes some constraints that favor the binary values and improves reconstruction results.

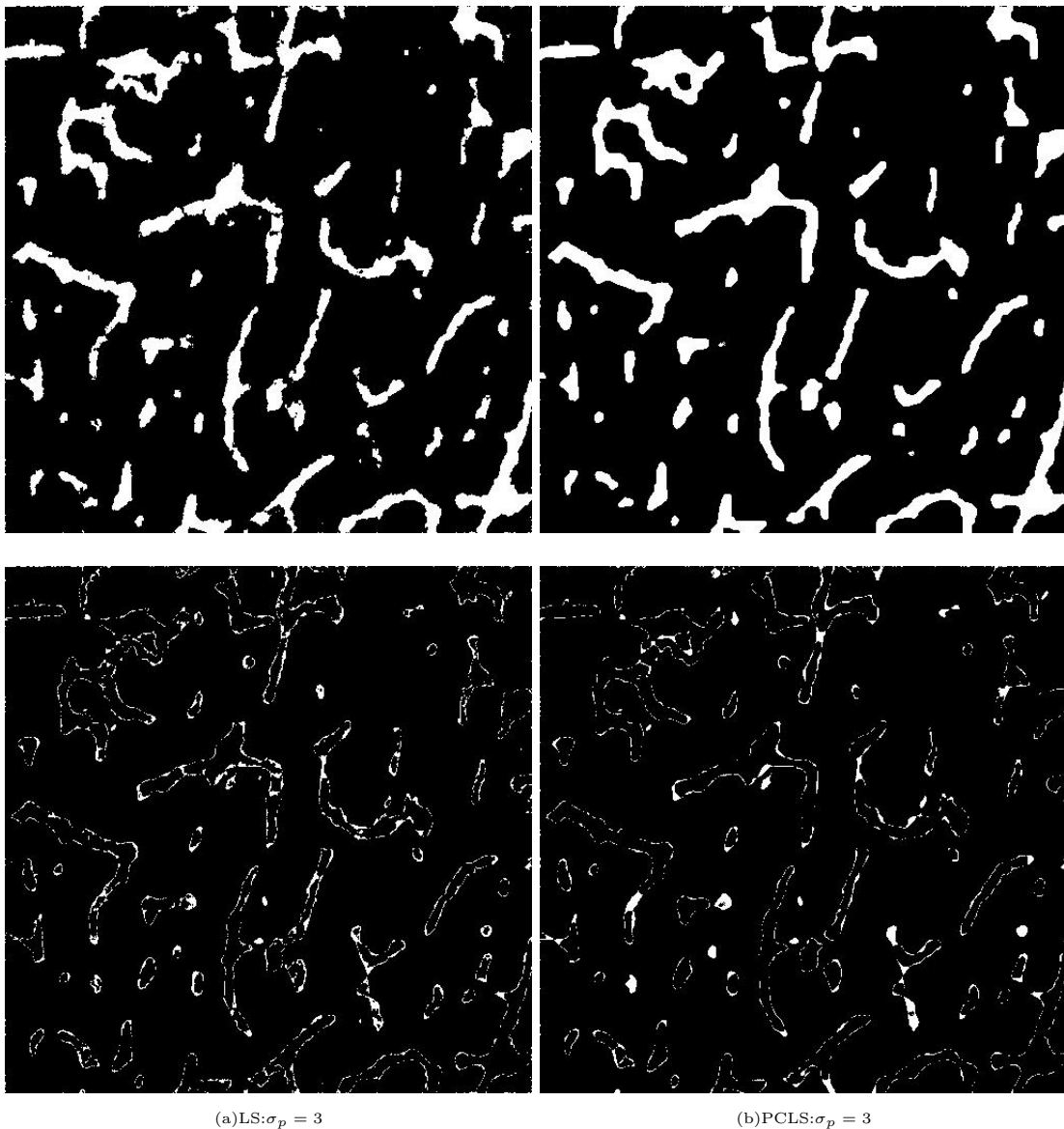


Figure 4.23: Binary dense bone reconstructed images and difference maps with  $\sigma_p = 3$ , 20 projection angles and 729 X-rays per projection.

## 4.6 Conclusion

In this chapter, the main issue is binary tomography reconstruction of bone microstructure from a limited number of projections. We focused on two regularization methods: TV regularization method and Level-set regularization method.

For the TV regularization methods, two TV based algorithms have been compared. The first algorithm is the classical TV regularization method. In the second approach, a convex constraint has been added to enforce the binary condition. The optimal solutions are obtained with the ADMM algorithm. And for the LS regularization methods, the first level-set method is based on a representation of the function to be reconstructed with

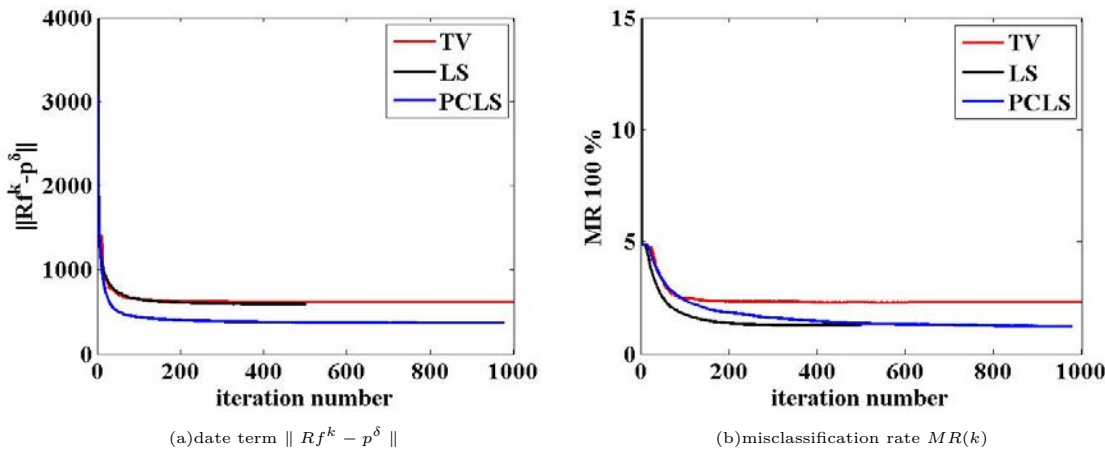


Figure 4.24: Evolution curves of data term, normalized error and misclassification rate with the iteration number for big sparse bone image with  $\sigma_p = 3$ , 20 projection angles.

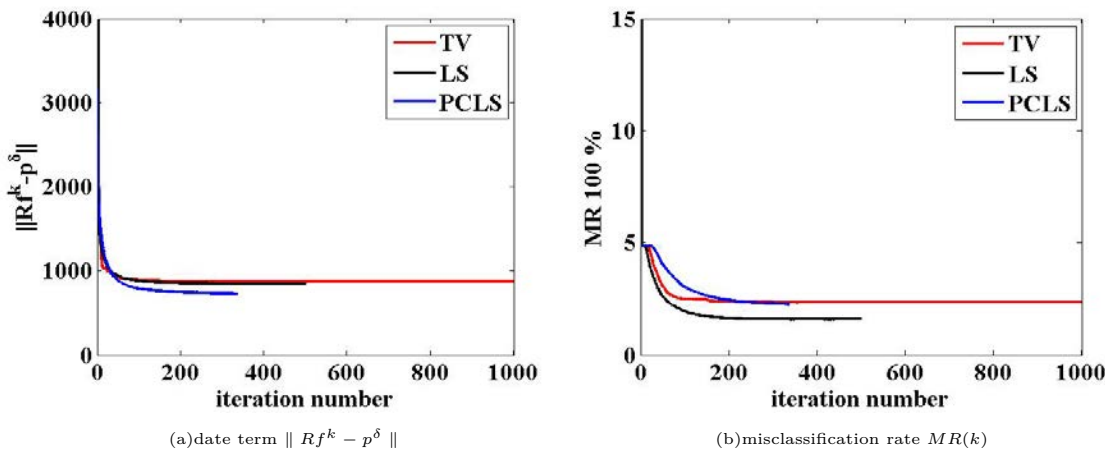


Figure 4.25: Evolution curves of data term, normalized error and misclassification rate with the iteration number for big sparse bone image with  $\sigma_p = 6$ , 20 projection angles.

a Heaviside distribution which leads to a nonlinear inverse problem formulation of the binary tomography problem; the second one (PCLS) uses piecewise constant functions and a minimization of an augmented Lagrangian including the binary constraint.

The performance of these algorithms are compared under different levels of noise on two small images (a disk image and CT bone cross-section image) and two big images (sparse and dense CT bone cross-section images) with different number of projections. And the reconstruction results are discussed very carefully. The regularization parameter are mainly carefully chosen with the Morozov discrepancy principle. Reconstruction errors are localized on boundaries for all kinds of images.

In order to escape from the local minima, we will try to add some stochastic perturbations to the reconstructed images obtained in the reconstruction process to find the global optimal. This method will be detailed in the next chapter.



# Chapter 5

---

## Stochastic Optimization Methods for Binary Tomography Reconstruction

---

### 5.1 Introduction

In chapter 4, we have presented the binary reconstruction results of bone microstructure from a limited number of projections with TV regularization and level-set regularization methods. The two regularization approaches have been compared for several noise levels and number of projections on different bone cross-section images. Rather good reconstruction results were obtained with TV regularization methods. And the reconstruction results obtained with the classical level-set and piecewise constant level-set regularization methods are very similar. The level-set regularization outperforms the TV regularization for large images with complex structures. Yet, for both TV and LS regularization methods, some reconstruction results are still present on the boundaries of the reconstructed images, and some regions are lost when the projection number is low. The reason is that the discrete tomography problem is non-convex and the reconstructed image corresponds to a local minimum of the non-convex regularization functional.

Therefore, it is very interesting to escape the local minimum achieved by TV or level-set regularization methods by global optimization methods. Simulated annealing methods are efficient but they are often very slow [[Gidas \(1995\)](#), [Cot \*et al.\* \(1998\)](#), [Catoni \(1992\)b](#), [Azen-cott \(1992\)](#)]. Algorithms based on stochastic differential equations have been proposed for the global optimization of non-convex functions [[Gidas \(1995\)](#), [Parpas and Rustem \(2009\)](#), [Chow \*et al.\* \(2009\)](#), [T.S.Chiang and S.J.Sheu \(1987\)](#)]. Stochastic partial differen-

tial equations methods based on level-set have been used for image processing tasks like segmentation [Juan *et al.* (2006)]. Moreover, the convergence properties of the stochastic partial differential equation obtained with the sub-differential of the TV regularization semi-norm has been studied in [Barbu *et al.* (2009)].

The main contribution of this chapter is to use the stochastic level-set and TV regularization methods for the binary tomography problem to improve the reconstructed images obtained with the corresponding deterministic scheme. First, the reconstruction results obtained with the new stochastic level-set regularization method are compared with the ones obtained with the classical simulated annealing method. Then a new stochastic approach is presented based on the TV regularization and the Alternate Direction of Minimization method (ADMM) [Afonso *et al.* (2011)].

Different noise terms based on stochastic TV regularization method are compared including a boundary noise term or a more homogeneous perturbation based on the gradient of the data term of the regularization functional. Compared with stochastic level-set regularization method which only modifies the shape of the 0 and 1 regions located on the boundaries, the originality of the stochastic TV regularization method is twofold. First, the random change of the boundary (0 and 1 region) which is performed in a new way with the gradient of the image or with wavelets. Moreover, random topological changes are included to reveal new regions that can not be detected with shape changes. The numerical results for the both stochastic level-set and TV regularization method are illustrated on thresholded bone micro-CT cross-sections for various noise levels and numbers of projections.

This paper is organized as follows. After the introduction, the new stochastic partial differential equations and various types of stochastic noises used for the stochastic level-set and TV regularization methods are presented. Next, the simulation details and the numerical results achieved on noisy bone CT cross-sections for different noise levels and numbers of projections are reported and discussed before the conclusion.

## 5.2 Stochastic Optimization Methods Based on Level-set and TV regularizations

### 5.2.1 Global optimization strategy

**Gradient flow and stochastic perturbation** Global optimization is a classical issue in inverse problems. The aim of this chapter is to escape the local optima obtained with the deterministic level-set or TV regularization method with stochastic optimization methods. Let  $(\Omega, \mathcal{F}, P)$  be a probability space, given an objective function  $g : \mathbb{R}^m \rightarrow \mathbb{R}$ , the global minimum is:

$$\min_x g(x) \quad x \in \Omega \tag{5.1}$$

where  $\Omega$  is an admissible set for  $x \in \mathbb{R}^m$ ,  $\mathcal{F}$  is set of events, and  $P$  is a probability measure for the events. Stochastic gradient method is well-known in the field of convex optimization [Gilbert and Nocedal (1992), Bertsekas and Tsitsiklis (2000)]. A random trajectory  $X(t)$  governed by the following diffusion process is often used [Gidas (1995), Parpas and Rustem (2009), Chow *et al.* (2009), T.S.Chiang and S.J.Sheu (1987), Geman and Hwang (1986)]:

$$dX(t) = -\nabla g(X(t))dt + \eta(t)dW(t) \quad t \in [0, \infty] \quad (5.2)$$

where  $W=(W_1(t), \dots, W_m(t))$  is a standard  $m$ -dimensional Brownian motion and  $\eta(t)$  the stochastic noise strength. With an appropriate annealing schedule and under appropriate conditions on the function  $g(x)$ , the transition probability of  $X(t)$  converges weakly to a probability measure which has its support on the set of global minimizers [Gidas (1995), Parpas and Rustem (2009), Chow *et al.* (2009), T.S.Chiang and S.J.Sheu (1987), Geman and Hwang (1986)]. In order to escape the local minima generated by the level-set or TV regularizations, stochastic search algorithms based on the former regularization functionals will be used that generate random trajectories. The main idea of the stochastic method is to combine a gradient flow  $\nabla g(X(t))$  which leads to a local minimum quickly and a stochastic perturbation which can push the trajectory  $X(t)$  out of the traps of the local minimizers.

**Intermittent Diffusion method (ID)** In the classical approach for stochastic optimization problems, the diffusion coefficient function  $\eta(t)$  is continuously decreasing to zero [T.S.Chiang and S.J.Sheu (1987), Geman and Hwang (1986)]. In contrast, an intermittent diffusion strategy has been proposed in 2009 [Chow *et al.* (2009)]. The main idea of this method is to allow the trajectory  $X(t)$  jump off a local minimizer to another another local minimizer randomly by setting the diffusion coefficient  $\eta(t) > 0$  intermittently on random time steps (Fig.5.1). The diffusion coefficient function is defined as:

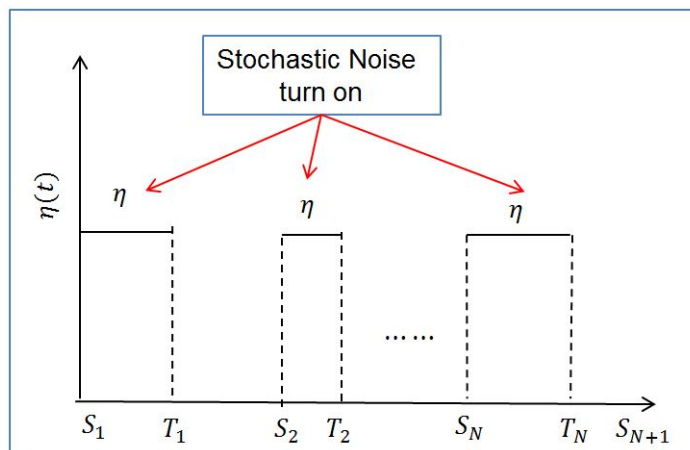


Figure 5.1: Intermittent strategy for diffusion coefficient function  $\eta(t)$ .

$$\eta(t) = \sum_j^N \eta_j I_{[S_j, T_j]}(t) \quad (5.3)$$

where  $0 = S_1 < T_1 < S_2 < T_2 \cdots < S_N < T_N = T$  and  $I_{[S_j, T_j]}$  is the characteristic function of time interval. The discontinuous function  $\eta(t)$  turns off the stochastic diffusion in the time intervals  $[T_j, S_{j+1}]$ , while in the time intervals  $[S_j, T_j]$ , the stochastic diffusion becomes active and the trajectory will not rest at the local stationary points and will escape the traps of local minima. In our work, we use the same stochastic noise strength during the whole stochastic diffusion optimization process.

### 5.2.2 Stochastic optimization based on Level-set regularization method

In our simulations, stochastic optimization algorithm based on level-set regularization was used to improve the reconstruction results. And also classical simulated annealing method was tested for comparison. Therefore, we first detailed the classical simulated annealing algorithm and then present the stochastic level-set method in this section.

#### Classical annealing method

A synthetic review of classical simulated annealing method can be found in [Azencott (1992), Catoni (1992)a, Cot *et al.* (1998)]. Here, We denote  $U$  the data term  $U = \|Rf_b - p^\delta\|$ ,  $f_b$  is the binary reconstructed image with deterministic level-set regularization method. We consider the objective function  $U$  to be minimized on a finite configuration space  $\mathbb{E}$  which is the set of binary images.

$$\mathbb{E} = \{f_b = (f_k)_{1 \leq k \leq N} \quad f_k \in \{0, 1\} \quad \forall k \in [1, N]\} \quad (5.4)$$

In order to apply the classical simulated annealing algorithm, we have to define a Markov chain,  $(f^n)_{n \in \mathbb{N}}$ , on the finite state space  $\mathbb{E}$ , where a point  $f^n$  in the state space is defined by the set  $(f_k^n)_{0 \leq k \leq N}$  of the pixel values. Simulated annealing stochastically searches the finite state space and ensures the convergence to the best possible approximation of the global minimum  $U_{min}$  of the energy function  $U$  with a good cooling down algorithm [Azencott (1992), Catoni (1992)a, Cot *et al.* (1998)].

The convergence of the algorithm requires the definition of a symmetric irreducible communication kernel  $q_0$  on the state space  $\mathbb{E}$ . We first define a neighborhood system  $N(f^n)$  of the element  $f^n \in \mathbb{E}$ . The boundary  $\partial\Omega_1$  between the 0 and the 1 regions is calculated with a Sobel filter. In order to define a test image  $z$ , one pixel is selected at random on the boundary and it is changed:

$$z \in N(f^n) \iff \exists k, f_k^n \neq z_k, f_k^n \in \partial\Omega_1 \quad (5.5)$$

With the communication kernel  $q_0(z, f^n)$ , all the new states in the neighbourhood of

$f$  are equiprobable:

$$q_0(z, f^n) = \begin{cases} \frac{1}{|N(f^n)|} & \text{if } z \in N(f^n) \\ 0 & \text{otherwise} \end{cases} \quad (5.6)$$

Given a cooling schedule  $(\beta_n)_{n \in \mathbb{N}}$ , an arbitrary initial point  $f^0$ , the classical simulated annealing algorithm defines an inhomogeneous Markov chain, with transitions constructed recursively as follows:  $P(f^{n+1} = z | f^n = f) = q(z, f)$  with:

$$q(z, f) = \begin{cases} q_0(z, f) \exp(-\beta_n(U(z) - U(f)))^+ & \text{if } z \neq f \\ 1 - \sum_{h \neq f} q(h, f) & \text{if } z = f \end{cases} \quad (5.7)$$

where  $[a]^+ = \max(a, 0)$  and  $q(z, f)$  is the probability to transform  $f$  into  $z$ . In stage  $n$ , given the current state  $f^n$ , a new position  $z$  is sampled from the communication kernel  $q_0$ . Thus, if  $U(z) > U(f^n)$  the proposal  $z$  may be accepted but this becomes increasingly unlikely for large  $n$  since  $\beta_n \rightarrow \infty$ . In the beginning of the simulation, the temperature is high and the state space is explored freely. As  $\beta$  increases, the stationary distribution becomes increasingly concentrated around the minima of  $U$  [Azencott (1992), Catoni (1992)a, Cot et al. (1998)]. It is well known that the annealing schedule is an important factor in the efficiency of the optimization process. With a finite state space and a logarithmic cooling schedule,  $\beta_n = \beta_0 \log(n + 1)$ , with  $\beta_0 > 0$ , it can be shown that under regularity assumptions the convergence towards the global optima is ensured but the convergence rate is low. Several techniques have been used to speed up the simulated annealing method but the modifications are rather empirical [Szu and Hartley (1987), Ingber (1989)]. And the results obtained seems to be very dependent on the complexity of the objective function. They will not be considered here.

### Level-set stochastic noise based on Stratanovitch formulation

Level-set methods have been much studied for image processing tasks [Aubert and Kornprobst (2006)]. A stochastic approach based on the level-set formalism has been proposed for segmentation purposes [Juan et al. (2006)]. The stochastic level-set method was investigated here to obtain a smooth evolution of the boundary curve between 0 and 1 region. We summarize the main aspects of the method in this section. As demonstrated by Juan et al. [Juan et al. (2006)], if the Stratanovich integral is used for the stochastic evolution, the evolution of boundary curve or zero level-set function is independent of the level-set function  $\theta$  used to implicitly represent it. It was proposed to improve the reconstruction image with the following stochastic partial differential equation for the level-set function  $\theta$ , for  $x \in D$ :

$$d\theta(x, t) = \delta\theta(x, t) + \eta(t)|\nabla\theta(x, t)| \circ dW(t) \quad (5.8)$$

where  $\circ$  denotes the Stratanovitch convention [Prato and J.Zabczyk (1992)] and  $\delta\theta$  is the gradient calculated as explained in Section 4.3.1. Using the definition of the Stratonovich

integral [Prato and J.Zabczyk (1992)], the equation can be transformed to get the following Itô stochastic differential equation [Juan *et al.* (2006)]:

$$d\theta(x, t) = \delta\theta(x, t) + \eta(t)|\nabla\theta(x, t)|dW(t) + \frac{1}{2}\eta(t)(\Delta\theta(x, t) - |\nabla\theta(x, t)|\text{div}(\frac{\nabla\theta(x, t)}{|\nabla\theta(x, t)|})) \quad (5.9)$$

The stochastic search is performed with an intermittent diffusion method: level-set and stochastic level-set schemes are applied successively on random time intervals and with random diffusion strengths  $\eta$  [Chow *et al.* (2009)]. This method was compared with the simulated annealing method in [Wang *et al.* (2015)]. A faster convergence is obtained with the stochastic level-set approach. Yet, with this method, only the boundaries between the 0 and 1 regions are modified. No new region is revealed by the algorithm and it is not very efficient for the higher noise levels.

### 5.2.3 Stochastic optimization based on Total Variation regularization method

As mentioned in the last section, stochastic level-set method only modify the boundaries between the 0 and 1 regions. This method neither reveal the lost regions in the reconstructed image, nor be adaptive for the higher noise levels. Therefore, stochastic search methods based on TV regularization were proposed to solve these problems. The main advantage of stochastic TV based method is that the random shape and boundaries variations can be included in a new way and that topology changes can be also added.

#### Singular stochastic diffusion equation with additive and multiplicative noises

**General framework** Let  $D$  is a bounded open subset of  $\mathbb{R}^2$ , ( $V = H_0^1(D)$ ,  $\|\cdot\|_1$ ,  $H = L_2(D)$ ,  $|\cdot|$ ), and a filtered probability spaces  $(\Omega, \mathcal{F}, \{\mathcal{F}\}_t, \mathcal{P})$ . The singular stochastic diffusion equation of the random trajectory of  $X(t)$  on  $H$  [Prato and J.Zabczyk (1992), Prévôt and Röckner (2007)] is given as:

$$\left\{ \begin{array}{ll} dX(t) = \text{div}(\text{sgn}(\nabla)(X(t)))dt - R^*(RX(t) - p^\delta) + \sigma(X(t), t)dW(t) & \text{in } (0, \infty) \times D \\ X(t) = 0 & (0, T) \times \partial D \\ X(0) = x & \text{in } D \end{array} \right. \quad (5.10)$$

where  $X \in H = L^2()$ ,  $W(t)$ ,  $t \in [0, T]$ ,  $T > 0$ , is a Wiener process with covariance operator  $C$  [Prato and J.Zabczyk (1992), Prévôt and Röckner (2007)], the map  $\sigma(\cdot, t)$  takes its values in the space of Hilbert-Schmidt operators. The multi-valued function  $u \rightarrow \text{sgn}(u)$  from  $\mathbb{R}^2$  into  $2^{\mathbb{R}^2}$  is defined by:

$$\left\{ \begin{array}{ll} \frac{u}{|u|_2} & \text{if } u \neq 0 \\ \{v \in \mathbb{R}^2 : |v|_2 < 1\} & \text{if } u = 0 \end{array} \right. \quad (5.11)$$

where  $|u|_2$  is the Euclidean norm. This type of equation (Eq.5.10) has been extensively studied with additive and multiplicative noise [Barbu *et al.* (2009)], with an evolution of the form:

$$dX(t) = \mathbf{div}(\mathbf{sgn}(\nabla X(t)))dt + \sigma(X(t))dW(t) \quad (5.12)$$

**TV stochastic noises** In this part, we consider a coupling of ADMM with a stochastic diffusion for the augmented Lagrangian but we study several new noise terms. In the ADMM algorithm, the  $f$  iterate is obtained with a minimization of the augmented Lagrangian  $\mathcal{L}$ , for the parameters  $((g_i^{k+1}), h^{k+1}, (\lambda_i^k), \lambda_C^k)$ :

$$f^{k+1} = \arg \min_f \mathcal{L}(f, (g_i^{k+1}), h^{k+1}, (\lambda_i^k), \lambda_C^k) \quad (5.13)$$

More precisely, the iterate  $f^{k+1}$  is obtained with the first-order optimality condition:

$$\nabla \mathcal{L}(f^{k+1}) = 0 \quad (5.14)$$

In order to improve the discontinuities of the reconstructed image and to reveal new regions, we propose to add several types of random perturbation to the gradient with respect to  $f$  of the Lagrangian regularization functional. We thus add some noise to the iterate  $f^{k+1}$ , and we consider the following stochastic partial differential equation for different types of noise  $\sigma$  :

$$df(t) = -\nabla \mathcal{L}(f, (g_i^{k+1}), h^{k+1}, (\lambda_i^k), \lambda_C^k)dt + \sigma(f(t), t)dW(t) \quad (5.15)$$

We introduce in the following three different noise terms corresponding to shape and topology changes.

1) A gradient dependent noise term written (Algorithm  $(A_1)$ ):

$$\sigma(f(t), t)dW(t) = \eta_1 \left( \frac{\partial f}{\partial x} dW_1(t) + \frac{\partial f}{\partial y} dW_2(t) \right) \quad (5.16)$$

where  $(W_k(t))_{k=1,2}$  are independent Wiener random fields on  $H$  with a continuous covariance function  $C_k$  with a bounded integral kernel  $r_k$ , and  $\eta_1$  a positive constant that controls the strength of the noise. The gradient of the function  $f$  is used to detect the boundaries. This type of noise will be associated to a stochastic perturbation of the shape of the 0-1 regions with a change of their boundaries. The aim is to improve the efficiency of the method with random perturbations localized on the reconstruction errors, without changing the regions that are well restored.

2) An additive noise with an adapted covariance operator (Algorithm  $A_2$ ):

Let us assume that the noise covariance operator  $C : H \rightarrow H$  is a linear symmetric non-negative compact operator with eigenvalues  $\eta_k$  and with a complete normalized eigen-

functions  $(\nu_k)_{k \geq 1}$  system:

$$C\nu_k = \eta_k \nu_k \quad (5.17)$$

and that it is a trace class operator:

$$\|C\|_{L_1} = \text{Tr}(C) = \sum_{k=1}^{\infty} \eta_k < \infty \quad (5.18)$$

Under the former assumptions, the C-Wiener process  $W(t)$  has the following series representation [Prato and J.Zabczyk (1992), Prévôt and Röckner (2007)]:

$$W(t) = \sum_{k=1}^{\infty} \sqrt{\eta_k} \omega_t^k \nu_k \quad (5.19)$$

where  $\{\omega_t^k\}$  is a sequence of independent, identically distributed standard Brownian motions in one dimension. In this work, the eigenfunctions  $\nu_k$  will be the one obtained from a truncated wavelet decomposition of the boundary. The eigenvalues  $\{\eta_k\}_{k \in J}$  corresponding to the high frequency wavelets used for the decomposition of the boundary are set to a constant value  $\eta_2$ . The other eigenvalues of the covariance operator are set to zero. The noise term can thus be written:

$$\sigma(f(t), t) dW(t) = \eta_2 \sum_{k \in J} \omega_t^k \nu_k \quad (5.20)$$

where  $\eta_2$  is a positive constant. With this approach, the covariance of the noise is adapted to the boundary between the 0 and 1 regions since only the wavelets corresponding to the decomposition of the transition regions are taken into account. The aim is to apply the random perturbation on the discontinuities between the 0 and 1 regions. This type of noise term is expected to improve the performance since it is localized on boundaries reconstruction errors.

3) A nonlinear gradient dependent noise term is also considered given by:

$$\sigma(f(t)) dW(t) = \eta_3 (1 - f(t)) R^*(Rf(t) - p^n) dW(t) \quad (5.21)$$

where  $\eta_3$  is a positive constant and  $W(t)$  a  $C$ -Wiener random field with a bounded kernel. This noise term is proportional to the gradient of the data term of the objective functional. It is larger in the 0 regions of the image. The rationale behind this choice is to modify the topology of the 0 and 1 regions. With this type of random perturbation, new regions may be introduced depending on the value of the gradient of data term. This type of noise can be added to the noise terms used in the algorithms  $(A_1)$  and  $(A_2)$  leading to the algorithms  $(A_3)$  or  $(A_4)$  respectively.

**Microlocal analysis and filter for stochastic diffusion equations** As defined in Section.3.1.3, the Radon transform for  $f \in L^1(\Omega)$  is the line integral on the X-ray beam

$L(\phi, s)$ :

$$Rf(\phi, s) = R_\phi f(s) = \int_{L(\phi, s)} f(\vec{r}) dl \quad (5.22)$$

where  $\vec{r}$  is the spatial position in the Cartesian coordinate system.

Microlocal analysis is useful to understand how the Radon transform  $R$  detects the singularities [E.T.Qinto (1993)]. Let  $x_0 \in \mathbb{R}^n$ ,  $\xi_0 \in \mathbb{R}^n \setminus 0$ , the distribution  $f$  is in the Sobolev space  $H^\alpha$  microlocally near  $(x_0, \xi_0)$ , if and only if there is a cut-off function  $\psi \in C_c^\infty([0, 2\pi] \times \mathbb{R}^n)$  with  $\psi(x_0) \neq 0$  such that the Fourier transform  $\widehat{(\psi f)}(\xi) \in L_2(\mathbb{R}^n, (1 + |\xi|^2)^\alpha)$  and a smooth function  $u(\xi)$  homogeneous of degree zero on  $\mathbb{R}^n \setminus 0$  and with  $u(\xi_0) \neq 0$  such that the product  $u(\xi)\widehat{\psi f}(\xi) \in L_2(\mathbb{R}^n, (1 + |\xi|^2)^\alpha)$ . The  $H^\alpha$  wavefront set of  $f$ ,  $WF^\alpha(f)$ , is the complement of the set near which  $f$  is microlocally in  $H^\alpha$ .

Principle of the microlocal analysis for parallel X-ray beam lines is shown in Fig.5.2. As shown in [E.T.Qinto (1993)], if  $Rf$  is in  $H^{\alpha+1/2}$  near  $(\phi_0, s_0)$ , then  $f$  is  $H^\alpha$  in directions  $\pm\theta_0$  at all points on the line  $L(\phi_0, s_0)$  and if  $Rf$  is not in  $H^{\alpha+1/2}$  near  $(\phi_0, s_0)$ , then at some point  $x \in L(\phi_0, s_0)$ ,  $(x, \theta_0)$  or  $(x, -\theta_0)$  is in  $WF^\alpha(f)$ . With limited data, if  $x \in L(\phi, s)$  the only wavefront directions we see at  $x$  are the directions perpendicular to the line, with directions  $\pm\theta$  (point  $x_2$ ). Other wavefront directions at points on  $L(\phi, s)$  are not visible from this data (point  $x_3$ ). These properties will be used to improve the stochastic diffusion methods.

In order to take account of the microlocal properties of the Radon transform, we have tested the effect of a filter,  $F$ . With this filter, the stochastic noise is applied to the points of the boundary for which the exterior normal is parallel to one of the projection directions  $\theta^*$ . The aim of this filter is to put stochastic noise on singularities on the boundaries which are difficult to reconstruct.

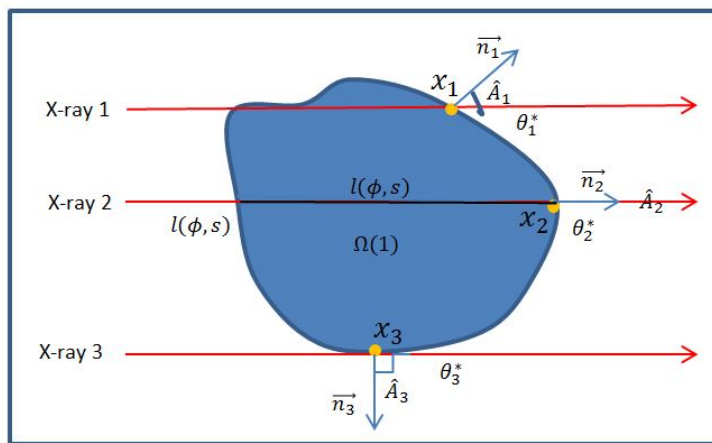


Figure 5.2: Principle of the microlocal analysis for parallel X-ray beam lines.

Let  $x \in \partial\Omega$  on the boundary between the 0 and 1 regions of a binary reconstructed image,  $\bar{n}(x)$  the exterior normal to the boundary at  $x$ , we define  $\hat{A} = (\bar{n}, \theta^*)$  as the angle between  $\bar{n}$  and  $\theta^*$ . For a threshold  $\alpha > 0$ , the noise terms based on TV regularization are

multiplied by the filter  $F$  defined by:

$$F(x) = \begin{cases} 1 & \text{if } \text{abs}(\hat{A}) < \alpha \text{ for one projection direction } \theta^* \\ 0 & \text{otherwise} \end{cases} \quad (5.23)$$

## 5.3 Simulations and Discussions

In the following part, we have compared the convergence properties of the stochastic level-set method and of TV based stochastic methods separately. The simulation details and numerical results are presented in this section.

### 5.3.1 Simulation details

In this part, the projection operator  $R$  is still taken as the discrete approximation of the Radon transform implemented on Matlab Image Toolbox. The stochastic level-set method and the stochastic TV based methods are applied to two small images of size of  $256 \times 256$ , which are shown in Fig.5.3. The two images are experimental bone cross-sections reconstructed from Filtered Back Projections (FBP) with 400 projections and 400 X-rays per projections and subsequently thresholded. They are denoted  $f^*$  and considered as ground-truth images. For both stochastic methods, an intermittent diffusion is applied and the deterministic and stochastic schemes are applied successively and iteratively. At the end of each deterministic or stochastic run, the image is binarized.

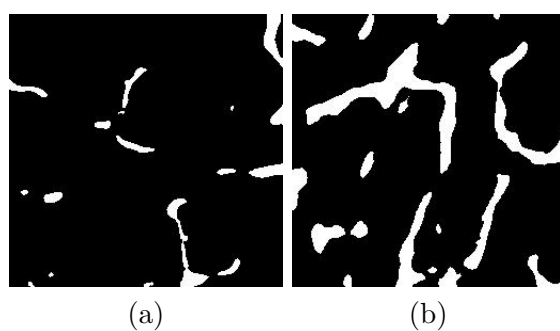


Figure 5.3: Reconstructed images of the bone cross-section from 400 projections with the FBP algorithm, central regions size of  $256 \times 256$  of Fig.2.13: (a) Low density bone image; (b) High density bone image.

The stochastic methods were tested for  $M = 5$ ,  $M = 10$ ,  $M = 15$  or  $M = 20$  equally spaced noisy projections,  $N_r = 367$  X-rays per projection, with a Gaussian noise added to the projection. The noise distribution is also characterized by the standard deviation of the noise  $\sigma_p$  or peak to peak signal to noise ratio  $PPSNR$  (defined in Eq.4.33). The noise standard deviations and  $PPSNR$  are summarized in Table.5.1 for low and high density bone cross-sections. The noise level  $\delta$  is estimated by  $\delta = \sqrt{MN_r}\sigma_p$ .

Table 5.1: The noise standard deviations  $\sigma_p$  and peak to peak signal to noise ration  $PPSNR$  for low and high density bone images

	$\sigma_p = 3$	$\sigma_p = 6.5$	$\sigma_p = 10$	$\sigma_p = 20$
<b>low density bone image</b>	15 dB	8.5 dB	5 dB	1.5 dB
<b>high density bone image</b>	20 dB	14 dB	6 dB	3.7 dB

### Level-set based method

The stochastic level-set method was tested on the high density bone image for  $M = 10$  and  $M = 15$  with a low standard deviation  $\sigma_p = 3$  and  $\sigma_p = 6.5$ . We summarized the implementation of this method in [Wang *et al.* (2014), Wang *et al.* (2015)]. To obtain a good accuracy, the  $\epsilon$  parameter should be sufficiently small,  $\epsilon = 0.03$ . The regularization parameter  $\beta_1$  was set to 0 because the  $H_1$  term dominates the  $TV$  term [DeCezaro *et al.* (2009)]. First, a deterministic level-set regularization scheme is applied, starting with an initial level-set function  $\theta_0 = 0$  to obtain a binary reconstructed image  $f_0$ . The iterations are stopped when the iterates stagnate  $\frac{\|f^{k+1} - f^k\|_2}{\|f^k\|_2} < 0.01$ . The regularization parameters were chosen to obtain the best decrease of the regularization functional. At the end of this first optimization step, the Morozov discrepancy principle [Morozov (1984)] is not satisfied. The data term is much higher than the noise level,  $\|p^\delta - Rf_b\| >> \delta$ . Some reconstructions errors are still present at the boundaries between the 0 and 1 regions in the image  $f_0$  obtained with the deterministic level-set method.

For instance, the reconstructed images  $f_0$  obtained with level-set algorithm and the corresponding error maps for the high density bone images are displayed in Fig.5.4 with the projections number  $M = 10$  and the standard derivation of noise on projection  $\sigma_p = 6.5$ .

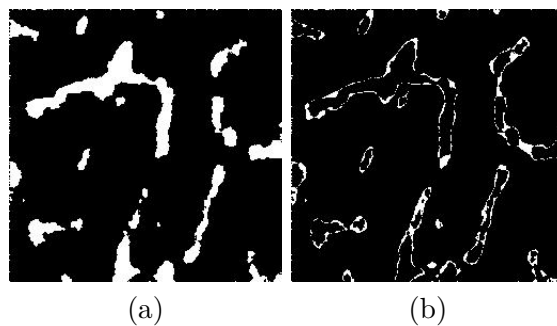


Figure 5.4: (a) Reconstruction of the high density image  $f_0$  obtained with the level-set regularization for  $\sigma_p = 6.5$  ( $PPSNR=14$  dB) and  $M=10$  projections,  $MR = 4.46\%$ ; (b) Corresponding error map.

The intermittent stochastic algorithm is then applied to this initial image  $f_0$ . When the stochastic diffusion is used, to discretize Eq.5.9, we have used an explicit scheme with

finite differences, the WENO scheme [Jiang and Peng (2000)] with spatial discretization step  $\Delta x = 1$  and time step  $\Delta t = 0.1$ . The noise strength  $\eta$  and the number of iterations  $T$  are chosen randomly with a uniform distribution in  $[0.01, 0.1]$  and  $[1, 100]$ . While when the stochastic diffusion is not applied, a deterministic level-set was applied with 100 iterations. At the end of this process, a binary reconstructed image was obtained by thresholding, from the grey-level reconstructed image with the minimum  $\|Rf - p^\delta\|$ . This binary reconstructed image was used in a signed distance function to reinitialize the level-set function  $\theta$  for the next stochastic diffusion step. The uncertainty on the optimal misclassification rate (MR) estimated from several noise realizations and changes of 10% of the regularization parameters is  $\Delta MR = 0.05$ .

### TV based method

The stochastic TV method was tested on the low and high density bone image with a standard deviation  $\sigma_p = 20$  and  $\sigma_p = 20$ . The images were first reconstructed with TV regularization and the ADMM deterministic algorithm. The iterations are stopped when  $\|\frac{f^{k+1} - f^k}{f^k}\| < 0.01$ . The final image obtained at the end of the optimization process is denoted as  $f^m$ . The best parameters  $(\mu, \beta)$  which are chosen satisfy the Morozov discrepancy principle [Morozov (1984)],  $\|Rf^m(\mu) - p^\delta\| \approx \delta$  at the iteration  $m$ . The  $\beta$  parameter selected leads to a smooth and fast convergence rate. After binarization, the initial binary reconstructed image is denoted as  $f_0$ . The discrepancy term of  $f_0$  is well-above the noise level and the Morozov principle is not fulfilled any longer. A local minimizer is again obtained. Similarly to the reconstruction results obtained with the deterministic level-set method, some errors are still present on the boundary regions of the image. Especially, for the low density bone image, large regions have disappeared from the restored image.

Two examples of the reconstructed images  $f_0$  obtained with TV algorithm and the corresponding error maps for the low density and high density bone images are displayed in Fig.5.5 and Fig.5.6 with the projections number  $M = 10$  and the standard deviation of noise on projection  $\sigma_p = 20$ .

The infinite-dimensional Wiener processes were approximated by Gaussian random field on the image grid. The discretization of the stochastic partial differential equation and of the Wiener processes were performed with classical finite difference methods and the Euler-Maruyama method [Kloeden and Platen (1992)]. The C-Wiener processes were approximated with stationary Gaussian random fields with a correlation function  $C$  given by its Fourier transform  $\tilde{C}(\mathbf{k}) = (|\mathbf{k}|^2 + 1)^{-2}$ . These random fields were generated via FFT with independent normal distributed random numbers.

For comparison, some simulations have been performed in which the stochastic diffusions are replaced by a successive TV regularization minimizations separated by binarization steps, which means the stochastic diffusions were "off" during the whole simulations (Algorithm  $A_0$ ).

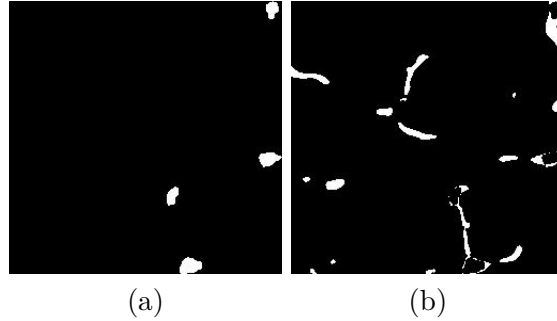


Figure 5.5: (a) Reconstruction of the low density image  $f_0$  obtained with the TV regularization for  $\sigma_p = 20$  (PPSNR=1.5 dB) and  $M=10$  projections,  $MR = 3.14\%$ ; (b) Corresponding error map.

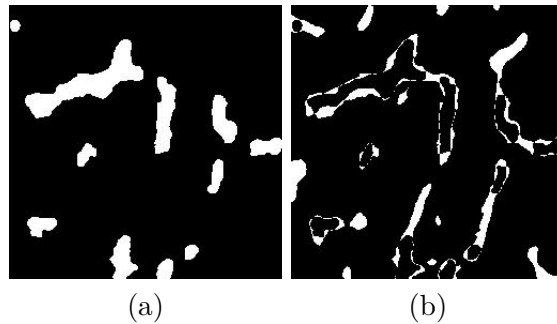


Figure 5.6: (a) Reconstruction of the high density image  $f_0$  obtained with the TV regularization for  $\sigma_p = 20$  (PPSNR=6 dB) and  $M=10$  projections,  $MR = 8.12\%$ ; (b) Corresponding error map.

For the algorithm ( $A_2$ ), we assume that the image  $f$  admits a sparse representation in an orthogonal wavelet basis  $\{\phi_k, k \geq 0\}$ . The index set describes the various levels of the resolution, the different positions and types of wavelet [Daubechies *et al.* (1992)]. The image  $f$  can thus be written  $f = \mathcal{W}^* \mathbf{v}$ , where  $\mathbf{v} \in l_2$  is a wavelet coefficients vector, and  $\mathcal{W}^*$  a synthesis operator. In this work, we have used the orthogonal Daubechies wavelet basis (Matlab implementation) and a 2-level wavelet decomposition of the images. Only the high frequency wavelet coefficients with the vertical, horizontal and diagonal details are taken into account in the noise term. These coefficients corresponds to the boundary between the 0 and 1 regions.

For the algorithms  $A_3$  and  $A_4$ , the homogeneous noise term is calculated at each iteration with the formula  $\eta_3(1 - f^k)Z_k\sqrt{\Delta t}R^*(Rf^k - p^n)$  where the  $(Z_k)_{k \geq 0}$  are spatially correlated Gaussian random variables in  $R^{N^2}$ . The time step  $\Delta t$  is fixed to 0.1.

The stochastic algorithm is performed alternatively with its deterministic version on random time steps in the range  $[0, T_{max}]$  with  $T_{max} = 100$  and with stochastic noise strength  $\eta_i$ , ( $i=1,2$  or 3). For each type of noise, the noise strength parameters  $\eta_1$ ,  $\eta_2$ ,  $\eta_3$  are chosen by trial and error to obtain the best decrease of the data term  $\|Rf_b^k - p^\delta\|$ , where  $f_b^k$  is the binarization of the grey-level image.

### 5.3.2 Numerical results

In this section, the numerical results obtained with the different optimization methods are presented. In order to have quantitative results, the binarization of the grey-level image,  $f_b^k$ , is obtained at each iteration with a threshold of 0.5 and the data term  $\frac{\|Rf_b^k - p^n\|}{n}$  is calculated. The efficiency of the reconstruction process is evaluated with the misclassification rate  $MR$ :

$$MR = \frac{\sum |f_b(i) - f^*(i)|}{N^2} \times 100\% \quad (5.24)$$

where  $f_b$  is the binarized version of the reconstructed image and  $f^*$  is the ground truth. The uncertainty on the optimal misclassification rate,  $MR(\%)$ , estimated from several noise realizations and changes of 10% of the regularization parameters, is  $\Delta MR = 0.05\%$ . The negative rate  $nMR(\%)$ , positive rate  $pMR(\%)$  are also evaluated.

$$\begin{cases} nMR = \frac{\sum_{i=1}^{N^2} |f_b(i) - f^*(i)|}{N^2} \times 100\% & \text{if } f_b(i) - f^*(i) < 0 \\ pMR = \frac{\sum_{i=1}^{N^2} |f_b(i) - f^*(i)|}{N^2} \times 100\% & \text{if } f_b(i) - f^*(i) > 0 \end{cases} \quad (5.25)$$

With the same input data, the FBP algorithm followed by thresholding leads to very bad reconstruction results with misclassification rates  $MR$  between 30% and 40%.

#### Level-set based method

The results have been published in [Wang *et al.* (2014), Wang *et al.* (2015)]. The reconstructed images obtained with only deterministic level-set method, then improved by stochastic level-set and simulated annealing methods, for 10 projections and 367 X-rays per projection and the standard deviations  $\sigma_p = 3$  and  $\sigma_p = 6.5$  are displayed in Fig.5.7 and Fig.5.8 respectively.

The evolution of the data discrepancy term  $\|Rf_b^k - p^\delta\|$  is displayed on Fig.5.9 for different number of projections and noise levels, and for the two global optimization methods. On this plot, the initial value of the discrepancy term is the one obtained after the first level-set scheme and it is well above the noise levels,  $\delta = 182, 223, 394, 482$  for  $(\sigma_p = 3, M = 10)$ ,  $(\sigma_p = 3, M = 15)$ ,  $(\sigma_p = 6.5, M = 10)$ ,  $(\sigma_p = 6.5, M = 15)$  respectively. The level-set algorithm can not escape this local minimum. With the iterations, a significant decrease of the data term is obtained towards these noise levels for both stochastic methods. The decrease of the misclassification rate as a function of the number of iterations is displayed on Fig.5.10 for the same number of projections and noise levels.

At the end of numerical simulations of stochastic level-set, the errors on the boundary of the images are much lower. The smooth evolution of the boundary proves to be more efficient than the Markov chain approach.

Table.5.2 summarizes the misclassification rate obtained at the end of simulations. As seen from the table, a large decrease of the misclassification rate was achieved with

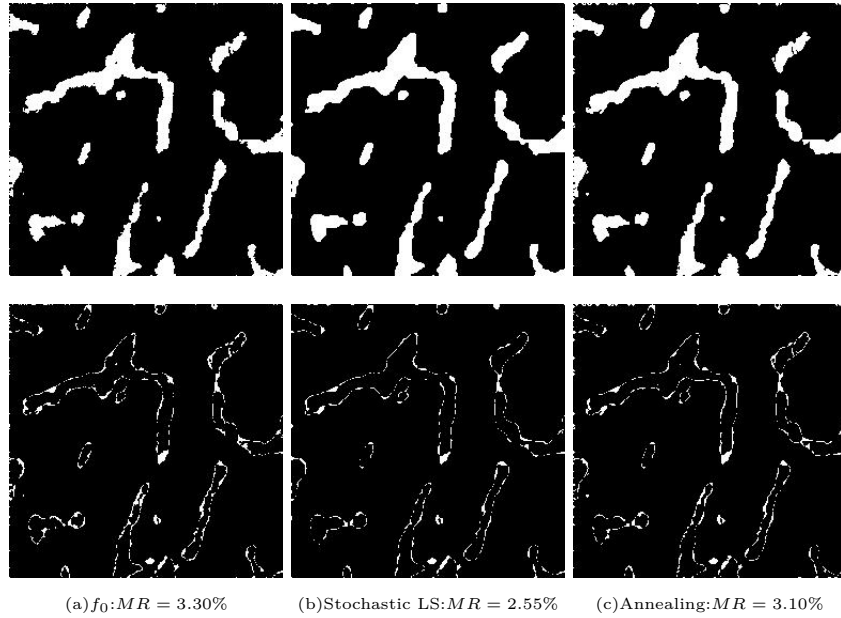


Figure 5.7: Binary reconstructed images of bone cross-section images and difference maps from 10 noisy projections ( $\sigma_p = 3$ ) with deterministic level-set, then stochastic level-set and simulated annealing method.

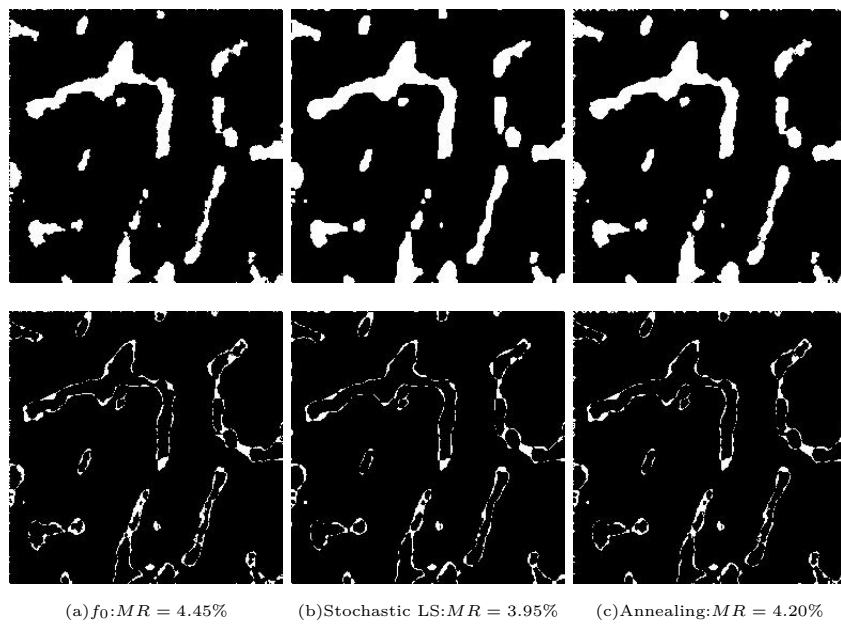


Figure 5.8: Binary reconstructed images of bone cross-section images and difference maps from 10 noisy projections ( $\sigma_p = 6.5$ ) with deterministic level-set, then stochastic level-set and simulated annealing method.

the stochastic level-set approach. Better reconstruction results are obtained with the stochastic level-set algorithm than with the simulated annealing minimization under the same starting conditions and with the same iteration number, for all noise levels and numbers of projections. And the misclassifications rates obtained with the TV methods

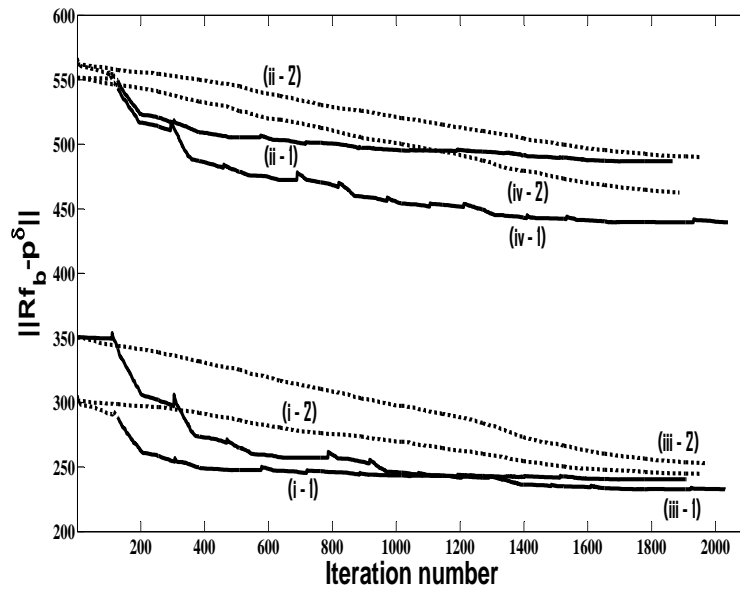


Figure 5.9: Evolution of the data term with the iteration number: the dotted lines corresponds to the simulated annealing and the plain lines to the stochastic level method; (i)  $M=15$ ,  $\sigma_p = 3$ ; (ii)  $M=15$ ,  $\sigma_p = 6.5$ ; (iii)  $M=10$ ,  $\sigma_p = 3$ ; (iv)  $M=10$ ,  $\sigma_p = 6.5$ .

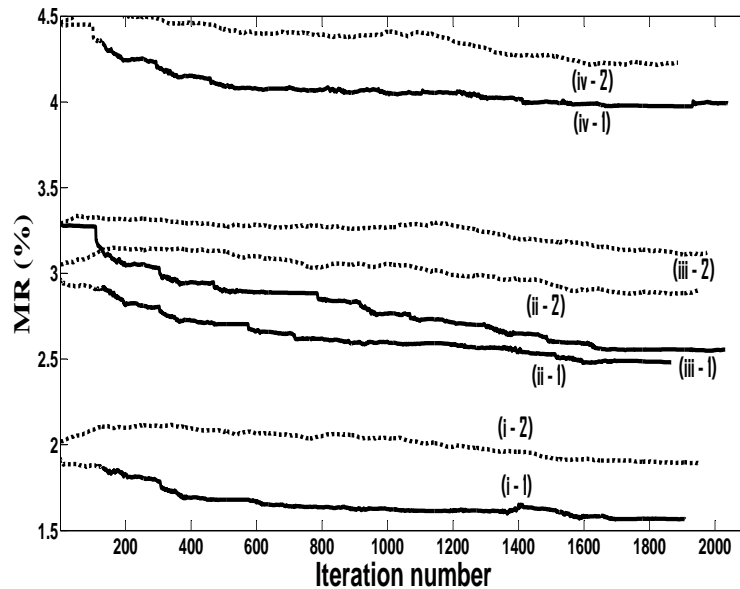


Figure 5.10: Evolution of the misclassification rate with the iteration number:the dotted lines corresponds to the simulated annealing and the plain lines to the stochastic level method; (i)  $M=15$ ,  $\sigma_p = 3$ ; (ii)  $M=15$ ,  $\sigma_p = 6.5$ ; (iii)  $M=10$ ,  $\sigma_p = 3$ ; (iv)  $M=10$ ,  $\sigma_p = 6.5$ .

are also presented in this table. The TV deterministic optimization gives misclassifications rates that are a little higher than the ones achieved with the stochastic level-set method. Some improvement is obtained with the stochastic TV scheme ( $A_4$ ) with a low noise strength. The best misclassification rates are similar for the two stochastic search methods

for these low noise levels for  $M=15$ . The stochastic TV method outperforms the stochastic LS scheme for a lower number of projection angles  $M=10$ .

Table 5.2: Misclassification rates  $MR$  ( % ), negative rates  $nMR$  ( % ), positive rates  $pMR$  ( % ),  $\|Rf - p^\delta\| - \delta\|/\delta$  obtained with the two level-set methods, and the two TV methods.

$M, \sigma_p$	LS	Stochastic LS	Simulated annealing	TV	Stochastic TV
<b>M=15</b>	2.02	1.56	1.90	1.73	1.51
	1.51	0.71	0.87	0.89	0.86
	0.51	0.85	1.03	0.84	0.65
	0.36	0.08	0.10	0.16	0.07
<b>M=15</b>	3.05	2.48	2.90	2.71	2.48
	2.35	1.29	1.58	1.49	1.43
	0.70	1.18	1.32	1.22	1.05
	0.18	0.03	0.03	0.02	0.01
<b>M=10</b>	3.29	2.55	3.10	2.41	2.08
	2.61	1.31	1.80	1.39	1.14
	0.68	1.24	1.30	1.01	0.94
	0.86	0.23	0.34	0.34	0.09
<b>M=10</b>	4.46	3.97	4.20	3.40	3.12
	3.54	2.26	1.68	2.21	1.98
	0.92	1.72	1.52	1.19	1.14
	0.37	0.09	0.15	0.09	0.03

Yet, the stochastic level-set method corresponds to a shape evolution and does not modify the topology of the 0 and 1 regions of the reconstructed images. And the improvement of the reconstruction with stochastic level-set method is not clear for low density images where many regions are missing in the first reoncnstructed images and also for the higher noise levels. The stochastic TV method is much more effective in these cases, as detailed in the following subsection. It is thus interesting to study methods to add stochastic noise in the framework of the TV regularization and random perturbations of the topology of the images to reveal new regions.

### TV based method

Two examples of the reconstructed images  $f_0$  obtained with the deterministic TV algorithm and the corresponding error maps for the low density and high density bone images are displayed in Fig.5.5 and Fig.5.6 with the projections number  $M = 10$  and the standard deviation of the noise on the raw projections  $\sigma_p = 20$ . Similarly to the reconstruction results obtained with the deterministic level-set method, some errors are still present on the boundary regions of the image. Especially, for the low density bone image, large regions have disappeared from the restored image.

**Dense image** For the dense bone image, The reconstructed images and the corresponding difference maps for  $M = 10$  projection angles and the standard derivation  $\sigma_p = 20, 30$  with the TV based algorithms  $A_0 \dots A_4$  are displayed in Fig.5.11, Fig.5.12 and Fig.5.13, Fig.5.14 respectively. From the reconstructed images and difference maps, better reconstructed images are obtained with stochastic approaches. A significant improvement was obtained with the algorithms  $A_1$  and  $A_2$  where the stochastic noise is concentrated on the boundaries. And the best reconstruction results were achieved with the stochastic schemes  $A_3$  and  $A_4$ , which also added some additional noise proportional to the derivative of the gradient of the grey-level reconstructed image.

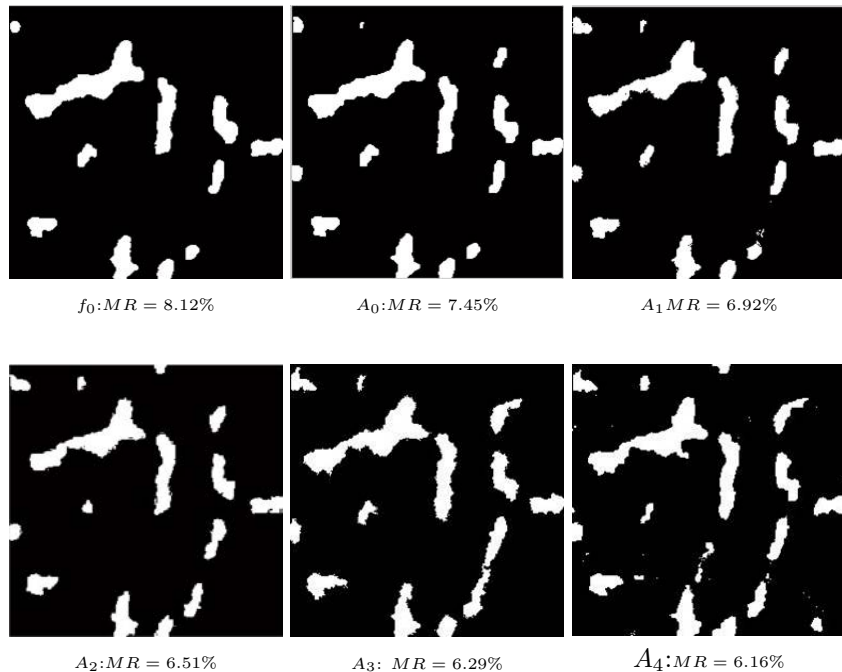


Figure 5.11: Binary reconstructed images of the high density image for 10 noisy projections ( $\sigma_p = 20$ ) with TV based algorithm.

The evolution curves of the discrepancy term  $\|Rf_b^k - p^n\|$  for the binary image starting from the best image  $f_0$  obtained with the TV regularization with box constraints, with  $M = 10$  projection angles and the standard deviation of the noise on projection  $\sigma_p = 20$  and  $\sigma_p = 30$  are displayed in Fig.5.15 and Fig.5.16 as a function of the iteration number for the algorithms  $(A_0), (A_1), (A_2), (A_3), (A_4)$ . The time of every stochastic TV iteration is very similar for the algorithms  $(A_1) \dots (A_4)$  and it is 20 % longer than the time of the TV iterations, and 30 times shorter than the time of one stochastic LS iteration. With the iterations, some decrease of the discrepancy term related to the binary image towards the noise level  $\delta = 1210$  ( $\sigma_p = 20$ ) and  $\delta = 1817$  ( $\sigma_p = 30$ ) are observed for these stochastic algorithms. The results for  $M = 15$  are very similar. The change of the discrepancy term is below 5 % for different noise realizations.

The evolution curves of the misclassification rates are displayed on Fig.5.17 and Fig.5.18

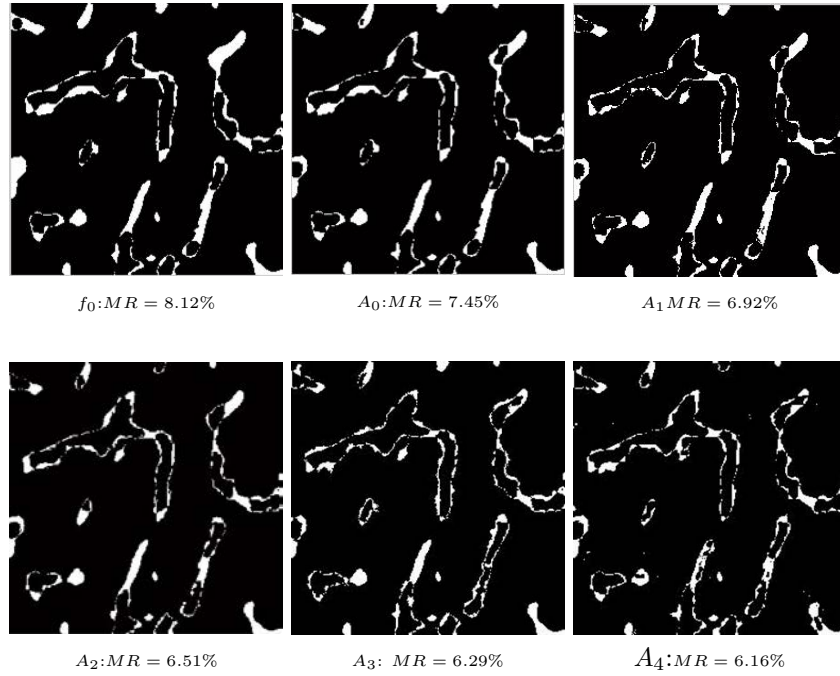


Figure 5.12: Corresponding difference maps of the high density image for 10 noisy projections ( $\sigma_p = 20$ ) with TV based algorithm.

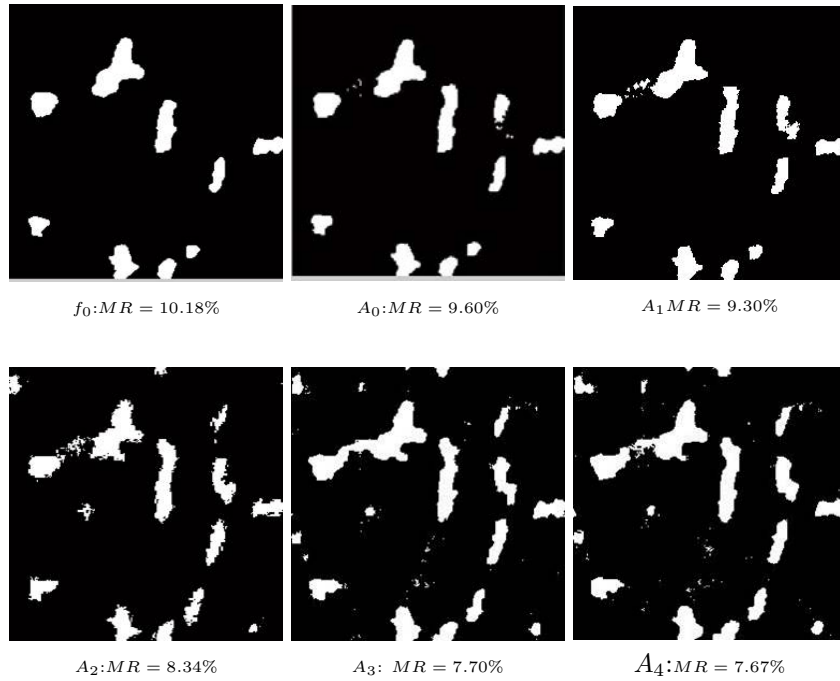


Figure 5.13: Binary reconstructed images of the high density image for 10 noisy projections ( $\sigma_p = 30$ ) with TV based algorithm.

for the same projection number  $M = 10$  and the same noise levels  $\sigma_p = 20, 30$ , with the same algorithms. There is a clear correlation between the decrease of the discrepancy term and the decrease of the misclassification rate. Similar decreases are obtained for a higher

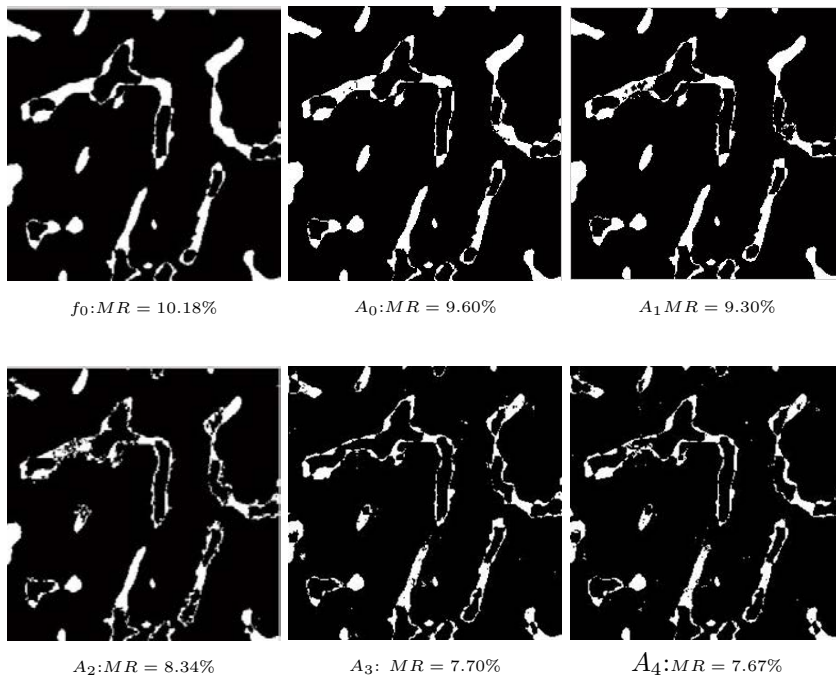


Figure 5.14: Corresponding difference maps of the high density image for 10 noisy projections ( $\sigma_p = 30$ ) with TV based algorithm.

number of projections  $M = 15$ .

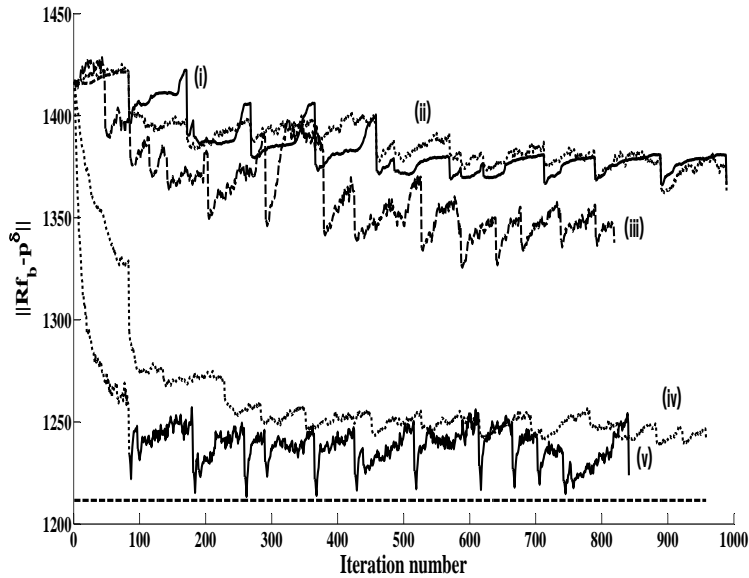


Figure 5.15: Evolution of the discrepancy term as the function of the iteration number for the high density bone image  $M = 10$ ,  $\sigma_p = 20$  and for the algorithms  $A_0$ (i),  $A_1$ (ii),  $A_2$ (iii),  $A_3$ (iv), and  $A_4$ (v). The noise level  $\delta$  is displayed for comparison with dotted lines.

The miclassification rates, negative miclassification rates, positive miclassification rates and  $\frac{\|Rf - p^\delta - \delta\|}{\delta}$  achieved for the final binary reconstructed images for various number

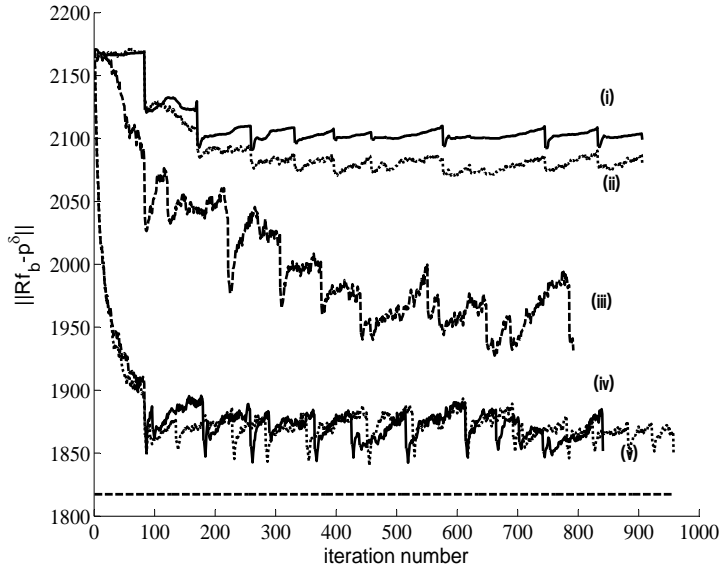


Figure 5.16: Evolution of the discrepancy term as the function of the iteration number for the high density bone image  $M = 10$ ,  $\sigma_p = 30$  and for the algorithms  $A_0$ (i),  $A_1$ (ii),  $A_2$ (iii),  $A_3$ (iv), and  $A_4$ (v). The noise level  $\delta$  is displayed for comparison with dotted lines.

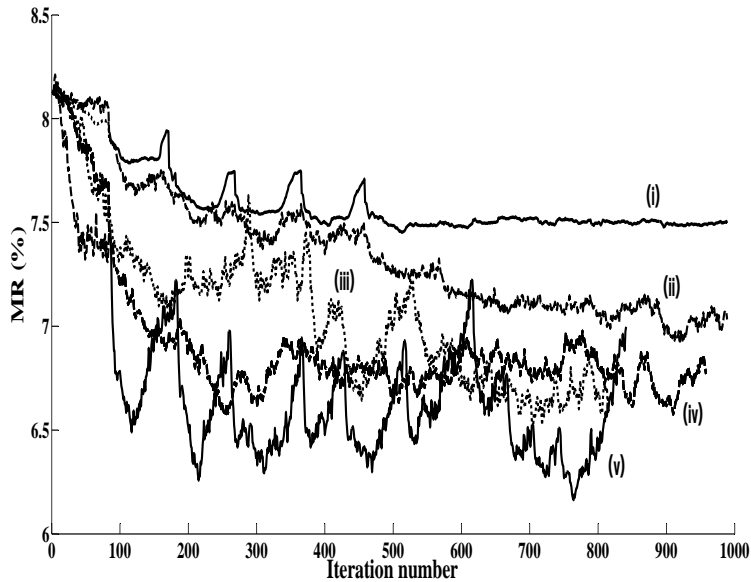


Figure 5.17: Evolution of the misclassification rate as the function of the iteration number for the high density bone image  $\sigma_p = 20$  and for the algorithms  $A_0$ (i),  $A_1$ (ii),  $A_2$ (iii),  $A_3$ (iv), and  $A_4$ (v).

of projections and noise levels are summarized in Table 5.3.

In our simulations, the stochastic methods are more efficient than a deterministic TV regularization used repeatedly  $A_0$ . Boundary stochastic noise is more successful to improve the reconstructed images  $f_0$ . Yet, the best reconstruction results are achieved with both boundary noise and nonlinear gradient dependent noise  $A_3$  and  $A_4$ . The two types of

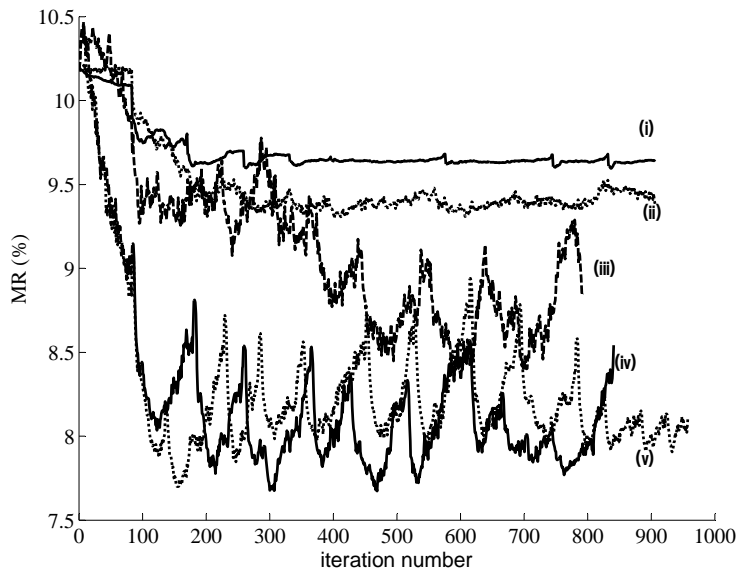


Figure 5.18: Evolution of the misclassification rate as the function of the iteration number for the high density bone image  $\sigma_p = 30$  and for the algorithms  $A_0$ (i),  $A_1$ (ii),  $A_2$ (iii),  $A_3$ (iv), and  $A_4$ (v).

Table 5.3: Misclassification rates  $MR$  ( % ), negative rates  $nMR$  ( % ), positive rates  $pMR$  ( % ),  $\| Rf - p^\delta \| - \delta \| / \delta$  obtained with the stochastic algorithm based on the Total Variation for high density bone image.

$M, \sigma_p$	<b>TV</b>	Stochastic TV				
		$A_0$	$A_1$	$A_2$	$A_3$	$A_4$
<b>M=15</b>	7.18	6.89	6.82	6.60	5.03	5.03
	1.68	1.68	1.44	1.27	1.86	1.84
	5.50	5.22	5.38	5.33	3.17	3.19
	0.16	0.14	0.15	0.16	0	0
<b>M=15</b>	9.54	9.36	7.29	9.17	6.58	6.30
	1.33	1.21	1.29	0.92	2.11	1.73
	8.21	8.15	7.99	8.25	4.47	4.57
	0.16	0.16	0.15	0.17	0.01	0.01
<b>M=10</b>	8.12	7.45	6.92	6.51	6.57	6.16
	1.87	1.69	1.32	1.28	2.42	2.02
	6.26	5.76	5.61	5.23	4.15	4.15
	0.17	0.13	0.13	0.11	0.03	0.01
<b>M=10</b>	10.18	9.60	9.30	8.34	7.70	7.67
	1.19	1.30	1.34	1.74	2.13	2.24
	9.0	8.30	7.96	6.60	5.56	5.43
	0.19	0.15	0.14	0.08	0.03	0.02

noise may be understood as the shape and topological stochastic modifications of the initial reconstructed image  $f_0$ .

**Sparse image** For instance, the reconstructed images and the corresponding difference maps for the low density bone cross-sections for  $M = 10$  projection angles and the standard derivation  $\sigma_p = 10, 20$  with the TV based algorithms  $A_2$  and  $A_4$  are displayed in Fig.5.19 and Fig.5.20 respectively. Many bone structures are lost in the first reconstructed image  $f_0$  obtained with a deterministic TV regularization method. Adding only wavelet dependent additive stochastic noise (algorithm  $A_2$ ) seems to be useless. The reason is that this method only concentrates on the shape derivative and is not able to find the lost regions. Adding boundary stochastic noise and homogeneous stochastic noise at the same time (algorithm  $A_4$ ) leads to better reconstruction results. Some lost structures were found at the end of global optimization process.

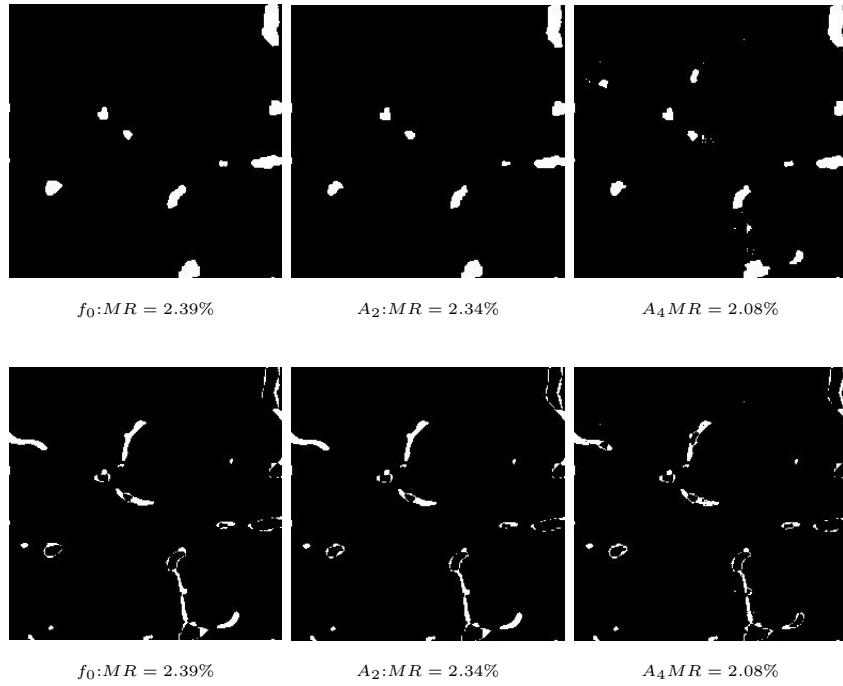


Figure 5.19: Binary reconstructed images and corresponding difference maps of the low density image for 10 noisy projections ( $\sigma_p = 10$ ) with deterministic TV method and TV based algorithm  $A_2, A_4$ .

The evolution curves of the discrepancy term  $\|Rf_b^k - p^\delta\|$  and of the misclassification rates  $MR(f_b^k)$  are displayed on Fig.5.21 and Fig.5.22 for the binary image starting from  $f_0$  with the algorithm  $A_4$ .

The misclassification rates, negative misclassification rates, positive misclassification rates and  $\frac{\|Rf - p^\delta - \delta\|}{\delta}$  achieved for the final binary reconstructed images with the algorithm  $A_4$  are summarized in Table.5.4. The first reconstructed image  $f_0$  is not well reconstructed and the stochastic method based on TV seems not to be very efficient to improve the images

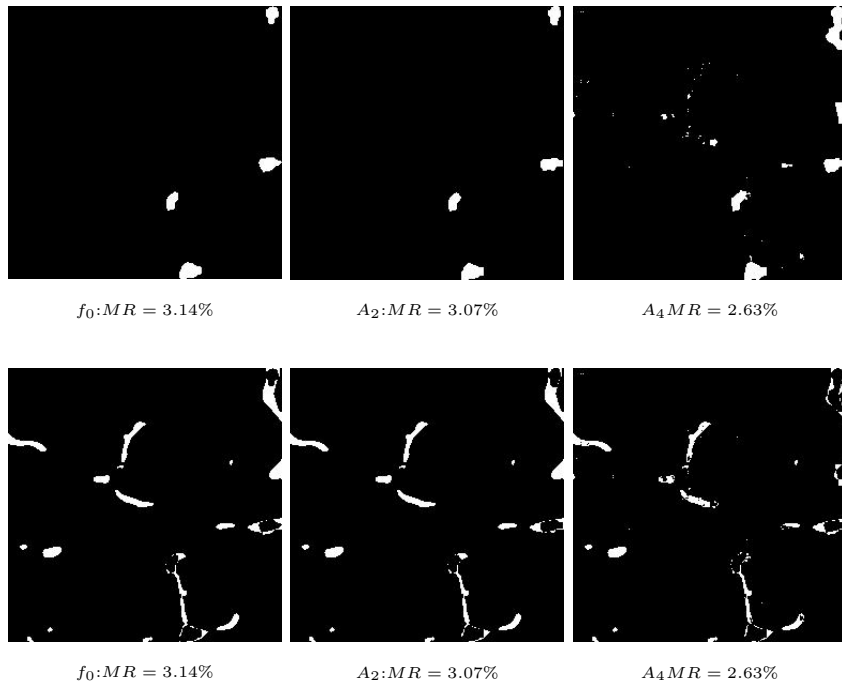


Figure 5.20: Binary reconstructed images and corresponding difference maps of the low density image for 10 noisy projections ( $\sigma_p = 20$ ) with deterministic TV method and TV based algorithm  $A_2$ ,  $A_4$ .

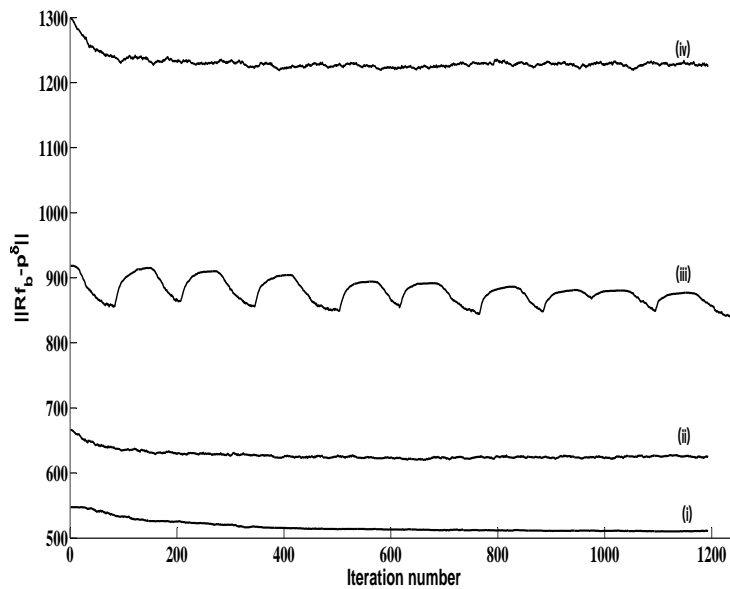


Figure 5.21: Evolution of the discrepancy term as the function of the iteration number for the low density bone image for the algorithms  $A_4$ , with  $M = 5, \sigma_p = 10$  (i);  $M = 10, \sigma_p = 10$  (ii);  $M = 20, \sigma_p = 10$  (iii);  $M = 10, \sigma_p = 20$  (iv).

with sparse bone structures. But the correlation between the decrease of the discrepancy term and of the misclassification rate is very clear for the four cases investigated.

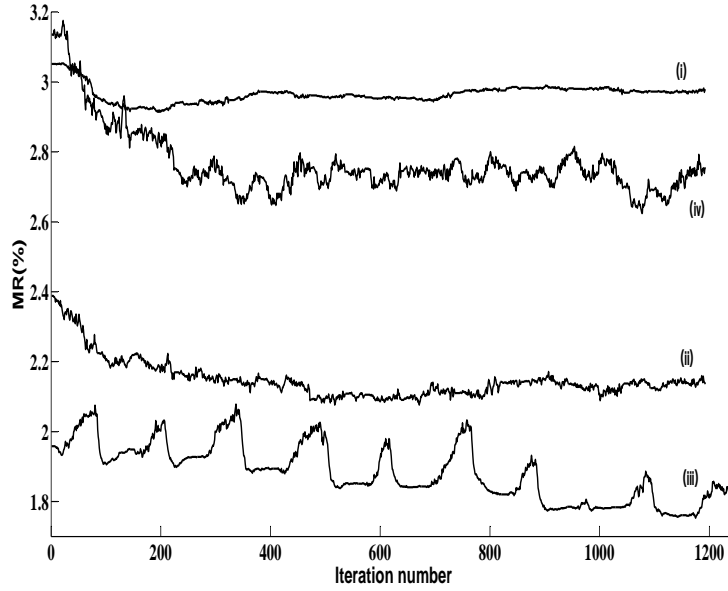


Figure 5.22: Evolution of the misclassification rate as the function of the iteration number for the low density bone image for the algorithms  $A_4$ , with  $M = 5, \sigma_p = 10$  (i);  $M = 10, \sigma_p = 10$  (ii);  $M = 20, \sigma_p = 10$  (iii);  $M = 10, \sigma_p = 20$  (iv).

Table 5.4: Misclassification rates  $MR$  ( % ), negative rates  $nMR$  ( % ), positive rates  $pMR$  ( % ),  $\|Rf - p^\delta\|/\delta$  obtained with the stochastic algorithm based on the Total Variation ( $A_4$ ) for sparse image.

$M, \sigma_p$	$M=5$	$M=10$	$M=10$	$M=10$
	$\sigma_p = 10$	$\sigma_p = 10$	$\sigma_p = 20$	$\sigma_p = 20$
TV	3.05	2.39	3.14	1.96
	0.17	0.47	0.07	0.23
	2.88	1.91	3.06	1.72
	0.30	0.13	0.11	0.13
Stochastic TV ( $A_4$ )	2.91	2.08	2.62	1.67
	0.2	0.51	0.34	0.30
	2.71	1.56	2.29	1.37
	0.25	0.06	0.05	0.06

**Micro-local analysis** In this part, we used a filter taking into account wavefront set properties of the Radon transform to refine the reconstruction results obtained with TV based stochastic approaches. As mentioned in section 5.3.1, a first binary reconstructed image  $f_0$  was obtained with a deterministic TV and ADMM algorithm. Its data term is well-above the noise level  $\delta$  and the Morozov principle is not fulfilled. Some reconstruction errors are still present in the boundaries and then the stochastic optimization was applied. In this work, we just considered the best TV based stochastic algorithm  $A_4$  (Section 5.2.3) and the new algorithm  $A_5$ , which was obtained by multiplying the wavelet based boundary

noise terms of the algorithm  $A_4$  with a Filter  $F$  defined in Section 5.2.3.

Similarly to the other TV based stochastic algorithms, for algorithm  $A_5$ , the parameters  $\eta_1, \eta_2$  and  $\alpha$  are chosen by trial and error to obtain the best decrease of discrepancy term. The stochastic diffusions are performed on random steps in the range  $[0, T_{max}]$  with  $T_{max} = 100$  and the deterministic TV ADMM algorithms were stopped when they achieved the minimum values of  $\|Rf^k - p^\delta\|$ .

Our optimization method is tested with  $M = 10$  equally projections which were corrupted with two Gaussian noises with the standard derivations  $\sigma_p = 5$  and  $\sigma_p = 10$  corresponding to  $PPSNR$  of 16dB and 11dB respectively. An example was given in Fig.5.23 to show how the micro-local analysis is implemented.

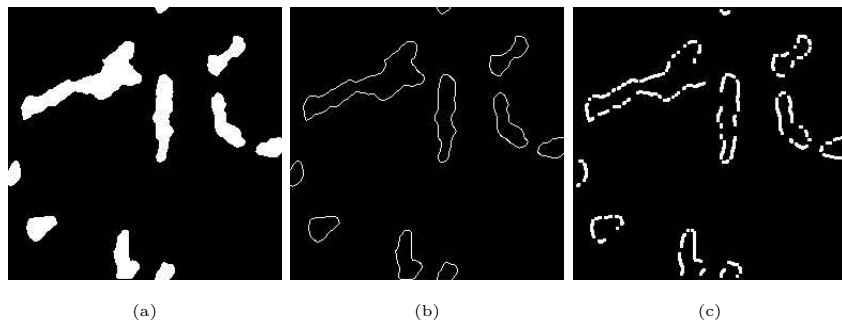


Figure 5.23: Principle of micro-local analysis. (a) A first reconstructed image  $f_0$  with deterministic TV regularization method for  $M = 15$  and  $\sigma_p = 20$ . (b) Corresponding boundary obtain by 'sobel' operator. (c) Filter of the reconstructed image  $f_0$  with  $\alpha = 6^\circ$

The final binary reconstructed images and corresponding difference maps with the two TV based algorithms  $A_4$  and  $A_5$  for  $M = 10$ ,  $\sigma_p = 5, 10$  are shown in Fig.5.24 and Fig.5.25 respectively. The threshold  $\alpha$  in of the filter in algorithm  $A_5$  was set to  $6^\circ$ .

The decrease of the discrepancy term  $\|Rf_b^k - p^\delta\|$  as a function of iteration  $k$  and the corresponding misclassification rate  $MR(f_b^k)$  of algorithm  $A_4$  and  $A_5$  are displayed in Fig.5.26 and Fig.5.27.

The stochastic algorithm with a filter  $A_5$  leads to a better decrease of the discrepancy term and misclassification rate. From the comparison with the reconstructed images obtained with the algorithm  $A_4$ , we see that some errors on the boundaries were reduced and some new regions appeared in the final reconstructed images.

**Smoothing filter** At the end of this section, a smoothing filter was introduced to improve the reconstruction results. For example, in Fig.5.13, the reconstructed image with algorithm  $A_3$  is too noisy even if some errors were reduced and some lost structures were found. In order to suppress the isolated points in the reconstructed images, a smoothing filter of size  $3 \times 3$  is defined as:

$$f(i, j) = \begin{cases} 1 & \sum_{m=-1}^1 \sum_{n=-1}^1 f(i+m, j+n) > TH_s \\ 0 & \text{otherwise} \end{cases} \quad (5.26)$$

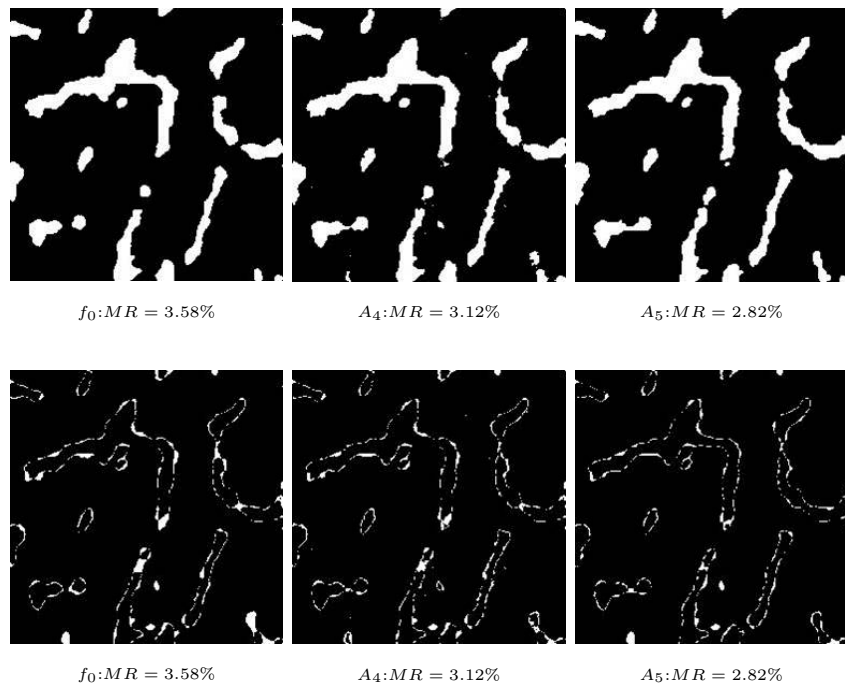


Figure 5.24: Binary reconstructed images and corresponding difference maps of the high density image for 10 noisy projections ( $\sigma_p = 5$ ) with deterministic TV method, TV based algorithm  $A_4$ ,  $A_5$ .

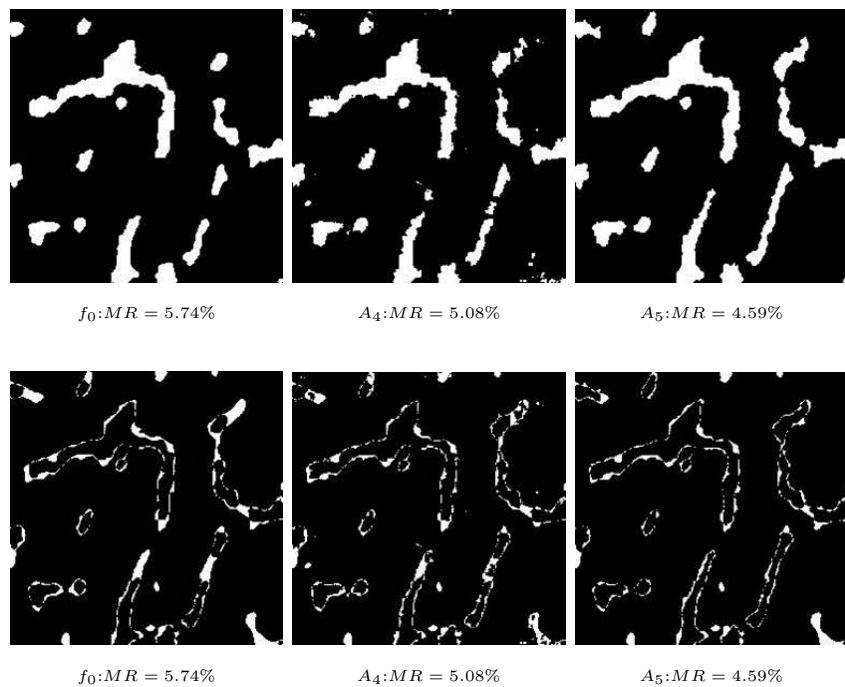


Figure 5.25: Binary reconstructed images and corresponding difference maps of the low density image for 10 noisy projections ( $\sigma_p = 10$ ) with deterministic TV method and TV based algorithm  $A_2$ ,  $A_5$ .

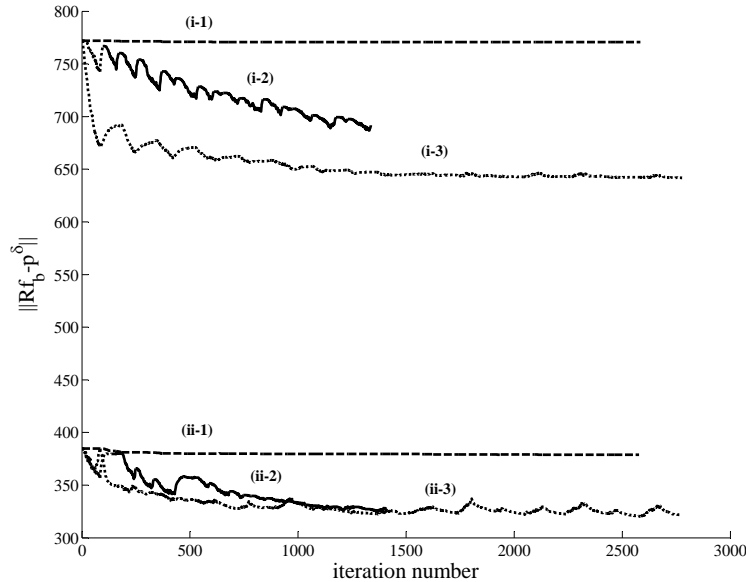


Figure 5.26: Evolution of  $\|Rf_b^k - p^\delta\|$  as the function of iteration  $k$  for  $M = 10$  and  $\sigma_p = 10$  (i),  $\sigma_p = 5$  (ii) for the deterministic TV (1),  $A_4$ (2),  $A_5$ (3).

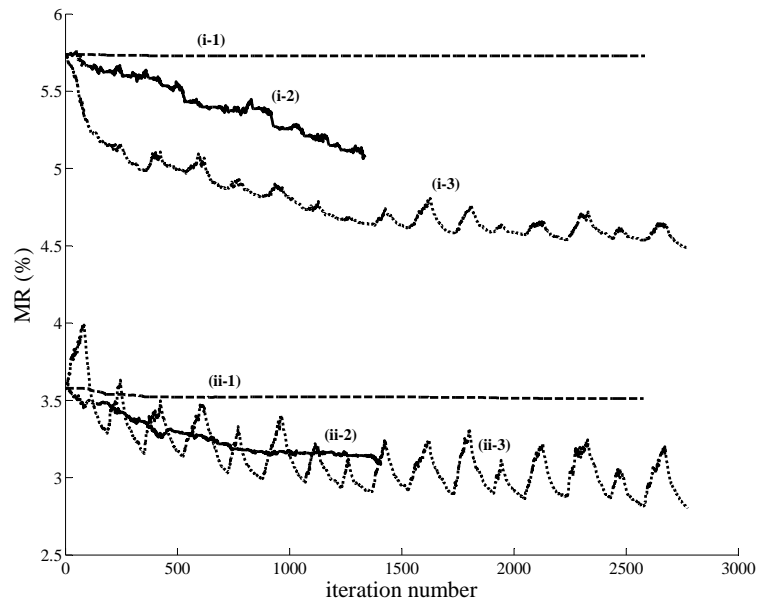


Figure 5.27: Evolution of  $MR(f_b^k)$  as the function of iteration  $k$  for  $M = 10$  and  $\sigma_p = 10$  (i),  $\sigma_p = 5$  (ii) for the deterministic TV (1),  $A_4$ (2),  $A_5$ (3).

where  $TH_s$  is a threshold. This smoothing filter was used in every binarization step in the intermittent stochastic optimization process. The final reconstructed image for algorithm  $A_3$  for  $m = 10$  and  $\sigma_p = 30$  with a smoothing filter  $TH_s = 5$  is shown in Fig.5.28. The smoothing filter has improved the reconstructed image slightly and removed some isolated points in the final reconstructed image.

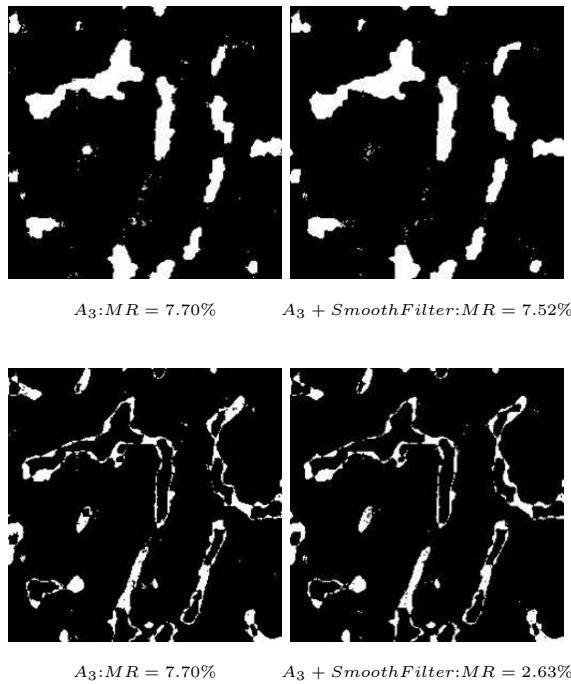


Figure 5.28: Binary reconstructed images and corresponding difference maps for algorithm  $A_3$  for  $m = 10$  and  $\sigma_p = 30$  without and with a smoothing filter  $TH_s = 5$ .

## 5.4 Conclusion

This work compares new stochastic diffusion methods to refine the binary reconstructed images of bone cross-sections from a few number of projections. A first reconstructed image was obtained with deterministic level-set or TV regularization methods. Then this image was refined with intermittent stochastic diffusion methods. In the level-set stochastic algorithm, the restoration was improved with a stochastic partial differential equation based on a Stratanovitch formulation. In the TV based stochastic optimization method, the boundary noise terms are implemented with a finite difference estimation of the gradient or with a wavelet decomposition and the homogeneous noise proportional to the gradient of the data term is also added.

First, the stochastic methods based on level-set and TV regularizations have improved the reconstructed images a lot if they are adapted to different conditions. The stochastic level-set algorithm leads to a clear improvement of the reconstruction of the boundaries between the 0 and 1 regions. It is very useful for low noise levels but it does not yield improved reconstructions for the higher noise levels and for the low density image. For the higher noise levels, the stochastic TV based approach is more efficient because it leads to a modification of the boundaries but it also reveals new regions in the image when two types of noise are included. The random fluctuations lead to shape and topology changes of the 0 and 1 regions in the restored image.

The stochastic methods are used for a poor first reconstruction obtained with a small projection number and high noise levels. For a higher projection numbers and for less noise

on the raw projection data, the inverse problem is less ill-posed and the stochastic methods are less useful to achieve a better reconstruction. For example, for the high density image, when  $M = 20$  and  $\sigma_p = 3$ , the discrepancy term  $\|Rf_0 - p^\delta\|$  of the first reconstructed image with deterministic TV ADMM algorithm is very closed to its noise level  $\delta$  and it is impossible to improve the reconstruction.

# Chapter 6

---

## Binary Reconstruction with Total Variation with a box constraint method on 3D images

---

### 6.1 Introduction

We have studied the performances, advantages and disadvantages of Total Variation (TV) regularization algorithm and Level-set (LS) algorithm for the binary reconstruction from a limited number of projections for 2D images, and how to improve the reconstruction results with a stochastic method in the previous chapters. We try to extend these methods from 2D images to 3D volumes to study the applicability of the proposed methods. In this chapter, the main aim is to extend Total Variation (TV) regularization algorithm from 2D images to 3D volumes.

In this work, we have chosen Reconstruction Toolkit (RTK) as the platform for our 3D reconstruction simulations because of its advantages. Firstly, the RTK is an open source and cross platform software only for fast circular Cone-Beam CT (CBCT) reconstruction based on the Insight Toolkit (ITK) and using GPU code extracted from Plastimatic. CBCT is a useful reconstruction method to produce CT images with isotropic sub-millimeter spatial resolution, high diagnostic quality, short scanning times of about 10-30 seconds [[Bamgbose et al. \(2007\)](#)]. RTK provides basic operators for reconstruction, multithreaded CPU and GPU versions, tools for respiratory motion correction, I/O for several scanners and preprocessing of raw data for scatter correction [[Rit et al. \(2014\)](#)].

This toolkit is developed by RTK consortium, including CREATIS, the Massachusset General Hospital, the Universite catholique de Louvain and IBA. Secondly, the forward and back projectors have been carefully designed in a typical object-oriented fashion to allow testing various implementations in order to provide a fast reconstruction. Thirdly, RTK was developed with C++ language which can cope with the memory directly. These features make RTK able to cope with a large volume data fast and efficiently. Last but not least, RTK has provided many currently used reconstruction algorithm such as Feldkamp-David-Kress (FDK) algorithm which can be used to compare with our proposed method. And RTK also can simulate phantoms such as Shepp-Logan which is commonly used to validate the effect of a reconstruction algorithm.

Because RTK has been developed on ITK, it is very closed to an ITK module. A typical ITK data pipeline and the sequence of the data pipeline updating mechanism are shown in Fig.6.1 and Fig.6.2 respectively. They are similar to the ones of RTK. Therefore, it is convenient to implement a reconstruction algorithm on RTK just by designing a corresponding filter consisting of many sub-filters in a correct sequence and inserting this filter into a RTK pipeline. The computing task will be implemented automatically by RTK and the output will be given at the end of reconstruction process.

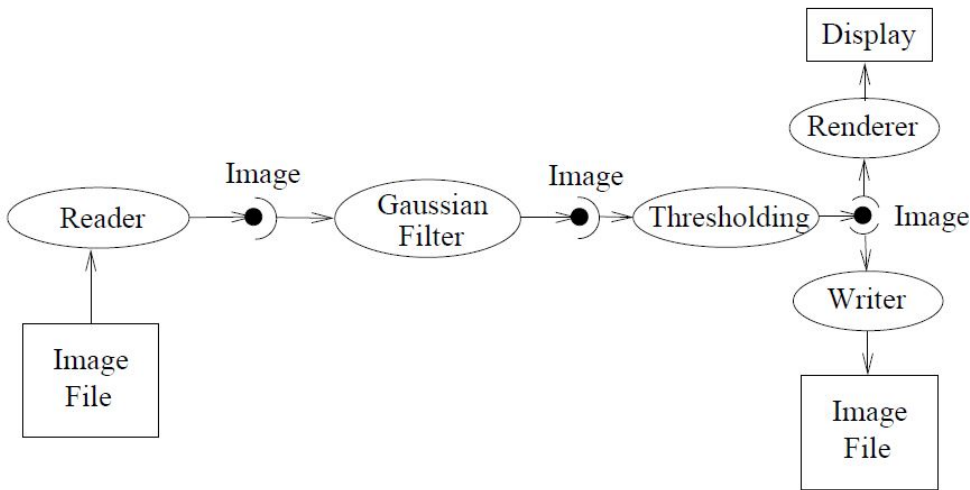


Figure 6.1: Data pipeline of ITK from [Rit and Mory (2015)].

The software guide about RTK is available on <http://wiki.openrtk.org/>, the relative doxygen documents can be found on <http://www.openrtk.org/Doxxygen/index.html>. From these websites, the installation, examples and user manuscripts of the necessary C++ project Integrated Development Environment (IDE), command line tools can be found.

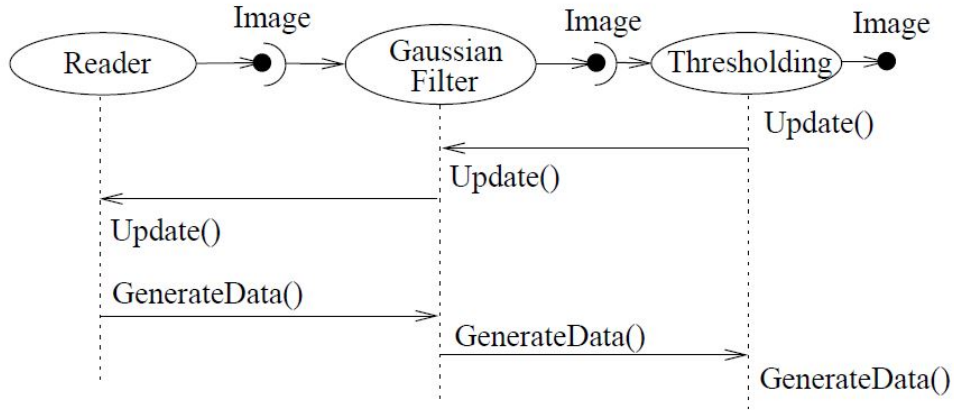


Figure 6.2: Sequence of the Data Pipeline updating mechanism of ITK from [Rit and Mory (2015)].

## 6.2 3D Reconstruction with TV Regularization with a Box Constraint Method on RTK

RTK is used for reconstruction only for Cone Beam CT (CBCT). RTK is based on ITK and it relies on many features of ITK, therefore, the implementation of an algorithm on RTK is similar to ITK. RTK is also constructed by many small filters such as "+", "-", "×" and so on. These filters are small black boxes which are invisible to us. We don't know how these filters realize the correct functions and what we can do is to combine these filters in a correct time sequence and give them suitable "inputs". We will obtain the outputs at the end of a RTK run. For example, a simple filter that computes  $\mu\nabla f + \beta$  should be constructed as Fig.6.3. In "MyFilter", firstly, three simple sub-filters to realize " $\nabla$ ", "+" and "×" functions are needed and combined in a good sequence. Secondly, the original inputs " $f$ ", " $\mu$ " and " $\beta$ " should be given to the correct filters.

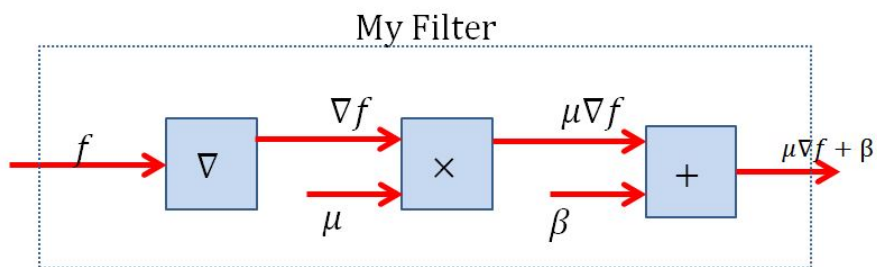


Figure 6.3: A simple composite RTK filter to compute  $\mu\nabla f + \beta$ .

If we want to implement TV regularization with a box constraint method on RTK, the first important thing is to decide the sequences of the implementations of TV algorithm on RTK. The second important task to do is to design a TV-ADMM filter according to

the sequence of implementations of the TV algorithms with the inputs: regularization parameter  $\mu$ , Lagrangian parameter  $\beta$ , the noisy projection data  $p^\delta$ , the initial empty 3D volume  $f_0$  and the geometry of CBCT system such as the projection angles, the distance from the X-ray source to the detector, the distance from the x-ray source to the object and so on. The geometry is an essential information to do a successful tomographic reconstruction.

### 6.2.1 The implementation of TV regularization with a box constraint for 3D volumes

The TV regularization with a box constraint functional  $E(f)$  for 3D reconstruction is the same as the one of the 2D reconstruction in chapter 4.2:

$$E(f) = \frac{\mu}{2} \|Rf - p^\delta\|_{L_2}^2 + J_{TV}(f) \quad s.t. \quad f \in [C_0, C_1]^n \quad (6.1)$$

Here,  $[C_0, C_1]$  is the convex set. The isotropic TV regularization term  $J_{TV}(f)$  based on computing the  $L_1$  norm of the gradient of the discrete 3D volume  $f$  is defined as:

$$J_{TV}(f) = \nabla f = \sum_{v=1}^V \sqrt{[\nabla_x f(v)]^2 + [\nabla_y f(v)]^2 + [\nabla_z f(v)]^2} \quad (6.2)$$

where  $v$  is the voxel position and  $V$  is the total number of voxel in volume  $f$ . In this section, the augmented Lagrangian method combined the Alternating Direction Minimization Method (ADMM) [Afonso *et al.* (2011), Afonso *et al.* (2010), Ng *et al.* (2010)] are still used to minimize the TV regularization functional  $E(f)$  to obtain the final reconstructed volume  $f$ . The problem of finding the  $\operatorname{argmin}_f E(f)$  is equivalent to the constrained problem:

$$\begin{aligned} \mathcal{L}(f, (g), h, (\lambda), \lambda_C) = & \sum_{v=1}^V (\|g_v\|_2 - \lambda^t(g - \nabla f) + \frac{\beta}{2}\|g - \nabla f\|_2^2) + \frac{\mu}{2}\|p^\delta - Rf\|_2^2 \\ & + I_C(h) + \frac{\beta}{2}\|h - f\|_2^2 - \lambda_C^t(h - f) \end{aligned} \quad (6.3)$$

$$g = \nabla f$$

$$h = I_c(f) \in [C_0, C_1]^n$$

The ADMM algorithm searches for the saddle points of augmented Lagrangian methods for 3D reconstruction is the same to the 2D reconstructions:

- minimizing  $\sum_{v=1}^V (\|g\|_2 - \lambda^t(g - \nabla f) + \frac{\beta}{2}\|g - \nabla f\|_2^2) + \frac{\mu}{2}\|p^\delta - Rf\|_2^2$  over  $g$  with:

$$g^{k+1} = \max\{\|\nabla f^k + \frac{1}{\beta}(\lambda^k)\| - \frac{1}{\beta}, 0\} \frac{\nabla f^k + \frac{1}{\beta}(\lambda^k)}{\|\nabla f^k + \frac{1}{\beta}(\lambda^k)\|} \quad (6.4)$$

- minimizing  $\frac{\mu}{2} \|p^\delta - Rf\|_2^2 + I_C(h) + \frac{\beta}{2} \|h - f\|_2^2 - \lambda_C^t(h - f)$  over  $h$  with:

$$h^{k+1} = \pi_C(f^k + \frac{\lambda_C^k}{\beta}) \quad (6.5)$$

$h^{k+1}$  can also be computed voxel-by-voxel, for each voxel  $v$ :

$$h_v^{k+1} = \begin{cases} C_0 & f_v^k < C_0 \\ C_1 & f_v^k > C_1 \\ f_v^k & otherwise \end{cases} \quad (6.6)$$

- updating Lagrange multipliers  $\lambda^k$  and  $\lambda_c$  at each iteration with:

$$\lambda_i^{k+1} = \lambda_i^k - \beta(g^{k+1} - \nabla f^k) \quad (6.7)$$

$$\lambda_C^{k+1} = \lambda_C^k - \beta(h^{k+1} - f^k) \quad (6.8)$$

Initially, the  $\lambda^0$  and  $\lambda_c^0$  were set to 0.

- $f^{k+1}$  is the zero of the gradient of Eq.6.3, that is to say:

$$\underbrace{\left( \sum_v \nabla_v^t \nabla_v + \frac{\mu}{\beta} R^t R + I \right) f^{k+1}}_A = \underbrace{\sum_v \nabla_v^t (g_v^{k+1} - \frac{1}{\beta} \lambda_v^k) + \frac{\mu}{\beta} R^t p^\delta + h^{k+1} - \frac{\lambda_C^k}{\beta}}_b \quad (6.9)$$

$f^{k+1}$  can be computed by a conjugate gradient algorithm aimed to solving the inverse problem  $Af = b$ . And because  $\nabla^t = -\text{div}$  if  $\nabla$  and  $\nabla^t$  are computed with circular padding on the borders,  $\nabla^t$  can be computed with a backward difference algorithm [Mory (2014)].

### 6.2.2 TVbox-ADMM filter

As described in the section above, the TV-ADMM filter was displayed on Fig.6.4. The initial Lagrange multipliers  $\lambda$  and  $\lambda_c$  were set as 0. The yellow connections between the sub-filters was used to deliver the input volumes: the initial reconstructed volume and the projection data. These connections will be created immediately when the "TV-ADMM" filter is called. The red connections are permanent during the whole TVbox reconstruction process and are created at the very beginning of a TVbox process. The purple connections are used only in the first iteration for initializing the Lagrange multipliers or telling the correct filter the format of output volumes. And after the first iteration, the purple connections will be abandoned and the green connections will be created. What's more, a small filter aimed to update the coefficient  $A$  of the Eq.6.2.1 was constructed as shown in Fig.6.5.

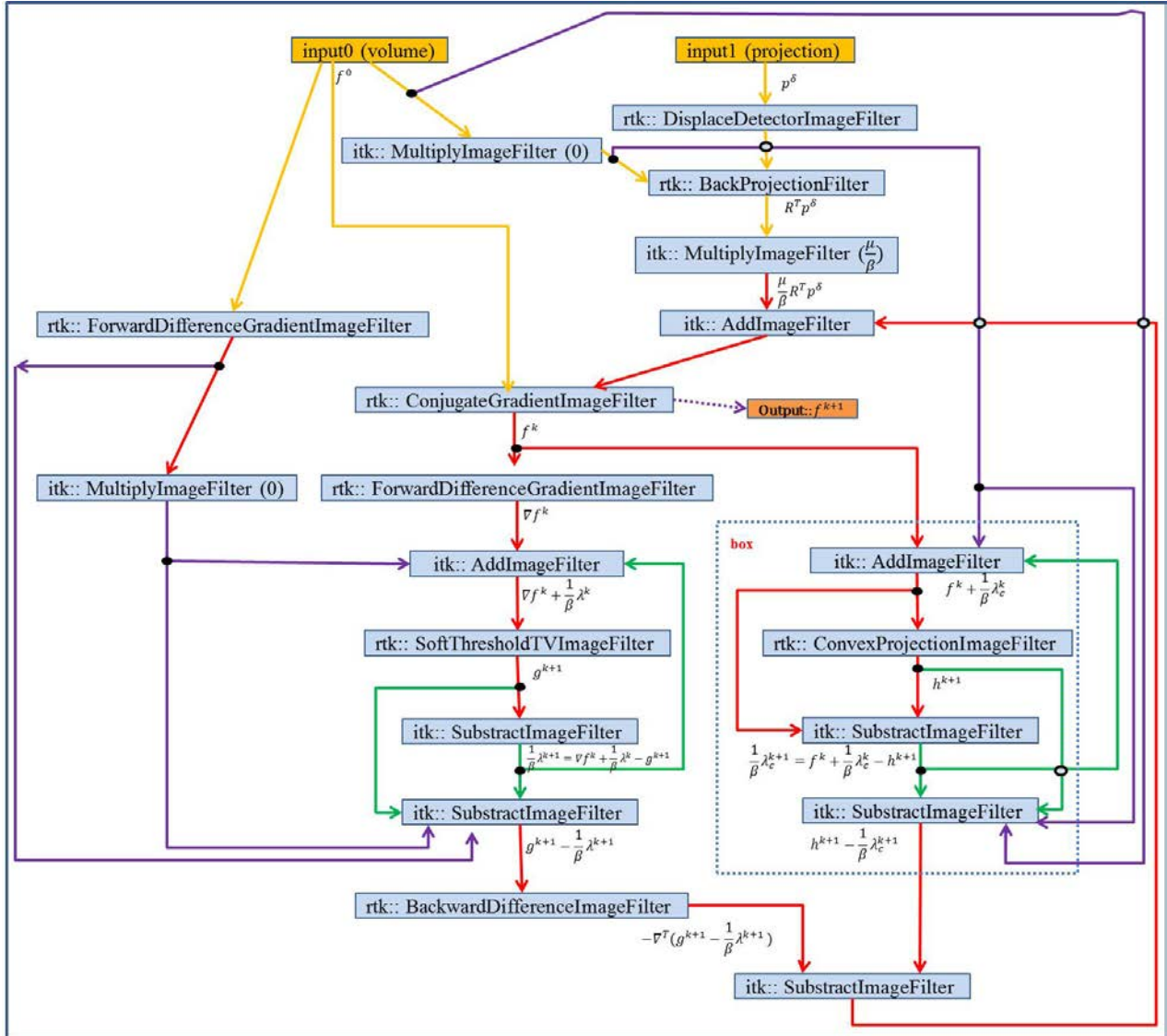
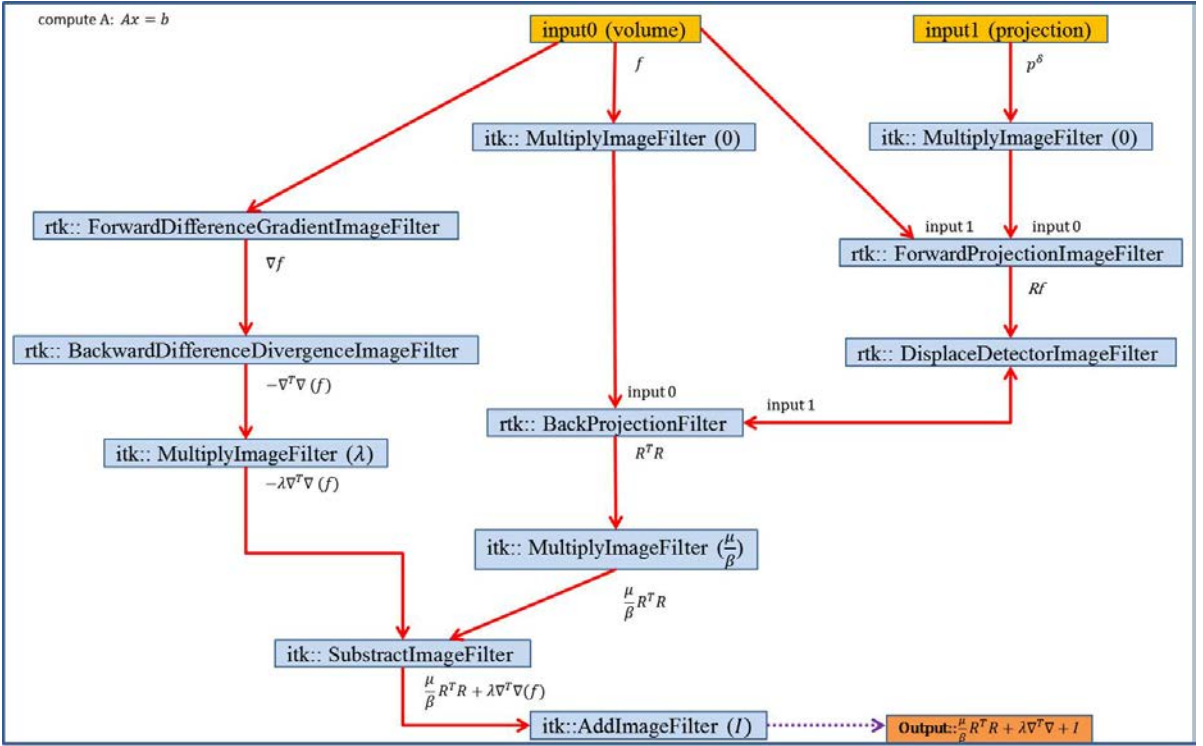


Figure 6.4: TVbox-ADMM filter

### 6.2.3 Basic global threshold method

Due to the weak signal of the projection volume, the voxel values of grey-level reconstructed trabecular bone structures volume are very small and it is very difficult to find a suitable threshold for every reconstruction with different noise levels and projection numbers. Therefore, a global threshold [Gonzalez and Woods (2002)] was used for every reconstruction of the real trabecular bone volume. The algorithm to find a global threshold of volume  $f$  is described as:

- Choose an initial threshold  $T_0 = \frac{\max(f) + \min(f)}{2}$ ;
- Segmente the volume  $f$  with  $T_0$  to obtain two groups:  $G_1$  with the voxel value  $\leq T_0$  and  $G_2$  with the voxel value  $> T_0$ ;
- Compute the average voxel values  $\mu_1, \mu_2$  for  $G_1, G_2$  respectively;

Figure 6.5: Filter to compute  $A$ .

- Compute a new threshold  $T_k = (\mu_1 + \mu_2)/2$ ;
- Repeat step2 to step3 until  $\Delta T = |T_{k+1} - T_k| < T_\epsilon$ , where  $T_\epsilon$  is a positive constant.

## 6.3 Numerical Simulations

### 6.3.1 Simulation details

In our experiments, the projection operator  $R$  is still taken as the discrete approximation of Radon transform, which is implemented on RTK. The TV regularization method with a box constraint was applied on a simple Shepp-Logan phantom of size  $256 \times 256 \times 256$  and a complex 3D trabecular bone volume of size  $627 \times 32 \times 627$  reconstructed with the FDK algorithm. The binary volumes were obtained by a simple thresholding method. These binary volumes are denoted  $f^*$  and considered as the ground-truth volumes. In order to obtain the best reconstruction results, the choice of the best regularization parameters is also based on the Morozov discrepancy principle [Morozov (1984)], satisfying  $\|Rf - p^\delta\| \approx \delta$ , where  $\delta$  was estimated as  $\delta = \sqrt{MN_r}\sigma_p$ . The iterations were stopped when the regularization functional stagnates. The final index  $m$  is determined by the stopping condition satisfying  $\|f^{m+1} - f^m\|/\|f^m\|_2 < 0.0001$ .

## Numerical results

In this section, we present the reconstruction results for the Shepp-Logan phantom and the real trabecular volume obtained with TV regularization with a box constraint method (TVbox). For the real trabecular volume, we have also tested the TV method without any box constraint.

### Shepp-Logan phantom

**Geometry configuration** For the geometry configuration of the CBCT system, the distance from the X-ray source to the detector (SDD) is 1536 mm, the distance from the X-ray source to the center of the object (SID) is 1000 mm. The simple Shepp-Logan phantom was reconstructed from a simulated projection data of size  $256 \times 256 \times 180$  at a voxel size of  $2 \times 2 \times 2$  mm and its origin is located at  $(-255, -255, -255)$  mm. The convex set for TVbox chosen is  $[0, 1]$  and the threshold for segmentation was set at 0.5 simply.

**Reconstruction results** The ground-truth volume  $f^*$  is displayed in Fig.6.6. For this simple phantom, the TVbox method was tested for  $M = 10$ ,  $M = 15$  and  $M = 20$  noisy projections (CBCT),  $N_r = 256 \times 256$  rays per projection angle, with a Gaussian noise added to the projection. The noise distribution is characterized by the standard deviation of the noise  $\sigma_p = 6, 11, 23$  and the corresponding peak to peak signal to noise ratio  $PPSNR = 13.6dB, 9.5dB, 5.25dB$  (defined in Eq.4.33). The noise level is still estimated as  $\delta = \sqrt{MN_r}\sigma_p$ . For instance, the reconstruction results obtained with  $M = 20$  projections are displayed in Fig.6.7, Fig.6.8 and Fig.6.9 for  $\sigma_p = 6$ ,  $\sigma_p = 11$  and  $\sigma_p = 23$  respectively. We can see that with the increase of noise levels, the reconstruction results become worse and the reconstruction errors are located inside and outside the surfaces of the ellipsoids of the Shepp-Logan phantom.

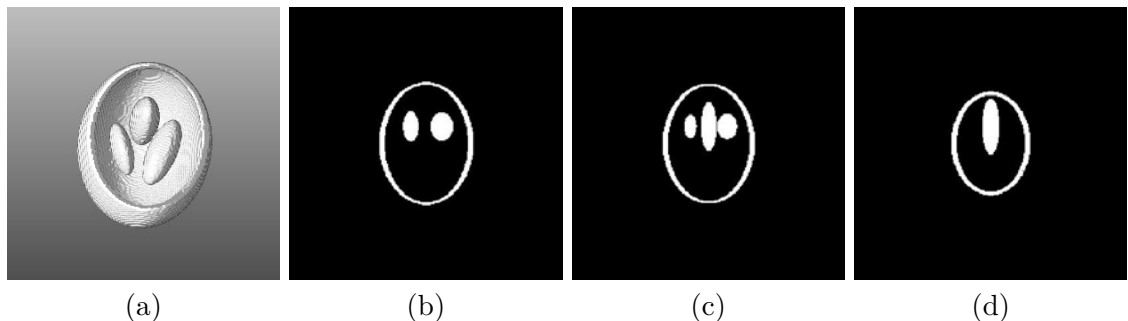


Figure 6.6: Binary reconstructed 3D Shepp-Logan volume of size  $256 \times 256 \times 256$  from 400 projections with the FDK algorithm and slices with the same viewpoint: (a) 3D display of Binary reconstructed Shepp-Logan volume; (b) The 130th slice; (c) The 140th slice; (d) The 160th slice.

The evolution curves of data term  $\|Rf^k - p^\delta\|$ , misclassification rate  $MR(k)$  and the reconstruction error  $\|f - f^*\|/\|f^*\|$  with the iteration number  $k$  for the Shepp-Logan

phantom with different noise levels are shown in Fig.6.10, Fig.6.11 and Fig.6.12. Table.6.1 summarizes the minimum error  $E_m$  and corresponding misclassification rate  $MR_m$  for the Shepp-Logan phantom with all noise levels and projection numbers obtained with the TVbox method.

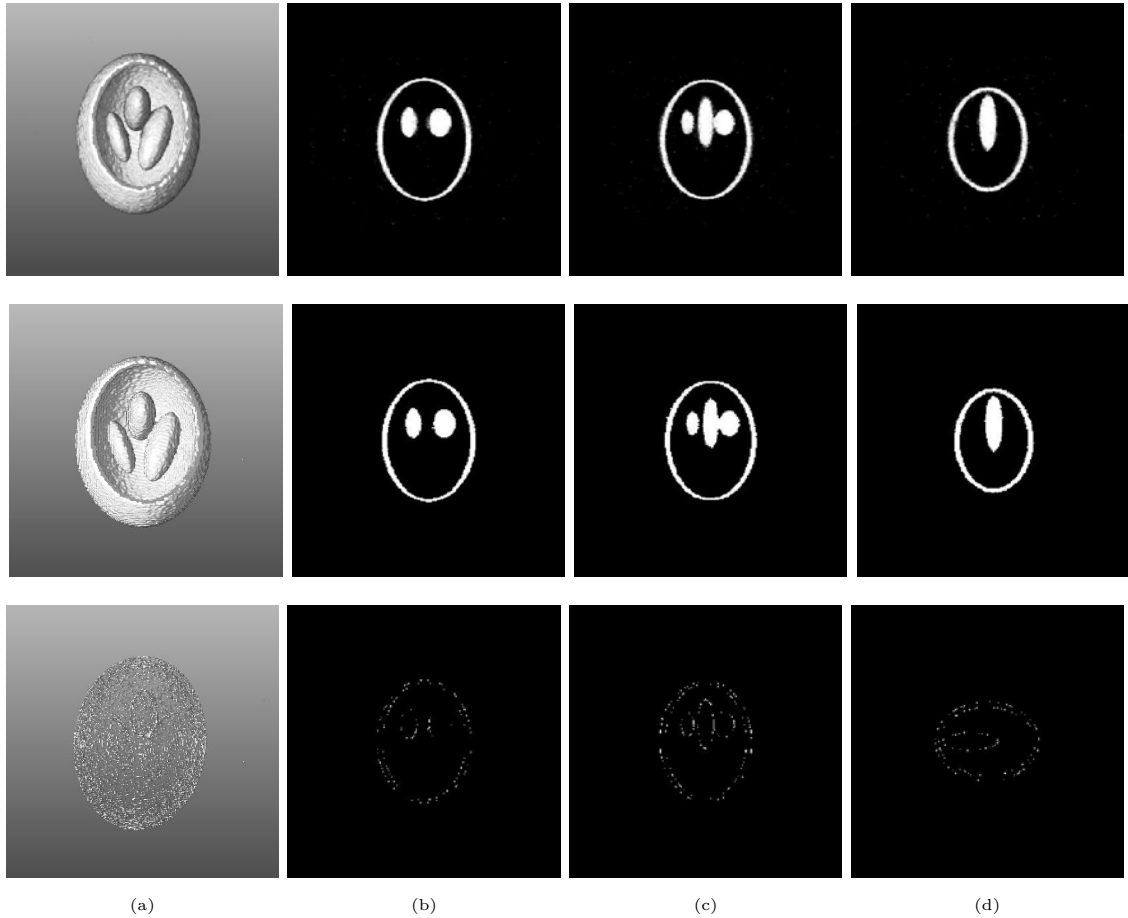


Figure 6.7: Grey-level (top) and binary (middle) reconstructed volumes of Shepp-Logan phantom and difference maps (bottom) from 20 noisy projections ( $\sigma_p = 6, PPSNR = 13.6\text{dB}$ ) with TV regularization with a box constraint method and then thresholded by 0.5. (a) 3D display of volumes;(b) The 130th slice; (c) The 140th slice; (d) The 160th slice.

The regularization parameter  $\mu$  was chosen according to the Morozov principle. There are clear correlations between the decrease of the discrepancy term  $\|Rf - p^\delta\|$  and the decreases of the misclassification rate  $MR$  and of the reconstruction errors  $\|f - f^*\|/\|f^*\|$ . In conclusion, with the increase of projection number and the decrease of the noise level, a better reconstruction result was obtained. There is only one exception: the misclassification rate for  $M = 15, \sigma_p = 11$ . It is always higher than the one obtained for  $M = 10$  projections with the same noise level though it also decreases with the iteration number  $k$ . The reason may lies in that we just chose 0.5 simply as a our threshold and this threshold is not suitable for this case. In the future, a more precise threshold parameter will be

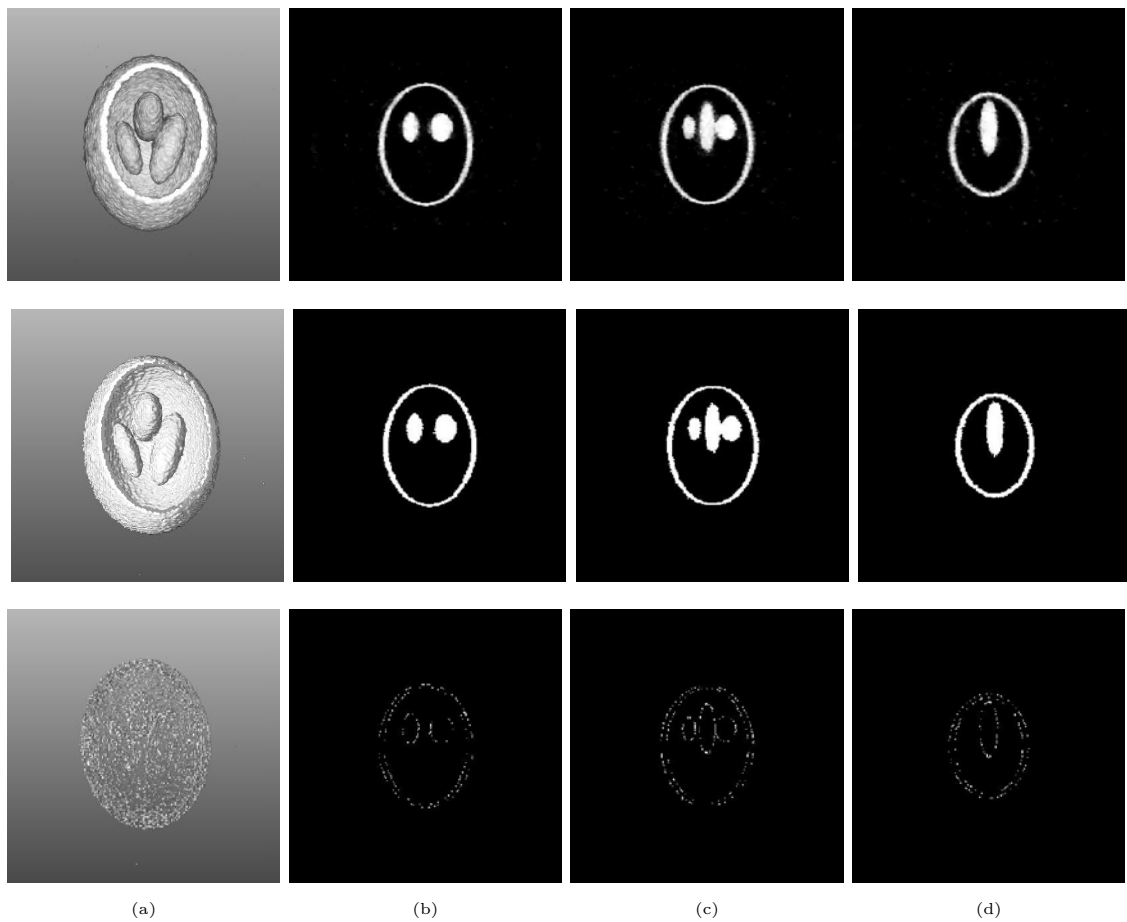


Figure 6.8: Grey-level (top) and binary (middle) reconstructed volumes of Shepp-Logan phantom and difference maps (bottom) from 20 noisy projections ( $\sigma_p = 11$ ,  $PPSNR = 9.5\text{dB}$ ) with TV regularization with a box constraint method and then thresholded by 0.5. (a) 3D display of volumes; (b) The 130th slice; (c) The 140th slice; (d) The 160th slice.

Table 6.1: Numerical error  $E_m$  and misclassification rate  $MR_m$  obtained with TV regularization with a box constraint method for different noise standard deviation  $\sigma_p$ , and  $PPSNR$  values for Shepp-Logan phantom.

	<b>M=10</b>	<b>M=15</b>	<b>M=20</b>
$\sigma_p=6$ , $PPSNR = 13.6 \text{ dB}$	$E_m=0.4570$ , $MR_m = 0.21 \%$	$E_m=0.3851$ , $MR_m = 0.12 \%$	$E_m=0.2796$ , $MR_m = 0.08 \%$
$\sigma_p=11$ , $PPSNR = 9.5 \text{ dB}$	$E_m=0.4226$ , $MR_m = 0.20 \%$	$E_m=0.4675$ , $MR_m = 0.19 \%$	$E_m=0.3423$ , $MR_m = 0.11 \%$
$\sigma_p=23$ , $PPSNR = 5.25 \text{ dB}$	$E_m=0.7160$ , $MR_m = 0.84 \%$	$E_m=0.6960$ , $MR_m = 0.78 \%$	$E_m=0.6099$ , $MR_m = 0.60 \%$

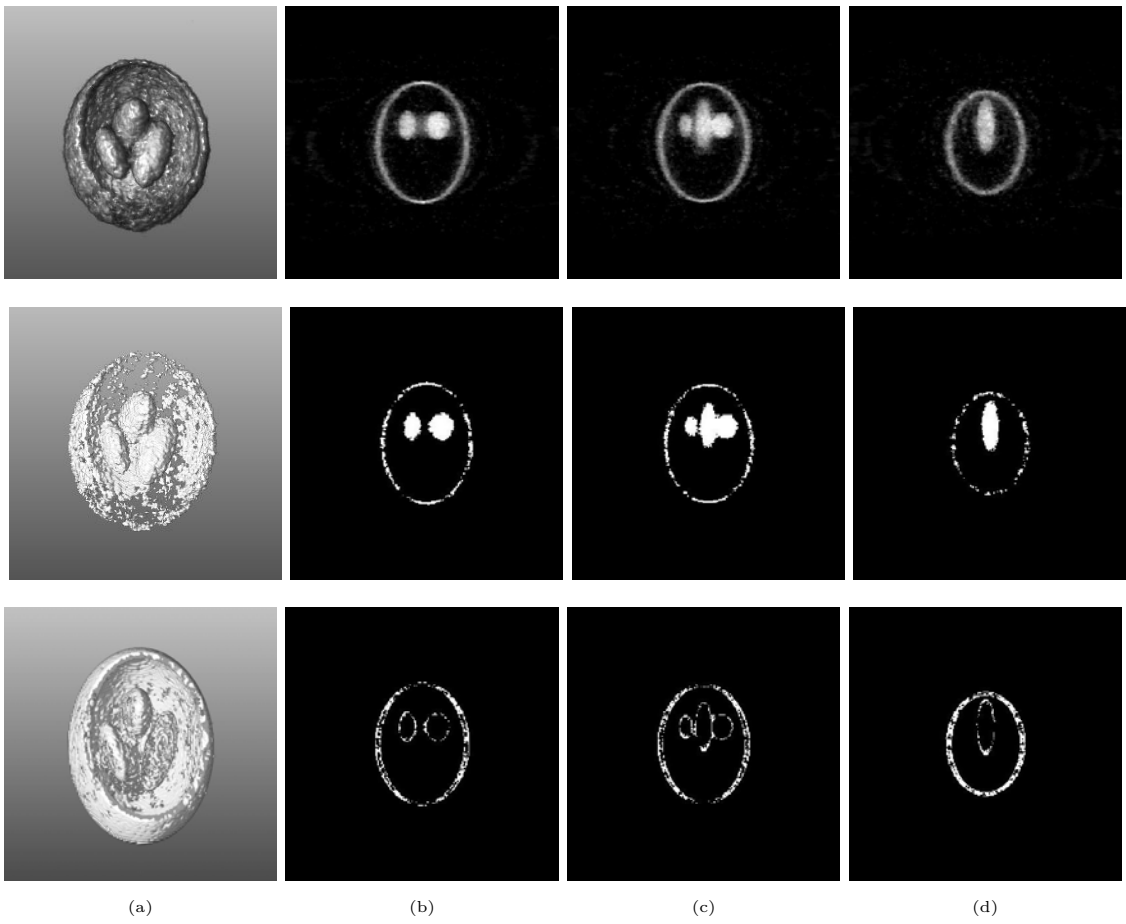


Figure 6.9: Grey-level (top) and binary (middle) reconstructed volumes of Shepp-Logan phantom and difference maps (bottom) from 20 noisy projections ( $\sigma_p = 23$ ,  $PPSNR = 5.25\text{dB}$ ) with TV regularization with a box constraint method and then thresholded by 0.5. (a) 3D display of volumes; (b) The 130th slice; (c) The 140th slice; (d) The 160th slice.

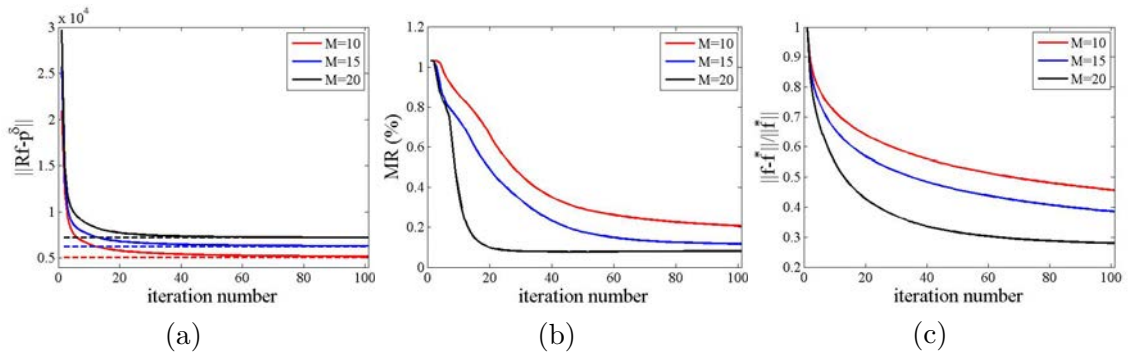


Figure 6.10: Evolution curves of data term, misclassification rate and the reconstruction error with the iteration number for Shepp-Logan phantom with  $\sigma_p = 6$  and  $PPSNR = 13.6\text{dB}$ . (a)  $\|Rf - p^\delta\|$ ; (b)  $MR$ ; (c)  $\|f - f^*\|/\|f^*\|$ .

investigated.

Because of the simple structures of the Shepp-Logan phantom, we can find that the

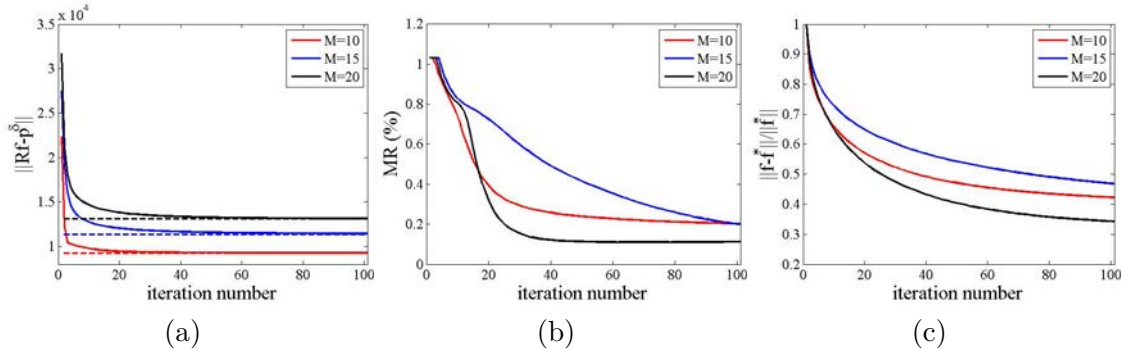


Figure 6.11: Evolution curves of data term, misclassification rate and the reconstruction error with the iteration number for Shepp-Logan phantom with  $\sigma_p = 11$  and  $PPSNR = 9.5$ dB. (b)  $\|Rf - p^\delta\|$ ; (c)  $MR$ ; (d)  $\|f - f^*\|/\|f^*\|$ .

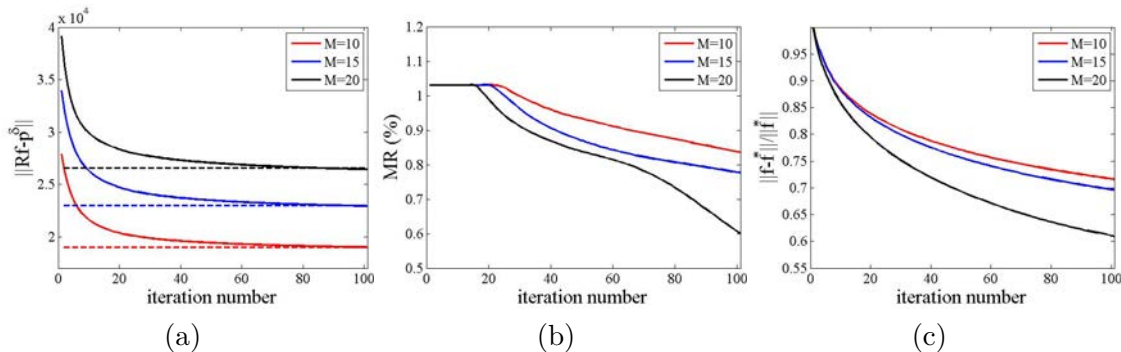


Figure 6.12: Evolution curves of data term, misclassification rate and the reconstruction error with the iteration number for Shepp-Logan phantom with  $\sigma_p = 23$  and  $PPSNR = 5.25$ dB. (b)  $\|Rf - p^\delta\|$ ; (c)  $MR$ ; (d)  $\|f - f^*\|/\|f^*\|$ .

TVbox method performs efficiently and it is able to reconstruct many details and structures from a very limited number of projections when the noise is low such as with  $\sigma_p = 6$ . When the noise level is high, there are a lot of reconstruction errors located inside and outside the surfaces of the ellipsoids. Similarly to the 2D cases, local minima were obtained, a global optimization method is needed to improve this reconstruction results. In the future, we will extend the stochastic optimization methods to 3D cases.

**Real trabecular bone volume** The TVbox algorithm was also applied on this 3D trabecular bone volume with complex microstructures to verify the efficiency of this method on RTK. Moreover, TV algorithm was also applied for comparison. The results are presented in this section.

**Geometry configuration** For the geometry configuration of the CBCT system, the distance from the X-ray source to the detector (SDD) is 100.01 m, the distance from the X-ray source to the center of the object (SID) is 100 m, the offset of the X-ray source in the  $x$  direction is -0.74m. The original bone projection data were obtained from SR micro-CT

at the ESRF and yields an original reconstructed volume made of  $1974 \times 1974 \times 1100$  voxels. To reduce the data set, the projections were cropped and subsampled to  $627 \times 32$ . The process is shown in Fig.6.13. A final volume of  $627 \times 627$  voxels at  $15 \mu\text{m}$  was reconstructed from the projections. Its origin is set at  $(-0.47, -0.47, 0.39)$  cm along the  $(x, y, z)$  directions to make the origin of the coordinate system located at the center of the reconstructed trabecular volume.

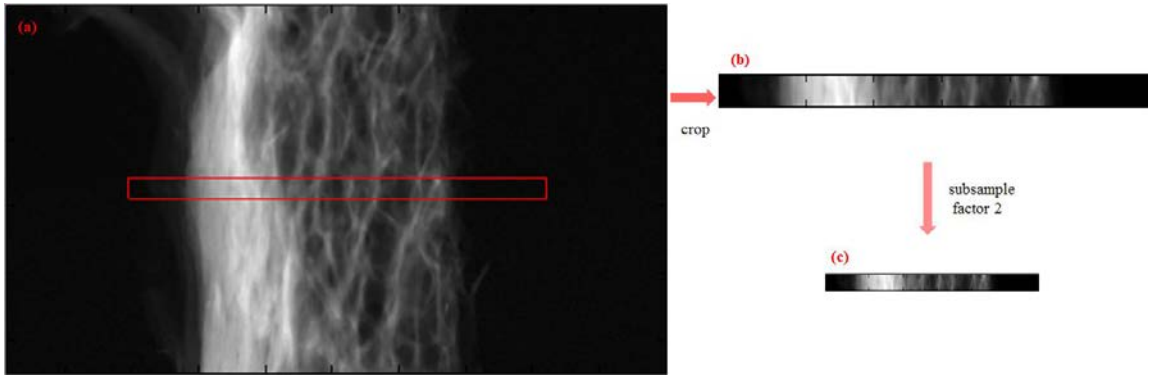


Figure 6.13: (a,b) A slice of the 3D projection sinogram of size  $1974 \times 1100$  obtained from SR micro-CT at the ESRF and a cropped slice of size  $1254 \times 64$ . (c) The original bone projection was obtained with a sample factor 2.

A grey-level trabecular volume was reconstructed from the real experimental projection data with 3000 projection angles with the FDK algorithm. The minimum voxel value of the grey-level reconstructed trabecular volume is  $0/\mu\text{m}^3$ , and the maximum voxel value is  $0.0003/\mu\text{m}^3$ , therefore, the convex set for TVbox chosen was  $[0, 0.0003]$ . And the threshold for segmentation was calculated with the basic global threshold method.

**Reconstruction results** This grey-level trabecular image was binarized with a threshold 0.00012 obtained with the global threshold method. The binary trabecular volume considered as the ground-truth was denoted  $f^*$  and is displayed in Fig.6.14.

For this complex volume, the TVbox and TV methods were tested for  $M = 200$  and  $M = 600$  noisy projections (CBCT),  $N_r = 627 \times 32$  rays per projection angle. The reconstruction results for TVbox algorithm are displayed in Fig.6.16 and Fig.6.17. The reconstructed volumes for TV algorithm are displayed in Fig.6.18 and Fig.6.19.

The evolution curves of data term  $\|Rf^k - p^\delta\|$  with the iteration number  $k$  for the real trabecular volume with different projection numbers are shown in Fig.6.15. The regularization parameters were chosen to obtain the best decrease of the regularization functional. For TVbox method, the iteration was stopped when the iterates stagnates  $\frac{\|f^{k+1} - f^k\|}{\|f^k\|} < 0.01$ . For the TV method, it is really difficult to find a good regularization parameter to make the data term reach a stable point after some iterations. The iterations were stopped when the minimum  $\|Rf^k - p\|^2$  was achieved. And the evolution curves of data term for TV method are well above the ones for TVbox method under the same conditions.

At the end of both TVbox and TV reconstruction processes, we have discarded the first and last slices (slice 1 and slice 32) of the final reconstructed volume with the two TV methods. Because we have discovered that the voxel values are extremely high or low compared to the other reconstructed slices. The reason may be that the two slices are located on the boundaries of trabecular volume, and some unknown border artefacts are present. What's more, for TV method, the third slice is singular sometimes. May be a box constraint can in TVbox method can prevent this case more or less.

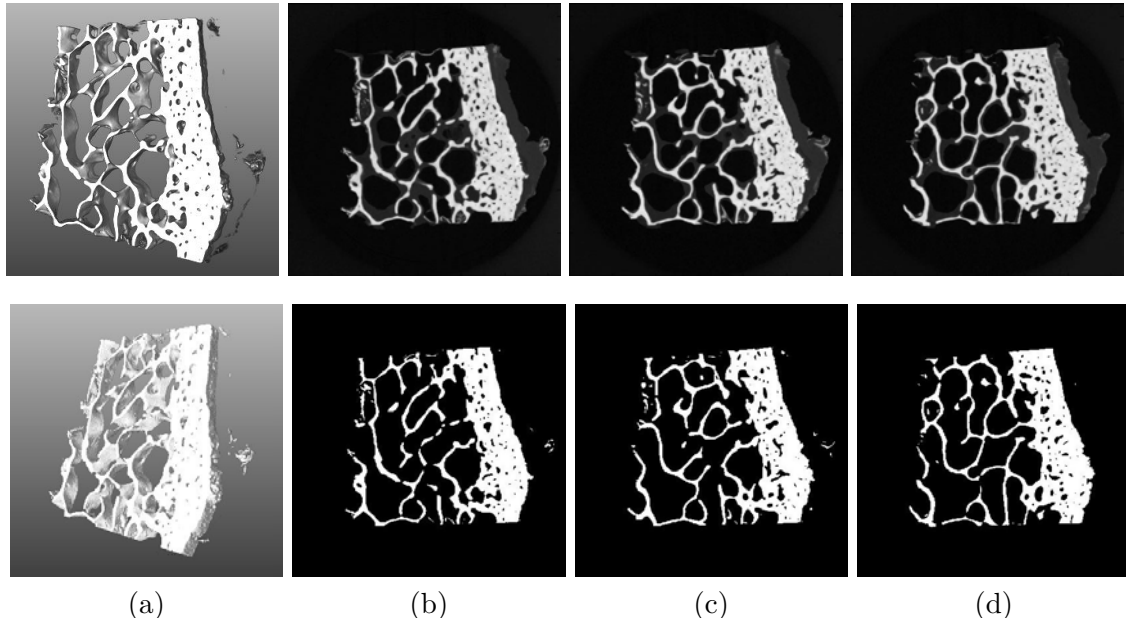


Figure 6.14: Grey-level and binary reconstructed real 3D trabecular bone volume of  $627 \times 627 \times 32$  voxels at  $15 \mu\text{m}$  from 3000 projections with the FDK algorithm. The global threshold  $TH = 0.00012$ . (a) 3D display of volumes; (b) The 3rd slice; (c) The 15th slice; (d) The 31st slice.

For both TVbox and TV methods, we can see with the decrease of noise level, the reconstruction results become better and the reconstruction errors are located inside and outside the surfaces of the trabecular of the real volume. The reconstruction results discussed in Chapter.4 have shown that the TVbox method gives the best reconstruction results in most cases, especially for large bone cross-section images. It is not the case for the trabecular volume investigated here. The misclassification rates obtained with the TV method are lower for 200 and 600 projections even if a higher value of the discrepancy term is obtained.

We have assumed that the reason may be a bad choice of convex set. We have made some tests with a larger convex set  $(0, 0.0005)$  for the TVbox method, but we found this convex set only has some effects on the first and last slices which are located in the boundaries of the trabecular bone volume. More researches are needed to make some improvements. With the TVbox method, the small lacunae present in the right part of the image have disappeared after binarization, especially when the projection number

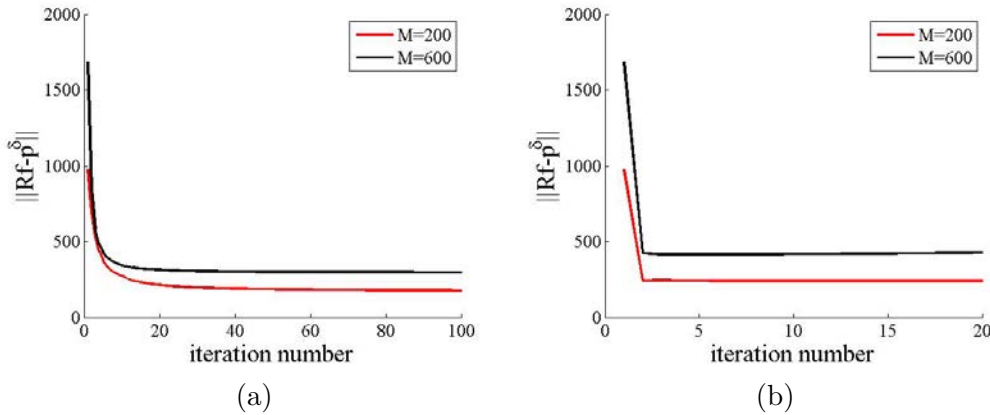


Figure 6.15: Evolution curves of data term with the iteration number for real 3D trabecular bone volume with 200 and 600 projections for TVbox and TV methods. (a)TVbox method; (b)TV method.

is low such as with  $M = 200$ . With the TV method, there are many artifacts outside the trabecular bone volume in the grey-level reconstructed images. And global threshold method seems a good way to remove these artifacts in binarization processes and a low misclassification rate is obtained after binarization.

In conclusion, it has been proved that both TVbox and TV methods are effective ways to reconstruct 3D volumes with a limited number of projections. Yet, the reconstruction results are still not very satisfactory. The data term discrepancy is still above the noise level (0). The reason may lies in the fact that there is inherently some noise due the physics of acquisition of the real projection data which will lead to a up-shift of the noise level of the projection data. Therefore, the choice of the regularization parameters is perhaps not very accurate.

In the future, we will consider four aspects to improve the reconstruction results. First, we should make some corrections to remove the noise inside the raw projection due the physics of acquisition. Secondly, we should find the reasons why that leads to a worse reconstruction for TVbox method to improve this algorithm. Thirdly, we should find a better segmentation method for binarization, only a global threshold is not a good choice. Moreover, there are a lot of reconstruction errors located on the surfaces of the trabecular bone to improve. Similarly to what we have done for the 2D images, local minima were obtained, a global optimization method maybe needed to improve the reconstruction results. We will extend the stochastic optimization methods to 3D volumes.

## 6.4 Conclusion

In this chapter, the topic is binary reconstruction of bone microstructure from a limited number of projections with TVbox algorithm on 3D images. TVbox algorithm was applied on a simple Shepp-Logan phantom of size  $256 \times 256 \times 256$  at a voxel size of 2

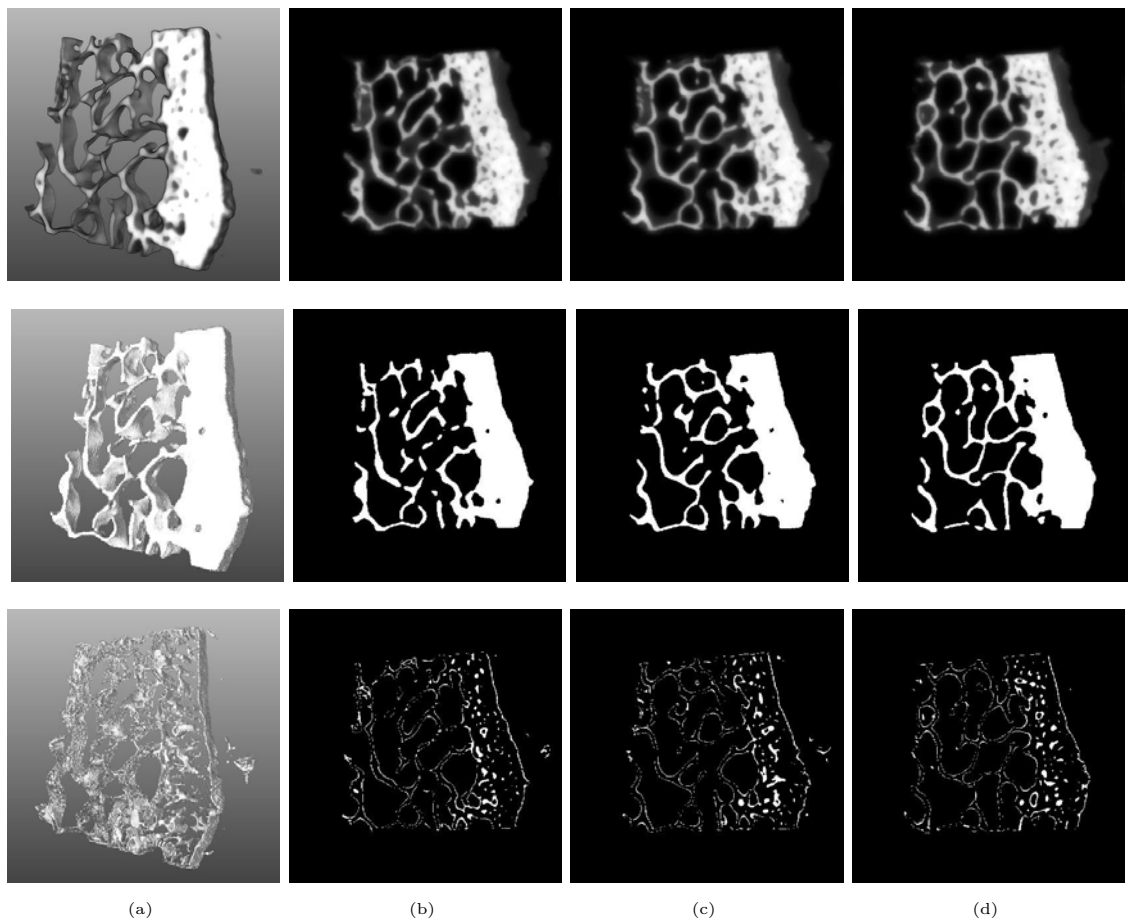


Figure 6.16: Grey-level (top) and binary (middle) reconstructed volumes of real 3D trabecular bone microstructures and difference maps (bottom) from 200 projections with TVbox method and then thresholded by 0.0001. (Slice 1 and 32 were discarded),  $E_m = 0.2713$ ,  $MR = 2.43\%$ . (a) 3D display of volumes; (b) The 3rd slice; (c) The 15th slice; (d) The 31st slice.

mm and a complex real 3D trabecular volume of size  $627 \times 627 \times 32$  at a voxel size of  $15 \mu\text{m}$ . Similarly to the reconstruction on 2D images with TVbox algorithm, the optimal solutions are obtained with the ADMM algorithm. The whole reconstruction processes were implemented on RTK.

For the Shepp-Logan phantom, the TVbox method was tested for  $M = 10$ ,  $M = 15$  and  $M = 20$  equally spaced noisy simulated projections,  $N_r = 256 \times 256$  X-rays per projection angle, with a Gaussian noise added to the projection. The noise distribution is characterized by the standard deviation of the noise  $\sigma_p = 6, 11, 23$  and the corresponding peak to peak signal to noise ratio  $PPSNR = 13.6dB, 9.5dB, 5.25dB$ . For the real 3D trabecular volume, the TVbox method was tested for  $M = 200$  and  $M = 600$  noisy projections and  $N_r = 627 \times 32$ , which are sub-selected from a real experimental projection data,  $N_r = 627 \times 32$  X-rays per projection angle. And the TV method was also applied to the same trabecular bone volume for comparison.

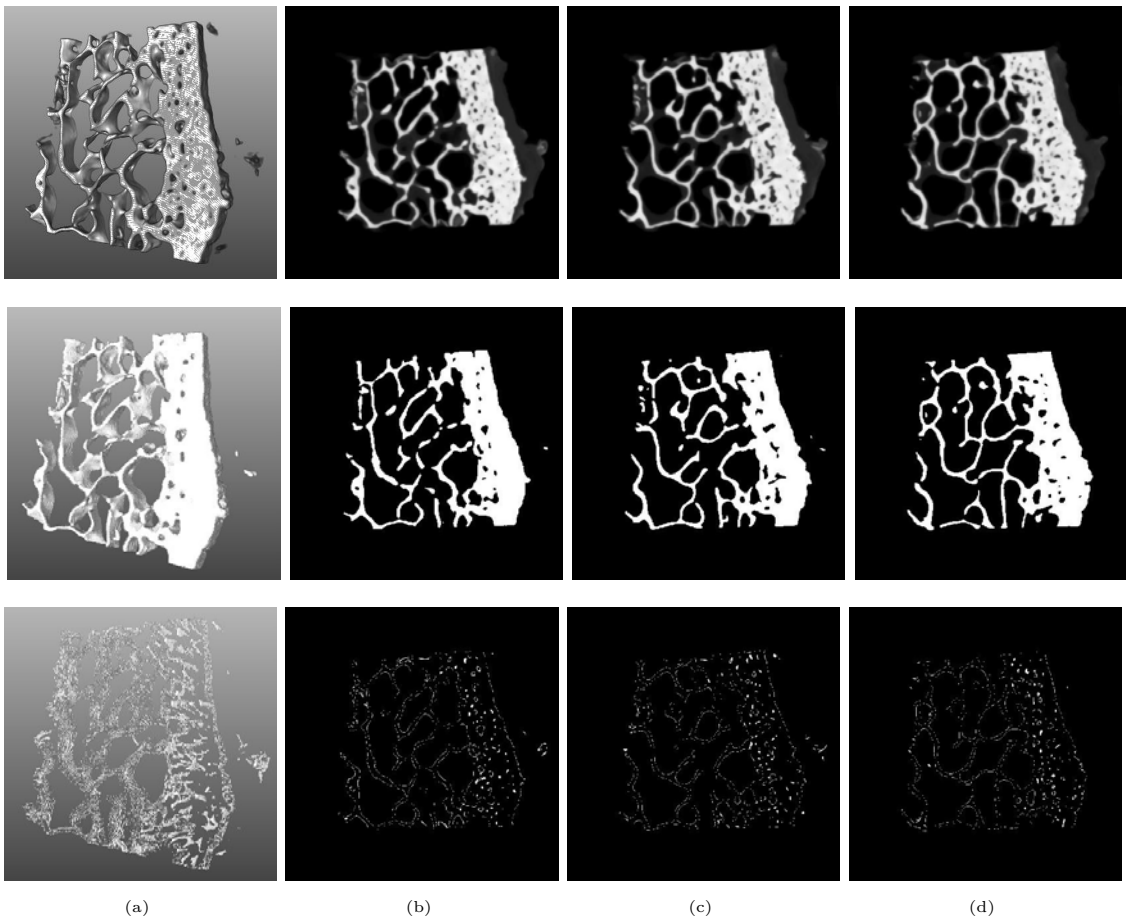


Figure 6.17: Grey-level (top) and binary (middle) reconstructed volumes of real 3D trabecular bone microstructures and difference maps (bottom) from 600 projections with TVbox method and then thresholded by 0.0001. (Slice 1 and 32 were discarded),  $E_m=0.1322$ ,  $MR = 1.08\%$ . (a) 3D display of volumes; (b) The 3rd slice; (c) The 15th slice; (d) The 31st slice.

In conclusion, there are clear correlations between the decrease of the discrepancy term  $\|Rf - p^\delta\|$  and the decreases of the misclassification rate  $MR$  and the reconstruction errors  $\|f - f^*\|/\|f^*\|$  for the simple Shepp-Logan phantom. It was proved once again that TV regularization algorithm is really good at keeping the edge informations for an simple structure approximating a sphere. While the situation is much more complex for the real trabecular volume. The regularization parameters were chosen carefully with Morozov discrepancy term. With the decrease of number of projections or the increase of noise level on the raw projection data, the decrease of the misclassification rate  $MR$  and of the reconstruction errors are located inside and outside the surfaces of reconstructed volumes. In contrast with the former results, the TV method outperforms the TV regularization method with box constraints for the 3D trabecular bone volume. Further studies are necessary to understand the role of the different parameters for the reconstruction results. And a global optimization is necessary to improve these bad reconstructed volumes. In

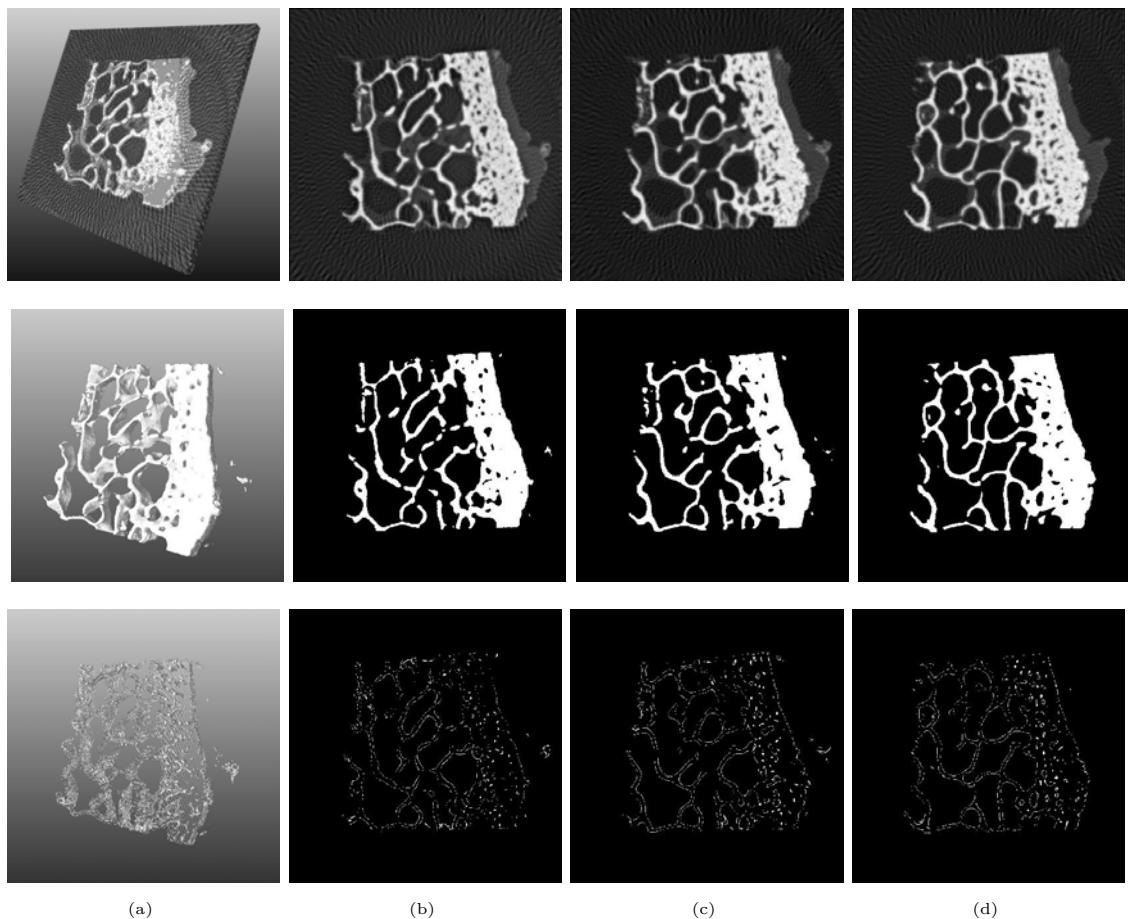


Figure 6.18: Grey-level (top) and binary (middle) reconstructed volumes of real 3D trabecular bone microstructures and difference maps (bottom) from 200 projections with TV regularization method and then thresholded by 0.0001. (Slice 1,2 and 32 were discarded),  $E_m=0.1538$ ,  $MR = 1.35\%$ . (a) 3D display of volumes; (b) The 3rd slice; (c) The 15th slice; (d) The 31st slice.

the future, we will try to extend the stochastic diffusion global optimization method to 3D images for an improvement.

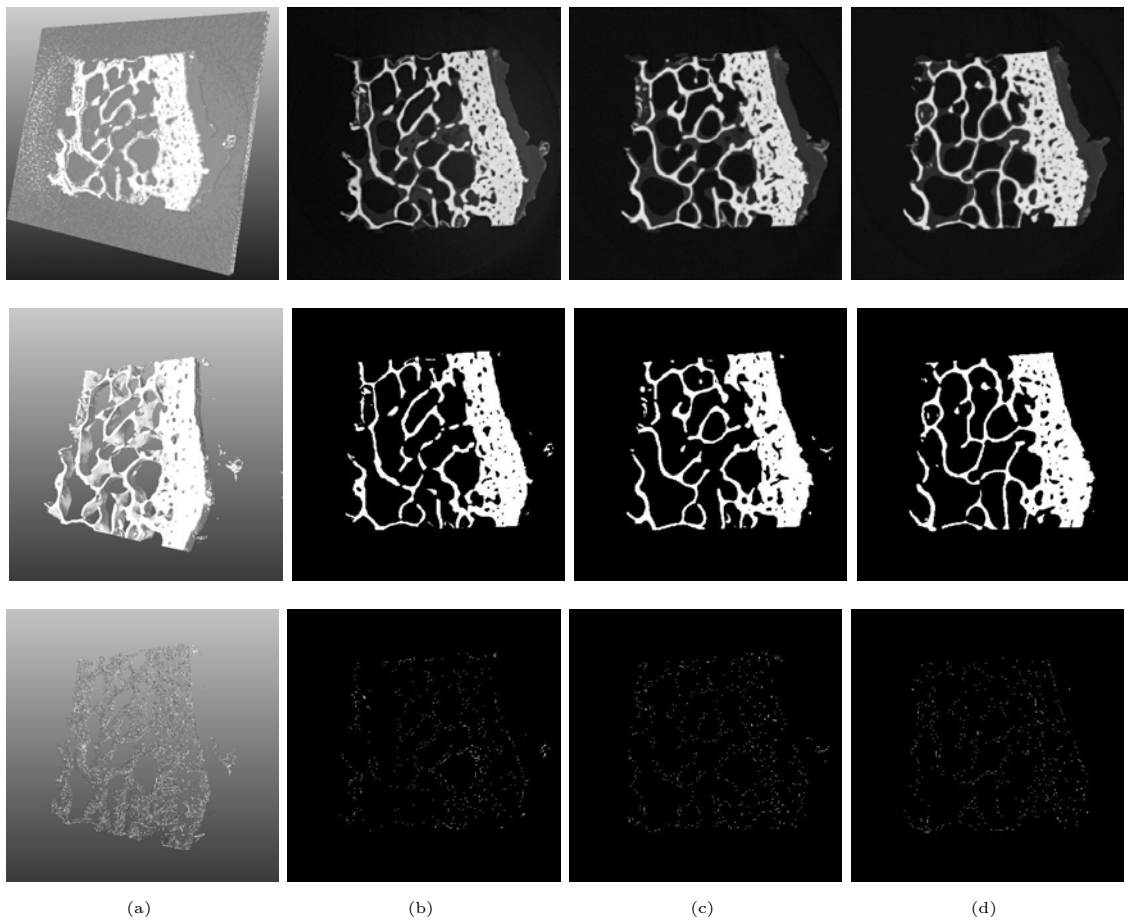


Figure 6.19: Grey-level (top) and binary (middle) reconstructed volumes of real 3D trabecular bone microstructures and difference maps (bottom) from 600 projections with TV regularization method and then thresholded by 0.0001. (Slice 1,2 and 32 were discarded),  $E_m=0.0791$ ,  $MR = 0.63\%$ . (a) 3D display of volumes; (b) The 3rd slice; (c) The 15th slice; (d) The 31st slice.



# Chapter 7

---

## Multi-level Reconstruction from a Limited Number of Projections

---

### 7.1 Introduction

Usually, the discrete tomographic reconstruction problem is considered for binary case. Many attempts can be found in the literature to solve the binary problem based on algebraic methods [Batenburg and Sijbers (2009), Cai and Ma (2010)], convex analysis [Capricelli and Combettes (2007), Schüle *et al.* (2005)a, Sixou and Peyrin (2012)], Markov random fields [Liao and Herman (2004)], TV regularization [Wang *et al.* (2016)] and so on. The binary tomography reconstruction results from a few views of projections with TV and level-set regularization methods and then the refinement of these reconstructed images with stochastic approaches have been presented in previous chapters.

Yet, there are few studies of multi-level tomographic reconstruction problems for the representation of more details inside the reconstructed images. In this chapter, we consider the reconstruction of an image with more than two grey levels. Firstly, we extend the level-set approach used for binary case to multi-level reconstruction. The discrete tomographic problem is formulated as a shape optimization problem with several level-set functions and regularized with Total-Variation-Sobolev terms. In the implementation, the grey-level reconstructed image was projected to a discrete reconstructed image by thresholding after a fixed time interval and the discrete reconstructed image was used in a signed distance function to reinitialize the level-set functions for the next level-set iteration. Then, the reconstruction results obtained with the new proposed level-set approach were compared

with the ones obtained with TV ADMM regularization method (explained in section 4.2). The simulations were applied on the simple Shepp-Logan phantom of size  $128 \times 128$  with several number of projections and two additive Gaussian noises on the raw projection data.

This chapter is structured as follows. A brief introduction is given in this first section. The nonlinear level-set formulation of the multi-level tomography is summarized in the second part. The numerical details and results are presented and discussed at the end of this chapter.

## 7.2 Level-set Regularization for Multi-level Tomography

### 7.2.1 New level-set regularization formulation

The new level-set method for multi-level tomography is based on the level-set formulation of the binary tomography in Section 4.3.1. For a bounded Lipschitz open subset  $\Omega \subset \mathbb{R}^2$ , we assume that the function to be reconstructed  $f$  can take different values ( $f_i$ ) on regular sets  $\Omega_i \subset \Omega$ , and the function  $f$  can thus be written  $f = \sum_i \chi_{\Omega_i}$ . In the following, for the sake of simplicity, we consider in this work only the case of three levels for the function (Fig. 7.1),  $f_1$ ,  $f_2$  and  $f_3$ . We suppose that the image  $f$  to be reconstructed can be represented with two level-set functions  $\theta_1$  and  $\theta_2$ :

$$f = f_1(1 - H(\theta_1))(1 - H(\theta_2)) + f_2H(\theta_1)H(\theta_2) + f_3H(\theta_2)(1 - H(\theta_1)) \quad (7.1)$$

where the two level-set functions  $\theta_1$  and  $\theta_2$  belongs to the first-order Sobolev space  $H_1(\Omega)$ .

With respect to  $\theta_1$  and  $\theta_2$ , the reconstruction problem becomes nonlinear and the Heaviside distribution function  $H(\theta)$  with the level-set functions  $\theta_1, \theta_2 \in H_1(\Omega)$  is equal 1 if  $\theta > 0$  and 0 otherwise. Similarly to the level-set method for binary tomography,  $H(\theta)$  is discontinuous, we should consider replacing the minimizers of the regularization functional [Egger and Leitao (2009), DeCezaro *et al.* (2009)] by the ones of a smoothed approximate regularization functional with a continuous function  $H_\epsilon(\theta)$  defined in Eq. 4.16. The regularization functional in Eq. 4.17 to be minimized can then be written as:

$$E(\theta_1, \theta_2) = \frac{\|RH(\theta_1, \theta_2) - p^\delta\|_2^2}{2} + \alpha(F(\theta_1) + F(\theta_2)) \quad (7.2)$$

where  $F$  is a regularization term for the level-set functions. In this work, we also considered a Total Variation- $H_1$  regularization functional [Egger and Leitao (2009), DeCezaro *et al.* (2009)] for each level-set function:

$$F(\theta) = \beta_1 \int |\nabla H(\theta)| dx + \beta_2 \|\theta\|_{H_1}^2 \quad (7.3)$$

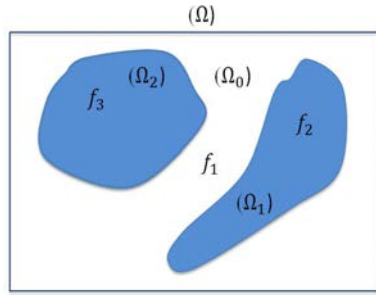


Figure 7.1: The sketch of  $f$  on  $\Omega$ .

The regularization parameters  $\beta_1, \beta_2$  determines the relative weights of the stabilizing terms. For the sake of simplicity, they were taken equal for the two level-set functions  $\theta_1$  and  $\theta_2$ .

### 7.2.2 Implementation of the level-set regularization approach

In the numerical implementation, it is necessary to replace to Heaviside function  $H$  and the Dirac function  $\delta$  by smoothed approximations. The following smooth approximations of the Heaviside function  $H$  was also used for multi-level tomography:

$$H_\epsilon(x) = \frac{1+2\epsilon}{2}(\operatorname{erf}(x/\epsilon) + 1) - \epsilon \quad (7.4)$$

where  $\epsilon$  is a real positive constant. The smoothing parameters  $\epsilon_1, \epsilon_2$  for  $\theta_1, \theta_2$  are given the same values in this work. Then the smoothed Tikhonov regularization functional is then given by:

$$E_\epsilon(\theta) = \frac{\|Rf(\theta_1, \theta_2) - p^\delta\|_2^2}{2} + \beta_1|H_\epsilon(\theta_1)|_{TV} + \beta_2\|\theta_1\|_{H_1}^2 + \gamma_1|H_\epsilon(\theta_2)|_{TV} + \gamma_2\|\theta_2\|_{H_1}^2 \quad (7.5)$$

where  $|\cdot|_{TV}$  is the Total Variation semi-norm. The minimizers of the Tikhonov functionals are found with a first-order optimality condition for the two level-set functions for the smoothed functionals,  $\frac{\partial E_\epsilon}{\partial \theta_1} = G_1(\theta_1, \theta_2) = 0$  and similarly  $G_2(\theta_1, \theta_2) = 0$ , with:

$$G_1(\theta_1, \theta_2) = \frac{\partial f}{\partial \theta_1} R^*(Rf(\theta_1, \theta_2) - p^\delta) + \beta_2(I - \Delta)(\theta_1) + \beta_1 \frac{\partial |H_\epsilon(\theta_1)|_{TV}}{\partial \theta_1} \quad (7.6)$$

where  $R^*$  denotes the adjoint of the forward projection operator. The derivatives of  $f$  with respect to  $\theta_1$  and  $\theta_2$  can be written:

$$\begin{aligned} \frac{\partial f}{\partial \theta_1} &= (f_2 - f_3)H(\theta_2)H'(\theta_1) - f_1H'(\theta_1)(1 - H(\theta_2)) \\ \frac{\partial f}{\partial \theta_2} &= f_2H'(\theta_2)H(\theta_1) + f_3H'(\theta_2)(1 - H(\theta_1)) - f_1(1 - H(\theta_1))H'(\theta_2) \end{aligned} \quad (7.7)$$

where the derivative  $H'$  is evaluated on the smoothed approximation of the Heaviside function  $H_\epsilon$ . The differential of the  $|H_\epsilon(\theta_1)|_{TV}$  is given by:

$$\frac{\partial |H_\epsilon(\theta_1)|_{TV}}{\partial \theta_1} = -\delta(\theta_1^k) \frac{\nabla \theta_1}{|\nabla \theta_1|} \quad (7.8)$$

From the current estimate  $\theta_1^k$ , the update  $\theta_1^{k+1} = \theta_1^k + \delta\theta$  is obtained with a classical Gauss-Newton method with a linearization of the condition  $G_1(\theta_1^k + \delta\theta) = 0$  [Sixou et al. (2013)].

$$V_k^* V_k \delta\theta + \beta_2(I - \Delta)(\delta\theta) - \beta_1 \delta(\theta_1^k) \nabla \cdot \frac{\nabla \delta\theta}{|\nabla \theta_1^k|} = -G(\theta_1^k) \quad (7.9)$$

where  $V_k$  is the operator  $V_k = R \frac{\partial f}{\partial \theta_1}(\theta_1^k)$ . And the same formula are implemented for the level-set function  $\theta_2$ . These symmetric linear systems are solved alternatively by a conjugate gradient method.

## 7.3 Simulations and Discussions

In this section, we present the simulation details and the results obtained with the TV regularization and proposed level-set methods.

### 7.3.1 Simulation details

The projection operator  $R$  is still taken as the discrete approximation of the Radon transform which is implemented on Matlab Image Toolbox. The TV and proposed level-set methods have been applied on a simple three grey-levels Shepp-Logan phantom displayed in Fig.7.2 of size  $128 \times 128$ , which is reconstructed from  $M = 400$  projections with  $N_r = 185$  X-rays per projection with Filtered Back Projections (FBP) and subsequently thresholded. In our simulation, this image regarded as the "ground-truth" image. This reference image has the values  $f_1 = 0$  (blue region),  $f_1 = 1$  (green region) and  $f_2 = 2$  (red region).

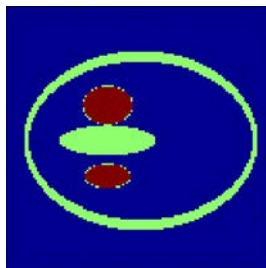


Figure 7.2: Reconstructed image of the bone cross-section of size  $128 \times 128$  from 400 projections with the FDK algorithm, as the "ground-truth" image.

The reconstruction methods were applied to the raw projection data  $p$  with Gaussian noises with various standard deviation  $\sigma_p$ . The noise level  $\delta$  of the noisy projection data  $p^\delta$  is given by  $\delta = \sqrt{MN_r}\sigma_p$ . Two different Gaussian noises have been added to the raw projection data  $p$  with the standard deviations  $\sigma_p = 3$  and  $\sigma_p = 6.5$  corresponding to Peak to Peak Signal to Noise Ratio (PPSNR) (defined in Eq.4.33) of  $18dB$  and  $12dB$ . The TV and level-set regularization methods were tested on a limited number of views,  $M$ , with  $M = 20, 30$  or  $50$ .

In our simulations, the TV ADMM iterations were stopped when the regularization functional stagnates:  $\frac{\|f^{k+1} - f^k\|}{\|f^k\|} \leq 0.01$ . And the TV regularization parameter  $\mu$  was chosen based on Morozov principle [Morozov (1984)] when it satisfies the condition:  $\frac{\|Rf(\mu) - p^\delta\| - \delta}{\delta} \leq 0.1$ , where  $f(\mu)$  is the reconstructed image obtained at the end of TV process with the regularization parameter  $\mu$ . In the proposed level-set method, the best initial level-set functions  $\theta_1$  and  $\theta_2$  were set to zero. As mentioned in section.4.5.1, the level-set

regularization parameters of  $\beta_1$  and  $\gamma_1$  were set to 0 because the  $H_1$  term dominates the TV term [DeCezaro *et al.* (2009), Egger and Leitao (2009)]. In the implementation, the grey-level reconstructed image was projected to  $f = \{0, 1, 2\}$  by thresholding after a fixed time interval  $T_{step}=100$  and the discrete reconstructed image was used in a signed distance function to reinitialize the level-set functions  $\theta_1$  and  $\theta_2$  for the next level-set iteration. The real positive constant  $\epsilon$  controls the scale of the smoothed Dirac function. The regularization parameters  $\beta_2, \gamma_2$  and the real positive constant  $\epsilon$  are chosen to obtain the best decrease of the discrepancy term  $\|Rf^k - p^\delta\|$ . In our simulations, the real positive constant  $\epsilon$  was set as 11 finally. And the image obtained for the value of discrepancy term that nearest to the noise level  $\delta$  is regarded as the best reconstructed image. At the end of reconstruction process, the grey-level reconstructed images were projected on the discrete values  $f = 0, 1, 2$  with the threshold 0.5 and 1.3.

### 7.3.2 Numerical results

The grey-level reconstructed images for  $\sigma_p = 3$  and  $\sigma_p = 6.5$  are displayed in Fig.7.3 and Fig.7.4 respectively. The discrete reconstructed images are displayed in Fig.7.5 and Fig.7.6. The corresponding difference maps are displayed in Fig.7.7 and Fig.7.8. In both cases, the reconstruction errors are located on the boundaries. For the level-set approach, many errors are located on the junction of the regions with different values. And with the increase of the number projection angles, the variances of the values of the gery-level reconstructed images decreased. When the noise level is high  $\sigma_p = 6.5$ , and projection number is low  $M = 20$ , there are a lot of isolated points in the images.

In order to evaluate the quality of reconstruction, we have calculated the evolution of the discrepancy term  $\|Rf^k - p^\delta\|$  and of the missclassification rate  $MR(k)$  as a function of the number of iterations  $k$  for the two reconstruction methods. The evolution curves of the discrepancy term  $\|Rf^k - p^\delta\|$  and the missclassification rate  $MR(k)$  as the function of iterations for  $\sigma_p = 3$  and  $\sigma_p = 6.5$  for level-set approach are displayed in Fig.7.9 and Fig.7.10. We chose the best reconstruction with the minimum value of the discrepancy term. While for TV regularization method, those curves are displayed in Fig.7.11 and Fig.7.12. We chose the best reconstruction according to the Morozov principle.

For comparison, the FBP algorithm has also been tested on the same phantom with the same noise levels and number of projections. The misclassification rates of the final reconstructed images obtained with level-set, TV regularization methods and FBP algorithm are summarized in Table 7.1 for the various noise levels and number of projections. In the most cases, the minimum errors were obtained with the TV regularization method.

The reconstruction results obtained with the TV ADMM algorithm are better than the ones obtained with the level-set method. TV regularization method is well-known to preserve image edges and provide good reconstruction images with sparse view sampling. The level line of the Shepp-Logan phantom is well restored with the TV regularization term which tends to minimize its perimeter. The boundaries of the reconstructed images

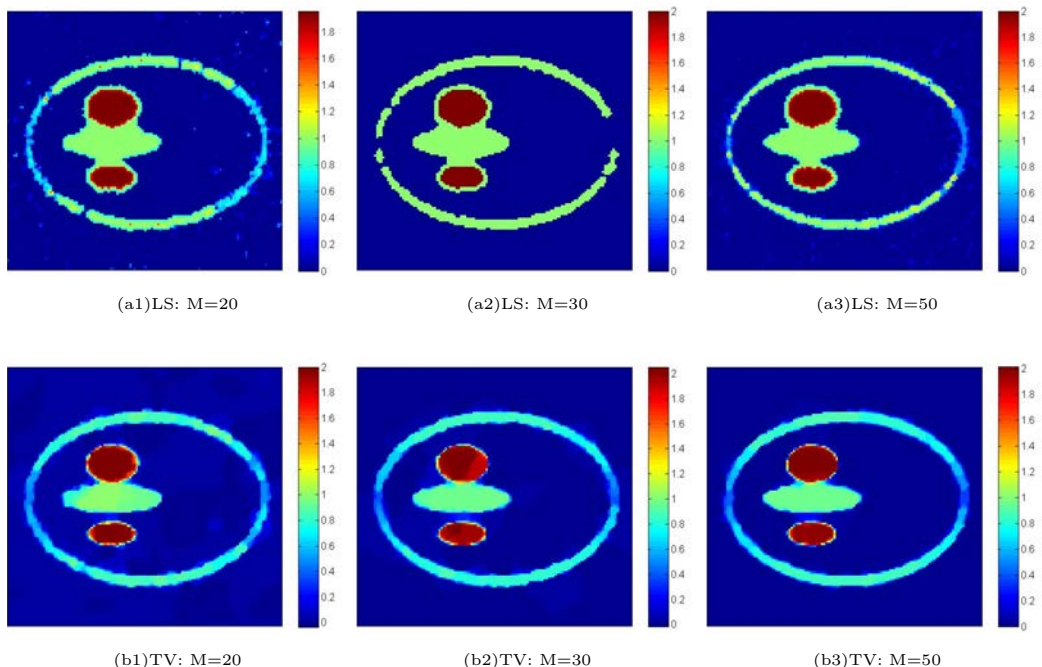


Figure 7.3: Grey-level reconstructed images LS and TV regularization methods with  $\sigma_p = 3$ .

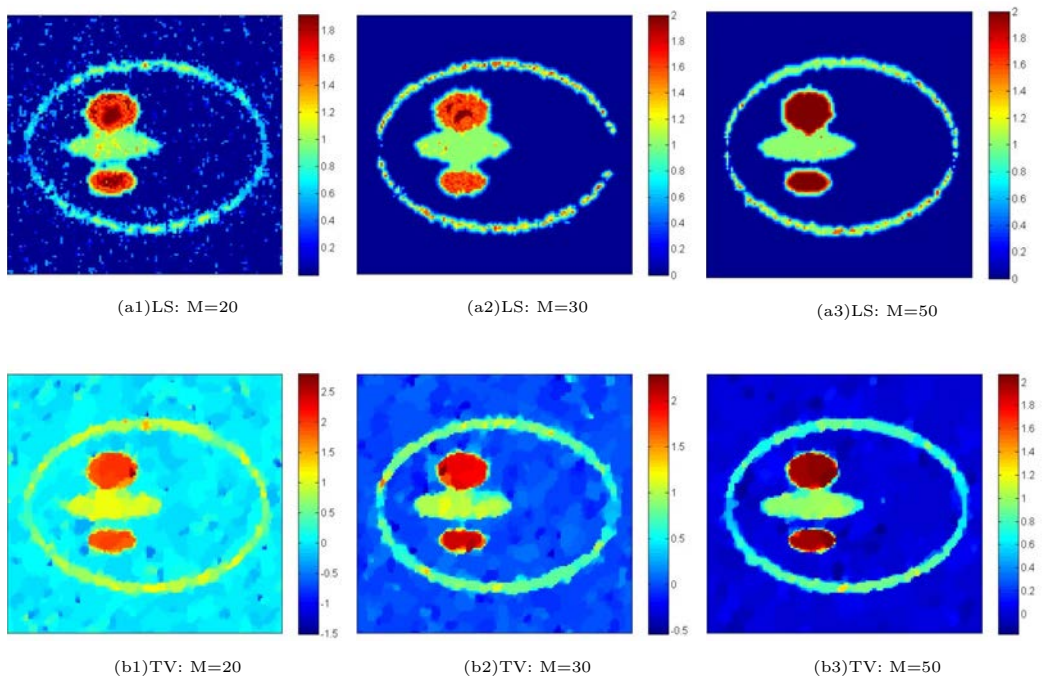


Figure 7.4: Grey-level reconstructed images LS and TV regularization methods with  $\sigma_p = 6.5$ .

obtained with TV regularization are much smoother. A more complex object will be tested as before in section 4.5 in the future because the level-set method may be a more efficient method for objects with a complex topology structure.

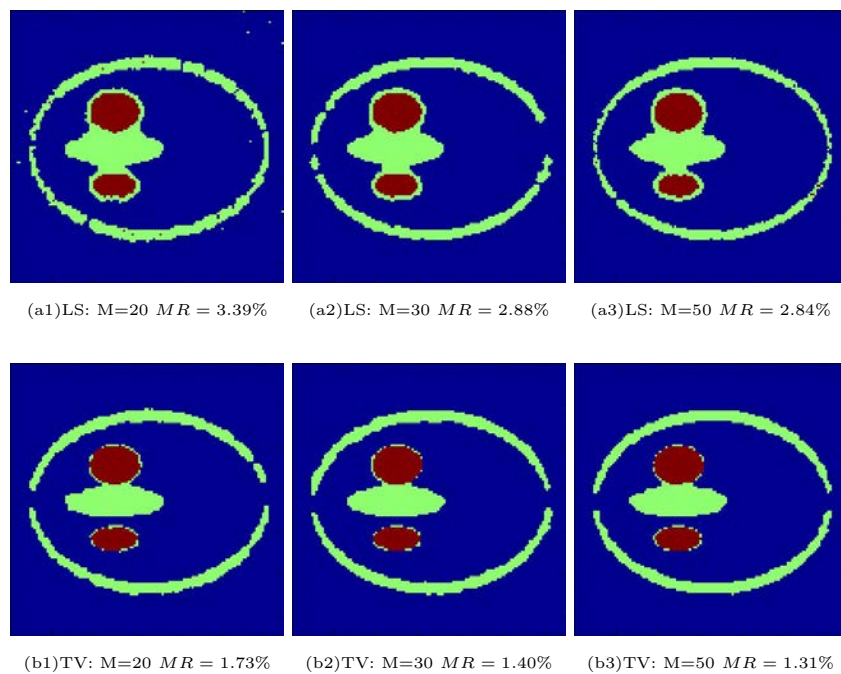


Figure 7.5: Discrete reconstructed images LS and TV regularization methods with  $\sigma_p = 3$  and thresholds are 0.5, 1.3.

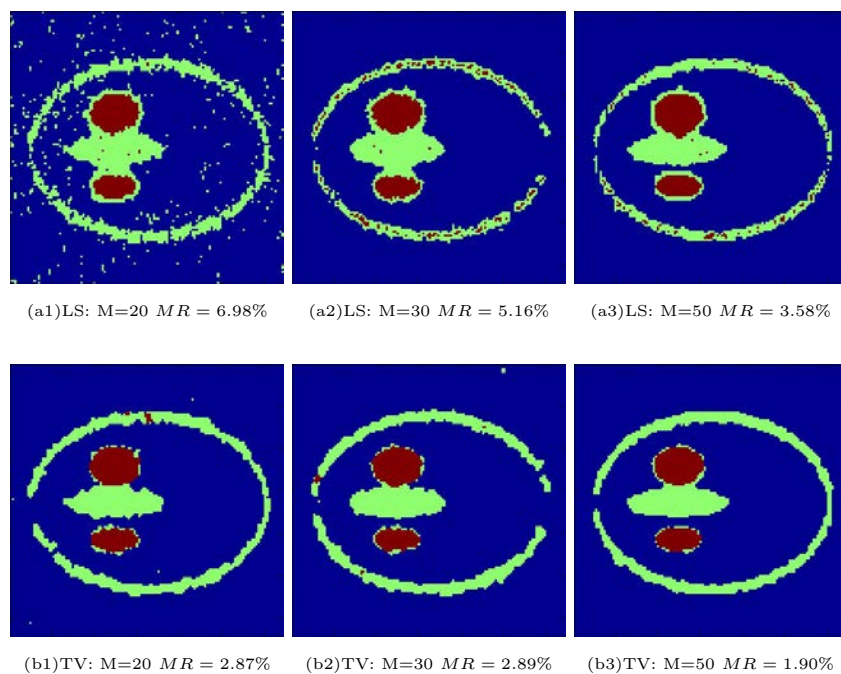
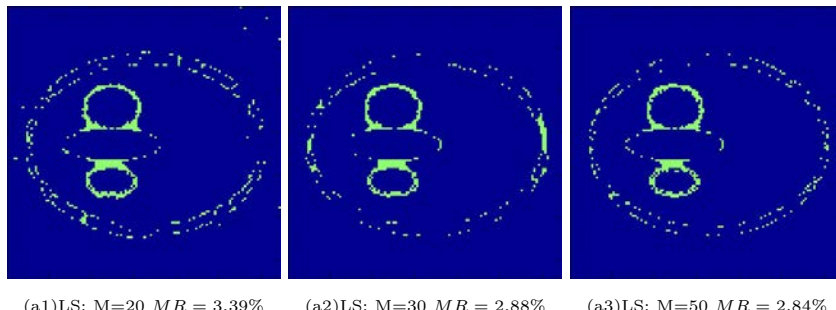
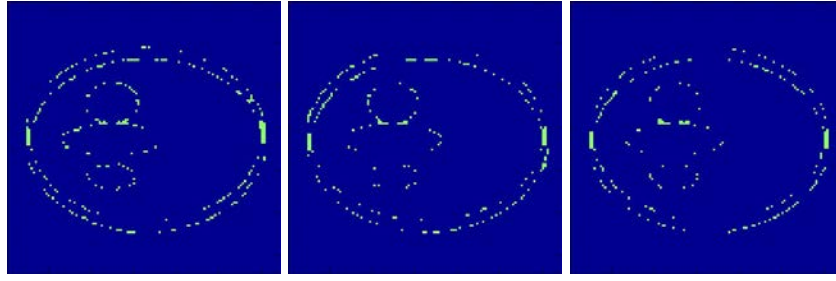


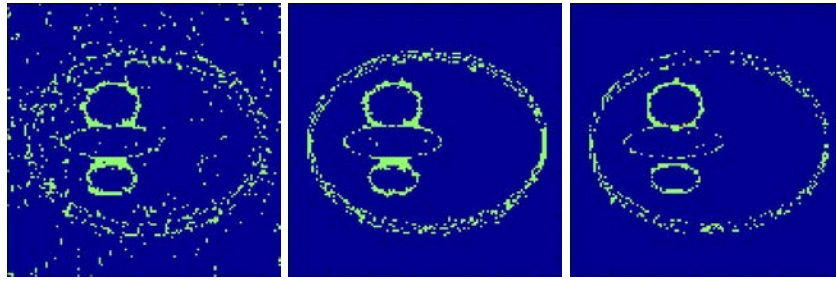
Figure 7.6: Discrete reconstructed images LS and TV regularization methods with  $\sigma_p = 6$  and thresholds are 0.5, 1.3.



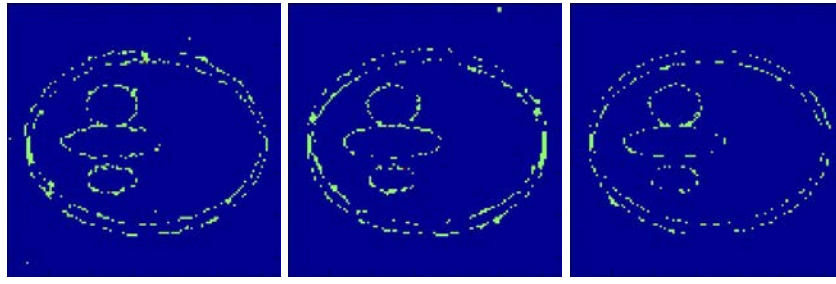
(a1)LS: M=20 MR = 3.39%    (a2)LS: M=30 MR = 2.88%    (a3)LS: M=50 MR = 2.84%



(b1)TV: M=20 MR = 1.73%    (b2)TV: M=30 MR = 1.40%    (b3)TV: M=50 MR = 1.31%

Figure 7.7: Discrete reconstructed images LS and TV regularization methods with  $\sigma_p = 3$ .

(a1)LS: M=20 MR = 6.98%    (a2)LS: M=30 MR = 5.16%    (a3)LS: M=50 MR = 3.58%



(b1)TV: M=20 MR = 2.87%    (b2)TV: M=30 MR = 2.89%    (b3)TV: M=50 MR = 1.90%

Figure 7.8: Discrete reconstructed images LS and TV regularization methods with  $\sigma_p = 6.5$ .

## 7.4 Conclusion

In this chapter, two reconstruction methods for multi-level discrete tomography with a limited number of projections have been compared. The first one is based on a represen-

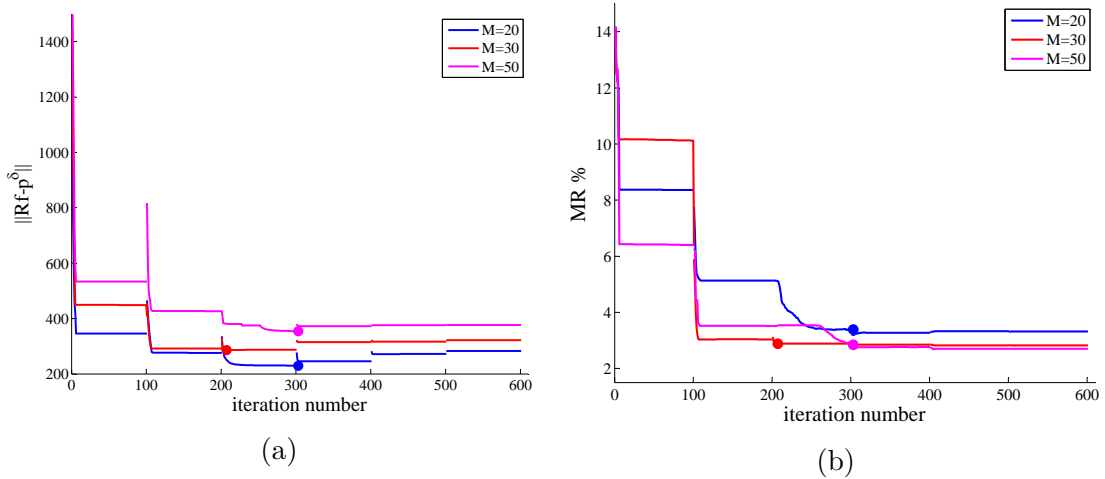


Figure 7.9: LS method with  $\sigma_p = 3$ : (a) Evolution of  $\| Rf^k - p^\delta \|$ . (b) Evolution of the misclassification rate  $MR(k)$ .

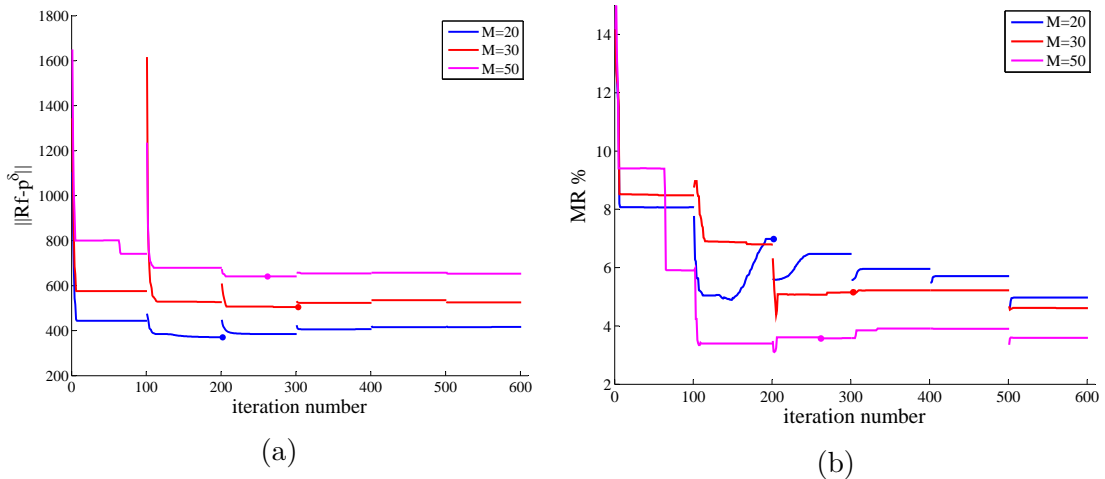


Figure 7.10: LS method with  $\sigma_p = 6.5$ : (a) Evolution of  $\| Rf^k - p^\delta \|$ . (b) Evolution of the misclassification rate  $MR(k)$ .

Table 7.1: Missclassification rates (%) obtained with level-set, Total Variation and FBP approaches.

	<b>LS</b>	<b>TV</b>	<b>FBP</b>
$\sigma_p = 3, M=20$	3.39	1.73	19.16
$\sigma_p = 3, M=30$	2.88	1.40	13.47
$\sigma_p = 3, M=50$	2.84	1.31	6.13
$\sigma_p = 6.5, M=20$	6.98	2.87	34.64
$\sigma_p = 6.5, M=30$	5.16	2.89	29.46
$\sigma_p = 6.5, M=50$	3.58	1.90	23.13

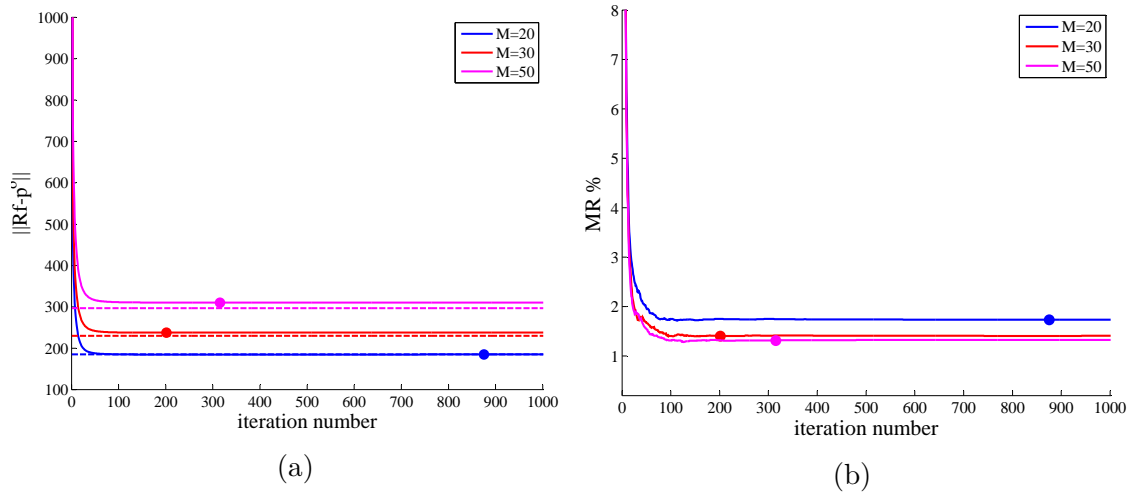


Figure 7.11: TV method with  $\sigma_p = 3$ : (a) Evolution of  $\| Rf^k - p^\delta \|$ . (b) Evolution of the misclassification rate  $MR(k)$ .

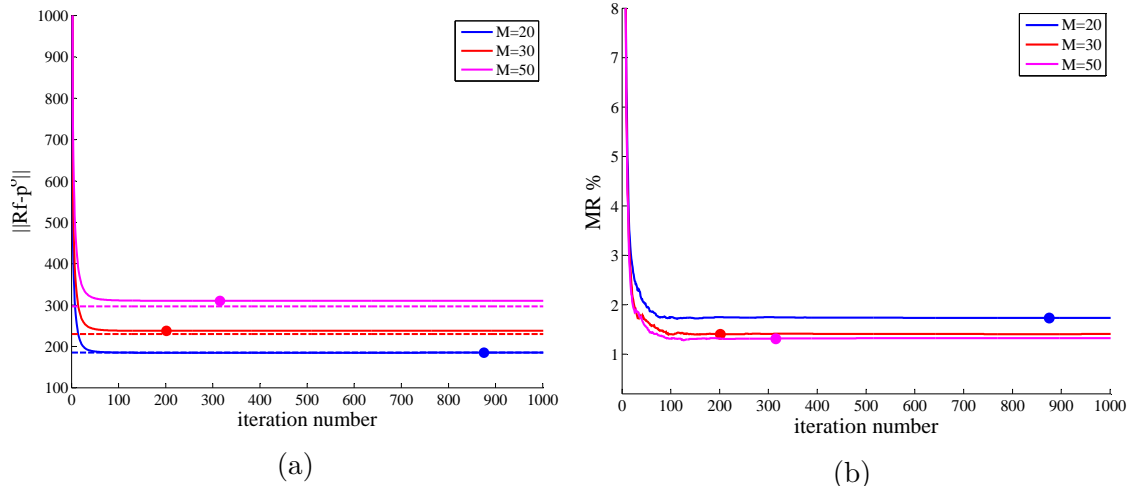


Figure 7.12: TV method with  $\sigma_p = 6.5$ : (a) Evolution of  $\| Rf^k - p^\delta \|$ . (b) Evolution of the misclassification rate  $MR(k)$ .

tation of the function to be reconstructed with several level-set functions which leads to a non-linear inverse problem formulation of the discrete tomography problem. The second method is the classical TV regularization approach. The optimal solution is obtained with the TV ADMM algorithm. The simple tests done on the simple Shepp-Logan phantom show that the TV regularization outperforms the level-set methods on most cases. Experiments on more complex objects would be necessary to further evaluate further the proposed level-set method.

# Chapter 8

---

## Conclusions and perspectives

---

### 8.1 Conclusions

In this thesis, we have investigated the tomography reconstruction methods of the trabecular bone microstructure from a limited number of projections. The main aim of this thesis is to obtain high quality reconstructed images with low dose and short scanning time.

First, this thesis focus on level-set and TV regularization methods. Both methods are compared with different noise levels and different projections numbers on two small images and two big bone cross-sections with elongated trabecular structures. We start from TV regularization without and with a box constraint on the image function to be reconstructed. The TV regularization functional is minimized by the Alternate Direction of Minimization method (ADMM) algorithm. Then a level-set scheme with  $H_1$ -TV regularization is also used to solve this nonlinear problem. TV regularization with a box constraint method gives the best reconstruction results. TV regularization without a box constraint is less effective for the big bone cross-section images than level-set regularization method. Yet, reconstruction errors are located on the boundaries of all the reconstructed images when the projection number is low and the noise level is high. Local minima were obtained.

Secondly, we try to escape the local minima and find the global optima. And a stochastic perturbation is a useful way to escape the local minima. We use stochastic level-set method and stochastic TV method to improve the poorly reconstructed images obtained with the corresponding deterministic schemes. The numerical results for the both stochastic level-set and TV regularization method are illustrated on thresholded bone micro-CT cross-sections for various noise levels and numbers of projections.

- The reconstructed images obtained with stochastic level-set were compared with the ones obtained with classical annealing method for the first step. The stochastic level-set method has a higher convergence speed. Yet, with this method, only the boundaries between 0 and 1 regions are modified. No new regions were revealed and this method is not suitable to high noise level or for a low bone density cross-section image.
- In the second step, a new stochastic approach is presented based on the TV regularization and the ADMM method. Different noise terms based on stochastic TV regularization method are compared including a boundary noise term or a more homogeneous perturbation based on the gradient of the data term of the regularization functional. Compared with stochastic level-set regularization method which only modifies the shape of the 0 and 1 regions located in the boundaries, the advantages of the stochastic TV regularization method is twofold. The random change of the boundary (0 and 1 region) which is performed in a new way with the gradient of the image or with wavelets. Moreover, random topological changes are included to reveal new regions that can not be detected with shape changes.

Thirdly, the next chapter is related to reconstruction with 3D volumes. In this part, TV box regularization method was applied to a simple 3D Shepp-Logan phantom and a real data volume with elongated 3D trabecular structures. All the simulations were implemented on Reconstruction toolkit (RTK). From the reconstruction results, TV regularization method was also proved to be a suitable method for 3D volumes.

The last chapter tried to extend level-set algorithm from binary case to multi-level case. The function to be reconstructed is represented with several level-set functions which will lead to a non-linear inverse problem formulation. In the implementation, the grey-level reconstructed image was projected to a discrete image by thresholding.

To summarize, this thesis works on the binary tomography reconstruction on 2D images and then try to extend to 3D volumes or to multi-level reconstructed images. We concentrated on two famous regularization reconstruction methods: TV and LS. The two methods were applied on different 2D binary CT images with different structures, image sizes and bone fractions with various noise levels and projection numbers to verify the effectiveness and limitations of the two methods. We found that the LS method is a good reconstruction method when the noise level is low compared with the TV method. TV method is much more suitable to reconstruct an image with a higher noise level. We have used a very limited number of projections, there are still a lot of reconstruction errors on the boundaries of the reconstructed images. That's why we try to use a global optimization method to refine the reconstruction results obtained with both TV and LS methods. In this work, we chose stochastic diffusions because this method combines the advantages of a gradient flow and stochastic perturbations to escape the local minima. At the end of these optimization processes, great improvements have been obtained. We try to extend the two methods to 3D volumes with more grey levels in the future. We have already made

some experiments in the last two chapters. We extended TV box regularization method to a simple Shepp-Logan phantom and a complex 3D trabecular bone volume. We also used LS method to reconstruct a simple image with 3 grey levels. Good reconstruction results were obtained. We should make more tests in the future.

## 8.2 Perspectives

This thesis is a preliminary work on binary or multi-level tomography reconstruction on 2D and 3D images. Many aspects remain to be investigated in the future. In the 3D real data volumes part, only TV box regularization method was tested on a small volume of size  $627 \times 627 \times 32$ . All the methods developed in this phd for small bone cross-sections images should be applied and compared for real 3D data volumes. Volumes with different densities and more or less complex structures can be investigated and tested in the future. First, the level-set algorithm also should be extended to the 3D real data volumes. These type of methods can be extended to the binary or to the multi-level cases. The TV and TVbox algorithm can also be compared extensively on 3D real data volumes. Moreover, stochastic perturbations should be used to improve the bad reconstruction results obtained with the corresponding deterministic methods when the projection number is low or the noise level is high. They can be useful to decrease the errors located on irregular boundaries also for 3D data volumes. The stochastic level set and the stochastic algorithm based on the TV method should be generalized and tested on 3D volumes.

Some methodological studies and the development of new algorithms could also be interesting. The main idea of the future work is to find new methods for including the binary or multi-level constraint and to use stochastic method to escape local minima related to the non convexity of the problem. Following the ideas in DART, we could make evolve the regularization functional. We could study in details various stochastic approaches for the multi-level reconstruction problem and different types of noise could be investigated. We could replace the convex constraint used for TV by a non convex one to enforce the values of the reconstructed function to move towards 0 and 1. Various algorithm can be studied, some of them similar to the difference of convex approach mentioned in the bibliographic part. The corresponding stochastic versions could also be studied in detail.



# Appendix



## Appendix A

---

# Mathematic Definitions of $L^2$ -norm, $H_1$ -norm and the least square problem

---

### A. $L^2$ -norm:

If  $x$  is a finite dimensional vector defined as  $x = (x_1, x_2, \dots, x_n)^T$ , the  $\|\cdot\|_2$ -norm of  $x$  is defined as:

$$\|x\|_2 = \sqrt{\sum_{k=1}^n |x_k|^2} \quad (\text{A.1})$$

If  $\Phi$  is a function of  $x$ :  $f = \Phi(x)$ , the  $L^2$ -norm of  $\Phi$  is defined as:

$$\|\Phi\|_{L^2}^2 = \Phi(x) \cdot \Phi(x) = <\Phi(x)|\Phi(x)> = \int |\Phi(x)|^2 dx \quad (\text{A.2})$$

### B. $H_1$ -norm:

Suppose  $\Omega$  is a open set and  $\Omega \subset R^d$  and  $\theta$  is a function of  $L^2(\Omega)$ , with weak derivatives  $\partial_{x_i}(\theta)$ ,  $1 \leq i \leq n$ , we call "Sobolev Space of order 1" on  $\Omega$ :

$$H_1(\Omega) = \{\theta \in L^2(\Omega), \quad \partial_{x_i}(\theta) \in L^2(\Omega), \quad 1 \leq i \leq n\} \quad (\text{A.3})$$

The space  $H_1$ -norm is defined as the inner product:

$$<\theta_1, \theta_2>_{H_1} = \int_{\Omega} (\theta_1 \theta_2 + \sum_{i=1}^n \partial_{x_i}(\theta_1) \partial_{x_i}(\theta_2)) dx \quad (\text{A.4})$$

It can be expressed as:

$$\|\theta\|_{H_1}^2 = <\theta, \theta>_{H_1} = \int_{\Omega} |\theta|^2 dx + \int_{\Omega} |\nabla \theta|^2 dx \quad (\text{A.5})$$

## C. The least square

Suppose  $\{x_i, y_i\}_{i=1}^n$ ,  $x_i \in [a, b]$  are different discrete points, we want to find a function  $f(x)$  defined on an interval  $[a, b]$  which makes the errors between  $f(x_i)$  and  $y_i$  minimum:

$$\min_{\bar{x}} \sum_{i=1}^n (f(x_i) - y_i)^2 \quad (\text{A.6})$$

For a linear system:  $Ax = y$ , the least square is defined as:

$$\min_{\bar{x}} \|Ax - y\|_2^2 \quad A \in C^{m*n}, y \in C^n \quad (\text{A.7})$$

and its solution is the product of the generalized inverse matrix of  $A$  and  $y$ ,  $x = A^\dagger y$ .

## Appendix B

---

### Basic Notions of TV regularization

---

#### A. The Total Variation

For a differentiable function defined on  $R$ , its Total Variation is defined as:

$$TV(f, \Omega) = \int_a^b |f'(x)|dx \quad (B.1)$$

For a differentiable function  $f$  defined on a bounded open set  $\Omega \in R^n$ , its Total Variation is defined as:

$$TV(f, \Omega) = \sup \left\{ \int_{\Omega} f(x) \operatorname{div}(\Phi(x)) dx : \Phi \in C_c^1(\Omega, R^n), \|\Phi\|_{L^\infty(\Omega)} \leq 1 \right\} \quad (B.2)$$

where  $C_c^1(\Omega, R^n)$  is the set of continuously differentiable vector functions of compact support contained in  $\Omega$ , and  $\|\Phi\|_{L^\infty(\Omega)} \leq 1$  is the essential supremum norm. If  $f$  is differentiable,  $TV(f, \Omega)$  could be expressed as:

$$TV(f, \Omega) = \int_{\Omega} |\nabla f(x)| dx \quad (B.3)$$

#### B. The subdifferential definition

Suppose  $f : I \rightarrow R$  is a real-valued convex function defined on an open interval  $(-\infty, +\infty)$ . For all  $x_0 \in I$ , its subdifferential  $\partial f(x_0)$  exists. It is the set of real numbers  $c$  making (B.4) true for all  $x \in I$  the following inequality:

$$f(x) - f(x_0) \geq c(x - x_0) \quad (B.4)$$

It can be shown that the set of subderivatives at  $x_0$  for a convex function is a nonempty closed interval  $[a, b]$ , where:

$$\begin{aligned} a &= \lim_{x \rightarrow x_0^-} \frac{f(x) - f(x_0)}{x - x_0} \\ b &= \lim_{x \rightarrow x_0^+} \frac{f(x) - f(x_0)}{x - x_0} \end{aligned} \quad (\text{B.5})$$

which are guaranteed to exist and satisfy  $a \leq b$ .

## C. Soft Thresholding Method

Let a vector  $x = (x_1, x_2, \dots, x_n)^t \in \mathbb{R}^n$ , we consider the following problem:

$$x^* = \underset{x}{\operatorname{argmin}} \|x - y\|_2^2 + \lambda \|x\|_2 \quad (\text{B.6})$$

The solution to this problem is given by the vectorial soft-thresholding operator  $ST$  of threshold  $\frac{\lambda}{2}$  defined as [Mory (2014)]:

$$x^* = ST_{\frac{\lambda}{2}}(y) = \max(\|y\|_2 - \frac{\lambda}{2}, 0) \frac{y}{\|y\|_2} \quad (\text{B.7})$$

## Appendix C

---

### Appendix about Level-set Method

---

#### Obtain the gradient $G(\theta)$

In the level-set section, we have the smoothed Tikhonov regularization functional like:

$$E_\epsilon(\theta) = \frac{\|RH_\epsilon(\theta) - p^\delta\|_2^2}{2} + \beta_1|H_\epsilon(\theta)|_{TV} + \beta_2\|\theta\|_{L_1}^2 + \beta_2\|\nabla\theta\|_{L_1}^2 \quad (\text{C.1})$$

The minimizers of the Tikhonov functionals are found with a first-order optimality condition for the smoothed functionals,  $G(\theta) = 0$ .

For a continuous function  $f(x) = \|Ax - b\|^2$  and a , according to the Taylor expression:

$$f(x + h) = f(x) + f'(x)h + \frac{f''(x)}{2!}h^2 + \dots \quad (\text{C.2})$$

Therefore,

$$\Delta(f(x)) = f(x + h) - f(x) = f'(x)h + \frac{f''(x)}{2!}h^2 + \dots \quad (\text{C.3})$$

And also:

$$\begin{aligned} \Delta(f(x)) &= f(x + h) - f(x) = \|A(x + h) - b\|^2 - \|Ax - b\|^2 \\ &= \|Ax - b\|^2 + 2\langle Ax - b, Ah \rangle - \|Ax - b\|^2 + \underbrace{\langle Ah, Ah \rangle}_{\text{ignore}} \end{aligned} \quad (\text{C.4})$$

Here, we just consider the first-order optimality condition, the term  $\langle Ah, Ah \rangle$  can be ignored, and the gradient of  $f(x)$  is given by:

$$G(f(x)) \approx 2A^*(Ax - b) \quad (\text{C.5})$$

Finally the gradient of the data term for the level-set function:

$$G\left(\frac{\|RH_\epsilon(\theta) - p^\delta\|_2^2}{2}\right) \approx H'_\epsilon R^*(RH_\epsilon(\theta) - p^\delta) \quad (\text{C.6})$$

We can also calculate the gradient for the other terms in the regularization functional

$$\begin{aligned} \|\theta + h\|_{L_2}^2 - \|\theta\|_{L_2}^2 &= 2 < \theta, h > + \underbrace{< \theta, \theta >}_{\text{ignore}} \\ \Rightarrow G(\|\theta\|_{L_2}^2) &\approx 2\theta \end{aligned} \quad (\text{C.7})$$

$$\begin{aligned} \|\nabla(\theta + h)\|_{L_2}^2 - \|\nabla\theta\|_{L_2}^2 &= 2 < \nabla\theta, \nabla h > + \underbrace{< \nabla h, \nabla h >}_{\text{ignore}} \\ \because \int \nabla\theta \int \nabla h &= - \int \Delta\theta h \\ \Rightarrow G(\|\nabla\theta\|_{L_2}^2) &\approx 2\Delta\theta \end{aligned} \quad (\text{C.8})$$

$$G(|H_\epsilon(\theta)|_{TV}) = -\delta_D(\theta) \nabla \cdot \frac{\nabla\theta}{|\nabla\theta|} \quad (\text{C.9})$$

where  $\delta_D$  is a Dirac distribution.

## Gaussian-Newton method

If  $\theta_{k+1}$  is the saddle point, with a small step  $\delta\theta$ , from  $\theta_k$  to  $\theta_{k+1} = \theta_k + \delta\theta$ , we have the gradient:

$$\begin{aligned} G(\theta_{k+1}) &= G(\theta_k) + G'(\theta_k)(\delta\theta) = 0 \\ \Rightarrow G'(\theta_k)(\delta\theta) &= -G(\theta_k) \end{aligned} \quad (\text{C.10})$$

From Eq.4.3.1, we have:

$$G(\theta_k) = H'_\epsilon R^*(R H_\epsilon(\theta_k) - p^\delta) + \beta_2(I - \Delta)(\theta_k) + \beta_1 \frac{\partial |H_\epsilon(\theta_k)|_{BV}}{\partial \theta_k} \quad (\text{C.11})$$

therefore,

$$\Rightarrow -G(\theta_k) = H'_\epsilon R^*(R H_\epsilon(\theta_k) - p^\delta) + \beta_2(I - \Delta)(\theta_k) + \beta_1 \frac{\partial |H_\epsilon(\theta_k)|_{BV}}{\partial \theta_k} \quad (\text{C.12})$$

Because:

$$\frac{\partial |H_\epsilon(\theta)|_{TV}}{\partial \theta} = -\delta_D(\theta) \nabla \cdot \frac{\nabla\theta}{|\nabla\theta|} \quad (\text{C.13})$$

$$\begin{aligned} \Rightarrow -G(\theta_k) &= V_k^* V_k \delta\theta + \beta_2(I - \Delta)(\delta\theta) - \beta_1 \delta_D(\theta_k) \nabla \cdot \frac{\nabla\delta\theta}{|\nabla\theta_k|} \\ \Rightarrow -G(\theta_k) &= \underbrace{(V_k^* V_k + \beta_2(I - \Delta) - \beta_1 \delta_D(\theta_k) \nabla \cdot \frac{1}{|\nabla\theta_k|})(\delta\theta)}_A \\ \Rightarrow -G(\theta_k) &= A\delta\theta \end{aligned} \quad (\text{C.14})$$

where  $V_k$  is the operator  $V_k = R H'_\epsilon(\theta_k)$ , and  $\delta_D$  is a Dirac distribution.

## Appendix D

---

### Cone Beam CT and image Physical Informations on RTK

---

Cone beam computed tomography (CBCT) is a medical imaging technique consisting of X-ray computed tomography where the X-rays are divergent, forming a cone [Scarfe *et al.* (2006)]. CBCT is a useful reconstruction method to produce CT images with isotropic sub-millimeter spatial resolution, high diagnostic quality, short scanning times of about 10-30 seconds [Bamgbose *et al.* (2007)].

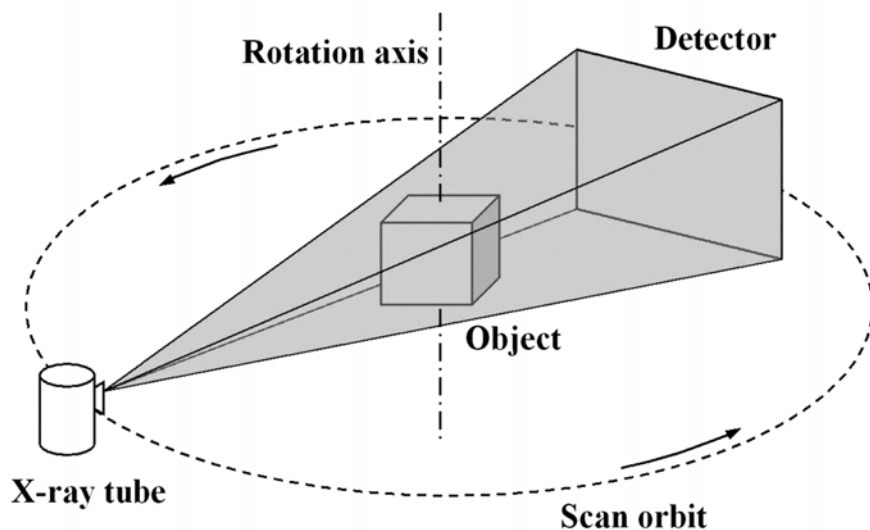


Figure D.1: Typical setup of Cone Beam CT system [Cai and Ning (2008)]

RTK is an open source and cross platform software only for fast circular Cone-Beam CT (CBCT) reconstruction. The geometry is an essential information to do a successful tomographic reconstruction. And the physical information of image is also very important to configure a correct geometry.

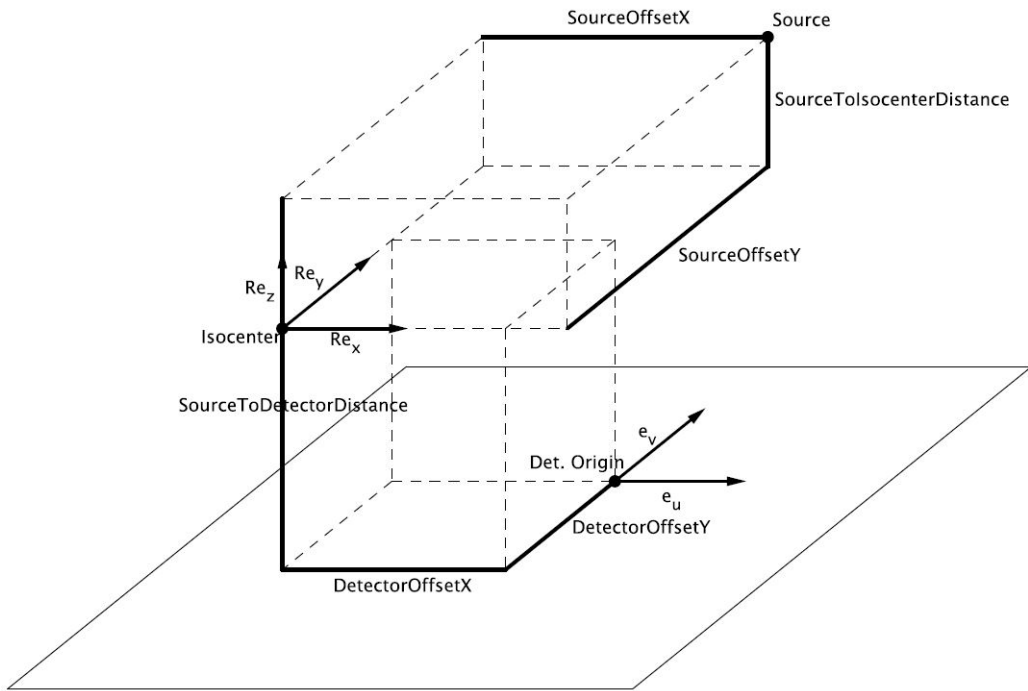


Figure D.2: Geometrical concepts associated with the RTK image [Rit and Mory (2015)]

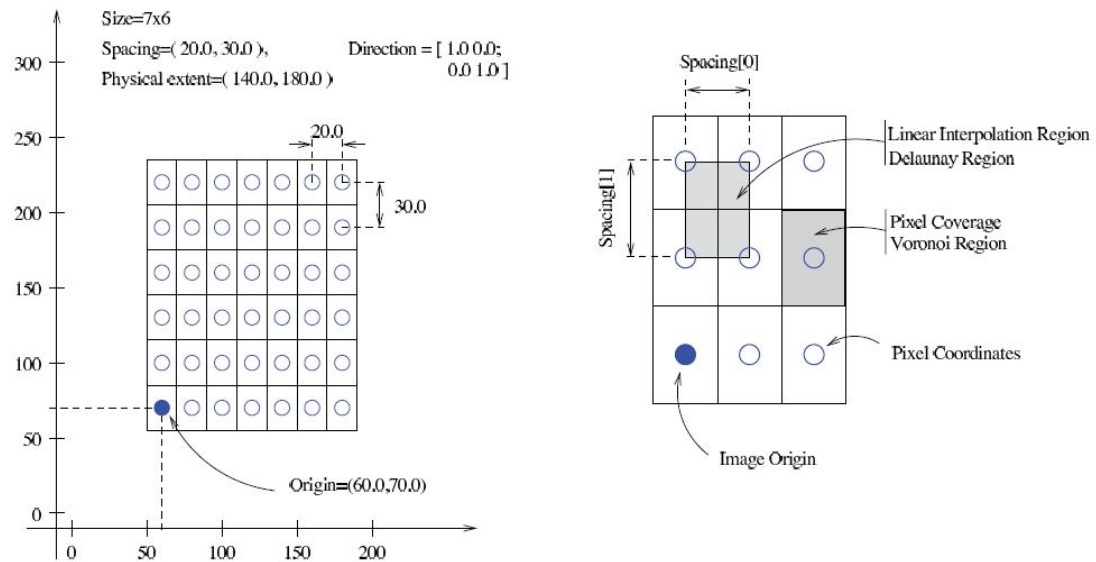


Figure D.3: Image physical information associated with the RTK [Rit and Mory (2015)]

The CT system configuration includes the distance from the X-ray source to the detector(SDD), the distance from the X-ray source to the center of the object(SID), the offsets of the X-ray sources at the directions ( $x, y, z$ ) corresponding to the origin of detector center. For the simple simulated Shepp-Logan phantom, the SDD is 1536mm and

---

the SID is 1000mm. For the real trabecular bone, the SDD is 100.01m and the SID is 100m, the offset at  $x$ -direction is -0.74cm. The volume size is the number of voxels at each directions, and the physical space is the distance between the centers of two voxels. For the simulated Shepp-Logan phantom, the volume size is  $256 \times 256 \times 256$ , the physical space is 2mm. The origin is  $(-255, -255, -255)$ mm along the  $(x, y, z)$  directions. For the real 3D trabecular bone volume, the volume size is  $627 \times 627 \times 32$ , the voxel size is  $15\mu\text{m}$ . The origin is defined at  $(-0.47, -0.47, 0.39)$ cm at the  $(x, y, z)$  directions to make the origin of the coordinate system located at the center of the trabecular volume. The real 3D trabecular bone was reconstructed from 3000 projections of size  $627 \times 32$  with a voxel size of  $15\mu\text{m}$ , obtained by cropping and then sub-selecting from 3000 ESRF CBCT projection data of size  $1974 \times 1100$  with a voxel size of  $7.5\mu\text{m}$ .



# Publications

## Journals:

- 1) L.Wang, B. Sixou, and F. Peyrin, "Binary tomography reconstruction with stochastic level-set method", *Signal Processing Letters*, vol.22, no.7, 2015.
- 2) B. Sixou, L. Wang, S. Rit, and F. Peyrin, "Binary Tomography Reconstruction with Stochastic Diffusion Based on Level-set and Total Variation Regularization", *International Journal of Tomography and Simulation*, vol.29, no.2, pp.1-26, 2016.
- 3) L. Wang, B. Sixou, S. Rit, and F. Peyrin, "Binary tomography reconstruction from few projections with level-set regularization methods for bone microstructure study", *International Journal of tomography and simulation*, vol.29, no.1, pp.1-17, 2016.
- 4) L. WANG, B. Sixou, S.Rit, F.Peyrin, "Binary tomography reconstruction from few projections with total variation regularization for bone microstructure studies", *Journal of X-ray Science and Technology*, vol.24, pp.177-189, 2016.

## Conferences:

- 1) B. Sixou, L. Wang, and F. Peyrin, "Bone microstructure reconstruction from few projections with level-set regularization", *IEEE International Symposium on Biomedical Imaging (ISBI)*, pp.1170-1173, 2013.
- 2) B. Sixou, L. Wang, and F. Peyrin, "Stochastic diffusion equation with singular diffusivity and gradient-dependent noise in binary tomography ", *New Computational Methods for Inverse Problems (NCMIP)*, Cachan, France, 2014.
- 3) L. Wang, B. Sixou and F. Peyrin, "Bone microstructure reconstructions from few projections with stochastic nonlinear diffusion", *Signal Processing Conference (EUSIPCO)*, pp.1826-1830, Spain, 2014.
- 4) L. Wang, B. Sixou, and F. Peyrin, "Binary tomography reconstructions of bone microstructure from few projections with stochastic level-set methods", *IEEE International Conference on Image Processing (ICIP)*, France, 2014.
- 5) L. Wang, B. Sixou and F. Peyrin, "Filtered stochastic optimization for binary tomography", *IEEE International Symposium on Biomedical Imaging (ISBI)*, pp.1604-1607, 2015.
- 6) L.Wang, B.Sixou, F.Peyrin, "Multi-level tomography reconstructions with level-set and TV regularization methods", *Signal Processing Conference (EUSIPCO)*, 2016, (Submitted).



# Bibliography

- [Afonso *et al.* (2010)] Afonso, M., Bioucas-Dias, J., and Figueiredo, M. (2010). Fast image recovery using variable splitting and constrained optimization. *IEEE Transactions on Image Processing*, 19(9):2345–2356.
- [Afonso *et al.* (2011)] Afonso, M., Bioucas-Dias, J., and Figueiredo, M. (2011). An augmented Lagrangian approach to the constrained optimization formulation of imaging inverse problems. *SIAM Journal on Scientific computing*, 20(3):681–695.
- [Andersen and Kak (1984)] Andersen, A. and Kak, A. (1984). Simultaneous Algebraic Reconstruction Technique (SART): A Superior Implementation of ART. *Ultrasonic Imaging*, 6(1):81–94.
- [Apostol *et al.* (2006)] Apostol, L., Boudousq, V., Basset, O., Odet, C., Yot, S., Tabary, J., Dinten, J., Boller, E., Kotzki, P., and Peyrin, F. (2006). Relevance of 2D radiographic texture analysis for the assessment of 3D bone microarchitecture. *Medical Physics*, 33:3546–3556.
- [Aubert and Kornprobst (2006)] Aubert, G. and Kornprobst, P. (2006). *Mathematical problems in image processing: partial differential equations and the calculus of variations*, volume 147. Springer Science & Business Media.
- [Azencott (1992)] Azencott, R. (1992). Sequential simulated annealing: speed of convergence and acceleration techniques. *Simulated annealing: Parallelization techniques*, 1:1–10.
- [Bamgbose *et al.* (2007)] Bamgbose, B., Adeyemo, W., Ladeinde, A., and Ogunlewe, M. (2007). Conebeam computed tomography (CBCT): the new vista in oral and maxillo-facial imaging. *Nigerian quarterly journal of hospital medicine*, 18(1):32–35.
- [Barbu *et al.* (2009)] Barbu, V., Da Prato, G., and Röckner, M. (2009). Stochastic non-linear diffusion equations with singular diffusivity. *SIAM Journal on Mathematical Analysis*, 41(3):1106–1120.
- [Barkaoui *et al.* (2014)] Barkaoui, A., Chamekh, A., Merzouki, T., Hambli, R., and Mkadem, A. (2014). Multiscale approach including microfibril scale to assess elastic constants of cortical bone based on neural network computation and homogenization method. *International journal for numerical methods in biomedical engineering*, 30(3):318–338.
- [Barkaoui and Hambli (2011)] Barkaoui, A. and Hambli, R. (2011). Finite element 3D modeling of mechanical behavior of mineralized collagen microfibrils. *J Appl biomater Biomech*, 9:199–205.

- [Batenburg and Sijbers (2006)] Batenburg, K. and Sijbers, J. (2006). Discrete tomography from micro-CT data: application to the mouse trabecular bone structure. pages 614240–614240.
- [Batenburg and Sijbers (2009)] Batenburg, K. J. and Sijbers, J. (2009). Generic iterative subset algorithm for discrete tomography. *Discrete Applied Mathematics*, 157:438–451.
- [Batenburg and Sijbers (2011)] Batenburg, K. and Sijbers, J. (2011). DART: A Practical Reconstruction Algorithm for Discrete Tomography. *IEEE Trans. Image Processing*, 20(9):2542–2553.
- [Becker *et al.* (2009)] Becker, S., Bobin, J., and Candes, E. (2009). NESTA: A fast and accurate first-order method for sparse recovery. *SIAM Journal on Scientific computing*, 4:1–39.
- [Beister *et al.* (2012)] Beister, M., Kolditz, D., and Kalender, W. A. (2012). Iterative reconstruction methods in X-ray CT. *Physica medica*, 28(2):94–108.
- [Benhali and Peyrin (2002)] Benhali, A. and Peyrin, F. (2002). *La Tomographie et La Tomographie médicale*. Hermès, Publ., Paris, France.
- [Bertsekas and Tsitsiklis (2000)] Bertsekas, D. P. and Tsitsiklis, J. N. (2000). Gradient convergence in gradient methods with errors. *SIAM Journal on Optimization*, 10(3):627–642.
- [Besag (1986)] Besag, J. (1986). On the statistical analysis of dirty pictures. *Journal of the Royal Statistical Society. Series B (Methodological)*, pages 259–302.
- [Bon (2016)] (January 30, 2016). Bone remodeling. website. [https://en.wikipedia.org/wiki/Bone\\_remodeling](https://en.wikipedia.org/wiki/Bone_remodeling).
- [Bonjour *et al.* (1994)] Bonjour, J. P., Theintz, G., Law, F., Slosman, D., and Rizzoli, R. (1994). Peak bone mass. *Osteoporosis international*, 4(1):S7–S13.
- [Borsic *et al.* (2010)] Borsic, A., Graham, B. M., Adler, A., and Lionheart, W. R. (2010). In vivo impedance imaging with total variation regularization. *Medical Imaging, IEEE Transactions on*, 29(1):44–54.
- [Bouxsein *et al.* (2010)] Bouxsein, M. L., Boyd, S. K., Christiansen, B. A., Guldberg, R. E., Jepsen, K. J., and Müller, R. (2010). Guidelines for assessment of bone microstructure in rodents using micro-computed tomography. *Journal of Bone and Mineral Research*, 25:1468–1486.
- [Bresson *et al.* (2007)] Bresson, X., Esedoḡlu, S., Vandergheynst, P., Thiran, J.-P., and Osher, S. (2007). Fast global minimization of the active contour/snake model. *Journal of Mathematical Imaging and vision*, 28(2):151–167.
- [Brooks and Di Chiro (1975)] Brooks, R. A. and Di Chiro, G. (1975). Theory of Image Reconstruction in Computed Tomography 1. *Radiology*, 117(3):561–572.
- [Brown *et al.* (2012)] Brown, E. S., Chan, T. F., and Bresson, X. (2012). Completely convex formulation of the Chan-Vese image segmentation model. *International journal of computer vision*, 98(1):103–121.

- [Bruyant (2002)] Bruyant, P. (2002). Analytic and iterative reconstruction algorithms in SPECT. *Journal Of Nuclear Medicine*, 43(10):1343–1358.
- [Burghardt *et al.* (2011)] Burghardt, A. J., Link, T. M., and Majumdar, S. (2011). High-resolution computed tomography for clinical imaging of bone microarchitecture. *Clinical Orthopaedics and Related Research®*, 469(8):2179–2193.
- [Cai and Ma (2010)] Cai, W. and Ma, L. (2010). Comparaison of approaches based on optimization and algebraic iteration for binary tomography. *Computer Physics Communications*, 181:1974–1981.
- [Cai and Ning (2008)] Cai, W. and Ning, R. (2008). Preliminary study of a phase-contrast cone-beam computed tomography system: the edge-enhancement effect in the tomographic reconstruction of in-line holographic images. *Optical Engineering*, 47(3):037004–037004.
- [Capricelli and Combettes (2005)] Capricelli, T. D. and Combettes, P. L. (2005). Parallel block-iterative reconstruction algorithms for binary tomography. *Electronic Notes in DISCRETE MATHEMATICS*, 20:263–280.
- [Capricelli and Combettes (2007)] Capricelli, T. and Combettes, P. (2007). *Advances in discrete tomography and its applications: A convex programming algorithm for noisy discrete tomography*. Birkhauser, Boston, MA.
- [Catoni (1992)a] Catoni, O. (1992a). Rough large deviation estimates for simulated annealing: Application to exponential schedules. *The Annals of Probability*, pages 1109–1146.
- [Catoni (1992)b] Catoni, O. (1992b). Rough large deviation estimates for simulated annealing: Application to exponential schedules. *The Annals of Probability*, pages 1109–1146.
- [Chalmond (1988)] Chalmond, B. (1988). Image restoration using an estimated Markov model. *Signal Processing*, 15(2):115–129.
- [Chambolle and Pock (2011)] Chambolle, A. and Pock, T. (2011). A first-order primal-dual algorithm for convex problems with applications to imaging. *Journal of Mathematical Imaging and Vision*, 40(1):120–145.
- [Chan *et al.* (2000)] Chan, T., Marquina, A., and Mulet, P. (2000). High-order total variation-based image restoration. *SIAM Journal on Scientific Computing*, 22(2):503–516.
- [Chan and Tai (2004)] Chan, T. F. and Tai, X.-C. (2004). Level set and total variation regularization for elliptic inverse problems with discontinuous coefficients. *Journal of Computational Physics*, 193(1):40–66.
- [Chan and Vese (2001)] Chan, T. and Vese, L. (2001). Active contours without edges. *IEEE Transactions on Image Processing*, 10:266–277.
- [Chow *et al.* (2009)] Chow, S.-N., Yang, T.-S., and Zhou, H. (2009). Global Optimizations by Intermittent Diffusion. *National Science Council Tunghai University Endowment Fund for Academic Advancement Mathematics Research Promotion Center*, 121.

- [Chung *et al.* (2005)] Chung, E. T., Chan, T. F., and Tai, X.-C. (2005). Electrical impedance tomography using level set representation and total variational regularization. *Journal of Computational Physics*, 205(1):357–372.
- [Clarke (2008)] Clarke, B. (2008). Normal bone anatomy and physiology. *Clinical journal of the American Society of Nephrology*, 3(Supplement 3):S131–S139.
- [Cormack (1963)] Cormack, A. M. (1963). Representation of a function by its line integrals, with some radiological applications. *Journal of applied physics*, 34(9):2722–2727.
- [Cormack (1973)] Cormack, A. (1973). Reconstruction of densities from their projections, with applications in radiological physics. *Physics in medicine and biology*, 18(2):195.
- [Cot *et al.* (1998)] Cot, C., Catoni, O., *et al.* (1998). Piecewise constant triangular cooling schedules for generalized simulated annealing algorithms. *The Annals of Applied Probability*, 8(2):375–396.
- [Daubechies *et al.* (1992)] Daubechies, I. *et al.* (1992). *Ten lectures on wavelets*, volume 61. SIAM.
- [DeCezaro *et al.* (2009)] DeCezaro, A., Leitao, A., and Tai, X. C. (2009). On multiple level-set regularization methods for inverse problems. *Inverse Problems*, 25(035004).
- [DeCezaro *et al.* (2013)] DeCezaro, A., Leitao, A., and Tai, X. C. (2013). On piecewise constant level-set (PCLS) methods for the identification of discontinuous parameters in ill-posed problems. *Inverse Problems*, 29(015003).
- [Defrise *et al.* (2011)] Defrise, M., Vanhove, C., and Liu, X. (2011). An algorithm for total variation regularization in high-dimensional linear problems. *Inverse Problems*, 27(6):065002.
- [Dorozhkin (2010)] Dorozhkin, S. V. (2010). Nanosized and nanocrystalline calcium orthophosphates. *Acta Biomaterialia*, 6(3):715–734.
- [Duan *et al.* (2009)] Duan, X., Zhang, L., and Xing, Y. X. (2009). Few-View Projection Reconstruction With an Iterative Reconstruction-Reprojection Algorithm and TV Constraint. *IEEE Transactions on Nuclear Science*, 56:1377–1382.
- [E.T.Qinto (1993)] E.T.Qinto (1993). Singularities of the X-ray transform and limited data tomography in  $\mathbb{R}^2$  and  $\mathbb{R}^3$ . *SIAM J.Math.Anal.*, 24:1215–1225.
- [Egger and Leitao (2009)] Egger, A. and Leitao, L. (2009). Nonlinear regularization for ill-posed problems with piecewise constant or strongly varying solutions. *Inverse Problems*, 25(115014).
- [Feldkamp *et al.* (1989)] Feldkamp, L. A., Goldstein, S. A., Parfitt, M. A., Jesion, G., and Kleerekoper, M. (1989). The direct examination of three-dimensional bone architecture in vitro by computed tomography. *Journal of bone and mineral research*, 4(1):3–11.
- [Flannery *et al.* (1987)] Flannery, B. P., Deckman, H. W., Roberge, W. G., and D'Amico, K. L. (1987). Three-Dimensional X-ray Microtomography. *Science*, 237(4281):1439–1444.
- [Folkens *et al.* (2002)] Folkens, P. A., Reeves, R. R., Stewart, B. S., Clapham, P. J., and Powell, J. A. (2002). *Guide to marine mammals of the world*. AA Knopf.

- [Frieden (1972)] Frieden, B. R. (1972). Restoring with maximum likelihood and maximum entropy. *JOSA*, 62(4):511–518.
- [Fruhauf *et al.* (2005)] Fruhauf, F., Scherzer, O., and Leitao, A. (2005). Analysis of Regularization Methods for the Solution of Ill-Posed Problems Involving Discontinuous Operators. *SIAM Journal on Numerical Analysis*, 43:767–786.
- [Geman and Geman (1984)] Geman, S. and Geman, D. (1984). Stochastic relaxation, Gibbs distributions, and the Bayesian restoration of images. *Pattern Analysis and Machine Intelligence, IEEE Transactions on*, (6):721–741.
- [Geman and Geman (1993)] Geman, S. and Geman, D. (1993). Stochastic relaxation, Gibbs distributions and the Bayesian restoration of images. *Journal of Applied Statistics*, 20(5-6):25–62.
- [Geman and Hwang (1986)] Geman, S. and Hwang, C.-R. (1986). Diffusions for global optimization. *SIAM Journal on Control and Optimization*, 24(5):1031–1043.
- [Gidas (1995)] Gidas, B. C. (1995). *Metropolis-type Monte Carlo simulation algorithms and simulated annealing*. Center for Intelligent Control Systems.
- [Gilbert and Nocedal (1992)] Gilbert, J. C. and Nocedal, J. (1992). Global convergence properties of conjugate gradient methods for optimization. *SIAM Journal on optimization*, 2(1):21–42.
- [Gilsanz (1998)] Gilsanz, V. (1998). Bone density in children: a review of the available techniques and indications. *European journal of radiology*, 26(2):177–182.
- [Gindi *et al.* (1993)] Gindi, G., Rangarajan, A., Lee, M., Hong, P., and Zubal, I. G. (1993). Bayesian reconstruction for emission tomography via deterministic annealing. In *Information Processing in Medical Imaging*, pages 322–338. Springer.
- [Goldstein and Osher (2009)] Goldstein, T. and Osher, S. (2009). The split Bregman method for L1-regularized problems. *SIAM Journal on Imaging Sciences*, 2(2):323–343.
- [Golob and Laya (2015)] Golob, A. L. and Laya, M. B. (2015). Osteoporosis: screening, prevention, and management. *Medical Clinics of North America*, 99(3):587–606.
- [Gonzalez and Woods (2002)] Gonzalez, R. C. and Woods, R. E. (2002). Digital image processing.
- [Gordon *et al.* (1970)] Gordon, R., Bender, R., and Herman, G. T. (1970). Algebraic reconstruction techniques (ART) for three-dimensional electron microscopy and x-ray photography. *Journal of Theoretical Biology*, 29(3):471–481.
- [Gouillart *et al.* (2013)] Gouillart, E., Krzakala, F., Mezard, M., and Zdeborová, L. (2013). Belief propagation reconstruction for discrete tomography. *Inverse Problems*, 29(035003).
- [Guglielmi and Scalzo (2010)] Guglielmi, G. and Scalzo, G. (2010). Imaging tools transform diagnosis of osteoporosis. *Diagnostic Imaging Europe*, 26(3):7–11.
- [Hadjidakis and Androulakis (2006)] Hadjidakis, D. J. and Androulakis, I. I. (2006). Bone remodeling. *Annals of the New York Academy of Sciences*, 1092(1):385–396.

- [Hansen (2001)] Hansen, P. C. (2001). *The L-curve and its use in the numerical treatment of inverse problems*. Advances in Computational Bioengineering. WIT Press, Southampton.
- [Heaney *et al.* (2000)] Heaney, R., Abrams, S., Dawson-Hughes, B., Looker, A., Looker, A., Marcus, R., Matkovic, V., and Weaver, C. (2000). Peak bone mass. *Osteoporosis international*, 11(12):985–1009.
- [Herman (2009)] Herman, G. T. (2009). *Fundamentals of Computerized Tomography Image Reconstruction from Projections*. Dordrecht: Springer.
- [Herman and Kuba (2007)] Herman, G. T. and Kuba, A. (2007). *Advances in discrete tomography and its applications*. Applied and Numerical Harmonic Analysis. Birkhauser, Boston, MA.
- [Holdsworth and Thornton (2002)] Holdsworth, D. W. and Thornton, M. M. (2002). Micro-CT in small animal and specimen imaging. *Trends in Biotechnology*, 20(8):S34–S39.
- [Hounsfield (1973)] Hounsfield, G. N. (1973). *Computerized transverse axial scanning (tomography)*, chapter 1, Description of system, pages 1016–1022. Br.J. Radiol.
- [Ingber (1989)] Ingber, L. (1989). Very fast simulated re-annealing. *Mathematical and computer modelling*, 12(8):967–973.
- [Inouye (1979)] Inouye, T. (1979). Image reconstruction with limited angle projection data. *Nuclear Science, IEEE Transactions on*, 26(2):2665–2669.
- [Jacobs *et al.* (1995)] Jacobs, P., Sevens, E., and Kunnen, M. (1995). Principles of computerised X-ray tomography and applications to building materials. *J.The sience of the Total Environment*, 167:161–170.
- [Jia *et al.* (2010)] Jia, X., Lou, Y., Dong, B., Tian, Z., and Jiang, S. (2010). 4D Computed tomography reconstruction from few-projection data via temporal non-local regularization. *Medical Image Comput.*, 13:143–150.
- [Jiang and Peng (2000)] Jiang, G.-S. and Peng, D. (2000). Weighted ENO schemes for Hamilton–Jacobi equations. *SIAM Journal on Scientific computing*, 21(6):2126–2143.
- [Juan *et al.* (2006)] Juan, O., Keriven, R., and Postelnicu, G. (2006). Stochastic motion and the level set method in computer vision: Stochastic active contours. *International Journal of Computer Vision*, 69(1):7–25.
- [Jung and Kleinheinz (2013)] Jung, S. and Kleinheinz, J. (2013). Angiogenesis-The key to regeneration. *Regenerative medicine and tissue engineering. InTech*, pages 453–73.
- [Kabienna (2015)] Kabienna, I. B. (2015). Simultaneous Iterative Reconstruction Technique by Selective Discrimination SIRT-DS. *International Journal of Innovative Research in Science, Engineering and Technology*, 4(10):10367–10374.
- [Kamphuis and Beekman (1998)] Kamphuis, C. and Beekman, F. J. (1998). Accelerated iterative transmission CT reconstruction using an ordered subsets convex algorithm. *Medical Imaging, IEEE Transactions on*, 17(6):1101–1105.

- [Kanis *et al.* (1994)] Kanis, J. A., Melton, L. J., Christiansen, C., Johnston, C. C., and Khaltaev, N. (1994). The diagnosis of osteoporosis. *Journal of bone and mineral research*, 9(8):1137–1141.
- [Kinahan and Rogers (1989)] Kinahan, P. E. and Rogers, J. (1989). Analytic 3D image reconstruction using all detected events. *Nuclear Science, IEEE Transactions on*, 36(1):964–968.
- [Kloeden and Platen (1992)] Kloeden, P. E. and Platen, E. (1992). Higher-order implicit strong numerical schemes for stochastic differential equations. *Journal of statistical physics*, 66(1-2):283–314.
- [Laskey (1996)] Laskey, M. A. (1996). Dual-energy X-ray absorptiometry and body composition. *Nutrition*, 12(1):45–51.
- [Launey *et al.* (2010)] Launey, M. E., Buehler, M. J., and Ritchie, R. O. (2010). On the mechanistic origins of toughness in bone. *Annual review of materials research*, 40:25–53.
- [Li *et al.* (2008)] Li, H., Zhang, H., Tang, Z., and Hu, G. (2008). Micro-computed tomography for small animal imaging: technological details. *Progress in natural science*, 18(5):513–521.
- [Liao and Herman (2001)] Liao, H. Y. and Herman, G. T. (2001). Automated estimation of the parameters of Gibbs priors to be used in binary tomography. *Electronic Notes in Theoretical Computer Science*, 46:393–412.
- [Liao and Herman (2004)] Liao, H. Y. and Herman, G. (2004). Automated estimation of the parameters of the Gibbs priors to be uses in binary tomography. *Discrete Applied Mathematics*, pages 249–170.
- [MELTON *et al.* (1989)] MELTON, L. J., KAN, S. H., FRYE, M. A., WAHNER, H. W., O’FALLON, W. M., and RIGGS, B. L. (1989). Epidemiology of vertebral fractures in women. *American Journal of Epidemiology*, 129(5):1000–1011.
- [Misch and Bortolotti (2009)] Misch, C. E. and Bortolotti, L. (2009). *Implantología contemporánea*. Elsevier España.
- [Morozov (1984)] Morozov, V. A. (1984). *Methods for solving incorrectly posed problems*. Springer-Verlag, Berlin-Heidelberg-New York-Toky.
- [Mory (2014)] Mory, C. (2014). *Tomographie cardiaque en angiographie rotationnelle*. PhD thesis, Lyon 1.
- [Mukundan *et al.* (2001)] Mukundan, R., Ong, S., and Lee, P. (2001). Discrete vs. continuous orthogonal moments for image analysis.
- [Müller and Rüegsegger (1994)] Müller, R. and Rüegsegger, P. (1994). Morphological validation of the 3D structure of non-invasive bone biopsies. *Bone Miner*, 25:S8.
- [Nadabar and Jain (1996)] Nadabar, S. G. and Jain, A. K. (1996). Parameter estimation in Markov random field contextual models using geometric models of objects. *Pattern Analysis and Machine Intelligence, IEEE Transactions on*, 18(3):326–329.
- [Natterer (1986)] Natterer, F. (1986). *The mathematics of computerized tomography*. Wiley-Teubner series in computer science. Vieweg+Teubner Verlag, UK.

- [Ng *et al.* (2010)] Ng, M. K., Weiss, P., and Yuan, X. (2010). Solving constrained total-variation image restoration and reconstruction problems via alternating direction methods. *SIAM Journal on Scientific computing*, 32:2710–2736.
- [Nuzzo *et al.* (2002)a] Nuzzo, S., Lafage-Proust, M. H., Martin-Badosa, E., Boivin, v., Thomas, v., Alexandre, C., and Peyrin, F. (2002a). Synchrotron radiation microtomography allows the analysis of three-dimensional micro-architecture and degree of mineralization of human Iliac Crest biopsies : effects of Etidronate treatment. *J Bone Min Research*, 17:1372–1382.
- [Nuzzo *et al.* (2002)b] Nuzzo, S., Peyrin, F., Cloetens, P., Baruchel, J., and Boivin, G. (2002b). Quantification of the degree of mineralization of bone in three dimension using synchrotron radiation microtomography. *Med Phys*, 19:2672–2681.
- [Palenstijn *et al.* (2013)] Palenstijn, W. J., Batenburg, K. J., and Sijbers, J. (2013). The ASTRA tomography toolbox. In *13th International Conference on Computational and Mathematical Methods in Science and Engineering, CMMSE*, volume 2013, page 40.
- [Panetta (2016)] Panetta, D. (2016). Advances in X-ray detectors for clinical and preclinical Computed Tomography. *Nuclear Instruments and Methods in Physics Research A*, 809:2–12.
- [Parpas and Rustem (2009)] Parpas, P. and Rustem, B. (2009). An algorithm for the global optimization of a class of continuous minimax problems. *Journal of Optimization Theory and Applications*, 141(2):461–473.
- [Peter and Peyrin (2011)] Peter, Z. and Peyrin, F. (2011). *Synchrotron Radiation Micro-CT Imaging of Bone Tissue, in Theory and Applications of CT Imaging and Analysis*.
- [Peyrin and Douek (2013)] Peyrin, F. and Douek, P. (2013). X-Ray Tomography. *Photon-Based Medical Imagery*, pages 161–205.
- [Peyrin and Engelke (2012)] Peyrin, F. and Engelke, K. (2012). CT imaging: Basics and new Trends. In *Handbook of Particle Detection and Imaging*, pages 883–915. Springer.
- [Peyré *et al.* (2011)] Peyré, G., Bougleux, S., and Cohen, L. D. (2011). Non-local regularization of inverse problems. *Inverse Problems and Imaging*, 5(2):511–530.
- [Prato and J.Zabczyk (1992)] Prato, G. and J.Zabczyk (1992). *Stochastic equations in infinite dimensions*, volume 152. Cambridge university press.
- [Prévôt and Röckner (2007)] Prévôt, C. and Röckner, M. (2007). *A concise course on stochastic partial differential equations*, volume 140. Springer.
- [Pérez and Heitz (1992)] Pérez, P. and Heitz, F. (1992). Une approche multiéchelle à l'analyse d'images par champs markoviens. *Traitemet du Signal*, 9(6):459–465.
- [Retraint *et al.* (1998)] Retraint, F., Peyrin, F., and Dinten, J. M. (1998). Three-dimensional regularized binary image reconstruction from three two-dimensional projections using a randomized ICM algorithm. *International journal of imaging systems and technology*, 9(2-3):135–146.
- [Rho *et al.* (1998)] Rho, J.-Y., Kuhn-Spearing, L., and Ziopoulos, P. (1998). Mechanical properties and the hierarchical structure of bone. *Medical engineering & physics*, 20(2):92–102.

- [Rit *et al.* (2014)] Rit, S., Oliva, M. V., Brousmiche, S., Labarbe, R., Sarrut, D., and Sharp, G. C. (2014). The Reconstruction Toolkit (RTK), an open-source cone-beam CT reconstruction toolkit based on the Insight Toolkit (ITK). In *Journal of Physics: Conference Series*, volume 489, page 012079. IOP Publishing.
- [Rit and Mory (2015)] Rit, S. and Mory, C. (2015). Rtk training. <http://training.kitware.fr/browse/116>.
- [Ritschl *et al.* (2011)] Ritschl, L., Bergner, F., Fleischmann, C., and Kachelriess, M. (2011). Improved total variation-based CT image reconstruction applied to clinical data. *Phys.Med.Biol.*, 56:1545–1561.
- [Rodan (1992)] Rodan, G. A. (1992). Introduction to bone biology. *Bone*, 13:S3–S6.
- [Rudin *et al.* (2013)] Rudin, L. I., Osher, S., and Fatemi, E. (2013). Nonlinear total variation based noise removal algorithms. *Phys.D.*, 60:259–268.
- [Rusko and Kuba (2005)] Rusko, L. and Kuba, A. (2005). Multi-resolution methods for binary tomography. *Electronics Notes in Discrete Mathematics*, 20:299–311.
- [Salomé *et al.* (1999)] Salomé, M., Peyrin, F., Cloetens, P., Odet, C. Laval-Jeantet, A. M., Baruchel, J., and Spanne, P. (1999). A Synchrotron Radiation Microtomography System for the Analysis of Trabecular Bone Samples. *Med. phys.*, 26(10):2194–2204.
- [Sato and Webster (2004)] Sato, M. and Webster, T. J. (2004). Nanobiotechnology: implications for the future of nanotechnology in orthopedic applications. *Expert review of medical devices*, 1(1):105–114.
- [Scarfe *et al.* (2006)] Scarfe, W. C., Farman, A. G., Sukovic, P., *et al.* (2006). Clinical applications of cone-beam computed tomography in dental practice. *Journal-Canadian Dental Association*, 72(1):75.
- [Schaffler and Burr (1988)] Schaffler, M. B. and Burr, D. B. (1988). Stiffness of compact bone: effects of porosity and density. *Journal of biomechanics*, 21(1):13–16.
- [Schüle *et al.* (2005)a] Schüle, T., Schnörr, C., Weber, S., and Hornegger, J. (2005a). Discrete tomography by convex-concave regularization and DC programming. *Discrete Applied Mathematics*, 151(1):229–243.
- [Schüle *et al.* (2005)b] Schüle, T., Schnörr, C., Webera, S., and Horneggerb, J. (2005b). Discrete tomography by convex-concave regularization and D.C programming. *Discrete Applied Mathematics*, 151:229–243.
- [Schüle *et al.* (2005)c] Schüle, T., Weber, S., and Schnörr, C. (2005c). Adaptive reconstruction of discrete-valued objects from few projections. *Electronic Notes in Discrete Mathematics*, 20:365–384.
- [Shi *et al.* (2010)] Shi, X., Liu, X. S., Wang, X., Guo, X. E., and Niebur, G. L. (2010). Type and orientation of yielded trabeculae during overloading of trabecular bone along orthogonal directions. *Journal of biomechanics*, 43(13):2460–2466.
- [Sidky *et al.* (2012)] Sidky, E. Y., Jørgensen, J. H., and Pan, X. (2012). Convex optimization problem prototyping for image reconstruction in computed tomography with the Chambolle–Pock algorithm. *Physics in medicine and biology*, 57(10):3065.

- [Sidky and Pan (2006)] Sidky, E. Y. and Pan, X. (2006). Accurate image reconstruction from few-views and limited-angle data in divergent-beam CT. *J.X-ray Sci. Techn.*, 14:119–139.
- [Sidky and Pan (2008)] Sidky, E. Y. and Pan, X. (2008). Image reconstruction in circular cone-beam computed tomography by constrained total variation minimization. *Phys.Med.Biol.*, 53:4777–4807.
- [Sixou *et al.* (2013)] Sixou, B., Wang, L., and Peyrin, F. (2013). Binary tomographic reconstruction of bone microstructure from few projections with level-set regularization. In *IEEE Symposium on Biomedical Imaging, San Francisco*.
- [Sixou and Peyrin (2012)] Sixou, B. and Peyrin, F. (2012). Reconstruction of bone microstructure from few projections with convex-concave and non local regularization. In *Biomedical Imaging (ISBI)*, pages 1443–1446, Barcelona, Spain.
- [Syn (2016)] (December 30, 2016). Synchrotron radiation. website. <http://rsc.riken.jp/eng/synchrotron/third.html>.
- [Szu and Hartley (1987)] Szu, H. and Hartley, R. (1987). Fast simulated annealing. *Physics letters A*, 122(3):157–162.
- [T.S.Chiang and S.J.Sheu (1987)] T.S.Chiang, C. and S.J.Sheu (1987). Diffusion for global optimization in  $\mathbb{R}^n$ . *SIAM J.Control Optim.*, 25:737–753.
- [Tai *et al.* (2007)] Tai, X.-C., Christiansen, O., Lin, P., and Skjælaaen, I. (2007). Image segmentation using some piecewise constant level set methods with MBO type of projection. *International Journal of Computer Vision*, 73(1):61–76.
- [Tai and Chan (2004)] Tai, X. C. and Chan, T. (2004). A survey on multiple level-set methods with applications for identifying piecewise constant functions. *International Journal of Numerical Analysis and Modeling*, 1:25–47.
- [Tao and An (1998)] Tao, P. D. and An, L. T. H. (1998). A DC optimization algorithm for solving the trust-region subproblem. *SIAM Journal on Optimization*, 8(2):476–505.
- [Tikhonov (1977)] Tikhonov, A. N. (1977). *Solutions of ill-posed problems*. Vh Winston.
- [Tikhonov *et al.* (2013)] Tikhonov, A. N., Goncharsky, A. V., Stepanov, V. V., and Yagola, A. G. (2013). *Numerical methods for the solution of ill-posed problems*, volume 328. Springer Science & Business Media.
- [Tsui *et al.* (1991)] Tsui, B. M., Zhao, X., Frey, E. C., and Gullberg, G. T. (1991). Comparison between ML-EM and WLS-CG algorithms for SPECT image reconstruction. *Nuclear Science, IEEE Transactions on*, 38(6):1766–1772.
- [Van Gompel *et al.* (2010)] Van Gompel, G., Batenburg, K. J., Van de Castele, E., Van Aarle, W., and Sijbers, J. (2010). A discrete tomography approach for super-resolution micro-CT images: application to bone. In *Biomedical Imaging: From Nano to Macro, 2010 IEEE International Symposium on*, pages 816–819. IEEE.
- [Vu and Knuiman (2002)] Vu, H. T. and Knuiman, M. W. (2002). A hybrid ML-EM algorithm for calculation of maximum likelihood estimates in semiparametric shared frailty models. *Computational statistics & data analysis*, 40(1):173–187.

- [Wang *et al.* (2014)] Wang, L., Sixou, B., and Peyrin, F. (2014). Binary tomography reconstructions of bone microstructure from few projections with stochastic level-set methods. In *Image Processing (ICIP)*, pages 1778–1782, Paris, France.
- [Wang *et al.* (2015)] Wang, L., Sixou, B., and Peyrin, F. (2015). Binary tomography reconstructions with stochastic level-set methods. *IEEE Signal Processing Letters*, 22(7):920–924.
- [Wang *et al.* (2016)] Wang, L., Sixou, B., Sit, S., and Peyrin, F. (2016). Binary Tomography Reconstruction From Few Projections With Level-set Regularization Methods For Bone Microstructure Study. *International Journal of Tomography and Simulation*, 29(1):1–17.
- [Weber *et al.* (2005)] Weber, S., Schüle, T., and Schnörr, C. (2005). Prior learning and convex-concave regularization of binary tomography. *Electronic Notes in Discrete Mathematics*, 20:313–327.
- [Wellington and Vinegar (1987)] Wellington, S. and Vinegar, H. (1987). X-Ray computerized tomography. *J. Petroleum technol.*, 8:885–898.
- [Wik (2015)] (December 22, 2015). Regularization. website. [https://en.wikipedia.org/wiki/Regularization\\_%28mathematics%29#Generalization](https://en.wikipedia.org/wiki/Regularization_%28mathematics%29#Generalization).
- [Wikipedia (2016)] Wikipedia (December 30, 2016). Scintillator. website. [https://en.wikipedia.org/wiki/Scintillator#Types\\_of\\_scintillators](https://en.wikipedia.org/wiki/Scintillator#Types_of_scintillators).
- [Yu and Wang (2010)] Yu, H. and Wang, G. (2010). A soft-threshold filtering approach for reconstruction from a limited number of projections. *Phys.Med.Biol.*, 55:3905–3916.
- [Zeng (2001)] Zeng, G. (2001). Image reconstruction—a tutorial. *Computerized Medical Imaging and Graphics*, 25(2):97–103.
- [Zhuge *et al.* (2015)] Zhuge, X., Palenstijn, W. J., and Batenburg, K. (2015). TVR-DART: a more robust algorithm for discrete tomography from limited projection data with automated gray value estimation.



**FOLIO ADMINISTRATIF**

THESE SOUTENUE DEVANT l'INSTITUT NATIONAL DES SCIENCES APPLIQUEES DE LYON

---

**NOM:** WANG

**DATE de SOUTENANCE:** 08/06/2016

**prénom:** lin

**TITRE :** Binary tomography reconstruction of bone microstructures from a limited number of projections

---

**NATURE:** Doctoral

**Numéro d'ordre:** 2016-LYSEI-048

**Ecole doctoral:** ÉLECTRONIQUE, ÉLECTROTECHNIQUE, AUTOMATIQUE

---

**RESUME:**

Discrete tomography reconstruction of bone microstructure is important in diagnosis of osteoporosis. One way to reduce the radiation dose and scanning time in CT imaging is to limit the number of projections. This method makes the reconstruction problem highly ill-posed. A common solution is to reconstruct only a finite number of intensity levels. In this work, we investigate only binary tomography reconstruction problem. First, we consider variational regularization methods. Two types of Total Variation (TV) regularization approaches minimized with the Alternate Direction of Minimization Method (ADMM) and two schemes based on Level-set (LS) regularization methods are applied to two experimental bone cross-section images acquired with synchrotron micro-CT. The numerical experiments have shown that good reconstruction results were obtained with TV regularization methods and that level-set regularization outperforms the TV regularization for large bone image with complex structures. Yet, for both methods, some reconstruction errors are still located on the boundaries and some regions are lost when the projection number is low. Local minima were obtained with these deterministic methods. Stochastic perturbations is a useful way to escape the local minima. As a first approach, a stochastic differential equation based on level-set regularization was studied. This method improves the reconstruction results but only modifies the boundaries between the 0 and 1 regions. Then partial stochastic differential equation obtained with the TV regularization semi-norm were studied to improve the stochastic level-set method. The random change of the boundary are performed in a new way with the gradient or wavelet decomposition of the reconstructed image. Random topological changes are included to find the lost regions in the reconstructed images. At the end of our work, we extended the TV regularization method to 3D images with real data on RTK (Reconstruction Toolkit). And we also extended the level-set to the multi-level cases.

---

**MOTS-CLES**

X-ray imaging, discrete tomography, inverse problem, TV regularization, level-set regularization, stochastic diffusion

---

**INTITULE ET ADRESSE DE L'U.F.R. OU DU LABORATOIRE**

Université de Lyon, CREATIS ; CNRS UMR5220 ; Inserm U1044 ; INSA-Lyon ; Université Lyon 1, 7 Av. Jean Capelle, 69621 VILLEURBANNE, France.

---

**Directeur de thèse:** Bruno Sixou, Maitre de conferences HDR

**Co-directeur de thèse:** Françoise Peyrin, Directeur de recherche CREATIS

---

**COMPOSITION DU JURY:**

**Thomas Rodet**

Professeur à l'ENS Cachan rattaché au SATIE

Rapporteur

**Jan Sijbers**

Professeur de University of Antwerp

Rapporteur

**Ali Mohammad-Djafari**

Directeur de recherche au LSS-CNRS

Examinateur

**Bruno Sixou**

Maitre de conferences HDR, INSA de Lyon

Directeur de thèse

**Françoise Peyrin**

INSA Lyon, Directrice de recherche CREATIS

Co-directeur de thèse

Cette thèse est accessible à l'adresse : <http://theses.insa-lyon.fr/publication/2016-LYSEI-048/thesis.pdf>